SEISMIC RESPONSE AND DESIGN OF SUBASSEMBLIES FOR MULTI-STOREY PRESTRESSED TIMBER BUILDINGS

Md Asif Iqbal

A thesis presented in partial fulfilment of the requirements for the degree of

Doctor of Philosophy

in

Civil Engineering

at the

University of Canterbury

Christchurch, New Zealand

July 2011

To my parents

Abstract

Timber has experienced renewed interests as a sustainable building material in recent times. Although traditionally it has been the prime choice for residential construction in New Zealand and some other parts of the world, its use can be increased significantly in the future through a wider range of applications, particularly when adopting engineered wood material, Research has been started on the development of innovative solutions for multi-storey non-residential timber buildings in recent years and this study is part of that initiative. Application of timber in commercial and office spaces posed some challenges with requirements of large column-free spaces. The current construction practice with timber is not properly suited for structures with the aforementioned required characteristics and new type of structures has to be developed for this type of applications.

Any new structural system has to have adequate capacity for carry the gravity and lateral loads due to occupancy and the environmental effects. Along with wind loading, one of the major sources of lateral loads is earthquakes. New Zealand, being located in a seismically active region, has significant risk of earthquake hazard specially in the central region of the country and any structure has be designed for the seismic loading appropriate for the locality.

There have been some significant developments in precast concrete in terms of solutions for earthquake resistant structures in the last decade. The “Hybrid” concept combining post-tensioning and energy dissipating elements with structural members has been introduced in the late 1990s by the precast concrete industry to achieve moment-resistant connections based on dry jointed ductile connections. Recent research at the University of Canterbury has shown that the concept can be adopted for timber for similar applications. Hybrid timber frames using post-

tensioned beams and dissipaters have the potential to allow longer spans and smaller cross sections than other forms of solid timber frames. Buildings with post-tensioned frames and walls can have larger column-free spaces which is a particular advantage for non-residential applications.

While other researchers are focusing on whole structural systems, this research concentrated on the analysis and design of individual members and connections between members or between member and foundation. This thesis extends existing knowledge on the seismic behaviour and response of post-tensioned single walls, columns under uni-direction loads and small scale beam-column joint connections into the response and design of post-tensioned coupled walls, columns under bi-directional loading and full-scale beam-column joints, as well as to generate further insight into practical applications of the design concept for subassemblies. Extensive experimental investigation of walls, column and beam-column joints provided valuable confirmation of the satisfactory performance of these systems. In general, they all exhibited almost complete re-centering capacity and significant energy dissipation, without resulting into structural damage. The different configurations tested also demonstrated the flexibility in design and possibilities for applications in practical structures.

Based on the experimental results, numerical models were developed and refined from previous literature in precast concrete jointed ductile connections to predict the behaviour of post-tensioned timber subassemblies. The calibrated models also suggest the values of relevant parameters for applications in further analysis and design. Section analyses involving those parameters are performed to develop procedures to calculate moment capacities of the subassemblies.

The typical features and geometric configurations the different types of subassemblies are similar with the only major difference in the connection interfaces. With adoption of appropriate values representing the corresponding connection interface and incorporation of the details of geometry and configurations, moment capacities of all the subassemblies can be calculated with the same scheme. That is found to be true for both post-tensioned-only and hybrid specimens and also applied for both uni-directional and bi-directional loading. The common section analysis and moment capacity calculation procedure is applied in the general design approach for subassemblies.

Acknowledgements

I want to express my gratitude towards my supervisors Associate Professor Stefano Pampanin and Professor Andy Buchanan for their guidance, support and encouragements during the course of this research. I am also grateful to Dr. Alessandro Palermo of University of Canterbury and Dr. Massimo Fragiacomo of University of Sassari, Italy for their help and advices.

This research was financially supported initially by Forest Industries Development Agenda and by Structural Timber Innovation Company (STIC) for the last two years. The materials used for experimental testing was supplied by Carter Hold Harvey. Their support is gratefully acknowledged.

I would to thank my fellow researchers at the University, in particular Mike Newcombe, Tobias Smith, Mike Cusiel, Alejandro Amaris and Dion Marriott. Their assistance at different times has been most helpful. I have to mention the help and support from the staff and technicians of the department throughout my time university. It would have been impossible for me to carry out the research without them. I have also received help from many past and present students, including some exchange students from Europe, over the past few years. They are too many to be named here but I am indebted to all of them.

I cannot appreciate enough the assistance from my wife Shahana, not only with help at home but also through continuous support and encouragements. I also want to thank my son Omar and my daughter Zainab for their endurance during the evenings and sometimes over the weekends, particularly in the last few months.

Table of Contents

List of Figures

List of Tables

List of Symbols

c	Depth of neutral axis
θ_{imp}	Imposed rotation at the rocking interface
ε_{pt}	Strain in the post-tensioning tendons
Δ_{pt}	Deformation in the post-tensioning tendons
l_{ub}	Unbonded length of post-tensioning tendons
ε_s	Strain in the mild steel or energy dissipaters
Δ_s	Deformation in the energy dissipaters
l'_{ub}	Unbonded length of energy dissipaters
C	Total compression force
C_s	Compression force in energy dissipaters
T_s	Tension force in energy dissipaters
T_{pt}	Tension force in post-tensioning tendons
λ	Re-centering ratio = $(M_{pt}+M_N)/M_s$
M_{pt}	Moment contribution from post-tensioning
M_s	Moment contribution from energy dissipaters

M_N Moment contribution from axial load

α_0 Steel reinforcement over-strength used as minimum value of re-centering ratio

l_w Width of wall

x_{pt} Distance of tendon from the centre of wall

$\varepsilon_{pt,t}$ Strain in post-tensioning tendons in tension

$\Delta_{pt,t}$ Deformation in post-tensioning tendons in tension

$\varepsilon_{pt,c}$ Strain in post-tensioning tendons in compression

$\Delta_{pt,c}$ Deformation in post-tensioning tendons in compression

$\varepsilon_{pt,i}$ Strain in post-tensioning tendon due to initial prestressing

ε_y Yield strain in post-tensioning tendon

$T_{pt,i}$ Initial tension in post-tensioning tendons

A_{pt} Area of post-tensioning tendons

E_{pt} Modulus of elasticity of post-tensioning tendons

ρ_{pt} Ratio of initial prestressing to yield stress of tendons

ε_t Strain in timber extreme fibre

L_{cant} Shear span of member

ϕ_{dec} Decompression curvature

N Axial load on member

E_{con} Modulus of elasticity of connection

b Width of member section

h Height of member section

f_c Compressive stress of timber

$\varepsilon_{y,t}$ Yield strain of timber

C_t Compressive force in timber

A_s Area of energy dissipaters

ϕ Reduction factor used in design ϕMn$\geq M^*$

M_n Nominal Moment (Capacity)

M^* Moment demand /

H_e Effective height of the structure

V_s Force in the U-shape Flexural Plates (UFP)

n Number of UFP

b Width of UFP

D Diameter of UFP

t Thickness of UFP

F_y Yield force of UFP

1 INTRODUCTION

1.1 Background

Traditionally timber has been the prime material for residential buildings in New Zealand. At the moment, more than 90% New Zealanders live in timber houses. The traditional houses are one or two-storied with light timber frames (Figure 1.1).

Figure 1.1 Traditional timber building constructions in New Zealand

Since the last decade of the twentieth century and particularly in the new millennium, with incremental demand for resources, there also has been an ever-increasing awareness about sustainable development for the welfare of the global environment. People and governments have been searching for the best possible ways to minimize the effects of global warming. One of the practical measures towards achieving that is to encourage use of carbon-sink material like timber. The building industry is one area that uses timber in significant quantities and has the potential to increase the amount in the near future. As a local material, it is also cost-effective in New Zealand. These facts have led the government to put extra emphasis on use of timber in the building industry.

Some multi-storey timber buildings have been constructed in New Zealand and other countries in recent times. As the height of the building increases with number of stories, it becomes more and more important to provide lateral resistance capacity to the building structural skeleton to resist the forces from environmental effects like strong wind and earthquakes. Typical multi-story buildings mostly use short span floors supported on plywood-sheathed shear walls for lateral resistance (Figure 1.2). These walls have limited openings which is not an attractive aspect from an architectural and serviceability point of view.

Figure 1.2 Multi-storey timber building in Canada with plywood shear walls (Courtesy: A. H. Buchanan)

The building industry has been trying to implement other types of construction to overcome this problem One practical option is to share the lateral loads between structural walls and frames which will reduce the demand on the walls thereby help reducing their sizes. In that case the frames have to be capable of resisting lateral forces, which will require proper moment-resisting capacities in the connections, in addition to carrying the gravity loads.

A major problem in design of multi-storey buildings in timber has been the difficulty of achieving proper moment-resisting frames. Several alternative solutions to provide moment-

resisting connections in timber construction have been studied and developed, for both lateral load resisting wall and frame systems (Halliday & Buchanan, 1993; Thomas, et al., 1993). Depending on the type of connection and structural details, alternative arrangements of mechanically fastened solutions ranging from nailed, bolted or dowel connections to glued or epoxied steel rods (Figure 1.3) are available for solid sawn timber in large sizes, glue laminated timber (glulam), or Laminated Veneer Lumber (LVL). Unfortunately these solutions have not found wide-spread applications in practical building structures, due to their general lack of cost-effectiveness and less-than- simple constructability.

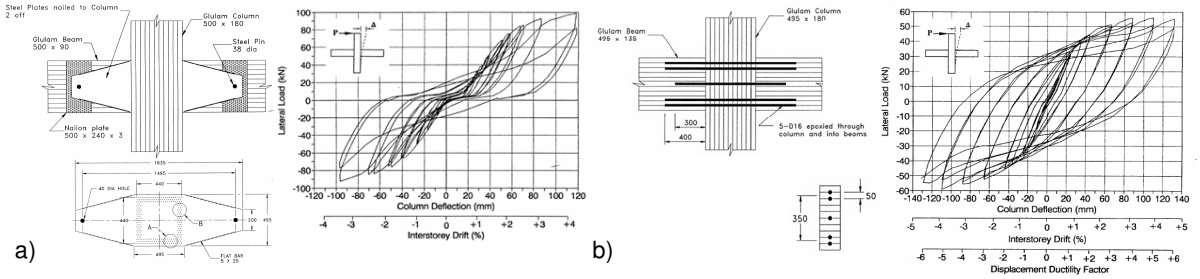

Figure 1.3 Connection details for frame systems a) multiple-nailed connection; b) epoxied rods glulam solution (Buchanan and Fairweather 1993)

As New Zealand is located in an active seismic region, timber buildings have to withstand the potential seismic loading and so proper seismic design of timber buildings is essential. In an overview of seismic resisting solutions for multi-storey glulam timber buildings, (Buchanan & Fairweather, 1993) proposed alternative arrangements for steel epoxied connections with or without additional steel sacrificial brackets to accommodate the inelastic behaviour. The multi-nailed connections in frames showed pinching (Figure 1.3a) while the epoxied rod connection (Figure 1.3b) showed satisfactory behaviour under cyclic loading with a stable dissipating hysteresis loop and limited stiffness degradation. However excessive residual (permanent) deformations would be expected after an earthquake event, with the difficulty of straightening the building to its original position.

There have been some significant new developments in the precast concrete industry in the late 1990s that have been notified by the structural engineering community. The joint US-Japan PRESSS (PREcast Seismic Structural Systems) research project (Priestley, 1991; Priestley, et al., 1999) provided practical solutions for practical building structures. The "Hybrid" systems (Stanton, et al., 1997) introduced by the PRESSS program with unbonded post-tensioning and energy dissipation systems is an exciting and structurally very promising solution for frames and walls designed for seismic regions. Although the idea was originally developed for concrete, it has the potential to be applied in other materials as well.

At present the timber industry is in a good position to adopt the PRESSS technology. Engineered timber product in the form of Laminated Veneer Lumber (LVL) is already available which has strengths comparable to concrete. It is possible to design and produce prefabricated LVL sections in large quantities in the factory with necessary arrangements for prestressing. So the practical facilities for design and construction of prefabricated timber buildings are available at present. As an added incentive, compared to tradition timber construction it should be easier and faster to build buildings applying this technology, which will result in significant savings in cost and time. Hybrid timber frames using post-tensioned beams and non-prestressed reinforcement (possibly acting as dissipaters when and if required) have the potential to allow longer spans and smaller cross sections than other forms of solid timber frames. Buildings with post-tensioned frames and walls can have larger column-free spaces which is a particular advantage for non-residential applications like offices.

The concept of hybrid systems in timber was developed at the University of Canterbury (Palermo, et al., 2005a). Over the past few years experimental studies have been first performed on small-scale wall, column and beam-column joint subassemblies (Palermo, et al., 2006a;

Palermo, et al., 2006b; Palermo, et al., 2006c). Procedures for modelling the behaviour of the connections have been developed through subsequent analytical studies of the subassemblies (Newcombe, et al., 2008a, 2008b). Research has been ongoing into global response of building frames and walls systems. As part of the investigation, experimental work on a 2/3-scale two-storied complete timber building model with frames and walls have been completed recently (Newcombe, et al., 2010a, 2010b). Analytical work is currently underway to develop a design procedure for this type of structures (Newcombe, et al., 2010).

While other researchers are focusing on whole structural systems, this research is concentrating on analysis and design of individual members and connections between members or between member and foundation. This thesis extends existing knowledge on the seismic behaviour and response of post-tensioned single walls, columns under uni-direction loads and small scale beam-column joint connections into the response and design of post-tensioned coupled walls, columns under bi-directional loading and full-scale beam-joints, as well as to generate further insight into practical applications of the design concept for subassemblies.

1.2 Objectives

The overall objective of this study is to develop methods of analysis and design for selected subassemblies of post-tensioned multi-storey timber buildings for seismic loading. The three structural subassemblies investigated in this research are:

1. post-tensioned walls,
2. post-tensioned columns and
3. post-tensioned beam-column joints.

The study has the following specific objectives:

- To define the seismic behaviour of each of the three subassemblies through experimental investigation

- To develop numerical models for each of the subassemblies, calibrated from the experimental results

- To formulate a detailed calculation scheme for predicting the structural capacity of each type of subassembly, using the numerical models

- To propose a general design procedure for each type of subassembly

1.3 Scope of the Research

This research involves timber frames and walls using hybrid or PRESSS-technology, thus based on unbonded post-tensioning techniques. Other types of systems such as ductile nailed connections or light timber frames are not considered herein. Only seismic lateral loads are considered in this research. The subassemblies are design for ultimate moment capacity only. Serviceability and shear capacity are not checked.

The general procedure for analysis and design of structures can be carried out as a two-level approach. While global analysis is performed with the whole building structures or complete structural systems from the structure, individual members or subassemblies are subject to local subassembly analysis.

Although these two different analyses are mutually dependent, since the member sections used in global analysis are based on analysis of individual members and each individual member has to

be analyzed and designed to meet the requirements put forward by the global analysis, the procedures are significantly different and they can be performed separately.

This study focuses on behaviour of subassemblies, three types in particular: walls, columns and beam-column joints. Two of the subassemblies: walls and beam-column joint have been investigated only as two-dimensional structures, hence for in-plane loading. The columns have been studied for both uni-directional and bi-directional loading.

1.4 Organization of the Thesis

Existing literature is reviewed in Chapter 2 to present the development and the state-of- the-art in post-tensioned timber technology. References have been made to related and still on-going research with other materials, especially reinforced concrete, using similar concepts.

Chapter 3 explains the basic theory of hybrid connection theory as proposed by the PRESSS program and further more recent developments. The procedure is summarised and additional aspects regarding application of the concept in timber are discussed.

Chapter 4, 5 and 6 gives details and results of the experimental studies that have been performed on the three types of subassemblies. Chapter 4 describes the experimental work on walls, while Chapters 5 and 6 details the investigations with Column and Beam-Column Joint respectively.

In Chapter 7 the experimental results are analyzed to develop numerical models of the tested structures. The results from numerical studies are compared with experimental results to validate the numerical models.

Based on the underlying concepts described in Chapter 3, section analyses of the tested subassemblies are performed in Chapter 8. The specimens used in the experimental study are

analyzed for calculation of the moment-rotation capacity and evaluation of the material stresses. Each of the different configurations of the three types of subassemblies has been investigated individually. The section analysis procedure is then extended to a generalized type of subassembly. A common procedure has been developed that can be followed for calculation of moment capacities of all the different subassemblies varying in type and configuration. A design approach with an example involving different options is also presented.

Chapter 9 presents the findings and conclusions of the research along with some recommendations for future study.

2 REVIEW OF RECENT INVESTIGATIONS

2.1 Introduction

There has been a significant amount of research done in the last few decades on seismic design of timber structures. In general, efforts have been focused towards developing ductility in moment resisting connections in order to achieve better performance during earthquakes. The relevant developments in these areas during the recent past are presented in chronological order and discussed

2.2 Moment Resisting Connections in Timber

2.2.1 Frames

As already mentioned in the previous chapter, a number of connections types have been developed in the last two decades for different types of timber structures. Ceccotti (1989) has done extensive research on connections using concentric rings of dowels, particularly for knee-joints in portal frames. The connections exhibited ductile behaviour (Figure 2.1) but developed slackness with rotation of the joint due to crushing of the timber surrounding the dowels.

Studies on a number of different connection types with glulam timber have been reported by Buchanan and Fairweather (Buchanan & Fairweather, 1993).

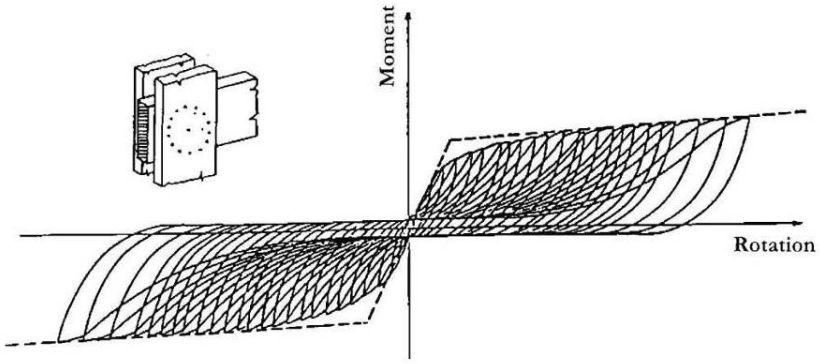

Figure 2.1 Hysteretic response of a dowelled connection (Ceccotti, 1989)

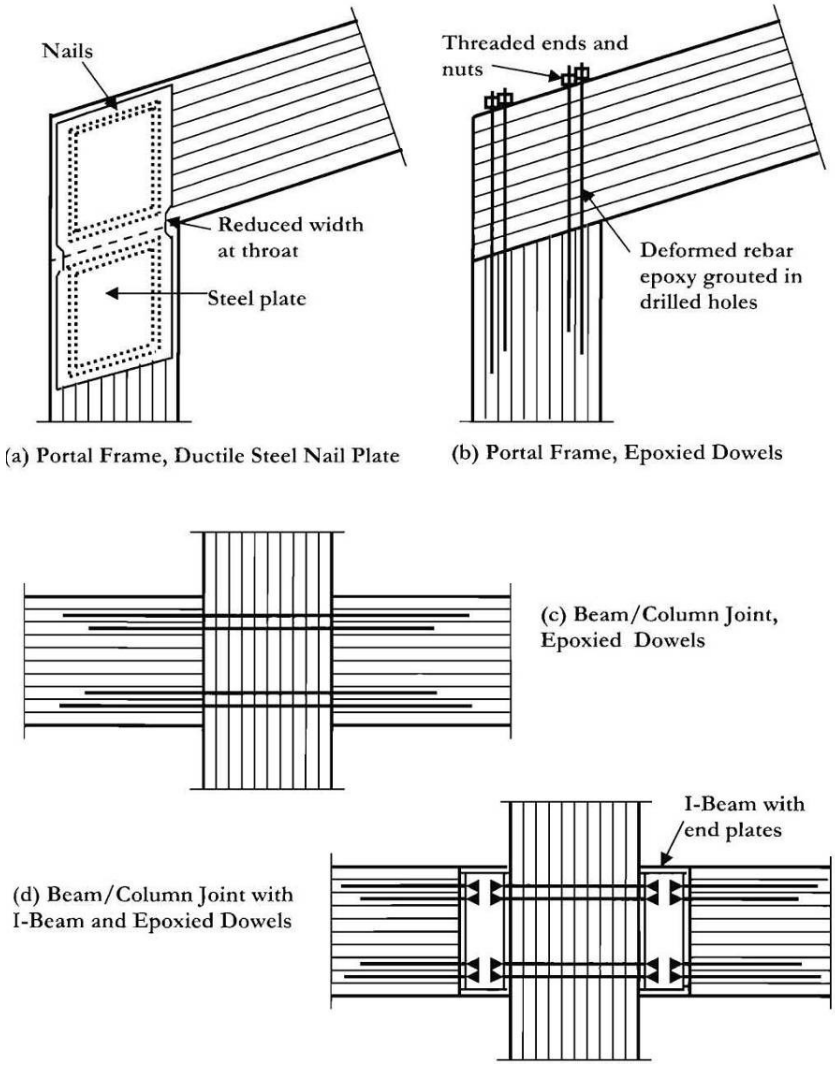

Figure 2.2 Ductile connections for glulam frames (after Buchanan and Fairweather1993)

This included steel nail plates (Figure 2.2a): the connection showed high energy absorption because of yielding of the necked steel plates. But there can be significant residual deformation and possible buckling of plates at high strain levels in the joint.

Another solution that was investigated involved reinforcing bars anchored within timber member with epoxy grout (Figure 2.2b). To absorb energy, the bars are designed to yield in alternate tension and compression during joint rotation. Epoxied bars were also implemented in beam-column joints (Figure 2.2c). While stable dissipating hysteresis loops and limited stiffness degradation can be found with the connection, excessive residual deformations could be expected after cyclic loading.

A modified concept with the epoxied bars attached to Steel I-sections between the members has been tested in timber connections (Figure 2.2d). In this case the steel sections are expected to yield to provide energy dissipation. Multiple nailed connections (Figure 2.3) in walls showed pinching phenomena in the hysteresis behaviour.

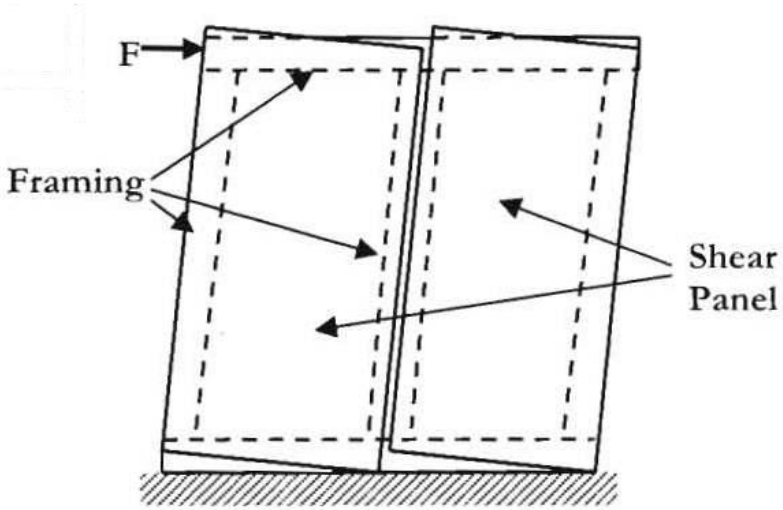

Figure 2.3 Nailed connections in walls

2.2.2 Walls

Nailed connections have been widely studied and implemented as a practical solution for multi-storey timber building. Experimental studies on plywood sheathed shear walls were, amongst others, carried out by (Deam, 1997; Filiatrault, et al., 2002; Filiatrault & Folz, 2002; Stewart, 1987). As in the case with frames, typical pinching hysteretic behaviour was observed (Figure 2.4 and 2.5).

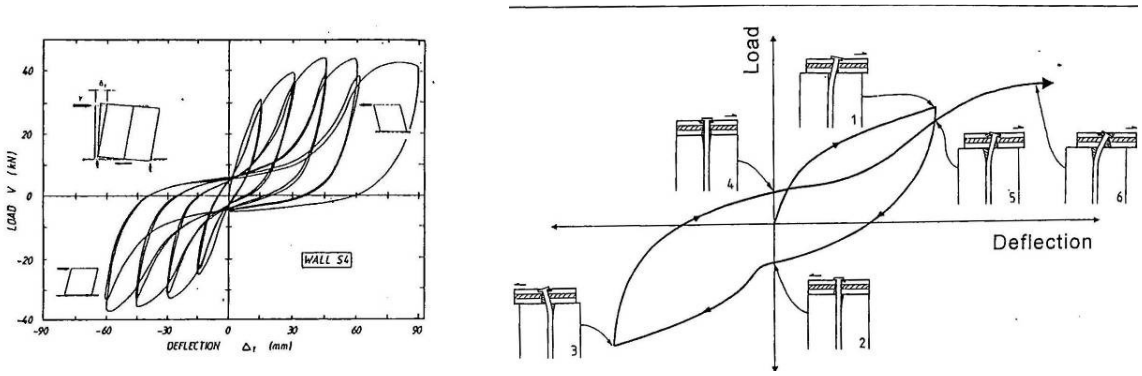

(a) (b)

Figure 2.4 Load-deflection plots of nailed wall connections (a) (Stewart, 1987) b) (Deam, 1997))

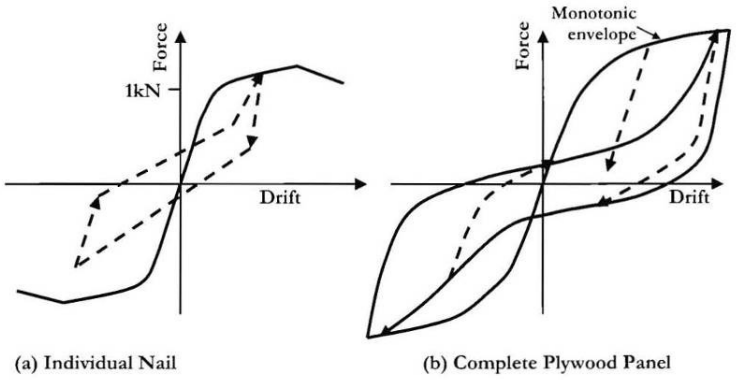

Figure 2.5 Hysteretic response of nailed plywood panel (Filiatrault & Folz, 2002)

Among the moment-resisting connections (Figure 2.5) discussed so far the multi-nailed connections exhibit stiffness degradation and pinching behaviour with local damage. The residual deformation may be relatively small due to the pinching. The epoxied rods or steel gusset plates (Figure 1.3), on the other hand, produce more energy dissipation but with significant residual deformations. Although the above mentioned moment-resisting connections posses ductility and thereby some level of energy dissipation capacity, they would exhibit either substantial structural damage or significant residual displacements after considerable cyclic loading from a major earthquake. Recent studies on performance-based seismic design and assessment procedures (Christopoulos, et al., 2003; MacRae & Kawashima, 1997) have emphasized the importance of limiting residual deformations due to consequent high repair costs.

2.3 Jointed Ductile Connections in Precast Concrete

In the early 1990s researchers in United States and Japan collaborated to launch a major research program on seismic applications of precast concrete. The PRESSS (PREcast Structural Seismic Systems) program had the objectives "to develop comprehensive and rational design recommendations needed for a broader acceptance of precast concrete construction in different seismic zones" and "to develop new materials, concepts, and technologies for precast concrete construction in different seismic zones" (Priestley, et al., 1999).

A new precast seismic resisting system called "Hybrid System" (Stanton, et al., 1997) was developed for both frames and wall from the research carried out under the project. The system comprising of precast elements connected by unbonded post tensioning steel and bonded reinforcing bars, has excellent seismic performance. There is a rocking motion between members resulting in a gap opening at the connection interface and inelastic deformation is accommodated through yielding of the reinforcement, resulting in no damage to the structural elements.

The hybrid system exhibits re-centering as well as energy dissipation. The unbonded post-tensioning offers re-centering and internally grouted mild steel bars provide energy dissipation. The energy dissipation may also come from external dissipation devices if they are used in place of internal steel bars. The system is characterised by a recentering dissipating hysteresis behaviour also referred to as "flag-shaped" (Figure 2.6).

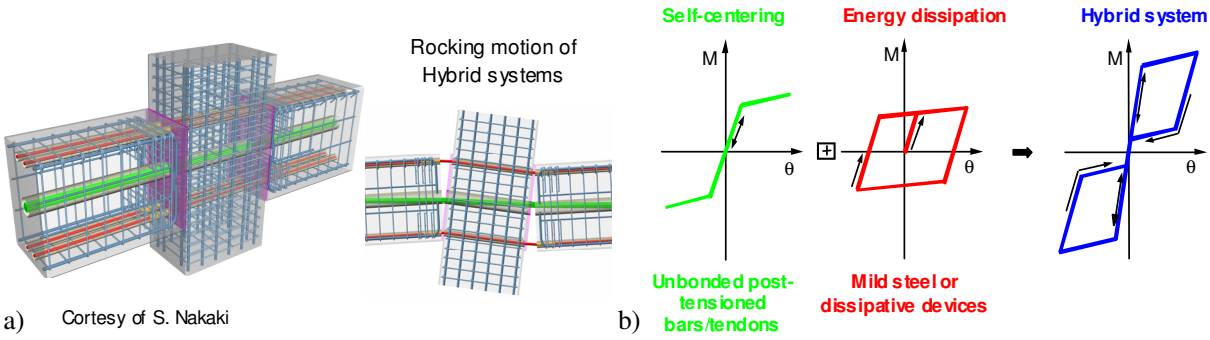

Figure 2.6 a) Hybrid systems developed under the PRESSS programme; b) idealized "flag-shaped" hysteresis behaviour in a hybrid connection (fib, 2003, NZS3101:2006)

The hybrid concept had also been implemented with external energy dissipation devices in place of internal reinforcing in concrete. In wall systems, external coupling devices were attached to the walls to dissipater energy during rocking of the walls. Several different arrangements of connectors to couple adjacent precast post-tensioned concrete wall panels were tested at National Institute of Standards and Testing (NIST) (Priestley, 1996; Schultz & Magana, 1996).

Different designs of welded loose plates and bolted ductile connections were adopted in vertical connections, incorporating flexural yield, tension/compression yield (TCY), shear yield (SY) and friction sliding/coulomb friction (CF) as the basic concept (Figure 2.7). These dissipative mechanisms were activated by the relative displacement of the adjacent walls during the rocking motion (Figure 2.8). The U-shaped flexural plates showed, amongst the others, particularly stable hysteretic behaviour without evident losses of stiffness or strength at high level of deformations.

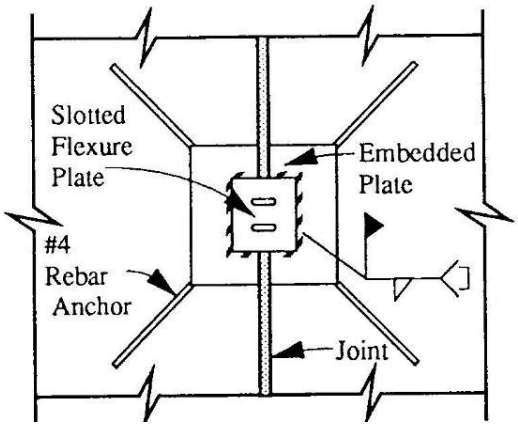

a) Slotted flexure plate (SFP)

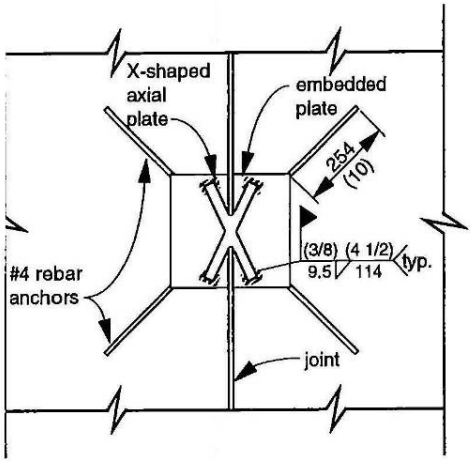

b) X-shaped axial plate (XAP)

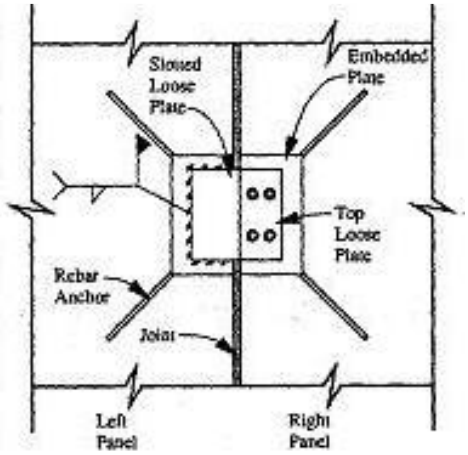

c) Vertical joint friction (VJF) connection

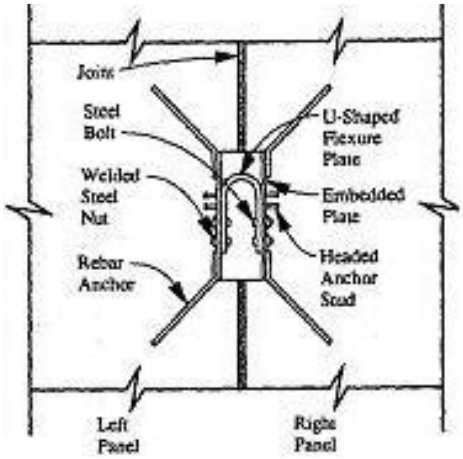

d) U-shaped flexure plate (UFP) connection

Figure 2.7 Alternative connectors/dissipaters between coupled walls for precast concrete walls as part of the PRESSS Program (Priestley, 1996; Schultz & Magana, 1996)

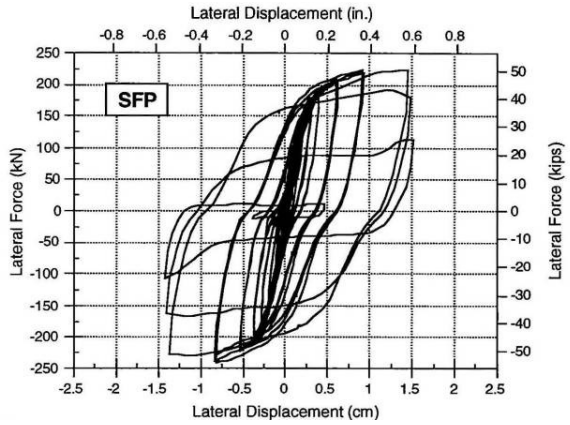

a) Slotted flexure plate (SFP)

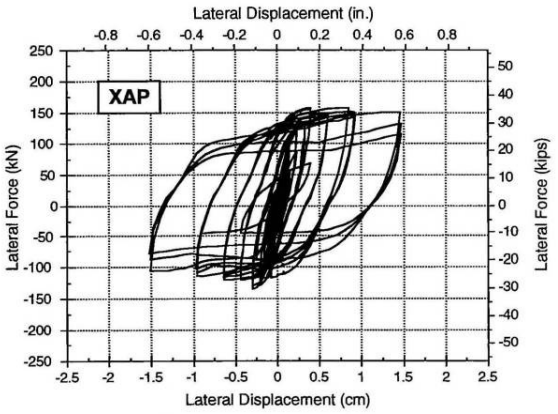

b) X-shaped axial plate (XAP)

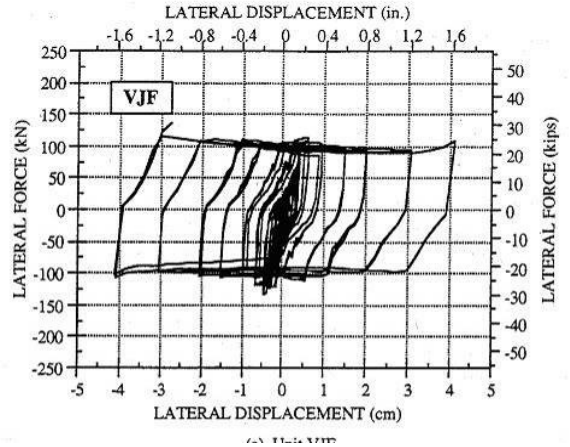

c) Vertical joint friction (VJF) connection

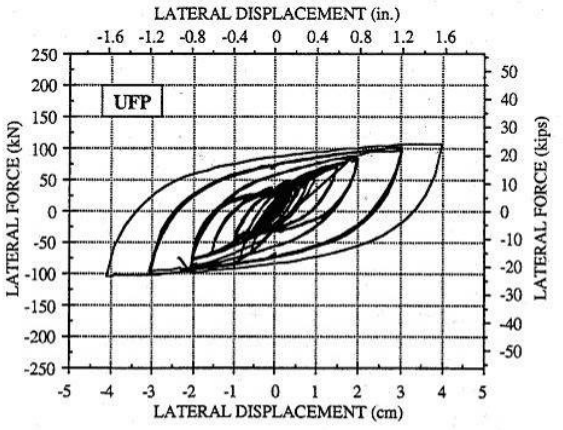

d) U-shaped flexure plate (UFP) connection

Figure 2.8 Load-displacement response of alternative connectors/dissipaters between coupled walls for precast concrete walls (Schultz & Magana, 1996)

Near the end of the PRESSS project in the late 90s, a 60% scale model of a five-storey precast/prestressed concrete building (Figure 2.9) was experimentally tested at UCSD (Priestley, et al., 1999), implementing state-of-the-art technology including the developments made during earlier stages of the project.

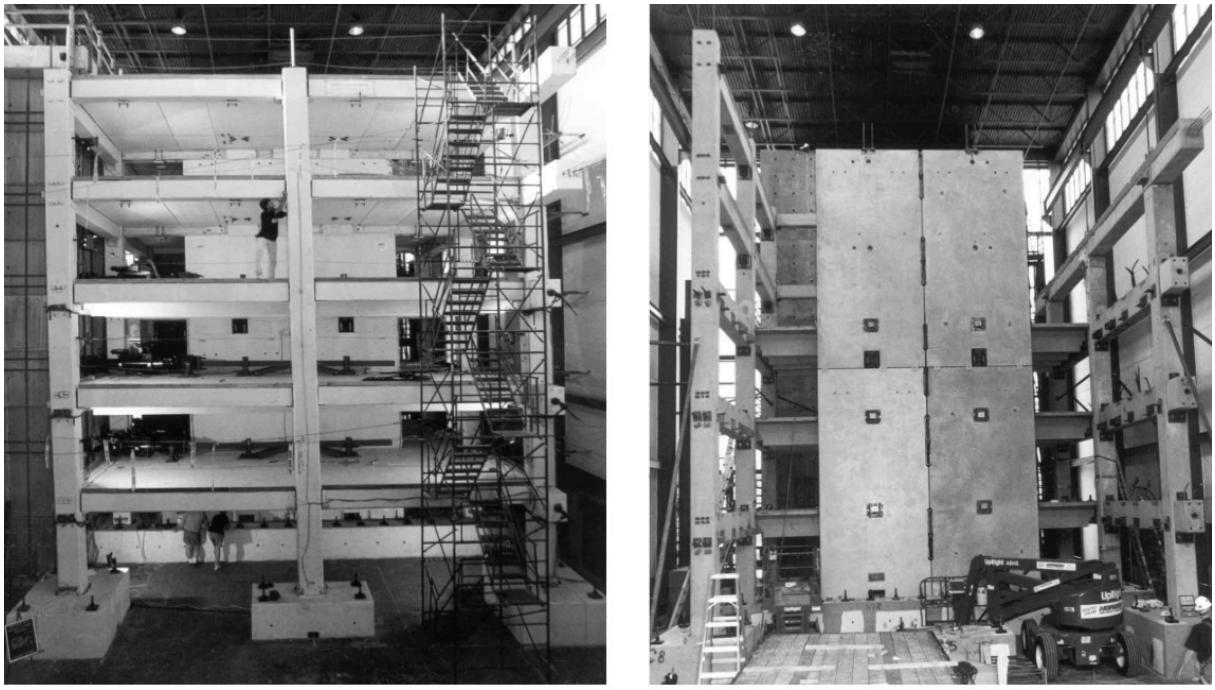

Figure 2.9 Five storey precast post-tensioned frame building (Priestley, et al., 1999)

The PRESSS program involved a number of research groups across United States. Extensive analytical investigations on unbonded post-tensioned precast concrete systems were carried out at Lehigh University. (Kurama, et al., 1999) studied wall (Figure 2.10) while analytical work on frames (Figure 2.11) was performed by El-Sheikh and others (El-Sheikh, et al., 1999).

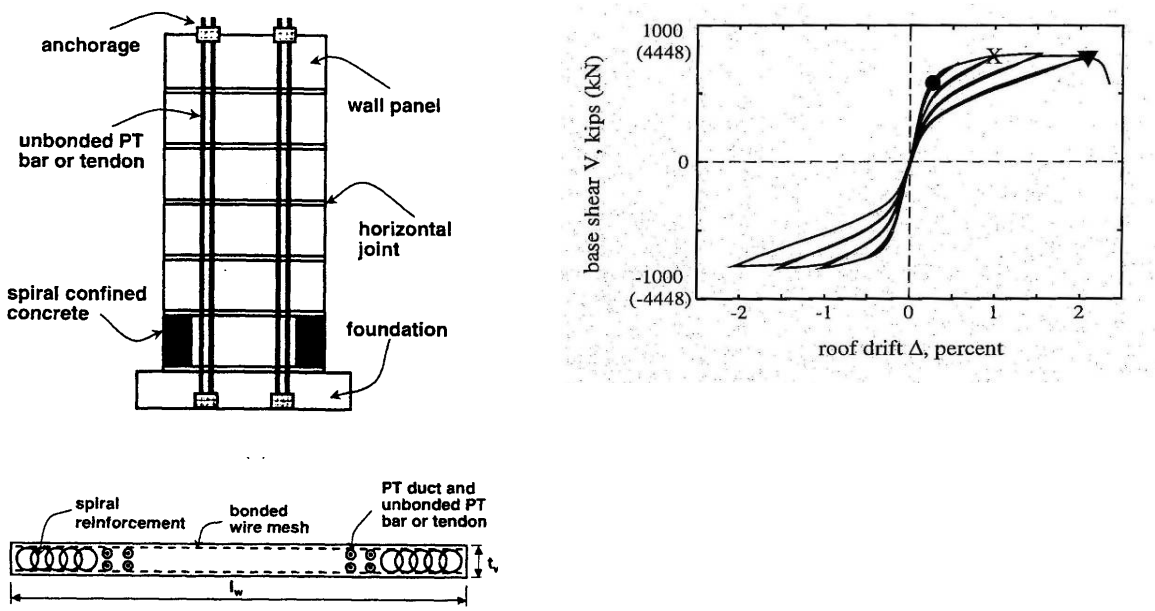

Figure 2.10 Details of Wall and load-drift plot of model studied by Kurama ((Kurama, et al., 1999))

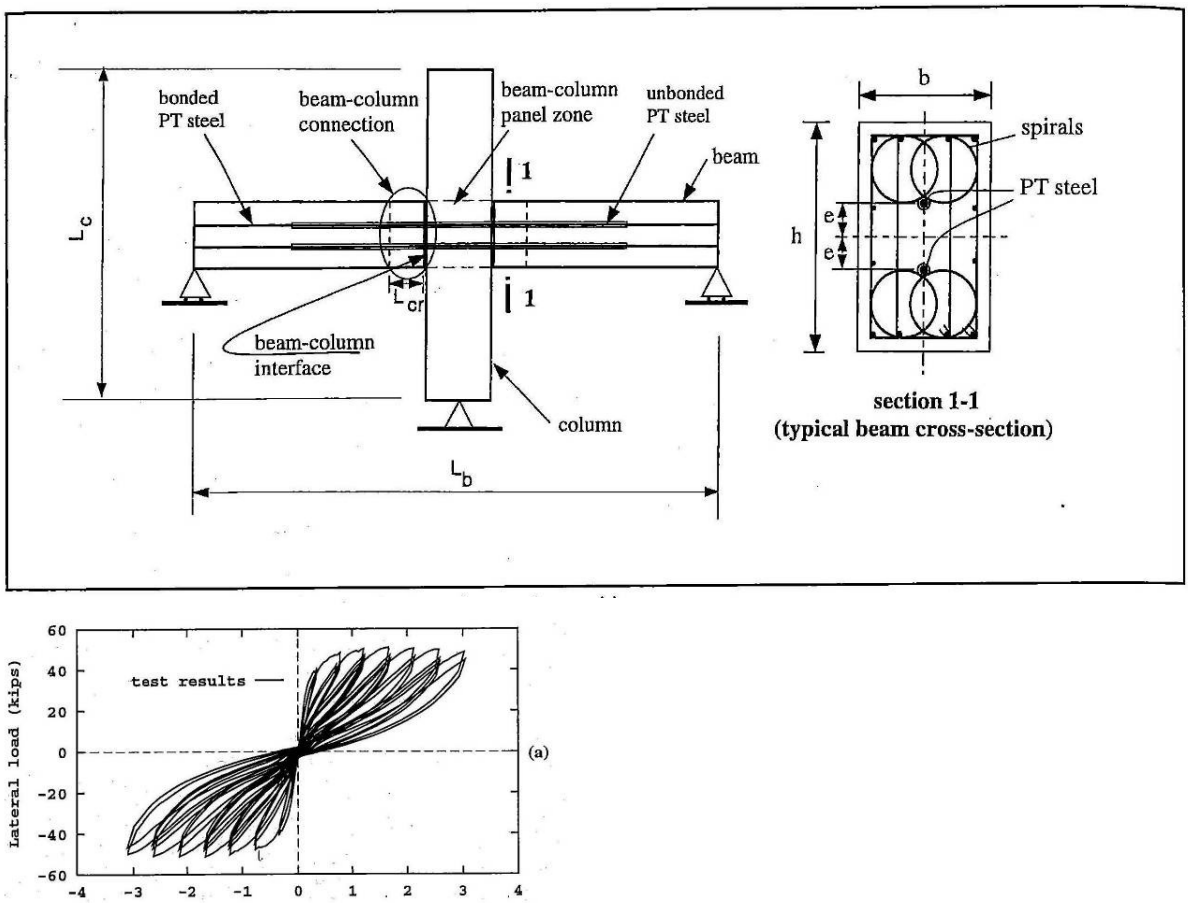

Figure 2.11 Frame and load-drift plot of model studied by El-Sheikh ((El-Sheikh, et al., 1999))

Kurama has also shown that supplemental viscous damping (Kurama, 2000) and friction damping (Kurama, 2001) can be other alternate means of energy dissipation to be used in hybrid systems.

Shortly after the PRESSS program was completed, precast concrete walls with unbonded post-tensioning were further investigated at University of Canterbury. (Rahman & Restrepo, 2000) tested half scale unbonded post-tensioned precast concrete walls (Figure 2.12). The walls showed stable response during the experiments with significant energy dissipation and virtually no residual deformation.

In a following research, (Holden, 2001) investigated two precast concrete wall specimens with dimensions similar to the specimens tested by Rahman and Restrepo. One wall was designed to emulate monolithic behaviour for comparison with the post-tensioned precast wall. Although the hybrid wall showed less than expected energy dissipation (Figure 2.13b) due to absence of yielding of the dissipaters in compression, it had negligible residual deformation compared to the emulated monolithic wall (Figure 2.13a).

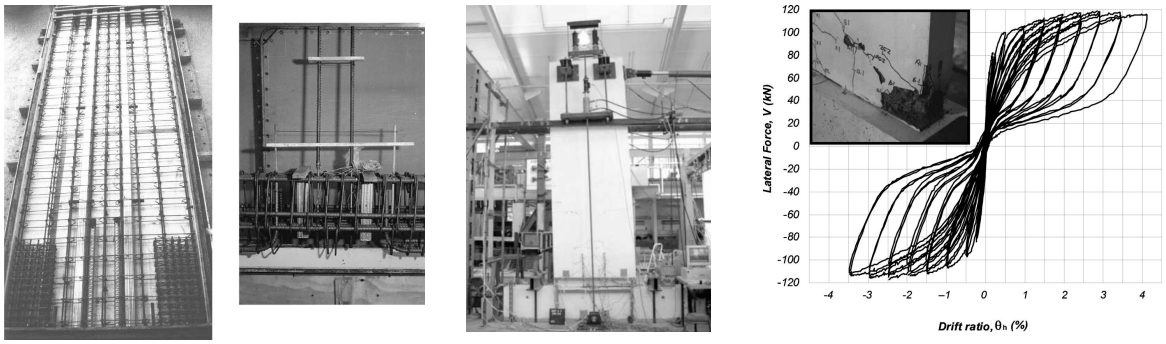

Figure 2.12 View of wall with energy dissipaters and load-deflection plot of the specimen (Rahman and Restrepo, 2000)

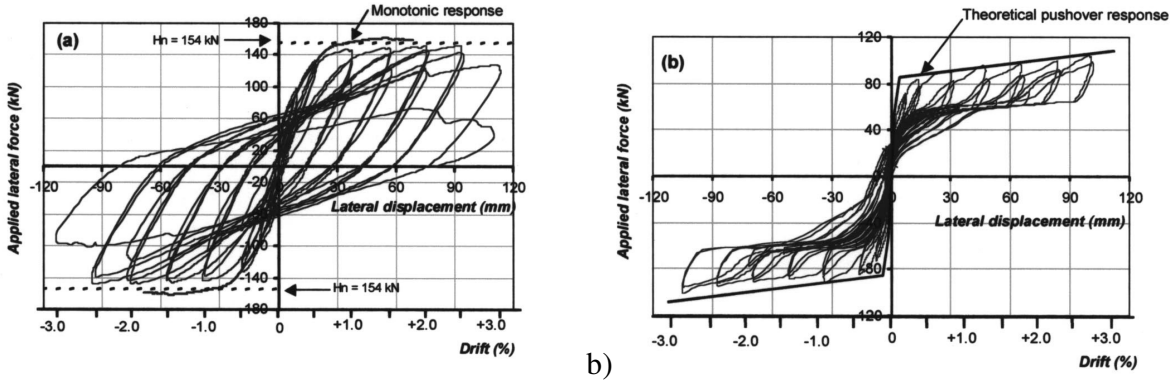

a) b)

Figure 2.13 Load-deflection plots of the a) emulated monolithic and b) precast wall specimen (Holden et al, 2001)

There has been significant research on this area at University of Canterbury over the past several years as presented as a recent overview by Pampanin (2010). Amaris et al. (2006) investigated alternative arrangements for jointed ductile connections through quasi-static cyclic tests on a series of 2/3 scaled beam-column subassemblies under uni- or bi-directional loading regime (Figure 2.14). The satisfactory results confirmed the flexibility and potential of the solutions for the development of the next generation of seismic resisting buildings.

Figure 2.14 Experimental Study of 3-dimensional Beam-Column Joint (Amaris et al. 2006)

Recently, (Marriott, 2009) has investigated post-tensioned rocking systems with hysteretic and viscous dampers for seismic applications (Figure 2.15). It was shown that the combination of the

two types of energy dissipation systems can produce highly efficient hybrid structures, particularly essential for near- field earthquakes and pulse-type ground motion.

The knowledge gathered from the research performed over the years has been accumulated and published as a PRESSS Design Handbook (NZCS, 2010) which serves as a guideline with the design examples for practitioners.

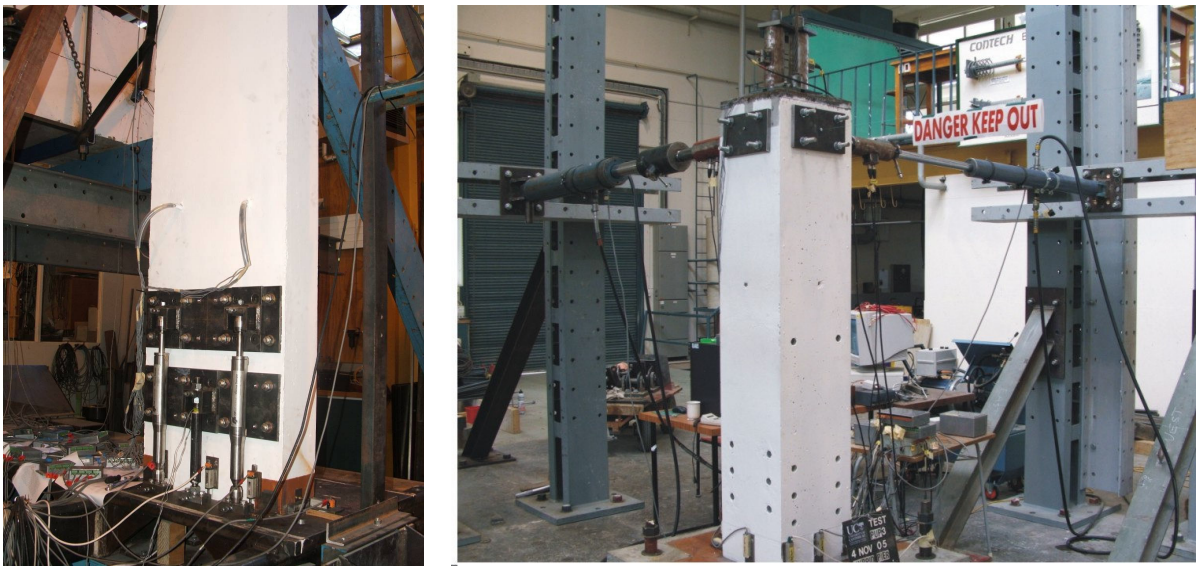

Figure 2.15 Hybrid wall and column experimental study (Marriott, 2009)

The concept has been already found applications in practical building structures in New Zealand. The first example of that is the new academic building at Victoria University of Wellington (Figure 2.16) where hybrid connections external energy dissipaters have been used (Cattanach & Pampanin, 2008; NZCS, 2010).

Figure 2.16 Application of PRESSS technology: Victoria University Building, Wellington (PRESSS Design Handbook, 2010, photo courtesy of Jasmax Ltd, Dunning Thortnon Consulting and Stefano Pampanin)

Another example of the hybrid concept is the new Southern Cross Hospital Building in Christchurch (Figure 2.17), where post-tensioned rocking walls coupled with U-shaped flexural plates have been designed.

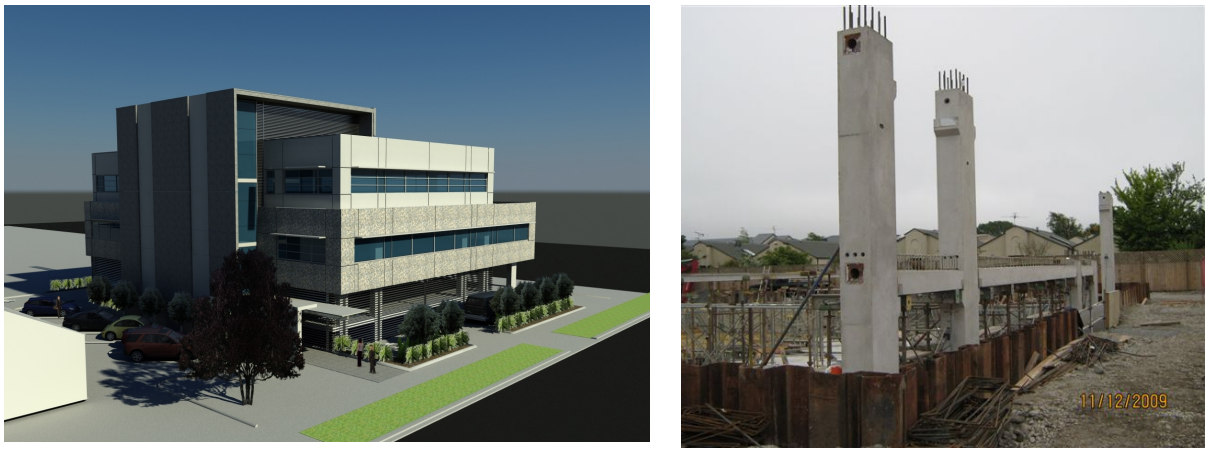

Figure 2.17 Southern Cross Hospital Building, Christchurch with UFP coupled walls (PRESSS Design Handbook, 2010, photo Courtesy Warren Mahoney, Structex Metro Ltd)

The research in precast concrete over the last two decades has produced solutions that have significantly advanced the technology for application of this type of structures in seismic zones. Compared to other types of ductile connections, the hybrid systems had the critical advantage of developing a plastic behaviour without any structural damage whilst providing full re-centering capacity and thus no residual (permanent) deformations at the end of the earthquake shaking.

2.4 Research into Post-Tensioned Timber Systems

Difficulty and cost of connections had been the major shortcoming in earlier solutions with timber. Residual deformations had been identified as another problem. As in concrete structures, prestressing added to the ductile connections discussed earlier for timber is able to eliminate the problem with residual deformations in timber buildings.

Based on the success of the hybrid technology in RC, some researchers have applied the concept to steel (Christopoulos & Folz, 2002) soon after it was introduced in concrete.

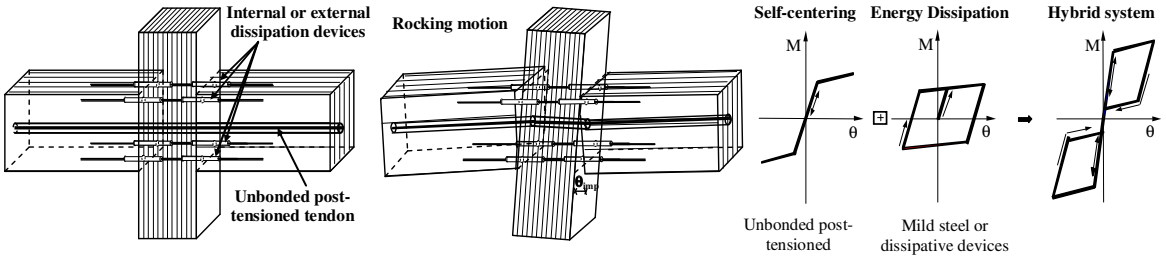

Figure 2.18 Hybrid LVL frame and idealized flag-shaped hysteresis loops (modified after (fib, 2003; Palermo, et al., 2005a))

A research initiative was started in late 2004 at the University of Canterbury to explore the feasibility of applying the hybrid concept in timber (Figure 2.18), particularly with LVL (Newcombe, 2005; Palermo, et al., 2005a), through experimentally testing timber beam-column joint with post-tensioning and internal or external energy dissipaters. Following the encouraging results of that study, a series of experimental work has been carried out with column and single wall (Figure 2.19) utilizing the same concept (Palermo, et al., 2006a; Palermo, et al., 2006b; Palermo, et al., 2006c).

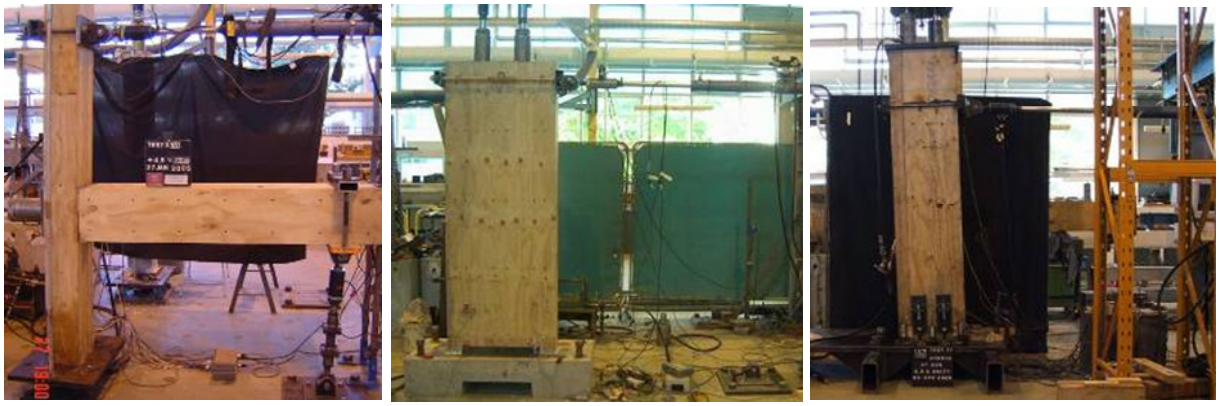

Figure 2.19 Beam-column joint, wall and column test specimens (Palermo, et al., 2006c)

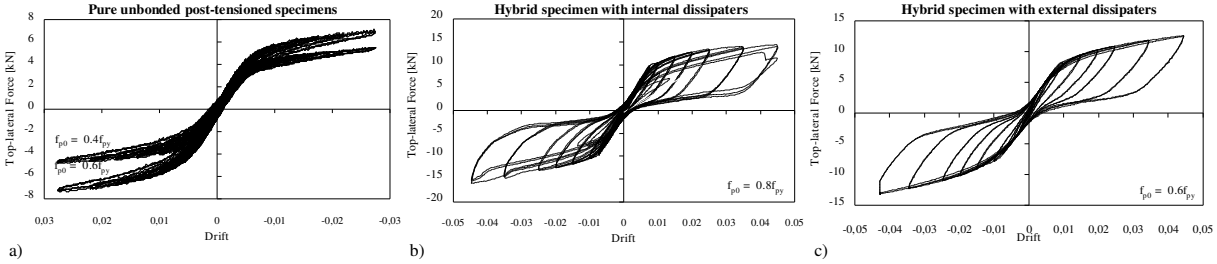

Figure 2.20 Lateral force-drift curve for timber beam-column joint: a) pure unbonded post-tensioned solution; b) hybrid solution with internal dissipaters; c) hybrid solution with external dissipaters (Palermo, et al., 2006b)

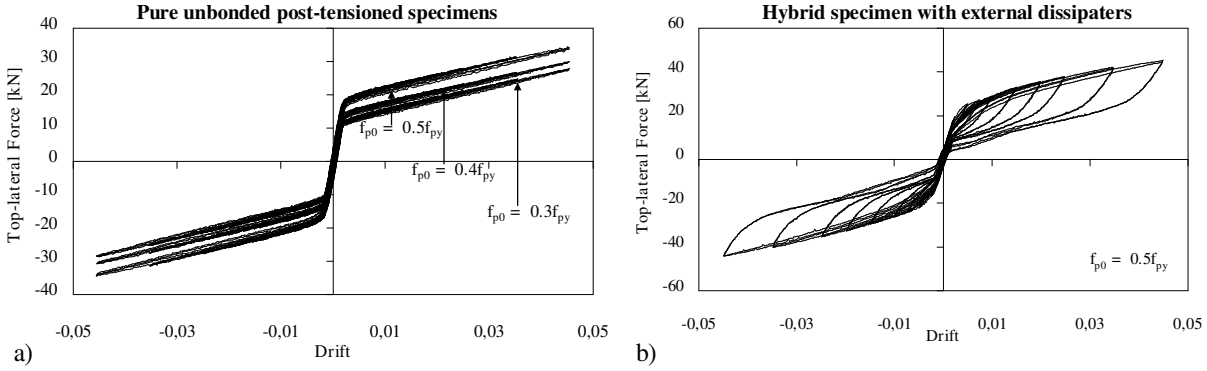

Figure 2.21 Lateral force-drift curve for timber column: a) pure unbonded post-tensioned solution; b) hybrid solution with external dissipaters (Palermo, et al., 2006b)

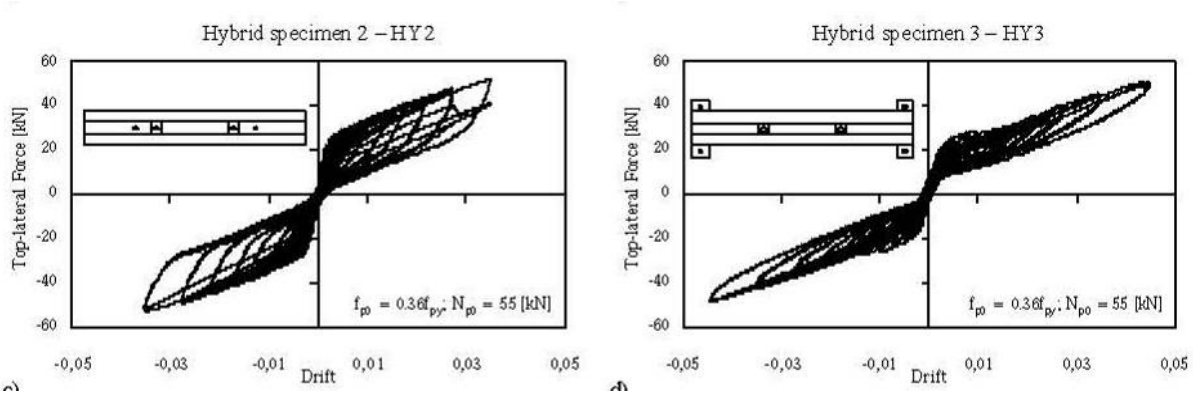

Figure 2.22 Lateral force-drift curve for timber wall: a) pure unbonded post-tensioned solution; b) hybrid solution with external dissipaters(Palermo, et al., 2006a)

Summarizing the results of these series of tests, it has been shown that the hybrid concept can be successfully applied in timber for multi-storey building structures. In particular, when considering the possible application of hybrid system to low rise multi-storey timber construction, Laminated Veneer Lumber has been shown to be a suitable material since it has a high level of homogeneity and also exhibits superior strength characteristics when compared to rough sawn or glulam timber.

More research was continued at the University of Canterbury on different aspects of post-tensioned timber systems. There was some experimental study on LVL walls with plywood sheet as coupling mechanisms (Smith, et al., 2007). Iqbal et al. (2007) presented results of experimental study on LVL walls coupled with UFPs. Comparisons of different types of wall systems have been done by Iqbal et al. (Iqbal, et al., 2010c). Experimental and analytical work on column under bi-directional loading was reported by Iqbal et al. (Iqbal, et al., 2008a, 2008b). The experimental and analytical study on full-scale beam-column joint has been reported in Iqbal et al (Iqbal, et al., 2009, 2010a; Iqbal, et al., 2010b).

There has been significant analytical work done on design of post-tensioned timber frame systems (Newcombe, et al., 2010; Newcombe, et al., 2008b, 2009b). Investigations on post-

tensioned timber systems with timber-concrete composite floors have also been performed (Newcombe, et al., 2009a; Newcombe & van Beerschoten, 2010).

Studies have been performed on complete timber buildings as well. Smith et al., (2008, 2009) looked into the feasibility of hybrid systems for multi-storey timber construction, considering moment-resisting frame systems and cantilever walls. Newcombe et al., ((Newcombe, et al., 2010a, 2010b) performed experimental study on two-thirds scale model of a two-storied timber building with frames and walls. Experimental work involving shake table studies of post-tensioned timber walls or scaled-down three and five storey frames has also been performed by Marriott et al., (2008) and Pino et al., (Pino, et al., 2010a, 2010b) respectively.

Figure 2.23 NMIT Building, Nelson (Photo courtesy Aurocon and M. Newcombe)

The technology has been already applied in practical timber building, the new Arts and Media building of Nelson Marlborough Institute of Technology (NMIT) in Nelson (Figure 2.23).

2.5 Summary of Review

Some innovative connections were developed for timber structures in the last two decades. Although they posses ductility and thereby some level of energy dissipation capacity, they would exhibit either substantial structural damage or significant residual displacements from a major earthquake. The hybrid concept developed for precast concrete and consisting of jointed ductile

connection, relying upon the combination of unbonded post-tensioned reinforcement and non-prestressed reinforcement, has been successfully implemented in seismic design of timber structures. Because of the inherent re-centering mechanism in the hybrid systems they have very good prospects of wide-spread application in design of timber structures with seismic resistance.

3 ANALYSIS AND MODELLING TECHNIQUES FOR PRESTRESSED TIMBER SYSTEMS

3.1 Introduction

The moment-rotation prediction procedure originally developed for precast concrete jointed ductile connections, later introduced in fib design guidelines and adopted in the NZS3101:2006 code provisions for jointed ductile connections, is presented here (Palermo, 2004; Pampanin, et al., 2001). It has been shown to be also applicable to timber connections (Newcombe, et al., 2008a). Some additional considerations are necessary for incorporating the material characteristics of timber. Different modelling approaches for representing the behaviour of the systems are also discussed here.

3.2 Moment-Rotation Calculation Procedure for Jointed Ductile Connections

3.2.1 Monolithic Beam Analogy

Presence of unbonded post-tensioning and energy dissipaters allows for gap opening at a hybrid connection. This means the strain in the concrete becomes unknown in addition to the position of the neutral axis. Strain compatibility thus does not apply at a section level. To address this issue, a global strain compatibility relationship between the parameters has been derived from an analogy (Figure 3.1) between the precast and a monolithic connection referred to as Monolithic Beam Analogy or MBA (Pampanin et al., 2001, fib 2003, NZS3101:2006).

In the monolithic cantilever the total displacement is given by the sum of elastic deformation and plastic rotation about the centroid of the plastic hinge. In case of the precast beam, in addition to the elastic deformation, there is an opening of a gap at the beam-column interface due to imposed rigid rotation about a zero-length plastic hinge at the joint interface similar to the

monolithic beam.

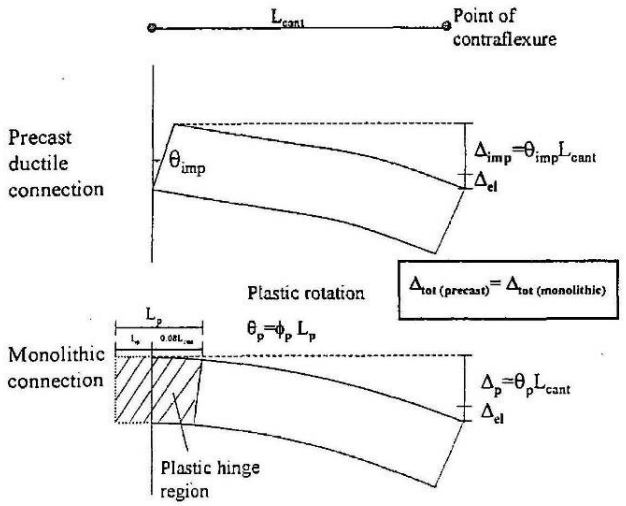

Figure 3.1 The monolithic beam analogy (Pampanin, et al., 2001)

For the same total imposed displacement, the elastic deformations are the same in the two beams with identical geometry and reinforcement. Then the plastic deformations in the two beams can be equated and the following relationship between concrete strain and neutral axis position is derived:

$$\varepsilon_c = \left[\frac{(\theta \cdot L_{cant})}{\left(L_{cant} - \frac{L_p}{2} \right) L_p} + \phi_y \right] \cdot c \qquad \textbf{3.1}$$

3.2.2 Modified Monolithic Beam Analogy

The Monolithic Beam Analogy (MBA) was originally focusing on the plastic domain of the rotation. The pre-yielding behaviour could in fact be described by referring to the decompression point and connecting linearly the decompression point to the yielding point.

The behaviour in the elastic domain was refined by (Palermo, 2004) considering both the elastic

and inelastic response during three different stages; decompression point, yielding point and ultimate point. It is summarised below with reference to Figure 3.2 for each range of deformation:

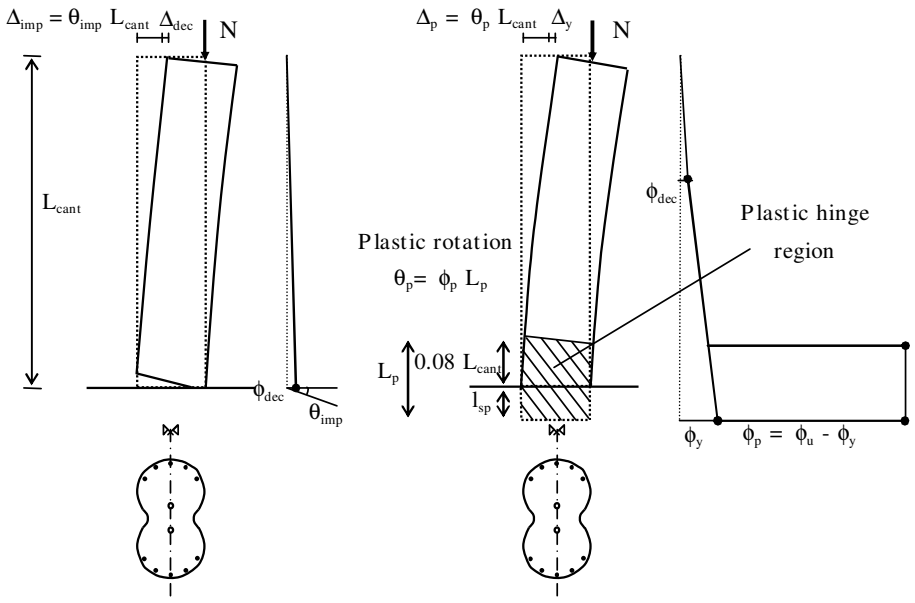

Figure 3.2 The modified monolithic beam analogy (Palermo, 2004)

Case 1: $0 \leq \theta \leq \theta_{dec}$ (pre-decompression point):

The gap opening does not occur at this range and there is no joint rotation ($\theta_{imp} = 0$). Strain capability is considered to be valid for the jointed member and hence the strain within the section can evaluated from section equilibrium directly.

$$\Delta = \Delta_{cant} = \phi \frac{L_{cant}}{3} \qquad \textbf{3.2}$$

Case 2: $\theta_{dec} \leq \theta \leq \theta_y$: (between decompression and yielding)

The following expression is conceived for the rocking connection in this range of deformation:

$$\Delta = \theta_{imp} L_{cant} + \phi_{dec} \frac{L^2_{cant}}{3} \qquad \textbf{3.3}$$

From the analogy between the monolithic and precast members:

$$\Delta_{mon} = \Delta \tag{3.4}$$

Now bringing in the expressions from equations 3.2 and 3.3 into equation 3.4 and simplifying:

$$\phi = 3\frac{\theta_{imp}}{L_{cant}} + \phi_{dec} \tag{3.5}$$

From equations 3.1 and 3.5:

$$\varepsilon_c = \left(3\frac{\theta_{imp}}{L_{cant}} + \phi_{dec}\right)c \tag{3.6}$$

For $\theta_y \leq \theta \leq \theta_u$: (between yielding and ultimate)

For this range of displacements the analogy is applied to equivalent elastic and plastic displacements.

$$\Delta_{mon} = \Delta_y + \Delta_p = \Delta \tag{3.7}$$

That can be expanded to the expression:

$$\Delta = \phi_y \frac{L^2{}_{cant}}{3} + (\phi_u - \phi_y)L_p\left(L_{cant} - \frac{L_p}{2}\right) \tag{3.8}$$

After rearrangement, the expression for the equivalent curvature becomes:

$$\phi = \left(\frac{\theta_{imp}L_{cant} - \frac{(\phi_y - \phi_{dec})L_{cant}^2}{3}}{\left(L_{cant} - \frac{L_p}{2}\right)L_p} + \phi_y\right) \tag{3.9}$$

From equations 3.1 and 3.9, the additional inclusion of the decompression curvature in the Modified Monolithic Beam Analogy is visible, when compared to the original Monolithic Beam Analogy.

After further simplification and rearrangement, the expression for the section stain becomes:

$$\varepsilon_c = \left(\frac{\frac{3\theta_{imp}}{L_{cant}} - (\phi_y - \phi_{dec})}{\frac{3L_p}{L_{cant}}\left(1 - \frac{L_p}{2L_{cant}}\right)} \right) c \qquad \textbf{3.10}$$

3.2.3 Calculation of Moment-Rotation Capacity

A simplified version of the method for determining the moment-rotation behaviour of a precast concrete hybrid connection (Pampanin, et al., 2001) and adopted by fib and NZS3101:2006 code provisions, is presented here.

Step 1: Fixing the interface gap Rotation θ_{imp}

The effective rotation at a hybrid connection can be related to geometry of the configuration.

Step 2: Guessing an initial depth of the neutral axis, c

Step 3: Evaluation of strain in the unbonded post-tensioned tendons and energy dissipaters

The deformed geometry of the connection is considered with an imposed rotation θimp and the assumed neutral axis depth c (Figure 3.3). The resulting displacement of the post-tensioning and energy dissipation can be determined by simple trigonometry.

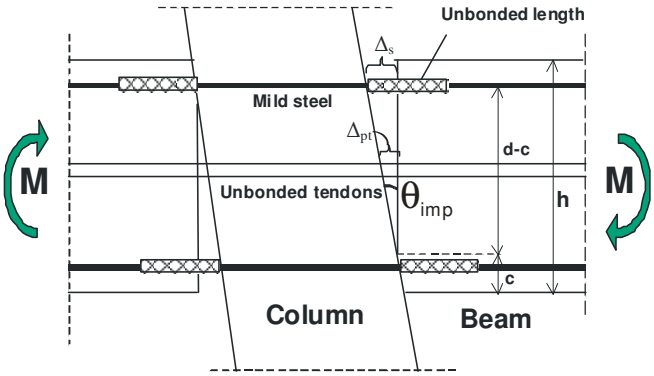

Figure 3.3 Controlled Rocking Mechanism in a jointed ductile Beam-Column Connection (Pampanin, et al., 2001)

By considering the displacements induced the strain in the post-tensioning and the energy dissipating steel reinforcement can be evaluated.

For the post-tensioning:

$$\varepsilon_{pt} = \frac{\Delta_{pt}}{l_{ub}} \qquad \textbf{3.11}$$

For the energy dissipaters:

$$\varepsilon_{s} = \frac{\Delta_{s}}{l'_{ub}} \qquad \textbf{3.12}$$

From the strains above the force generated by the post-tensioning and the energy dissipaters can be evaluated.

The MBA is applied to determine the expected stain at the extreme compression fibre of the section. Depending on the value of θ_{imp} either of Equation 3.6 or 3.10 is applied and the maximum strain in the section is obtained. Following this, a constitutive relation is applied to determine the stress distribution within the neutral axis.

Step 4: Section Equilibrium is verified and the Neutral Axis depth is updated

Equilibrium is enforced within the connection:

$$C - T_s + C_s^{'} = T_{pt} \qquad \textbf{3.13}$$

Step 5: Iteration until convergence

Steps 2 to 4 are repeated until equilibrium is satisfied and the neutral axis depth converges to a value. A new value of the neutral axis depth c' is then obtained that satisfies the above equilibrium condition.

Step 6: Evaluation of the Moment Capacity corresponding to the assumed rotation θ_{imp}

The moment contribution from the energy dissipaters and post-tensioning is evaluated and summed up for the rotation θ_{imp}.

The steps are summarised in Figure 3.4.

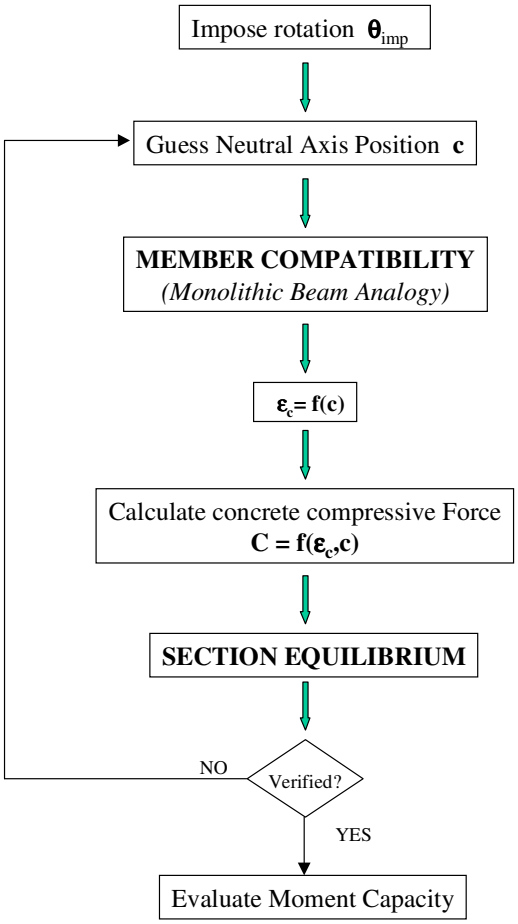

Figure 3.4 The moment-rotation procedure for jointed ductile connections (Pampanin, et al., 2001)

Once the moment contribution from the energy dissipation and post-tensioning is known, the connections re-centering ability must be verified. Therefore, the ratio of the moment from the self-centering component, the post-tensioning (and axial load for wall and column connections) and the energy dissipating moment must be greater than 1.0. The expression used for the self-centering ratio λ evaluated at the design displacement of concrete structures (NZS3101:2006):

$$\lambda = \frac{M_{pt} + M_N}{M_s} \geq \alpha_0 \tag{3.14}$$

Where: $\alpha_0 = 1.15$ is the minimum suggested value when explicit strain hardening of the energy dissipaters is not considered (later suggestions would be to adopt a minimum value of $\alpha_0 = 1.25$)

3.3 Application of Hybrid Connection Theory to Prestressed Timber

Alterations from the existing precast concrete design procedure are required due to unique material characteristics of timber and its connections. The key aspects that must be addressed for timber in the connection design procedure are the material stress-strain relationships, and the applicability of the MBA.

3.3.1 Timber properties and their implementation

An appropriate stress-strain relationship for timber must obviously be implemented into the connection design procedure in order to correctly evaluate the connection equilibrium. The stress-strain relationship must accurately model the timber subject to compression within the neutral axis depth.

For natural timber the stress-strain relationship can vary markedly depending on the variety and even the location within a specimen. For this study, only Laminated Veneer Lumber (LVL) was considered which has similar material properties to natural timber but much less variation in strength in stiffness. Figure 3.5 qualitatively shows the general stress-strain behaviour for clear timber.

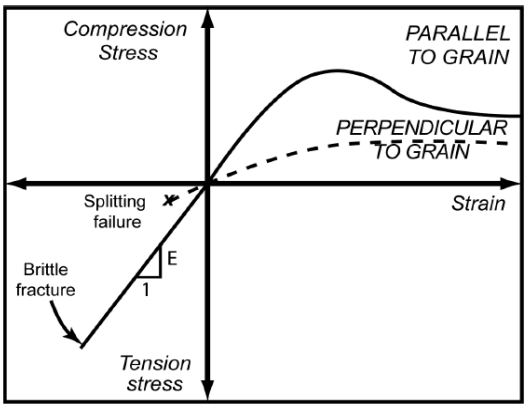

Figure 3.5 General Stress-Strain behaviour of Timber (Buchanan, 2007)

Timber is an assembly of numerous miniscule tubular fibres along the length and consequently is anisotropic in stiffness and strength. Different stress-strain relationships must be considered whether compression is applied parallel to grain or perpendicular to grain. Two particular cases are of interest for this investigation: the parallel to grain (for walls and columns) and perpendicular to grain bearing on parallel to grain (as expected for a beam-column connection). Material tests performed at the University of Canterbury on LVL small blocks of 45mm square in sections and 270mm in length show the general trends for compression applied parallel and perpendicular to the grain of the timber (Figure 3.6).

It is interesting to notice from test results for parallel-to-grain compression (Figure 3.6a), that there is variation in the initial stiffness that depends on the gauge length over which the axial displacement is recorded. For a small gauge length (90mm) in the centre of the specimen approximately the mean elastic modulus is inferred (14600MPa) but if the gauge length includes the end regions of the specimen (270mm) there is an apparent reduction in the elastic modulus (8000MPa).

These tests illustrate that there is an “end effect” that must be taken into account with timber connection design. Since the primary use of timber members with simply supported connections is to resist moment away from the end regions of a member a designer is usually only concerned with the elastic modulus away from the end regions. But the elastic modulus at the end regions will be essential for the design of hybrid timber connections (or other similar epoxied rods connections) because in this type of system the capacity of the connection is very much dependent on the stiffness of the material at the end of the beam.

The interface stiffness of perpendicular-to-grain bearing on parallel to grain specimens also varied significantly depending on the proportion of the gauge length over parallel versus perpendicular-to-grain timber. Assuming equal lengths of parallel and perpendicular timber, the effective initial stiffness approximated from the compression tests show that the effective modulus is reduced for a smaller gauge length, in a trend similar to the parallel-to-grain tests.

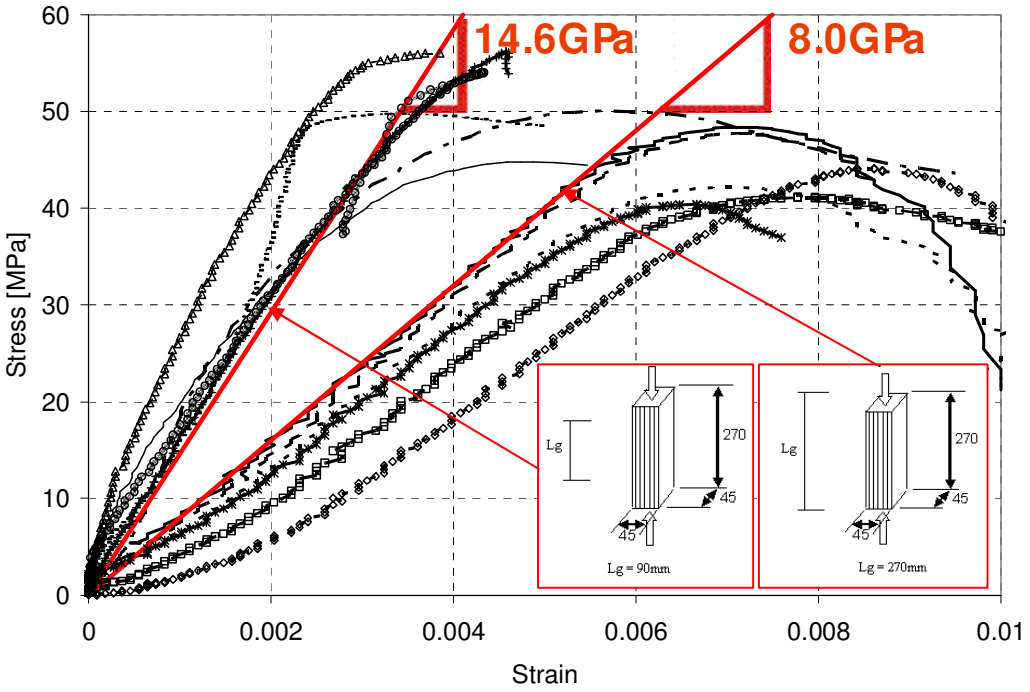

a)

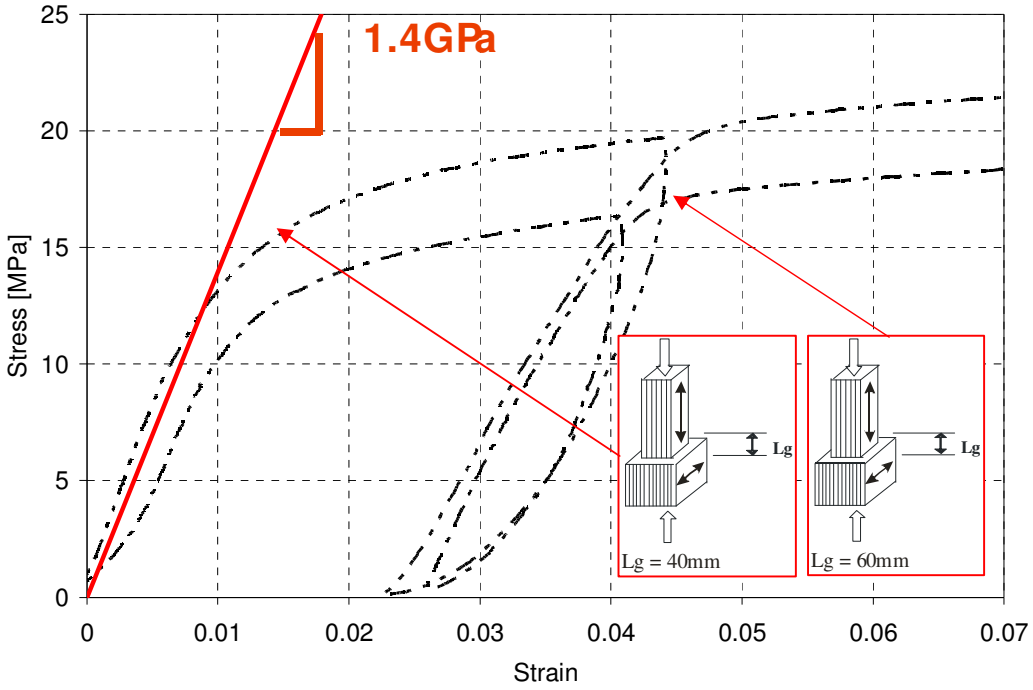

b)

Figure 3.6 Stress-strain relationships for LVL: a) Material tests on parallel-to-grain b) Material tests on parallel and perpendicular-to-grain interface (Davies 2006)

The stress-strain behaviour for a 40mm and 60mm gauge length is given in Figure 3.6b. Even with a significantly different gauge length, a similar interface elastic modulus of approximately 1400MPa is observed. This value is significantly different from the parallel and perpendicular elastic modulus and demonstrates that in this case there is an interaction from both.

An appropriate value of the connection modulus a correction factor can be determined for the end zone axial stiffness, applied as an effective connection modulus, from the post-tensioned-only (no additional non-prestressed reinforcement) subassembly experimental relationships. Thus the model can be calibrated by varying the elastic modulus until the analytical models match the experimental results.

Investigation of the strain profile of the timber within the compression zone of the connections

(Smith, 2006) demonstrated that a linear strain distribution can be assumed.

It may be necessary to model the plastic deformation of the timber in compression depending on the moment demands placed on the connections. One way of achieving that is by existing stress-strain models. In Figure 3.7 the material tests with a large gauge length (270mm) has been compared with a stress-strain model. The solid line is the best fit of the (Popovics, 1973) concrete stress-strain model. It can be considered to have matched most of the test results with sufficient accuracy.

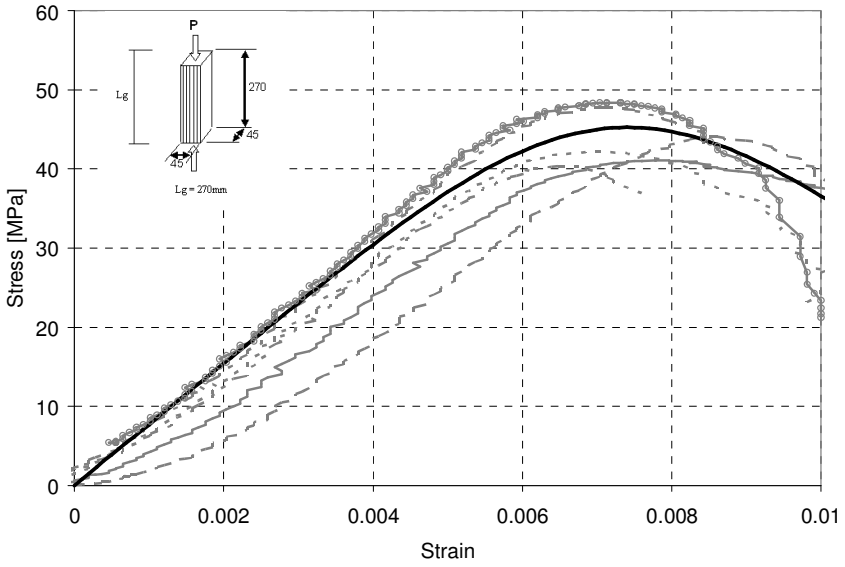

Figure 3.7 Popovics Concrete Stress-Strain relationship fitted to timber compression tests (Davies, 2006)

3.3.2 Alteration of the Modified Monolithic Beam Analogy

Firstly, the concept of an equivalent monolithic timber connection must be considered. For the equivalent monolithic concrete section the tension capacity of the concrete is assumed to be negligible. For timber, if the connection is strictly monolithic then there will be a significant contribution due to the tensile strain of the timber at the critical section. However, this is highly

inconsistent from the hybrid member that has no tensile contribution from the timber. Therefore, the equivalent 'monolithic' timber member will be assumed to have no tensile capacity of the timber, thus being better represented by a "traditional" epoxied rods connection. Thus the only variation in the MBA for timber, from precast concrete (or steel), is required in the plastic domain of displacement, where an equivalent plastic hinge is specified.

Also, it is evident that due to the low stiffness of the timber connections a large proportion of the displacement is within the elastic range. This indicates that the modified version of the MBA (Palermo, 2004), with refinements in the pre-yielding range and accounting for the effects of the decompression curvature (Equations 3.6 and 3.10), would be most appropriate.

3.4 Assumptions in Modelling Prestressed Timber Systems

3.4.1 Post-tensioned-only Connections

- The effect of the axial stiffness of the timber members has been not taken into consideration in the connection behaviour.
- For all the post-tensioned-only subassemblies considered there is no yield point as defined by the modified MBA. Hence, there is obviously no yielding of timber and the timber subject to compression within the neutral axial depth remains elastic. This implies that the timber connection remains in the elastic range while the modified MBA is applied.
- A linear stress-strain relationship is assumed for the timber in compression. Check on strain behaviour and limit are carried out in a second stage to confirm the assumptions on the elastic behaviour

3.4.2 Hybrid Connections

- For the behaviour of the energy dissipation devices, it was assumed there was no strain penetration or slippage since all the dissipaters used was external and there was no bonded internal mild steel in the specimens and all deformation occurred in the unbonded length of the energy dissipaters for all the tests considered.

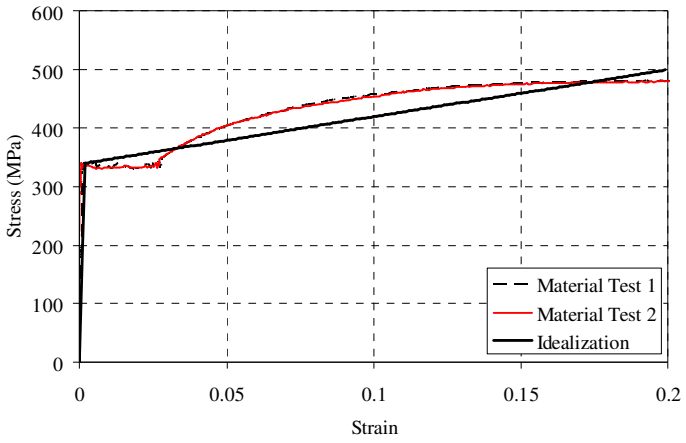

Figure 3.8 Idealised stress versus strain relationship compared with available material tests (Newcombe 2008)

- A simplified relationship (Figure 3.8) is also used for the unloading behaviour of the hybrid connection. Twice the lateral force required to produce yielding of the energy dissipation devices is subtracted from loading or backbone curve. This is a common approximation for the design of hybrid connections in concrete (Pampanin, et al., 2001), but might result in an over prediction of the unloading capacity or conversely an under prediction of the hysteretic area-based damping (Jacobsen, 1960). This under prediction for precast concrete is most commonly due to the cyclic Bauschinger Effect of the steel, as shown by Marriott et al. (2009). The unloading branch is simply used as an indication of the self-centering capacity of the connection.

- The overall geometry and arrangement of the connections are not significantly altered due to deformations in the external energy dissipation systems.

3.5 Modelling Cyclic Behaviour of Hybrid Systems

The cyclic behaviour of the subassemblies and connections has to be predicted with sufficient accuracy for any application of the system. Numerical models capable of representing the structure have been developed through analytical studies. Different modelling approaches have been used in concrete structures. An overview on alternative analytical approaches to characterise the behaviour of precast/prestressed connections can be found in (Pampanin & Nishiyama, 2002). A number of different models have been used for modelling walls and frame systems in concrete. In addition, two simplified models, namely, lumped plasticity model and multi-spring model have been proven particularly effective in capturing cyclic behaviour of hybrid systems.

3.5.1 Concrete Walls and Frames Modelling

As already mentioned in chapter 2, analytical investigation of unbonded post-tensioned precast concrete wall and frame systems were also performed at the Lehigh University in the late 1990s (El-Sheikh, et al., 1999; Kurama, et al., 1999). Finite element models with fiber elements were used for the analytical studies. The models were based on finite element code DRAIN-2DX (Prakash, et al., 1993) developed at the University of California at Berkeley.

Fiber elements were used to model the concrete wall panels while truss elements modelled the unbonded post-tensioning steel. Allen and Kurama (Allen & Kurama, 2002) also developed models of post-tensioned precast walls with fiber elements using the finite element software ABAQUS.

Since the non-linear deformations in a frame take place only at the connections in a jointed frame, the frame behaviour can be represented by the behaviour of the beam-column joint connections. That is why beam-column joints are often used to study frames. For the investigation of frames at Lehigh University, El-Sheikh and others used fiber element and spring element models of beam-column joint, both using DRAIN-2DX code (El-Sheikh, et al., 1999).

3.5.2 Lumped Plasticity Model

A lumped plasticity model can be efficiently adopted for hybrid connections where the main inelastic demand is accommodated within discrete critical sections (i.e. beam-column, column-foundation or wall-foundation interfaces). Due to the opening and closing of a single crack at the interface, an infinite curvature is developed at the critical section: therefore a moment-rotation relationship has to be preferred to a traditional moment-curvature when characterizing the section behaviour. Rotational inelastic springs in parallel, with appropriate hysteretic behaviour, can be assigned to represent the inelastic action at the beam-column (Figure 3.9a) and wall-foundation interface (Figure 3.9b) while elastic elements are used to represent the structural members as proposed by (Pampanin, et al., 2001) and subsequently adopted as modelling approach by the fib (2003). One rotational spring is assigned a Non Linear Elastic rule to represent the self-centring contribution (axial load and/or unbonded cables), while for the second spring an hysteresis rule representing the energy dissipation contribution is adopted (Figure 3.9c).

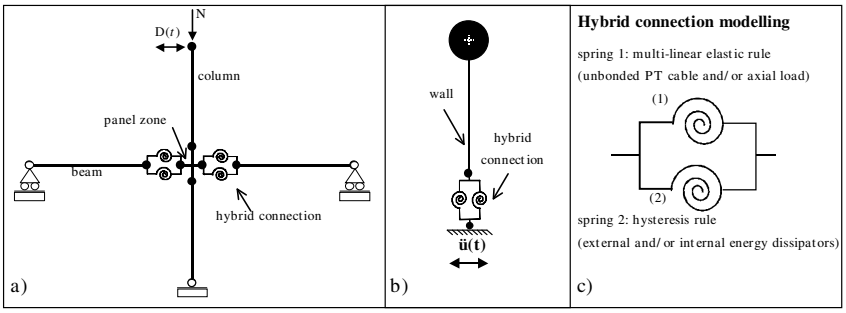

Figure 3.9 Lumped plasticity modelling: a) Schematic beam-column subassembly model; b) wall specimen model; c) details of the connection (Palermo, et al., 2005b)

The calibration of the two rotational springs can be obtained by evaluating the monotonic moment-rotation behaviour provided by each contribution, i.e. mild steel or energy dissipation devices, post-tensioned unbonded cable and axial load, referring to the Monolithic Beam Analogy procedure originally proposed by (Pampanin, et al., 2001) and subsequently refined by (Palermo, 2004), which relies on a member compatibility condition in terms of displacements between a monolithic and a hybrid solution. As represented in Figure 3.10, each curve contribution, obtained adopting the MBA (Monolithic Beam Analogy) can be linearized referring to the fundamental performance levels, i.e. the decompression point, loss of linearity point, yielding, serviceability and failure point. Figure 3.10 summarises the above mentioned calibration procedure assuming for the cyclic behaviour of dissipaters a Ramberg-Osgood hysteresis rule.

Lumped plasticity model has already been used (Newcombe, 2008; Newcombe, et al., 2008a) to model hybrid connections in timber with acceptable accuracy. Being conceptually simple and computationally less demanding it is particularly advantages for the initial stage of a more rigorous analysis.

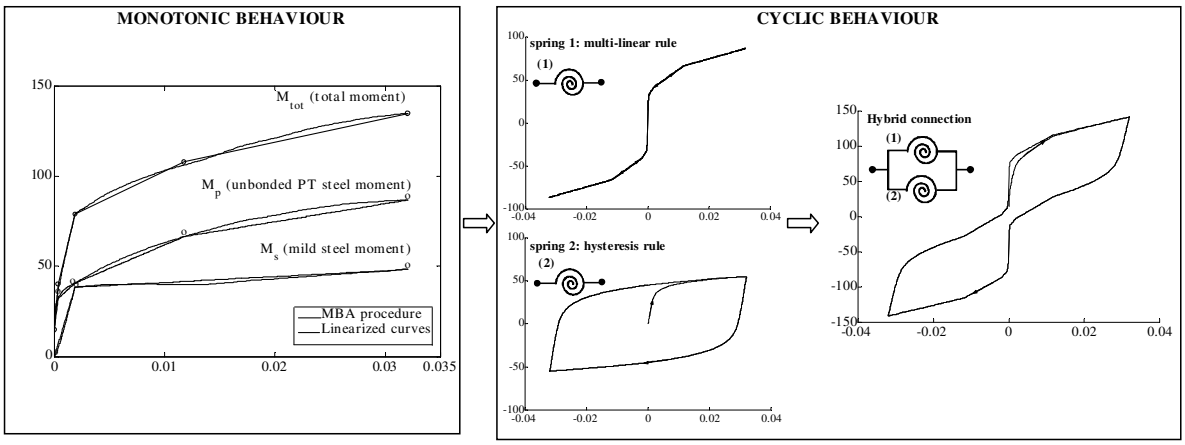

Figure 3.10 Calibration of springs referring to the Monolithic Beam Analogy Procedure (Palermo, et al., 2005b)

3.5.3 Multi-axial Spring Model

The model is characterised by representing the contact in the critical section (beam-to-column, wall-to-foundation) with a multi axial spring element. A simple approach that produced accurate results using two springs (Figure 3.11) was adopted to model walls of the PRESSS five-storey building at UCSD (Conley, 2000; Priestley, et al., 1999). Two compression-only springs provided the rocking behaviour in the model.

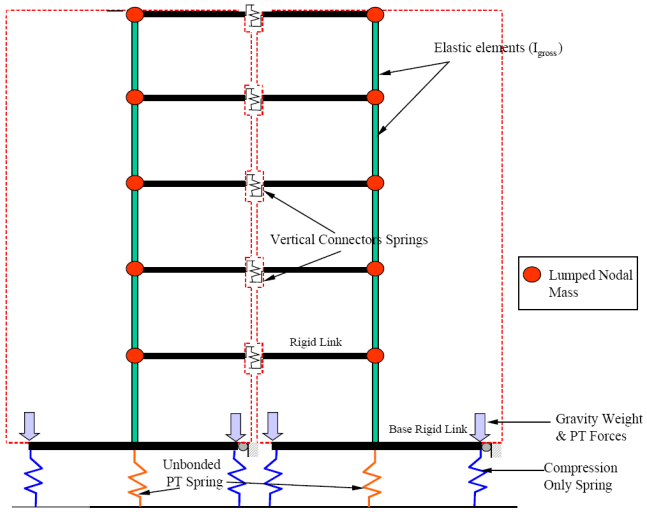

Figure 3.11 Model of PRESSS building walls (Conley, 2000)

Kim and others (Kim et al. 2002) developed a model (Figure 3.12) with multiple-spring element along rocking interface of a post-tensioned connection. The multi-spring elements consisting of nine (only two are shown in the figure for clarity) gap elements with bilinear compression-only characteristics, were available in DRAIN-2DX (Prakash, et al., 1993). It was suited well to capture the elongation of the tendons, mild steel and the beams. The tendons were modelled as truss elements while the beams and the column were represented by elastic frame elements. The joint was assumed to remain rigid as were the elements at the ends of the beams.

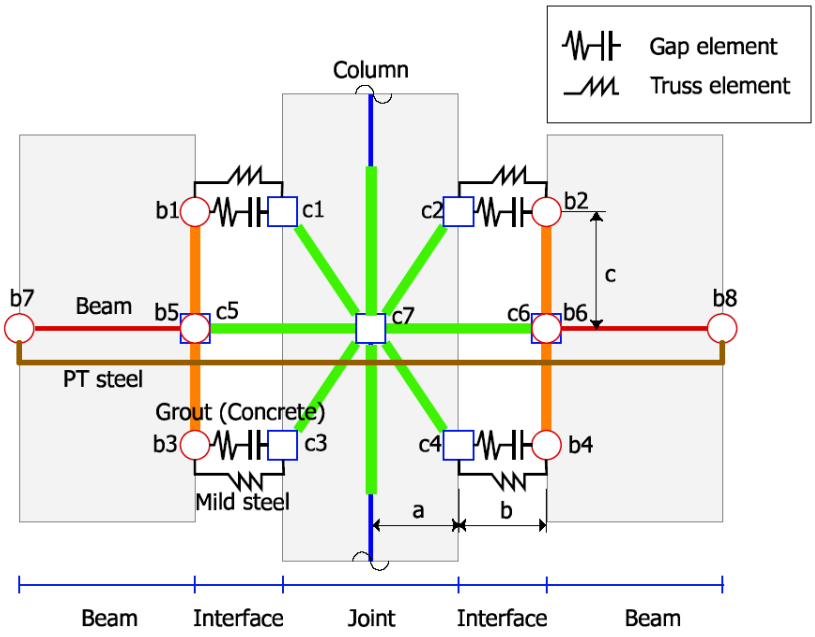

Figure 3.12 Multiple-spring model of beam-column joint (Kim, 2002)

Successively the two-spring model has been improved simulating the contact section interface with an increased number of springs and incorporated in the software Ruaumoko (Carr, 2005; Sepeith, 2004). The multi-spring contact element was set up for 2 to 10 contact points, representing the position of the springs; two different integration schemes, i.e. Gauss quadrature

and Lobatto integration, were used to optimise the position of the springs and calculate their weighting.

The model achieves a good simulation of the local stresses, strains, variation of the neutral axis position at joint opening and as well as allows considering the beam elongation effects. The characteristics of the springs can be properly chosen considering the different contact (unilateral, bilateral) behaviour of the section (concrete, steel etc.). The other elements characterising the hybrid connection, i.e. the unbonded post-tensioned cables and the external/internal energy dissipaters with unbonded length, are modelled with longitudinal springs, pretensioned in the case of the unbonded PT cables. The hysteretic rule for the unbonded PT cable can be assumed non-linear elastic, if the cables do not reach the yielding point, while for the energy dissipaters a proper hysteretic loop has to be chosen depending on the type of energy dissipater. Figure 3.13 shows the typical modelling of a typical beam-column subassembly and wall specimen. A representation in the case of straight cables is herein represented but the modelling can be easily extended to parabolic drafted cables. The beam, column and wall are represented by elastic finite beam elements (crack and/or uncracked section properties).

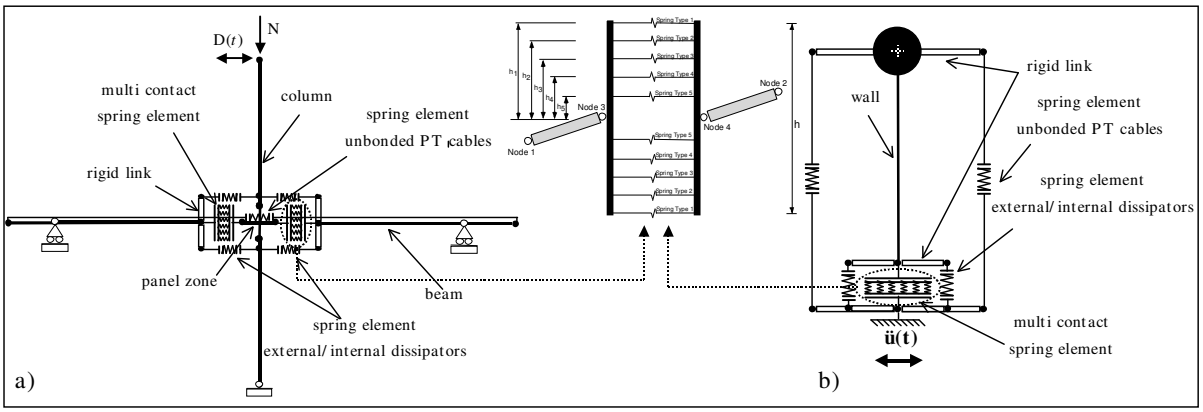

Figure 3.13 Multi spring modelling: a) Schematic beam-column subassembly model; b) wall specimen model (Palermo et al. 2005)

Newcombe (2008) has confirmed the potential of adopting the multi-spring model for modelling connections in hybrid post-tensioned timber systems. The analytical-experimental comparison with the quasi-static cyclic and/or pseudodynamic response of several small scale beam-column joints, column-to-foundation and single-wall-to-foundation connection have proved the accuracy of the model in characterizing the behaviour of the specimens.

3.6 Summary

The moment-rotation procedure originally proposed in literature for precast concrete jointed ductile connections have been proven applicable to hybrid timber connections. Proper representation of the material properties is critical for the computation. Numerical modelling approaches capable of accurately modelling cyclic behaviour of the systems are also available.

4 EXPERIMENTAL INVESTIGATION ON WALLS

4.1 Introduction

In terms of experimental investigation of the simulated seismic response of timber subassemblies, series of tests on wall-to-foundation, column-to-foundation and exterior beam-column subassembly were performed at the University of Canterbury under different testing protocols, ranging from quasi-static cyclic, to pseudodynamic, either with uni-directional and/or bidirectional displacement-controlled loading regime. The wall testing included double wall-to-steel foundation tests with and without different types of coupling arrangements, all with post-tensioning. The column-to-foundation tests were performed on a steel foundation under uni and bi-directional loading. Interior and exterior beam-column joints consisted of one or two beams and a single column held together by post-tensioning. The details of the experimental studies on walls are presented below. Experimental studies on Column and Beam-Column Joint will be described in the following chapters.

4.2 General Description of walls

The LVL wall specimens were designed as part of a structural system for a virtual multi-storey timber building. The prototype building has uniform bay lengths of 6m in both directions with frames in one direction and walls in the other direction. The LVL walls used in the tests were constructed in 2/3 scale using reasonable amount of resources in preparation and testing with expectation of achieving satisfactory results at the same time. The properties were accordingly scaled assuming same stress level between prototype and test specimen and a density constant approach. That means each specimen wall was 2m in height for the 3m storey height. The test

specimen had a total height of 2.46m and loaded at 2m from the base, with the extra height necessary for fixing arrangement of the loading jack and the prestressing anchorage. The 0.78m width was roughly 2/3rd of the 1.2m width of standard LVL produced. The 195mm thick walls were constructed from three layers of 65mm thick LVL blocks. There were vertical cavities throughout the length and the post tensioning cables were placed at the centres of these holes.

4.3 Components of Subassemblies and Material Properties

4.3.1 Laminated Veneer Lumber (LVL)

All of the experimental tests considered in this investigation used HySpan or Hy90 Laminated Veneer Lumber which is produced by Future Build a division Carter Holt Harvey in New Zealand (Futurebuild, 2006b). The material strengths and stiffness specified by Futurebuild are given in the Table 4.1 below.

The stiffness of LVL perpendicular to grain is not specified in future builds technical documents. However upon personal communication it was specified that the stiffness perpendicular to grain could be roughly taken as 1/20th of the parallel to grain stiffness. This would result in 660MPa and 450MPa for HySpan and Hy90 respectively.

Table 4.1 Characteristic Stresses of dry HySpan and Hy90 Laminated Veneer Lumber (futurebuild, 2006a)

Properties	Symbol	HySpan	Hy90
Modulus of Elasticity	E	13200 MPa	9000 MPa
Modulus of Rigidity	G	660 MPa	475 MPa
Characteristic Strengths:			
Bending	f'_b	48 MPa	35 MPa
Tension parallel to grain	f'_t	33 MPa	19 MPa
Compression Parallel to grain	f'_c	45 MPa	28 MPa
Shear	f'_s	5.3 MPa	5.3 MPa
Compression perpendicular to grain	f'_p	12 MPa	10 MPa

4.3.2 Post-Tensioning Tendons

For all experimental tests, 12.7mm 7-wire strands post tensioning reinforcement were used. In the following the term tendon will be used to refer to one 7-wire mono-strand tendon. The properties of each strand are summarized in Table 4.2.

Table 4.2 Post-tensioning strand properties

Nominal Diameter		12.7mm
Nominal Area	A_{pt}	99mm^2
Nominal Ultimate Stress	f_{pu}	1870 MPa
Elastic Modulus	E_{pt}	200000 MPa
Yield Stress	f_{py}	1560 MPa

4.3.3 Axial Energy Dissipation Devices

The mild steel energy dissipaters were based on the concept of replaceable "plug & play" devices, extensively developed and tested in post-tensioned concrete specimen subassemblies (Amaris, et al., 2006; Marriott, et al., 2008; NZCS, 2010; Pampanin, 2005) and recently applied in the construction practice (Cattanach & Pampanin, 2008). They were essentially mild steel bars encased in steel tables filled with epoxy. The bars were subject to axial alternate tension and compression during rocking of the connections. In this case, the dissipaters consisted of a 300 mm long 16mm diameter bars fused down to 8 mm for 120 mm of the length (Figure 4.1). The rod was threaded at both ends. A steel tube (Figure 4.2) with 26 mm outer diameter and 20 mm internal diameter was placed around the rod and filled with epoxy in order to prevent bucking during the compression cycle.

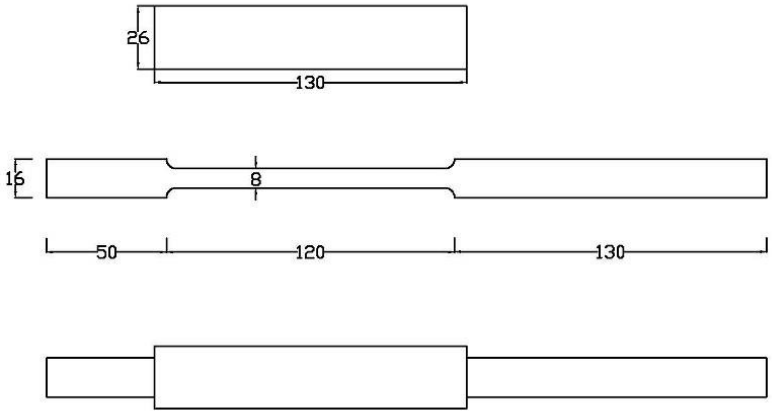

Figure 4.1 Dimensions of axial dissipater

Figure 4.2 View of axial dissipater

For all the axially loaded energy dissipation devices used as non-prestressed reinforcement in the beam-column joint, wall-to-foundation connection and some configuration of wall systems, Grade 300 mild steel bar was used. The steel had a characteristic yield stress of 300 MPa and an elastic modulus of 200000 MPa (PacificSteel, 2007). Experimental material testing indicates that a mean yield stress of the steel was approximately 340MPa.

Grade 300 mild steel plates were also used for the U-Shaped Flexural Plates (UFP), used as coupling and dissipating elements between two adjacent post-tensioned walls The yield stress used for the calculations was 345 MPa accounting for a 15% increase over characteristic yield stress (e.g. 300MPa) due to strain hardening.

4.3.4 U-Shaped Flexural Plates (UFP)

In the early 1970s, Kelly et al. (Kelly, et al., 1972) proposed rolling of mild steel plates in the form of U-shaped Flexural Plates (UFPs) for energy dissipation in structural walls.

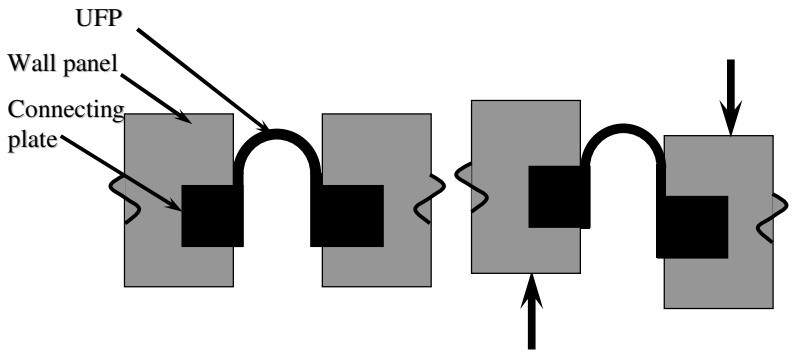

Figure 4.3 Arrangement and working mechanism of UFPs between walls

The steel plate in a UFP (Figure 4.3) is initially in a semi-circular shape with two equal straight sections on both sides. The two sides are attached to two structurally-separated walls. When there are lateral movements at the top of walls, the walls rock at the bottom resulting in relative vertical displacements between the two adjacent walls. If one side of the UFP moves relative to the other, the semi-circular portion rolls along the plate and work is done at the two points where the radius of curvature is changed from straight to the radius of the semi-circle and then from this radius to straight. Thus at any instant the energy dissipation is concentrated at two transverse surfaces and these two surfaces move along the plate.

Kelly et al. (Kelly, et al., 1972) provided equations for designing the UFP for practical applications. The yield load for a U-shaped plate is

$$V = \frac{2M_o}{D} \qquad \textbf{4.1}$$

Where M_o is the yield load moment and D is the average diameter of the plate. For a rectangular cross section with width b and thickness t,

$$M_o = ¼(bt^2) f_u \quad \textbf{4.2}$$

Where fu is the yield stress in simple tension

The strain which is developed during a test does not depend on the stroke and is given by

$$\varepsilon_{\max} = \frac{t}{D} \quad \textbf{4.3}$$

Combination of equations 4.1, 4.2 and 4.3 gives

$$V = ½(bt\ )(f_u \varepsilon_{\max}) \quad \textbf{4.4}$$

In general, this device is comparatively flexible in the elastic range and can be subjected to very large displacements capacity in the inelastic range. Tests carried out on U-shaped plates under reversed cyclic loading showed that the mode of failure is characterized by a localized kinking of the plate followed rapidly by complete transverse fracture. The two factors that influence the lifetime of a device are the stroke and the maximum strain. The number of cycles to failure tends to decrease with increasing strain and decreases very rapidly for strokes greater than twice the original bend length i.e. πD.

For the design of such a device, the stroke should be selected in such a way that the amount of material which is undeformed during a cycle of loading is minimized and the strain level is kept low enough to ensure that the specified lifetime is achieved. Kelly et al (Kelly, et al., 1972) carried out a large number of tests at different strain levels using several different stroke-to-radius ratios and the results were used to prepare a diagram of cycles against strain and stroke to predict the number of cycles to failure. A properly designed mild steel U-shaped plate can reliably produce lifetimes in excess of 100 cycles.

4.4 Experimental Investigation on Walls

4.4.1 Types of Specimens

Structural walls made of precast panels utilizing the recently developed hybrid concept develop a rocking motion at the base which could be used to activate energy dissipation elements (or simply to be considered additional reinforcement for increase stiffness and strength) at the base. Another solution is to use coupling beams as an additional source of strength as well as energy dissipation through yielding of the coupling beams. An efficient alternative to coupling beams are coupling links, or mechanical devices. While energy dissipation is primarily achieved through yielding of the coupling links throughout the height of the walls, almost the entire wall except the rocking base behaves virtually elastically and with a more regular deformed shape.

The experimental investigations of walls involved three types of specimens employing different concepts. The first type was rocking walls with only post-tensioning tendons. The second type was the typical hybrid specimen, with energy dissipaters in the form of mild steel axially-yielding bars in addition to the post-tensioning system. The third type was a coupled post-tensioned hybrid wall system, with U-shaped flexural plates (UFP) as the coupling mechanism.

4.4.2 Walls and Connections Details

The LVL walls (Figure 4.4) were constructed from HySpan LVL. Each of the LVL walls was 2460 mm high, 780 mm wide and 195mm deep. They were made of multiple blocks of LVL of same length and thickness with different widths to leave the holes for prestressing. The details are shown in figure below in Figure 4.5:

Figure 4.4 View of LVL walls

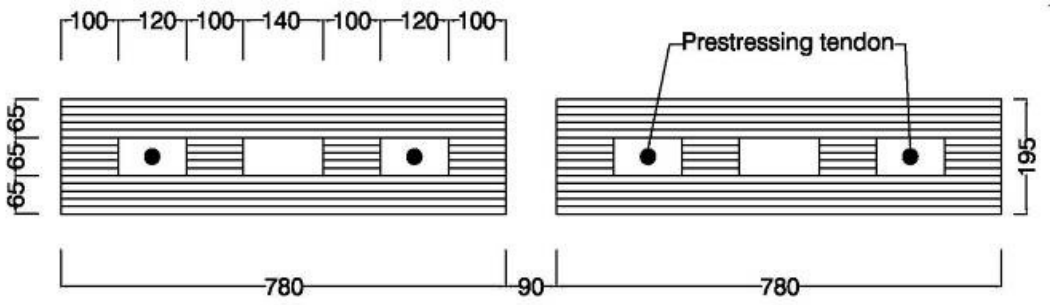

Figure 4.5 LVL walls section

Figure 4.6 Steel base with a single wall

Figure 4.7 Steel loading beam with pin connections and loading jack

Figure 4.8 Gap between the wall as seen from the top and rear view of the walls with instrumentation

A steel foundation (Figure 4.6) was constructed to accommodate the various types of testing. The use of the steel plate allowed the easy addition and removal of dissipater connections and shear

key devices, as well as provided a strong flat and regular surface on which a large amount of testing can be carried out without damage to the foundation. It also allowed holes for the tendons to be drilled and filled as needed. Although it was acknowledged that such a steel foundation would not represent the typical construction practise it was considered the most economical and time efficient option due to the large amount of testing to be carried out.

The walls were connected through horizontal loading beams, with pin connections at points of loading, to the loading jack (Figure 4.7). This arrangement ensured that the walls are constantly kept equal distance apart while the rocking motion takes place, recorded at the base by the instruments (Figure 4.8). One end of the dissipaters was anchored in the steel base and the other end was connected to the walls. Steel plates and brackets (Figure 4.9) were used to attach the end of the dissipaters to the walls. Each steel plate had eight holes for the screws. The holes were recessed to ensure that the screws were held in place. Eight ¼ gauge Tek-screws were used to attach each plate to the face of the wall. The arrangement ensured that there was no slippage in the attachment during testing. Figure 4.10 shows the whole assembly with the walls.

Figure 4.9 Attachment details of energy dissipaters to walls

Figure 4.10 Hybrid LVL walls with axial dissipaters

Figure 4.11 U-shaped flexural plates with attachments

Two types of UFP (Figure 4.11) arrangements have been investigated for connecting the UFPs to the walls: two single 8 mm thick UFPs (75mm, or 100mm width) connected along the two walls (Figure 4.12a) and four 5 mm thick UFPs (Figure 4.12b). The UFP devices were attached to the walls with welded brackets on the face of each wall. The brackets had holes for self-drilling

screws which were fixed to the face of the wall as shown in Figure 4.13. A disadvantage of this fixing method was that the bracket on one side of the wall had to be welded in place after inserting the UFPs. Alternative details of fixing the UFPs for rapid construction and post-earthquake intervention can be considered (e.g. Figure 4.14) for coupled wall test specimens (Figure 4.15).

a)  b) 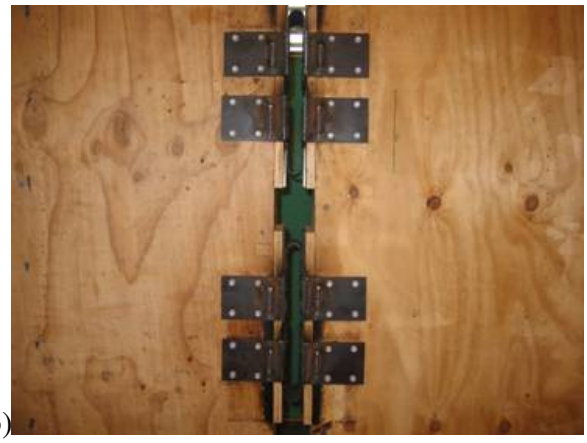

Figure 4.12 UFP between the LVL walls: a) single and b) double pair

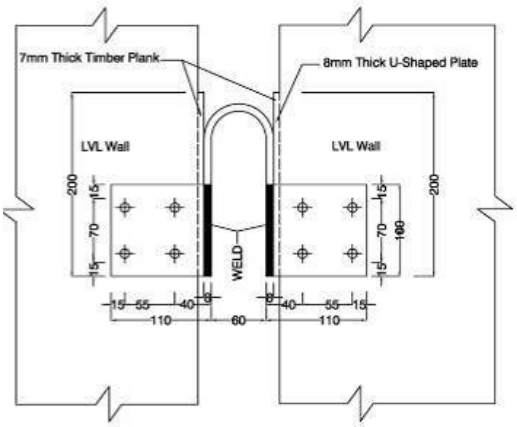

a)

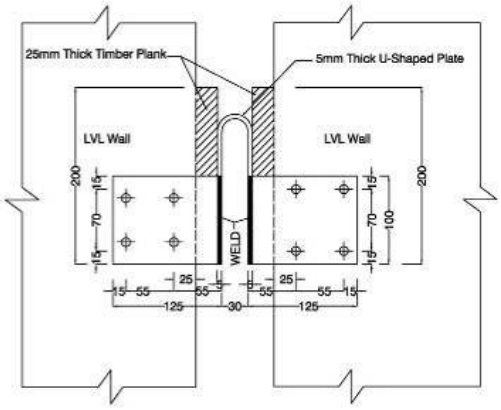

b)

Figure 4.13 UFP connection details: a) single pair; b) double pair

Figure 4.14 UFP connections in practical building application (NMIT Building, Nelson; photo courtesy M. Newcombe)

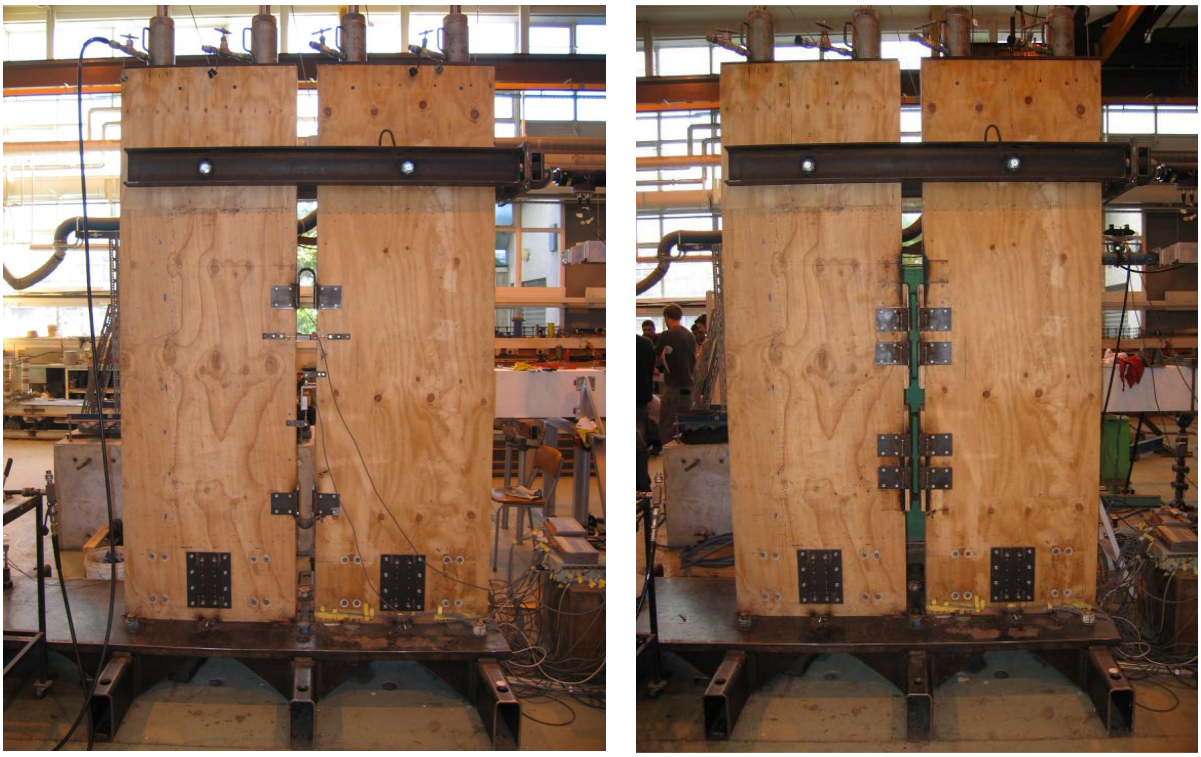

Figure 4.15 Hybrid LVL walls with UFP

4.4.3 Testing of Energy Dissipation Devices

Before testing the wall specimens, tests were carried out on the energy dissipating elements in order to confirm and characterize their behaviour. The axial dissipaters were tested under repeated cyclic loading simulating the deformations they were expected to go through during the tests of the walls specimens. Quasi-static cyclic tests (Figure 4.16) with increasing level of displacement (symmetric loading protocol) were carried out showed hysteresis loop with significant energy dissipation as shown in Figure 4.17. The dissipater showed a post-yield stiffness of around 10% of initial stiffness.

Figure 4.16 Test setup for axial dissipaters

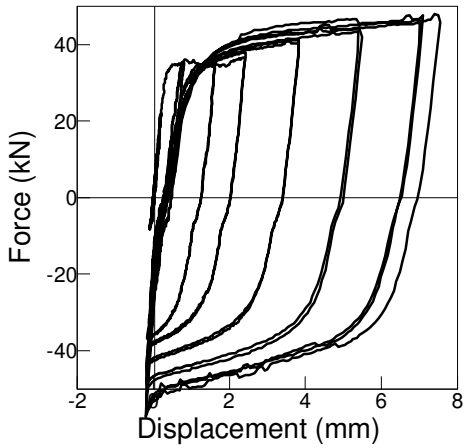

Figure 4.17 Force-displacement plot of 8mm diameter axial dissipater

Similarly, the UFP connectors were tested separately from the walls in order to better calibrate their cyclic hysteretic behaviour, including failure due to cycle fatigue. The test setup is shown in Figure 4.18. Quasi-static cyclic tests with increasing level of displacement (symmetric loading protocol) were carried out. The UFPs showed very stable and highly dissipating hysteresis loops as shown in Figure 4.19. In general, post-yield stiffness of around 5% to 10% of initial stiffness was observed.

Figure 4.18 UFP test setup

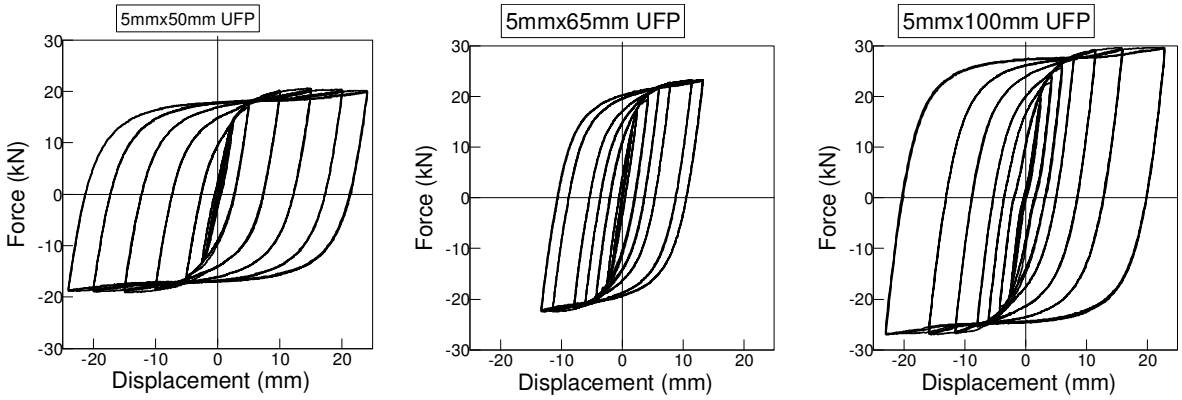

Figure 4.19 Load-deflection plots of UFPs

4.4.4 Details of Walls Specimens and Testing Programme

As mentioned earlier, three types of walls specimens were tested during this study. The post-tensioned-only specimen PT1, PT2 and PT3 were tested at initial post-tensioning levels of 30%, 40% and 50% of yield stress of the tendons, respectively. The hybrid specimen with 8mm axial dissipaters is designated HY.

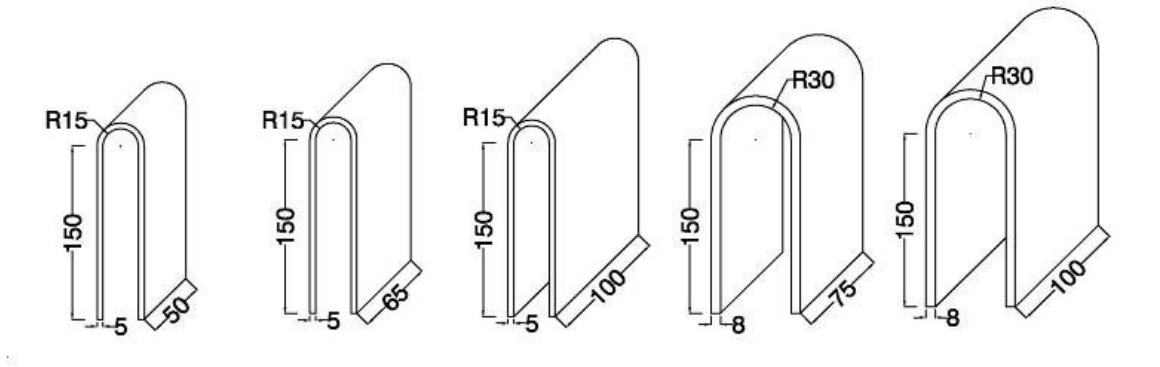

Figure 4.20 Sizes of UFPs used with specimens during testing

Different sizes of UFP (Figure 4.20) were tested with the walls. A plate thickness of 5 mm and radius of curvature of 15mm was adopted for three types, while the widths were 50mm, 65mm and 100mm. Two additional types with 8mm thick, curvature of 30mm and widths of 75 and 100mm were manufactured and tested with the LVL coupled walls. Two different arrangements

of the UFP were used during the testing programme. The single pair UFP arrangement comprised of UFPs made of 8mm thick steel plates, with widths of 75mm and 100mm. The specimens with these two sets of UFPs were designated HU1 and HU2 respectively. The double pair UFP arrangement had UFPs with plate thickness of 5mm varying from 50mm to 100mm in width. The specimens HU3, HU4 and HU5 had UFPs of 50mm, 75mm and 100mm thicknesses. HU6 had the same configuration of UFP as HU3 but with an initial prestressing level of 58.0 kN (40% of yield stress). The rest of the hybrid specimens had an initial prestressing of 43.5 kN (30% of yield stress).

Either quasi-static cyclic and pseudo-dynamic testing were carried out with the specimens expect PT1, PT2 and HU6. Specimens PT1 and HY were subject to three different earthquake records during the pseudo-dynamic tests. The rest of the specimens were tested under single earthquake motions.

Table 4.3 Details of wall specimens tested

Specimen	Type	Initial PT	Dissipaters	Testing Regime
PT1	PT-only	43.5kN	None	Quasi-Static Pseudo-dynamic
PT2	PT-only	58.0kN	None	Quasi-Static
PT3	PT-only	72.5kN	None	Quasi-Static
HY	Hybrid	43.5kN	4-8mm ϕ	Quasi-Static Pseudo-dynamic
HU1	Hybrid	43.5kN	4 -5mmx100mm UFP	Quasi-Static Pseudo-dynamic
HU2	Hybrid	43.5kN	4 -5mmx65mm UFP	Quasi-Static Pseudo-dynamic
HU3	Hybrid	43.5kN	4 -5mmx50mm UFP	Quasi-Static Pseudo-dynamic
HU4	Hybrid	43.5kN	2 -8mmx100mm UFP	Quasi-Static Pseudo-dynamic
HU5	Hybrid	43.5kN	2 -8mmx75mm UFP	Quasi-Static Pseudo-dynamic
HU6	Hybrid	58.0kN	4 -5mmx50mm UFP	Quasi-Static

4.4.5 Test Setup and Loading Protocols

The setup of the coupled walls is shown in Figure 4.22. The walls were loaded at a height of 2m above the foundation. There was a hinge connection between the two walls through a steel beam which actually simulated the diaphragm action, enforcing the same displacement to the walls. Four unbonded post-tensioned tendons, two per wall, were anchored at the top and bottom of the walls. The initial prestressing forces in the tendons were kept low (from 30% to 50% of yield force) to prevent possible yielding of the tendons during the tests. The loading protocol adopted for quasi-static cyclic testing is based on a modified version of the ACI T1.1-01 (ACI, 2001), originally proposed for the testing on innovative jointed precast concrete frame systems. The modification consisted in maintaining the target drift levels, but reduced the number of cycles, i.e. from three to two cycles, for each level of intensity, as shown in Figure 4.23. Both symmetric and asymmetric loading protocols were used, including small cycles at the beginning, to test the response of the specimen to different realistic loading regimes.

Pseudo-dynamic tests were performed to simulate the time-history response of the structural system subjected to an earthquake input ground motion and to assess the effect of hysteretic damping and re-centering on the overall response (maximum and residual displacements). As defined by Mahin and Shing (Mahin and Shing 1985), the displacement response of the walls under a specified earthquake motion was numerically computed at each time step of the equation of motion and quasi-statically imposed on the physical model, based on analytically prescribed inertia and viscous damping characteristics for the structure and the experimentally measured structural restoring forces. The concept is illustrated schematically in Figure 4.21.

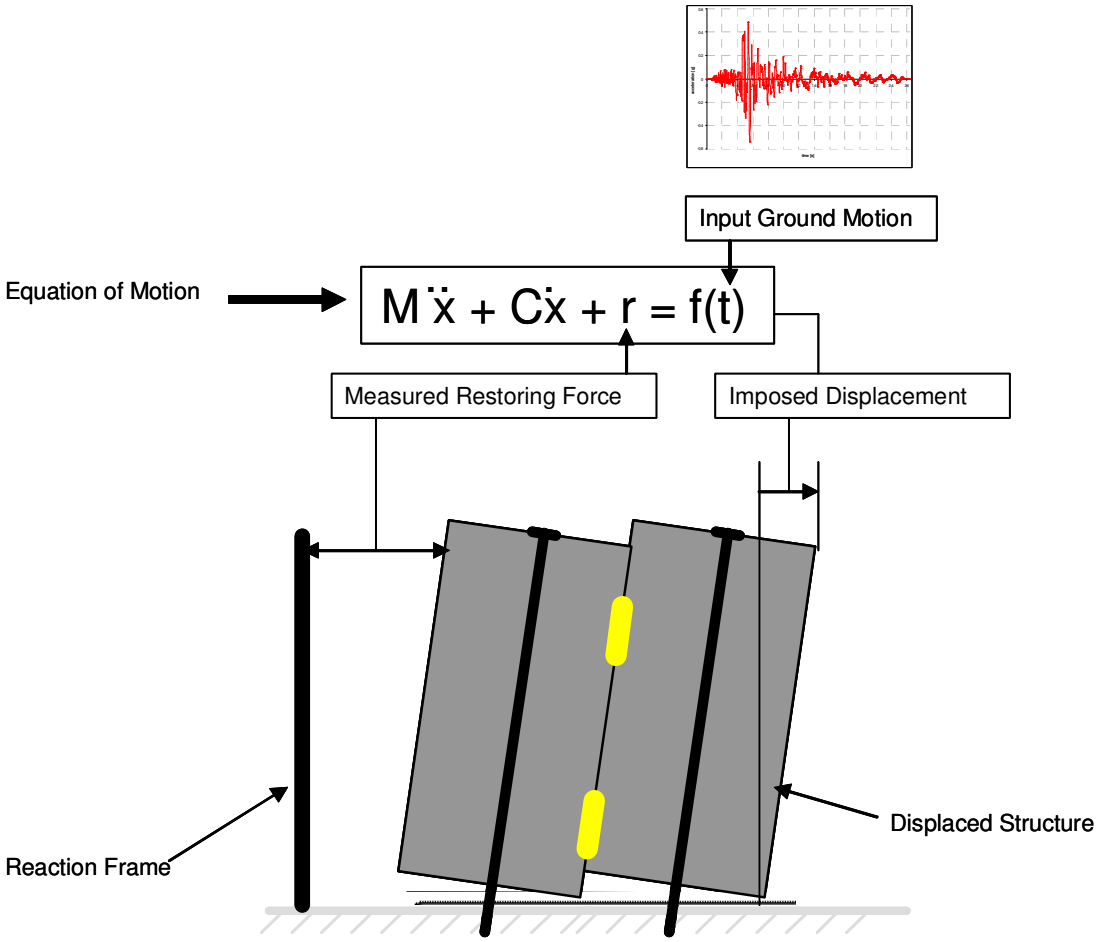

Figure 4.21 Concept of Pseudo-dynamic testing

The earthquake records chosen for the pseudo-dynamic tests were taken from a group of 20 historical records from California (Pampanin, et al., 2002) scaled to match the design spectrum defined by International Building Code (ICBO, 2000), as two thirds of the Maximum Credible Event (MCE) spectrum. The design-level spectrum or two thirds of MCE spectrum represented a probability of exceedence of 10% in 50 years while the MCE spectrum corresponded to a probability of exceedence of 2% in 50 years. These two also corresponded to the BSE-1 (Basis Safety Earthquake) and BSE-2 levels, respectively, defined in NHERP Provisions for the seismic

rehabilitation of buildings (FEMA, l997). BSE-1 implied Life Safety Performance level while BSE-2 represented Collapse Prevention Performance level.

Details of the earthquake records are shown in Table 4.5 and Figure 4.24 along with their response spectra when compared to the New Zealand Loading Standard (NZ1170.5) acceleration design spectrum with a PGA of about 0.4g for soil class B and a return period of 500 years for a high seismicity area. For the hybrid walls with UFPs, the ground motions were scaled up to 150% which represent a return period of approximately 1500 years according to New Zealand Standard NZS 1170.5 (SNZ, 2004).

The same test set-up as the quasi-static testing was used for the Pseudo-dynamic tests. However, as the walls were of 2/3rd scale, appropriate values of the scale-dependent relevant parameters had to be used with the pseudo-dynamic tests (Morcarz & Krawinkler, 1981). Assuming the constant density criterion in dimensional analysis and similitude rules, an amplification of 3/2 was applied to the accelerations while the duration (time) was reduced to $2/3^{rd}$ as explained by Palermo et al. (Palermo, et al., 2006a). The parameters and corresponding factors from prototype to model are given in Table 4.4.

Parameter	Scale Factor
Length	0.67
Mass	0.296
Acceleration	1.5
Period	0.67

Table 4.4 Scale factors for model parameters

A scaled equivalent mass of 148 kN s^2/m was assumed, calculated from the expected gravity loading of the wall in a single storey timber building multiplied by the scale factor of 0.296 (Palermo, et al., 2006a) for mass. An equivalent viscous damping of 5% (initial stiffness proportional) was assumed in the pseudo-dynamic algorithm.

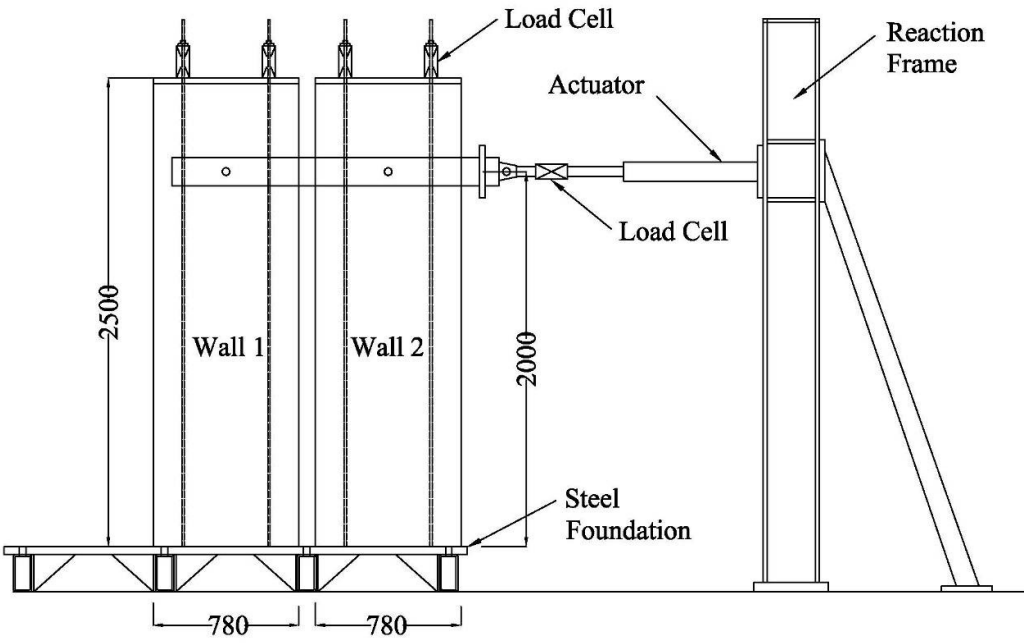

Figure 4.22 Test set-up of coupled wall system

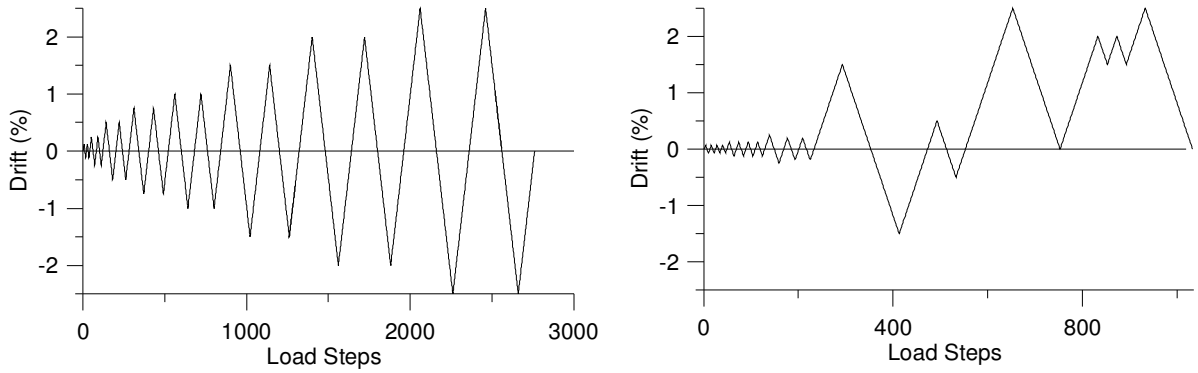

Figure 4.23 Symmetric and asymmetric loading protocols for quasi-static tests

Table 4.5 Characteristics of the adopted earthquake events

Label	Event	Year	M_w	Soil type	Duration (sec)	PGA (g,scaled)
EQ1	Landers	1992	7.3	D	44.0	0.334
EQ2	Loma Prieta	1989	6.9	D	39.6	0.363
EQ3	Cape Mendocino	1992	7.1	C	44	0.441

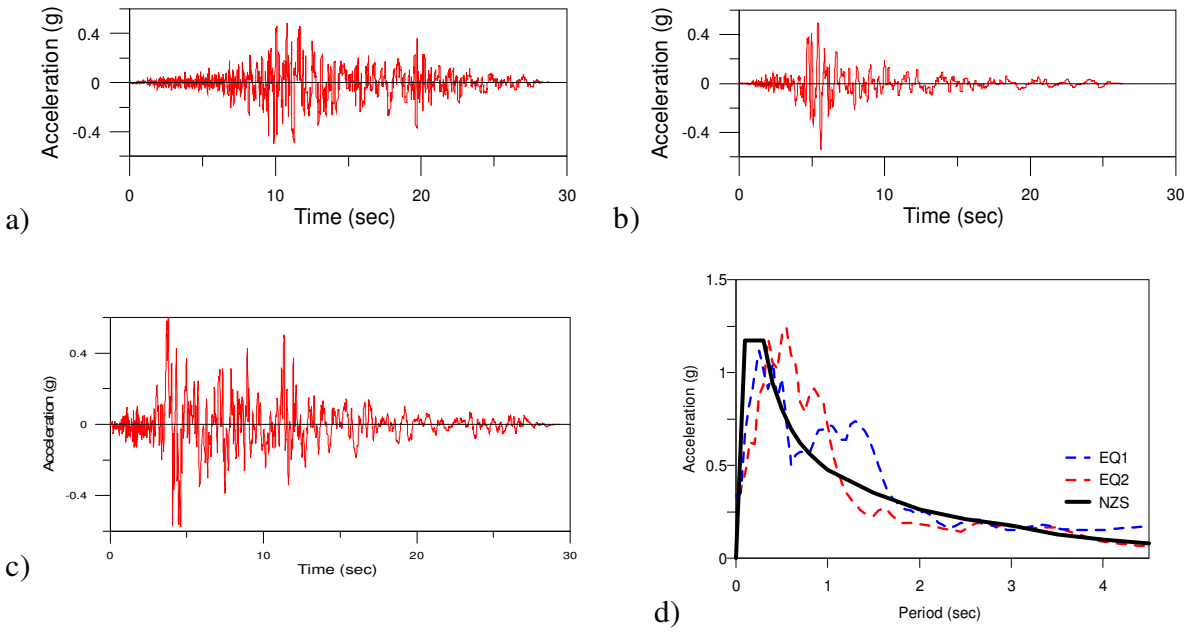

Figure 4.24 Scaled ground motions for pseudo-dynamic tests a) Landers b) Loma Prieta c) Cape Mendocino and d) corresponding response spectra compared to NZS1170.5

4.4.6 Experimental Results

Quasi-Static Test Results

The post-tensioned-only solution (Figure 4.25), i.e. with no energy dissipation devices, was first subjected to a number of small cycles of loadings. The specimen behaved elastically under these cycles without any gap opening at the base. Once the imposed displacements were big enough for gap opening to occur, the specimen showed (Figure 4.26) typical non-linear elastic behaviour with a "knee-point" (equivalent "yielding"), which was due to geometrical non-linearity (i.e. a sudden relocation of the neutral axis position at the critical rocking section). The stiffness after the "yielding" point corresponds to an increase in moment capacity due to the elongation in the tendons (Figure 4.27). No visible damage was observed. The behaviour was almost the same under the asymmetric loading with full recentering achieved, indicating no significant effect of the loading regimes.

Figure 4.25 Post-tensioned-only walls

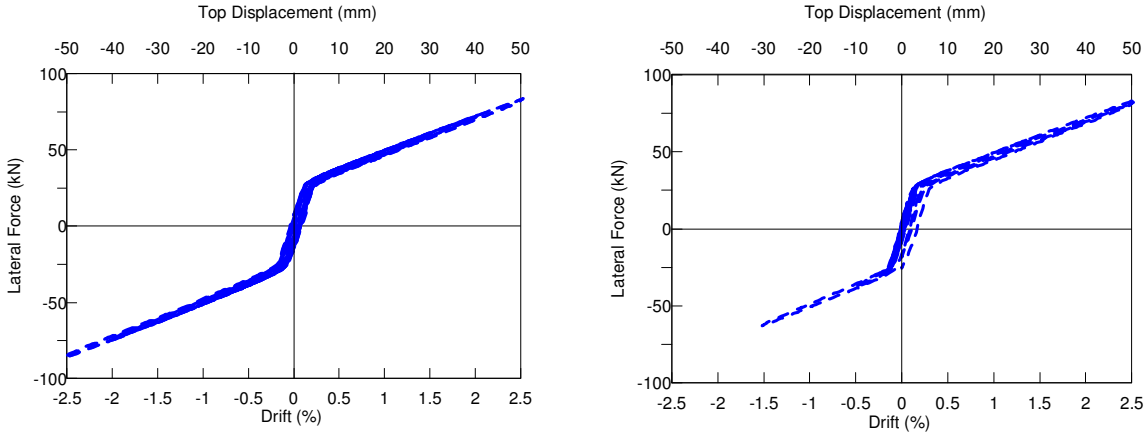

Figure 4.26 Force vs. drift results for coupled wall system, unbonded post-tension solution a) symmetric loading b) asymmetric loading

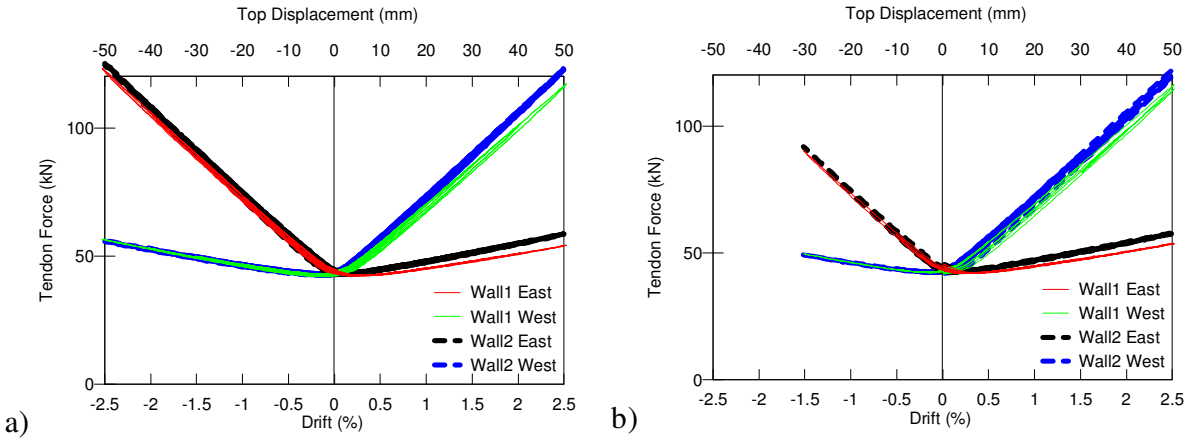

a) b)

Figure 4.27 Tendon Force vs. drift results for coupled wall system, unbonded post-tension solution a) symmetric loading b) asymmetric loading

For the hybrid solution, four additional dissipaters, located externally in the centre of each wall (two each side), were attached to the walls (Figure 4.28). Expected flag-shaped behaviour (Figure 4.29) was observed.

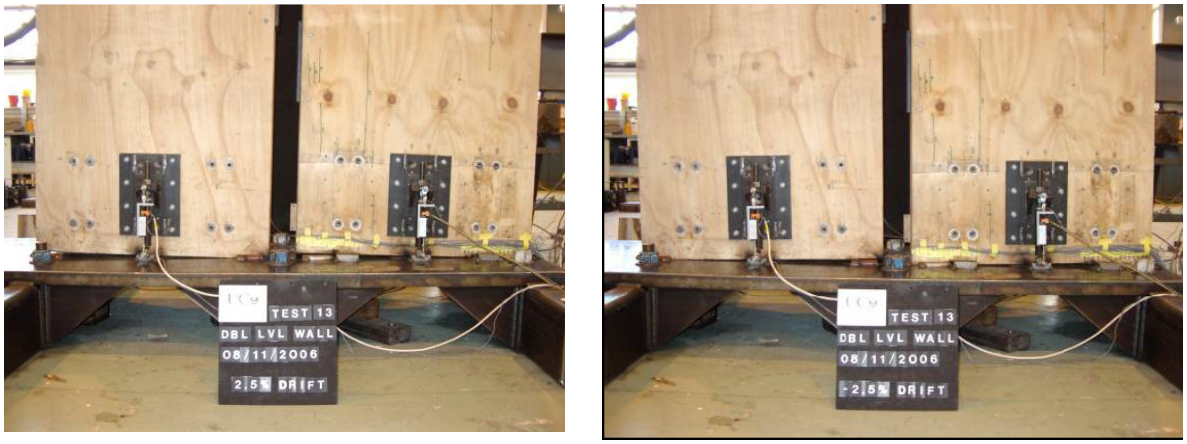

Figure 4.28 Hybrid walls

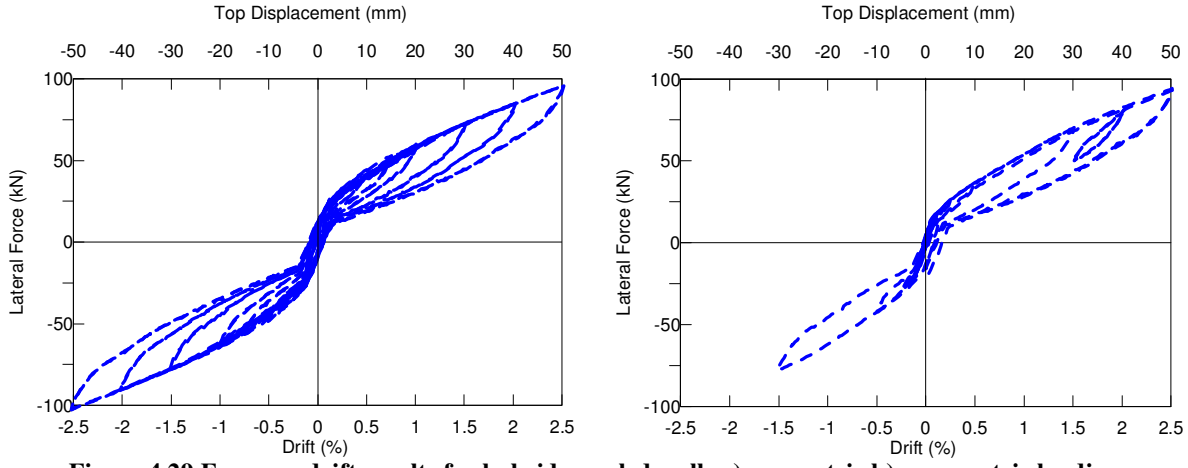

Figure 4.29 Force vs. drift results for hybrid coupled walls a) symmetric b) asymmetric loading

Figure 4.30 shows the views of the coupled walls and UFPs during a quasi-static test. One end of the actuator was fixed with the frame through a steel beam which had the potential to hold down the walls during rocking. But the beam was too slender and flexible to have any significant effect on uplift of the walls by restraining the motion. Figure 4.31a shows the force-displacements curve for the coupled wall system with a 5mm thick UFP, while Figure 4.31b shows the forces in

the prestressing tendons with changing drift. The location of the neutral axes with drifts is plotted in Figure 4.31c.

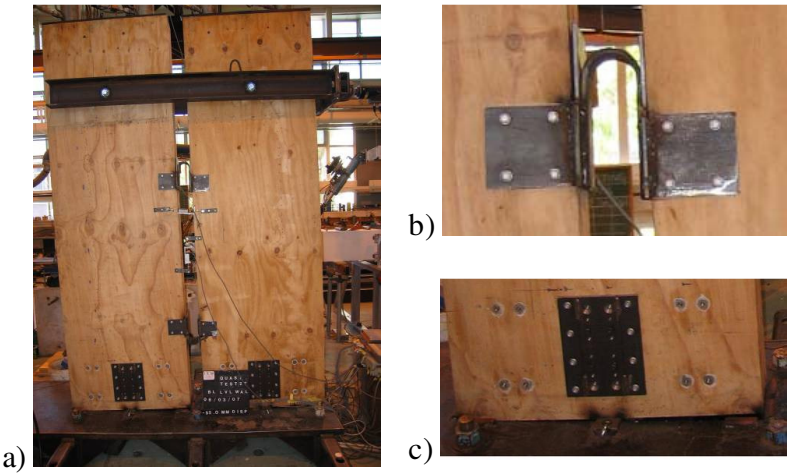

Figure 4.30 a) Rocking coupled walls with single pair UFP b) bending of plates during rocking of coupled walls c) gap opening at the base

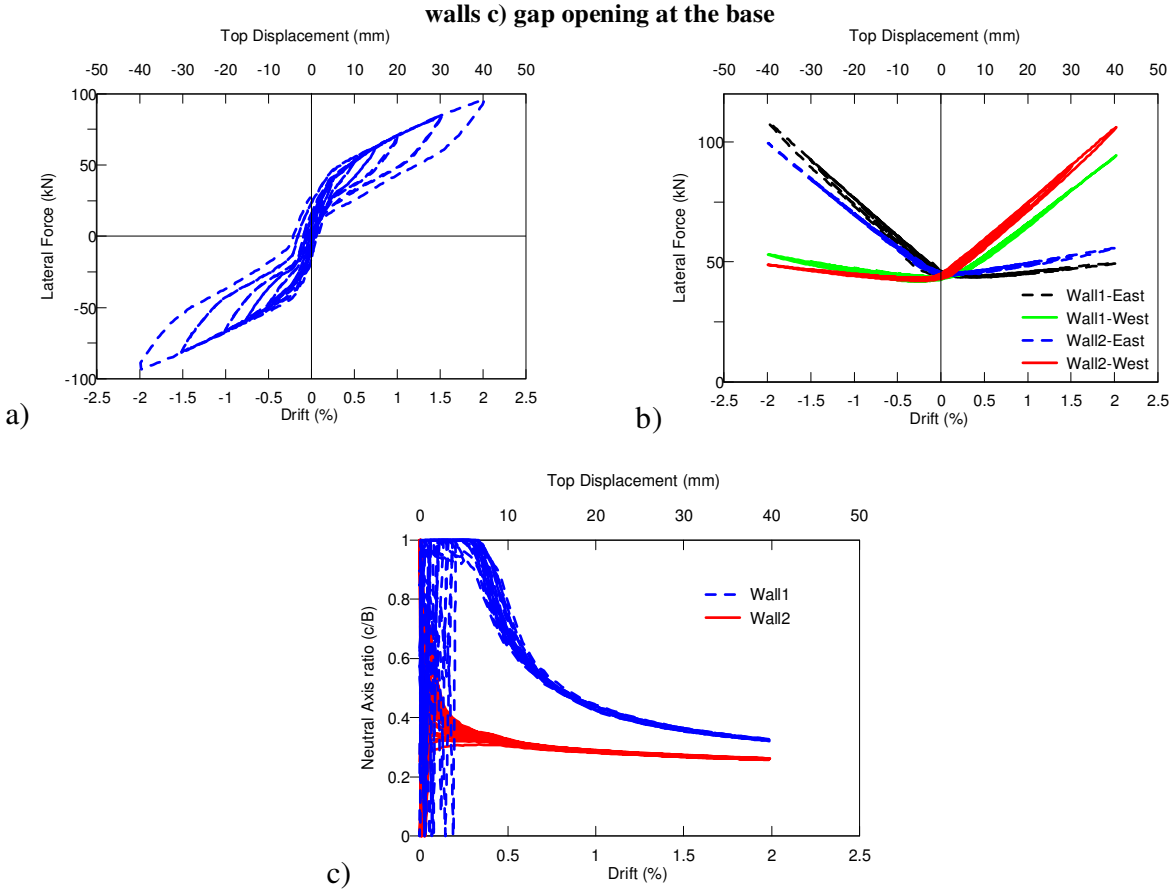

Figure 4.31 Force-displacement plot of a) Specimen HU1; b) tendon force vs. drift; c) location of neutral axis

The strength and hysteretic damping of the overall system can be controlled by varying the UFP properties. It is noticeable that similar levels of peak lateral force but different overall dissipation can be reached by combining different arrangements of UFPs with different levels of post-tensioning. The hysteretic behaviour due to different types of UFP can be seen in Figure 4.32 and Figure 4.33. In Figure 4.32 the force-displacements curves are for coupled wall systems with a double-pair of 5mm thick UFPs, varying the width of the plates. Figure 4.33 shows the overall force-displacement behaviour of walls with a single pair of 8mm thick UFPs of different widths, tested separately.

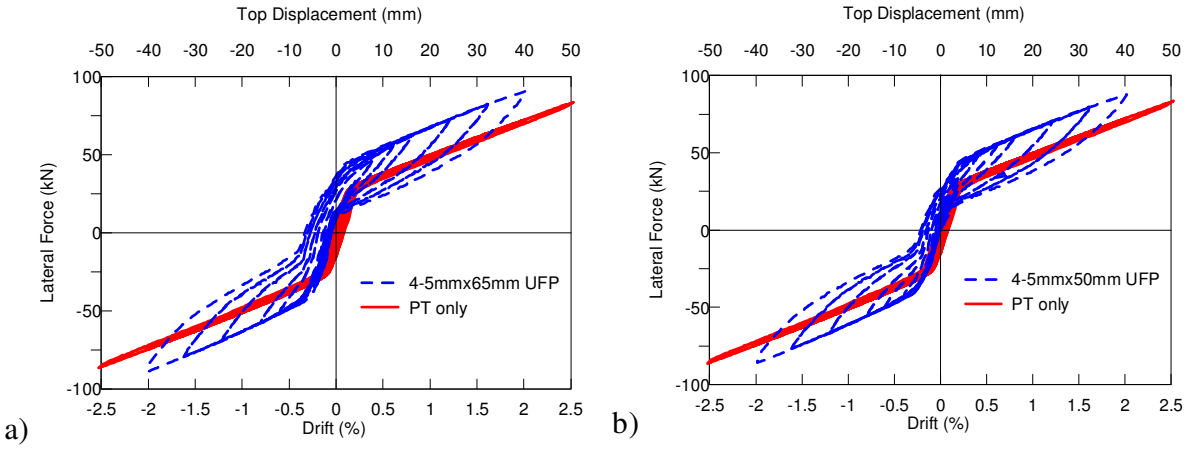

Figure 4.32 Comparisons of Specimen PT1 with a) Specimen HU2 and b) Specimen HU3

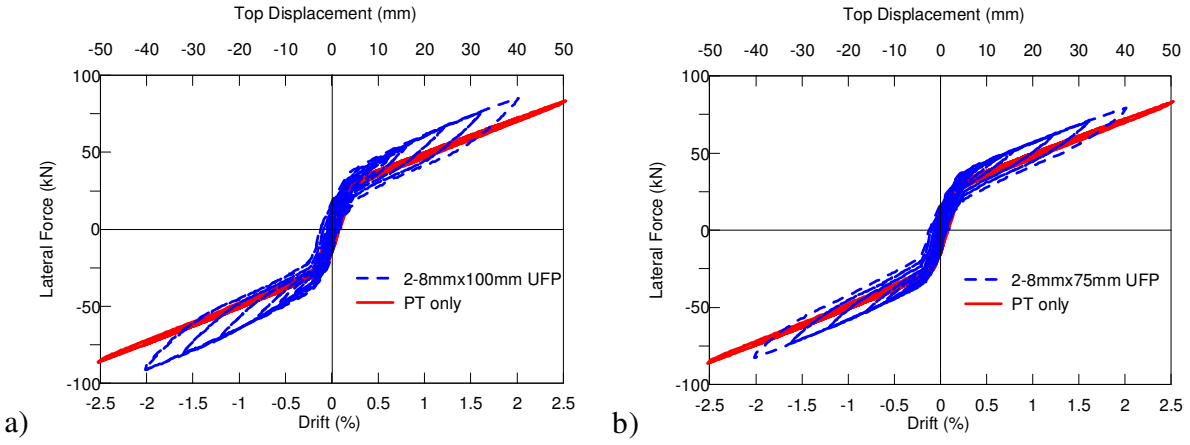

Figure 4.33 Comparisons of Specimen PT1 with a) Specimen HU4 and b) Specimen HU5

Pseudo-Dynamic Experimental Results

Figure 4.34 to Figure 4.36 show the pseudodynamic test results in terms of lateral force-drift under the above-mentioned accelerograms for both the unbonded post-tensioned-only and the hybrid systems. As expected, the results obtained confirmed the behaviour observed in the quasi-static testing. The three accelerograms produced different displacement/drift demand. The accelerograms used for the hybrid specimens were scaled up 50% to take advantage of the energy absorption from yielding of the dissipaters. Despite that it was evident that in most cases the hybrid solution reduces the maximum drift by about 20% to 50% compared to the pure unbonded post-tensioned solution.

The 50% higher intensity of the selected record corresponds to ground motions of approximately 1500 years according to New Zealand Standard NZS1170.5 (NZS 2004). As seen in the plots, full re-centering was obtained in all cases despite the higher intensity of the earthquake, partial asymmetry of the response and the 2% to 6% of additional damping depending on the drifts. Furthermore, upto 50% of lower levels of drift demands were achieved, because of the additional strength and dissipation contribution provided by the external dissipaters.

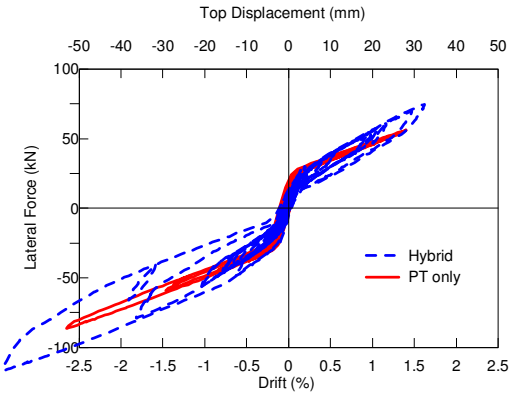

Figure 4.34 Force vs. drift results for Post-tensioned-only and Hybrid coupled wall system under Cape Mendocino ground motion

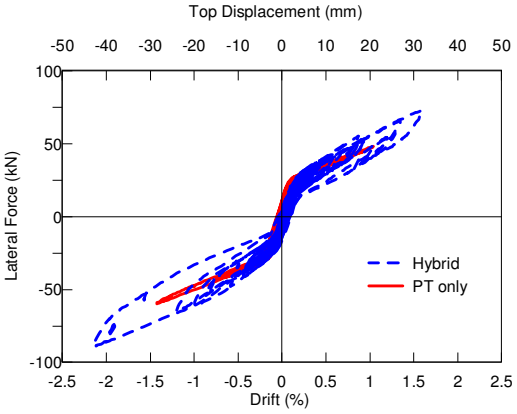

Figure 4.35 Force vs. drift results for Post-tensioned-only and Hybrid coupled wall system under Landers ground motion

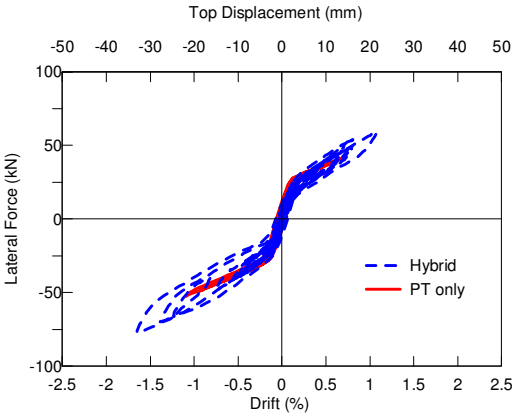

Figure 4.36 Force vs. drift results for Post-tensioned-only and Hybrid coupled wall system under Loma Prieta ground motion

Figure 4.37 to Figure 4.40 show the displacement response of different hybrid specimens, with single and double pairs of UFPs of 8mm and 5mm thickness respectively and of varying widths from 50mm to 100mm, during the pseudo-dynamic testing under the two earthquake records. The hybrid solutions always show fat hysteretic loops, due to energy dissipation provided by the UFPs. As typical of the flag-shape hysteresis behaviour, no significant residual deformations were observed although some minor slippage occurred at the base of walls during the tests.

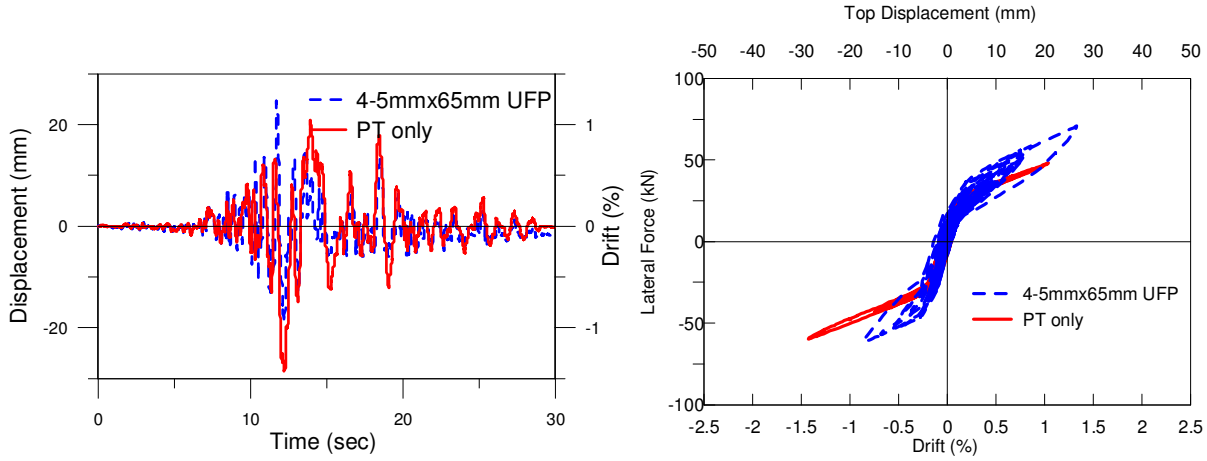

Figure 4.37 Displacement Time-history and force displacement plots of Specimen HU2 under 150% EQ1

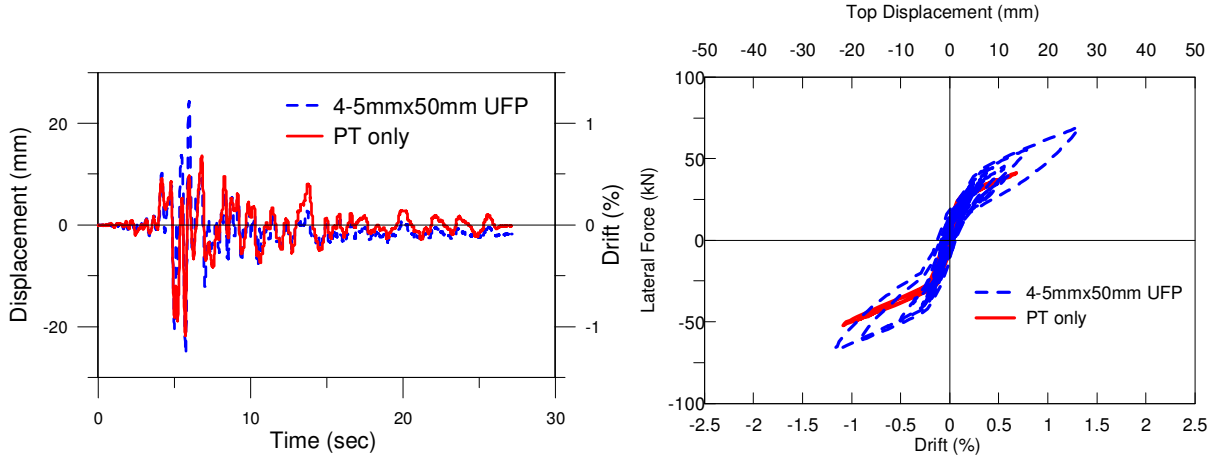

Figure 4.38 Displacement Time-history and force displacement plots of Specimen HU3 under 150% EQ2

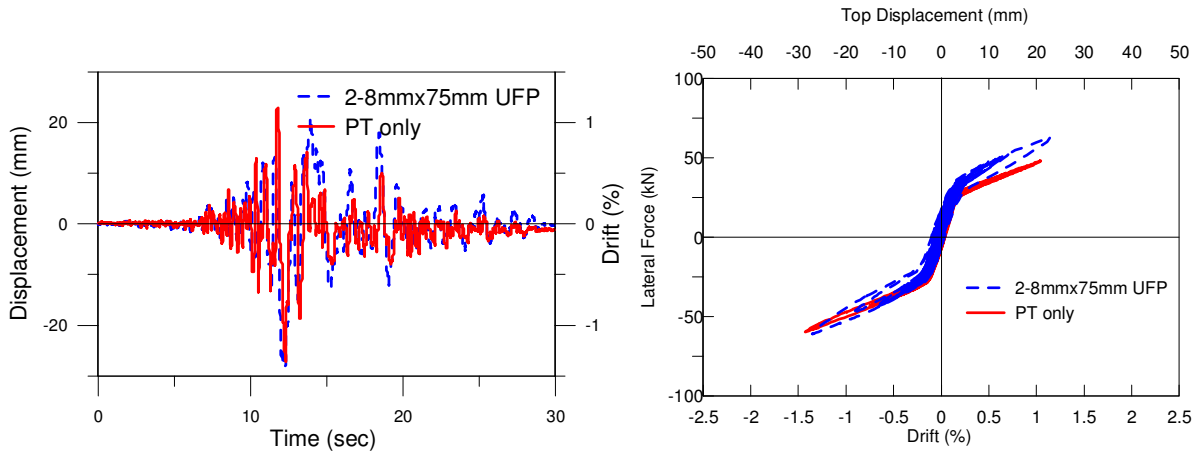

Figure 4.39 Time-history and force displacement plots of Specimen HU5 under 150% EQ1

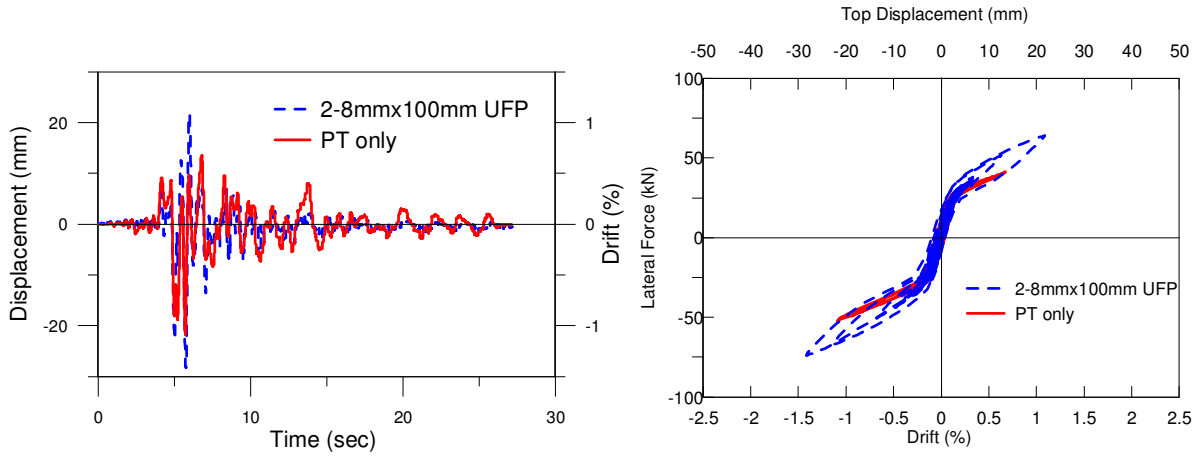

Figure 4.40 Time-history and force displacement plots of Specimen HU4 under 150% EQ2

Further Tests of Hybrid walls

To investigate the flexibility in design a series of tests were performed on the LVL walls with varying initial prestress levels and UFP sizes. The goal was to demonstrate ways to achieve a target moment capacity with different combinations and therefore with different values of the recentering ratio λ, as defined in chapter 3, which was the ratio of recentering moment over total overturning moment. The target value of λ for 2% drift was 3.

Figure 4.41a shows that the higher recentering moments can be achieved at the same drift with higher initial prestressing levels. It has been already that the amount of energy dissipation will vary with the size of the UFPs. These two elements can be combined to achieve a target moment capacity. Different combinations of the initial prestressing and UFP provide the flexibility in designing the system for desired values of the ratioλ. It is shown in the Figure 4.41b how that can be achieved. The λ achieved for specimens were HU1 and HU6 about 4 and 6 respectively. The higher than expected values were attributed to insufficient energy dissipation through the UFPs due to some flexibility in the connections.

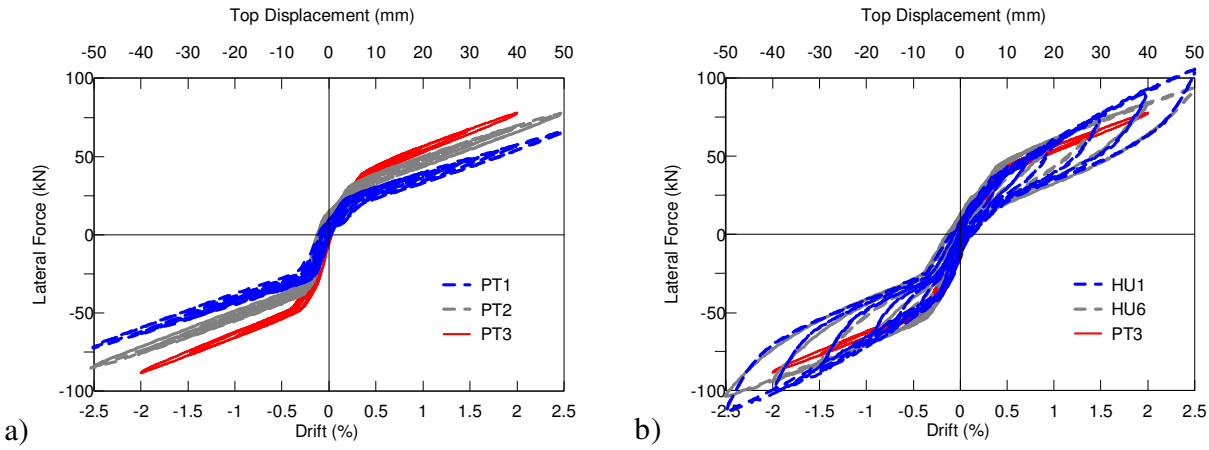

Figure 4.41 Force vs. drift results for coupled wall system with PT only and UFP dissipaters to produce same level of response

4.4.7 Comparative Performance of Different Types

The two types of hybrid arrangements (i.e. with axial dissipaters and coupled with UFP) can be compared with the post-tensioned-only system. Results of quasi-static tests of the two arrangements tested are presented in Figure 4.42. The typical "Non Linear Elastic" and "Flag Shape" hysteresis loops with full re-centering capacity were observed, respectively, in the unbonded post-tensioned-only and hybrid solutions. The change of the hysteretic behaviour due to the use of axial dissipaters can be compared more clearly from Figure 4.42a. In Figure 4.42b the force-displacements curve is that of a coupled wall system with 4-5mm thick UFP with 50mm width and 30mm radius, compared with the system without UFP and tested separately. The results of the walls with the two different energy dissipation systems show almost the same behaviour and roughly the same amount of energy dissipation (Figure 4.43). There was a small amount of residual deformation in case of the walls with UFP because of sliding at the bases of the walls.

The recentering capacity of this type of systems is measured by the parameter λ which is the ratio between the recentering moment and the moment provided by the energy dissipation elements. In

this case the two systems with axial dissipaters and UFP have comparable values of the ratio λ of about 3.

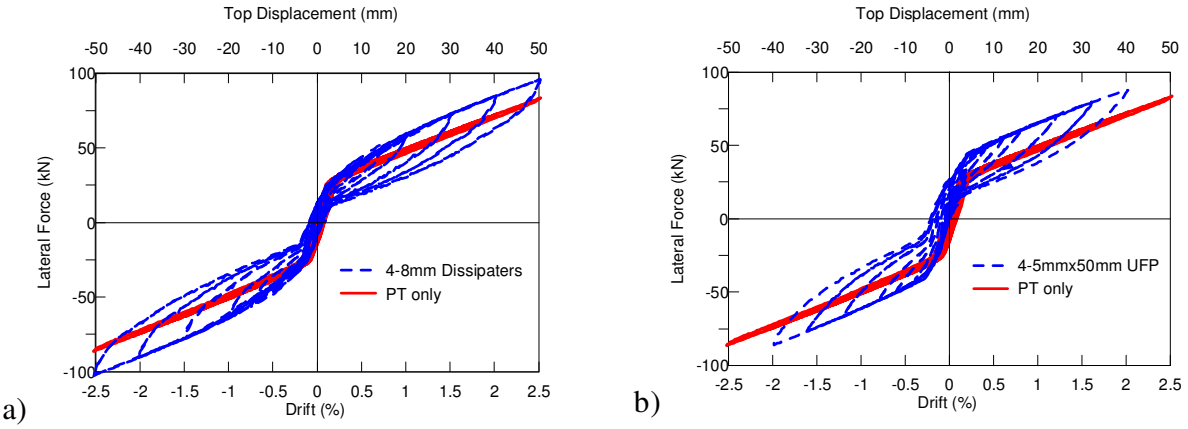

Figure 4.42 Force-displacement plots of a) Specimen HY and b) Specimen HU compared to Specimen PT

Figure 4.44 and Figure 4.45 show the displacement response of different specimens during the pseudo-dynamic testing under the two earthquake records, comparing the results of the post-tensioned-only solution with hybrid solutions with axial dissipaters and UFP respectively. As expected the hybrid solutions result show wider hysteretic loops when compared with the post-tensioning-only solution thanks to the additional energy dissipation as seen in the comparative plot below. As typical of the flag-shape hysteresis behaviour, no significant residual deformations were observed despite the irregular and asymmetric nature of the response.

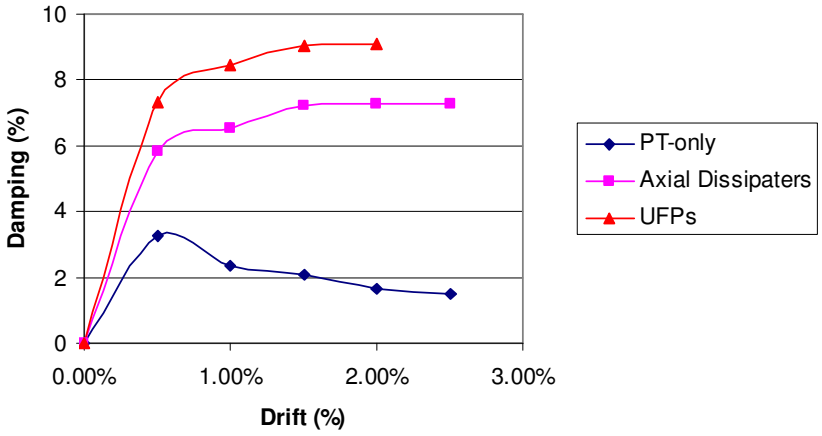

Figure 4.43 Damping vs. Drift plots for different types of Walls

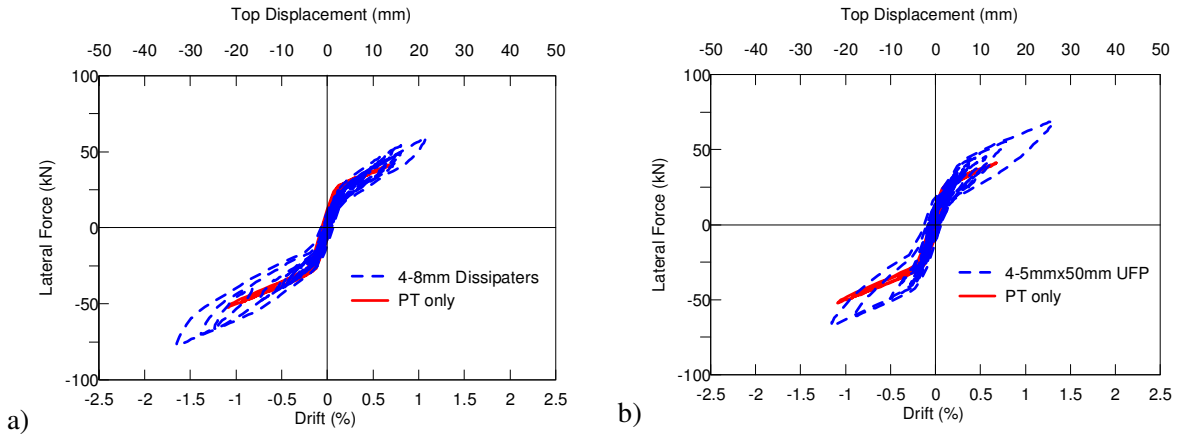

Figure 4.44 Pseudo-dynamic plots of a) Specimen HY and b) Specimen HU compared to Specimen PT

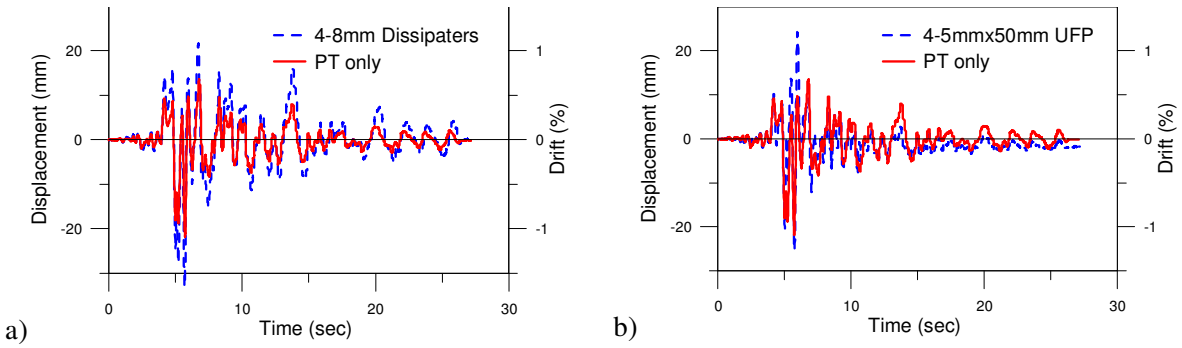

Figure 4.45 Time-history plots of a) Specimen HY and b) Specimen HU compared to Specimen PT

4.5 Summary

The expected behaviour of the walls was confirmed through the experimental investigations. Almost complete recentering was observed in all of them. In addition to that significant energy dissipation was achieved in the hybrid specimens. None of the specimens tested suffered any structural damage during testing. There was insignificant amount of residual deformations in some cases, mostly because of sliding at the bases. The three types of walls (i.e. PT-only, Hybrid with axial dissipaters and UFPs) demonstrated the flexibility and options available for design of practical structures.

5 EXPERIMENTAL INVESTIGATION ON COLUMNS

5.1 Introduction

A series of tests on a cantilever timber column connected to a steel foundation have been carried out. Both post-tensioned-only solutions and hybrid solutions with external dissipaters were investigated for the specimen. The experimental results for the column-to-foundation subassembly under bidirectional cyclic quasi-static and pseudo-dynamic loading are presented here.

5.2 Description of Column Specimens

The column specimen was originally designed as a timber bridge pier to have the moment capacity close to that of a concrete bridge pier tested as part of a recent research project at University of Canterbury (Marriott, 2009). However, it was also found to be representative of a column belonging to a multi-storey timber building carrying a gravity load of about 750kN. That approximately corresponds to a corner column at the ground floor level of a six-storied building with bay length of 10m in each direction. It had an inter-storey height of 3.2m and total vertical load of 5kN/m^2 on each floor. The column specimen tested was 2m in length, 450mm square in section with the sides made of 90mm thick LVL blocks. The prestressing tendons were placed through the central cavity and anchored at the top and bottom of the column.

5.2.1 Column and Connection Details

The column was constructed to have a hollow section by gluing together four Hy90 standard beam sections, each with a width of 360mm and thickness of 90mm (Figure 5.1a) to make a column 450mm square.

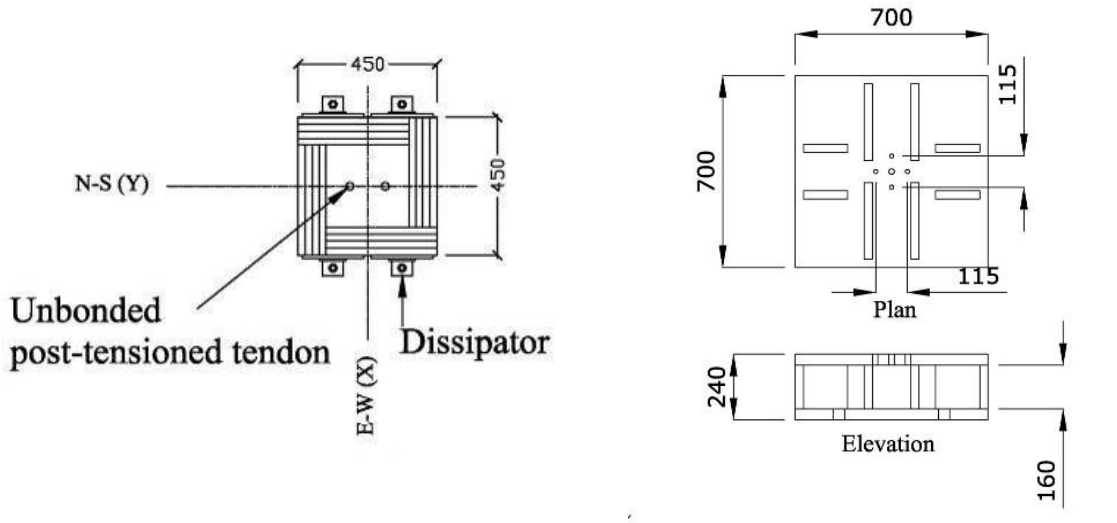

Figure 5.1 Details of column and steel base

A square sized steel base (Figure 5.1b) used for the wall specimens were for the column specimens. While it provided the necessary options of anchoring the energy dissipaters, like the case of the walls, this was also a convenient solution for the series of tests with different specimens.

As with the walls, half-circle shear keys (Figure 5.2) were placed along all four sides of the column to stop the column from sliding. The dissipaters were attached to the steel base through steel blocks welded to the base. The blocks had threaded holes in the centre which allowed the dissipaters to be put in and taken out easily keeping the column specimen in place. The top ends of the dissipaters were attached to the faces of the column with brackets and steel plates (Figure 5.2) which were in fixed to the column with coach screws. The arrangement was similar to that used for the walls.

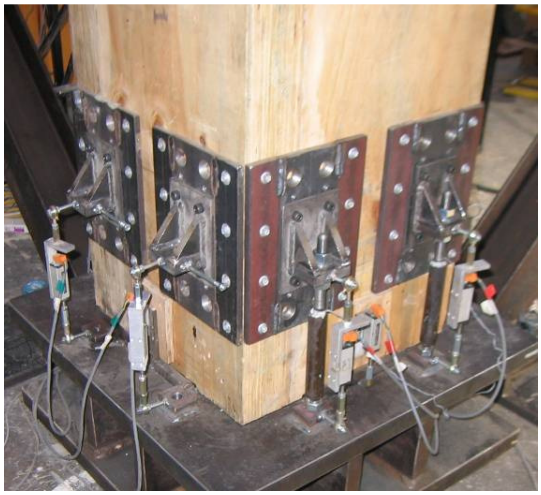

Figure 5.2 Connection details of column with steel base

5.2.2 Details of Specimens and Testing Programme

The column had combinations of post-tensioning and different arrangements of dissipaters as detailed in Figure 5.3 and Table 5.1. The different combinations produced specimens with variable recentering and dissipation capacities for experimental study.

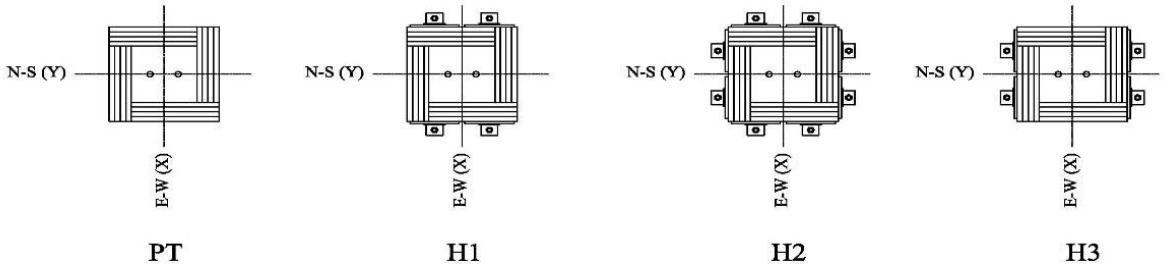

Figure 5.3 Details of specimens with designations

Table 5.1 Type and Properties of Specimens Tested

Specimen Type/ Designation	Post-tensioned only PT	Hybrid H1	Hybrid H2	Hybrid H3
Dimensions(mm)	450 X 450	450 X 450	450 X 450	450 X 450
Initial Post-tensioning	145.0 kN (72.5 kN X 2)	145.0 kN (72.5 kN X 2)	87.0 kN (43.5 kN X 2)	87.0 kN (43.5 kN X 2)
Dissipaters	None	4-8mm diameter	8-8mm diameter	4-8mm diameter

5.2.3 Test Setup and Loading Regime

The initial post-tensioning in the two tendons was provided through loading jacks placed just below the anchorage near the top ends of the tendons (Figure 5.4). The bottom end of the timber column was placed directly on the steel foundation. The post-tensioning tendons were anchored on a steel plate at the top of the column, and under the steel foundation at the bottom. There was no other contact between the tendons and the column, thus they were completely "unbonded". Instruments were placed at the top and bottom of the column (Figure 5.5) for measurements.

Figure 5.4 View of loading jacks and anchorage at top

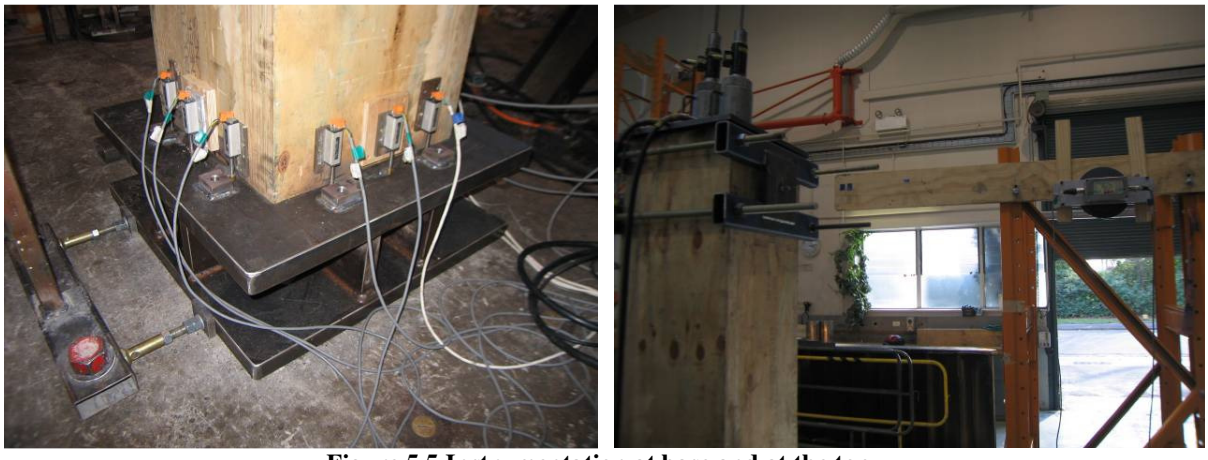

Figure 5.5 Instrumentation at base and at the top

Figure 5.6 Details of loading jacks and view of test setup

The load was applied simultaneously from two orthogonal directions through hydraulic actuators (Figure 5.6). The quasi-static loading protocol (Figure 5.7) consists of three cloverleaf-shaped cycles of increasing inter-storey drift (Figure 5.9a) following the acceptance criteria for moment-frames proposed by the ACI T1.1-01 and ACI T1.1R-01 (ACI, 2001) in each direction. The cantilever column was horizontally loaded in two directions at the expected point of contra-flexure within a frame system, i.e. the mid-level of the inter-storey height (Figure 5.8).

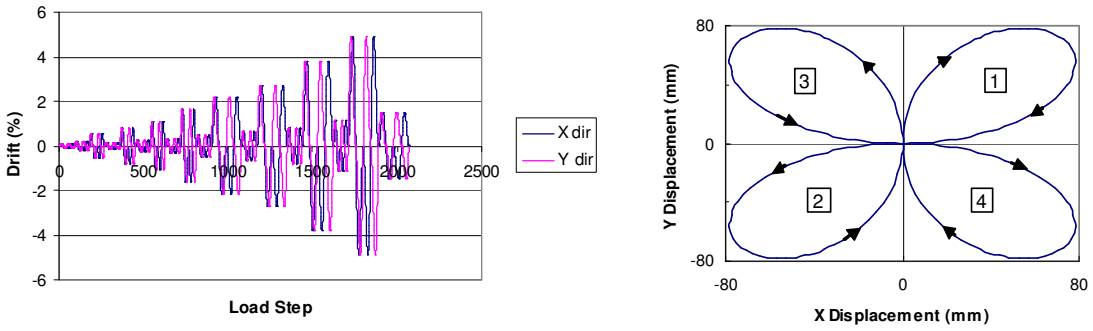

Figure 5.7 Details of loading protocol with sequence of quadrants

"Plug& Play" external replaceable mild steel energy dissipaters (Figure 5.9b) were added to the column for the hybrid tests. Again in this case, the energy dissipaters consisted of steel rods designed to yield in both tension and in compression. The 8mm diameter rods were encased in

steel tubes injected with epoxy to prevent buckling in compression. The top end of each external dissipater was connected to an external steel case fixed to the LVL column, and the bottom end was fixed to the steel foundation.

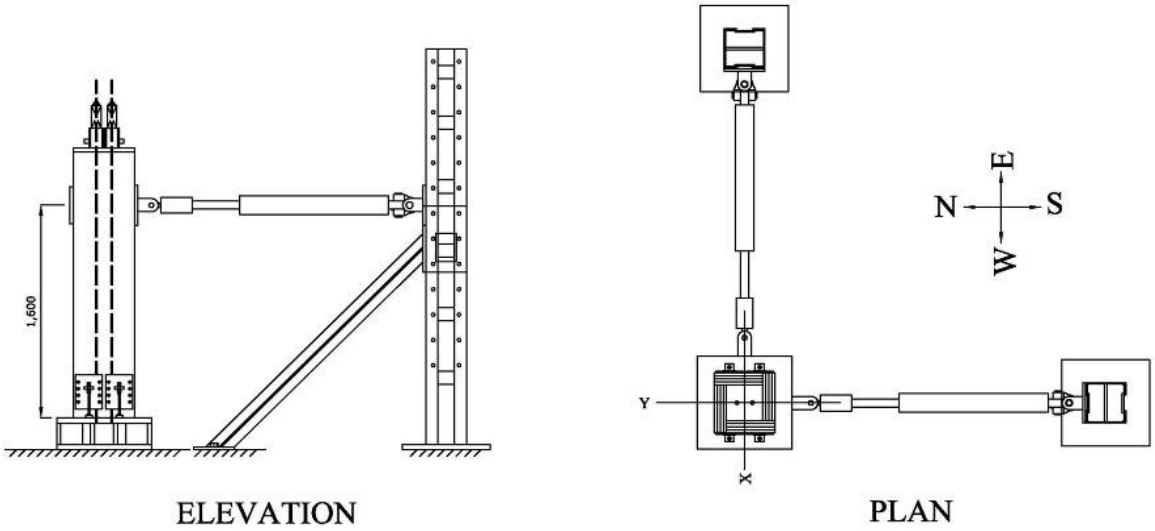

Figure 5.8 Column test setup

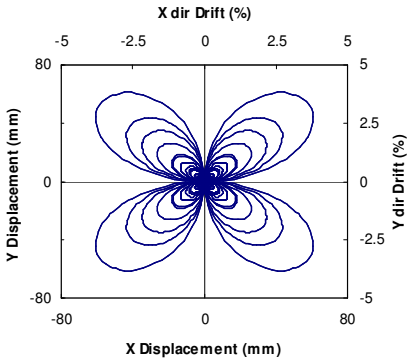

a)

b)

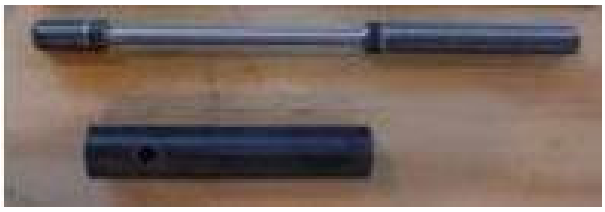

Figure 5.9 a) Complete loading protocol; b) energy dissipaters

5.3 Test Results

5.3.1 Quasi-Static Test Results

The column specimen has been tested for both two and three-dimensional quasi-static loading conditions. The two dimensional tests involve uni-directional loading protocol with alternate increasing cycles of small and large displacements. The three tests involve simultaneous loadings from two orthogonal directions which produce the resultant 'clover leaf' shaped protocol.

For the tests on the column subassembly, it was important to identify the effects of bi-directional loading, an therefore, it was decided to test the column under uni-directional loading after the bi-directional test has been perform to calculate the anticipated reduction in stiffness due to bi-directional loadings.

The specimen PT was tested with unbonded post-tensioning and no energy dissipaters. Figure 5.10 illustrates the recorded values of lateral forces with increasing drifts in the N-S and E-W directions respectively. The values of damping with varying drifts are shown in Figure 5.11.

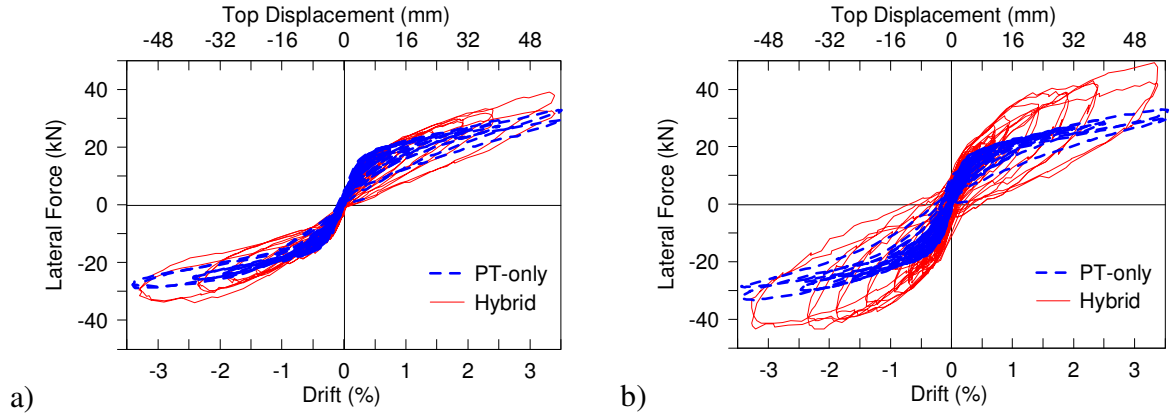

Figure 5.10 Load-displacement plots of specimens PT and H1 a) N-S direction; b) E-W direction

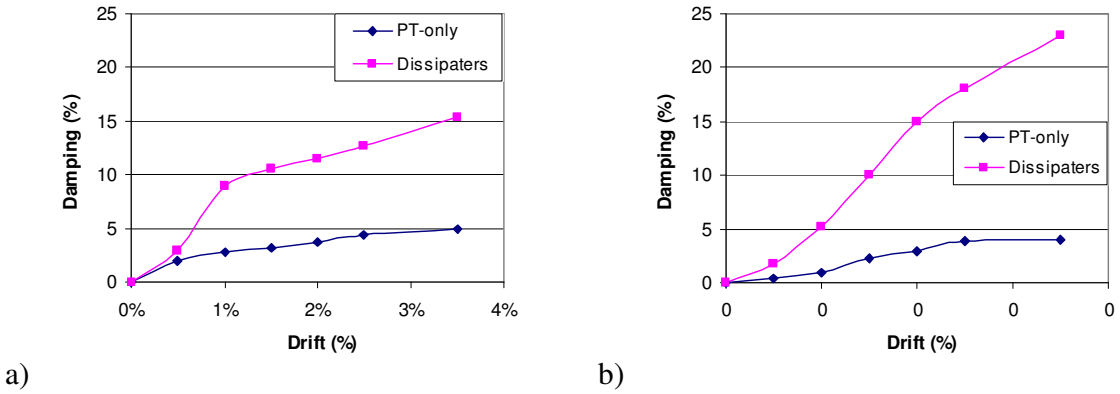

Figure 5.11 Damping-drift plots of specimens PT and H1 a) N-S direction; b) E-W direction

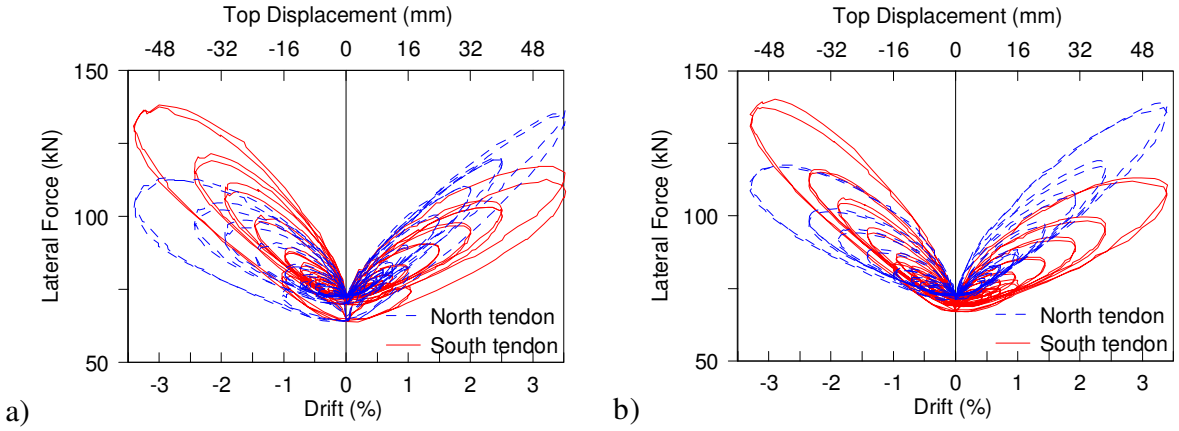

Figure 5.12 Plots of tendon forces vs. drift a) Specimen PT; b) Specimen H1

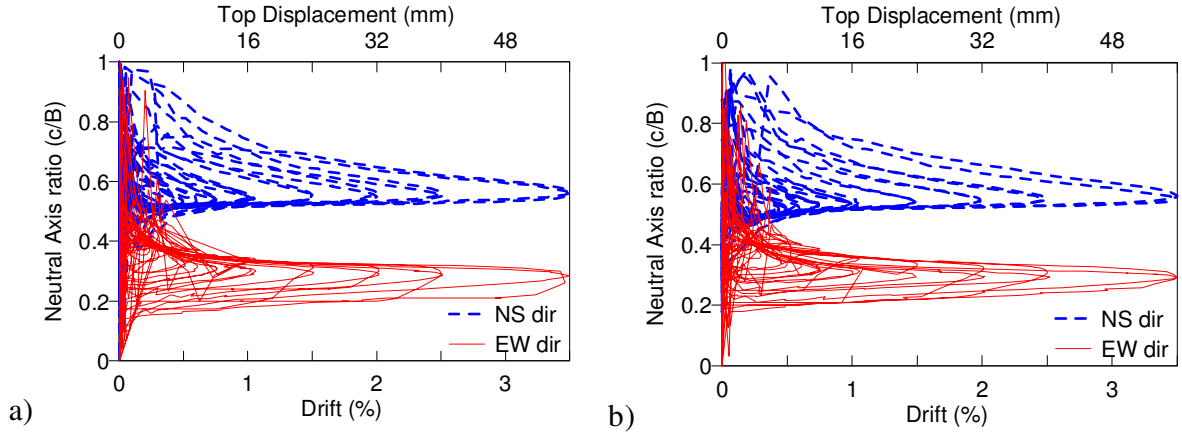

Figure 5.13 Plots of neutral axes locations: a) Specimen PT; b) Specimen H1

The hybrid specimen H1 represents the preferred combination of post-tensioning and energy dissipation. It consists of two external dissipaters placed at each of the two sides parallel to the plane of the tendons. This configuration was also followed in this research, adding the dissipaters to the same column tested with post-tensioning only (Specimen PT). The arrangement was designed to achieve a re-centering ratio of 6. Figure 5.10 illustrates the lateral forces at different drifts of the hybrid specimen. The tendon forces vs. drifts shown in Figure 5.12 indicated that the forces in the tendons remain roughly the same in the two specimens. It is visible from the force-drift plots that significant additional hysteretic dissipation with a maximum equivalent viscous damping of about 10% in the N-S direction and about 15% in the E-W direction is observed due to the presence of the energy dissipaters in the hybrid specimens. It is also important to notice that greater dissipation is achieved in the plane perpendicular to the tendons, but it also tends to get some residual displacements because of smaller recentering forces from the tendons in that plane. On the other hand, in the direction parallel to their plane (N-S) full recentering is achieved due to higher recentering forces from the tendons. The neutral axis plots (Figure 5.13) also show different locations of the neutral axis for the two directions, approximately equal to 0.6 and 0.3 of width of column at 3.5% drift, respectively.

To further investigate the recentering and energy dissipation characteristics, hybrid specimens H2 and H3 with different combinations of energy dissipaters in terms of number and arrangement were tested. Each of them had a different ratio of recentering vs. dissipation capacity. Specimen H2 (Figure 5.3) had two dissipaters at each of the four sides, twice as many dissipaters in total compared to Specimen H1. The load-displacement plots of Specimen H2 are shown in Figure 5.14. The two sets of dissipaters in orthogonal directions were complementary to each other and resulted in greater energy dissipation but the tendon forces were not adequate

for full recentering in such an arrangement. Specimen H3 had two dissipaters each at two sides that were perpendicular to the plane of the tendons (Figure 5.3). This way the dissipaters were further apart along the plane of the tendons compared to Specimen H1, requiring larger recentering forces in the tendons. Figure 5.15 shows the load-displacement plots. As expected, there were some residual displacements due to insufficient recentering forces from the tendons.

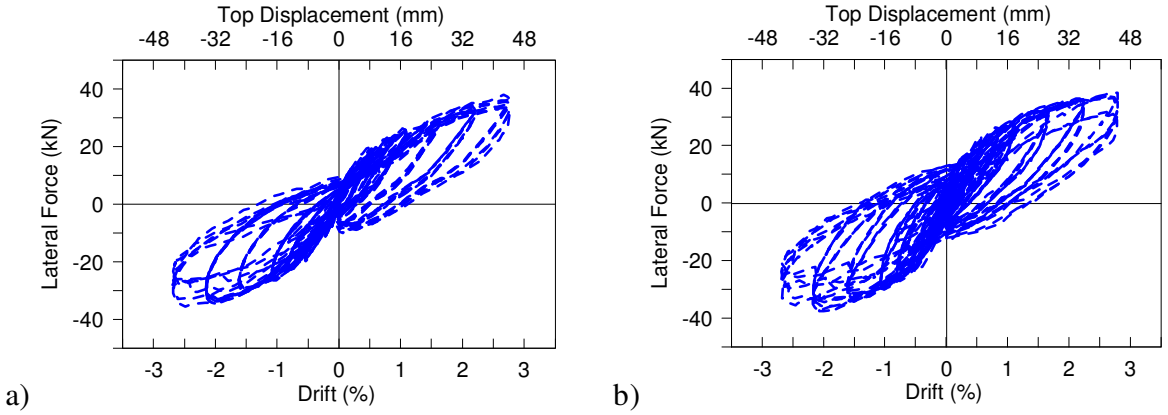

Figure 5.14 Load-displacement plots of Specimen H2 a) N-S direction; b) E-W direction

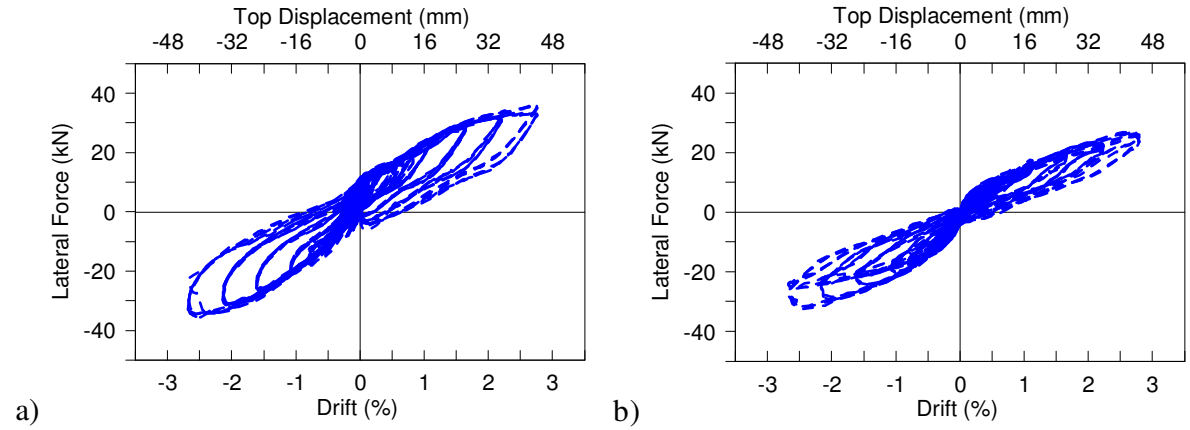

Figure 5.15 Load-displacement plots of Specimen H3 a) N-S direction; b) E-W direction

As shown in Figure 5.14, higher energy dissipation with about 10% to 12% of damping could be achieved through the increased number of energy dissipaters but in the absence of higher recentering capacity of the arrangement some residual displacements were observed at the end of the loading cycles. In the case of Specimen H3, there was increased energy dissipation compared to Specimen H1 in the direction parallel to the plane of the tendons (N-S) due to larger strains in

the dissipaters, but the recentering capacity was insufficient for full recentering. This showed that greater energy dissipation does not necessarily produce the best results and the optimum solution was the one with significant energy dissipation and minimum residual displacements.

5.3.2 Pseudo-Dynamic Test Results

A series of pseudo-dynamic tests was carried out to simulate slow motion dynamic response of the system when subjected to an earthquake input ground motion, in both post-tensioned-only and hybrid configurations. The effects of different additional dissipation capacity on the dynamic response were investigated and provided valuable information complementary to that obtained from the quasi-static tests.

Table 5.2 Characteristics of the adopted earthquake events

Event	Year	Mw	Station	Duration, sec	Scaling Factor	Component	PGA, g (scaled)
Landers	1992	7.3	Yermo Fire Station	44.0	2.2	360	0.334
						270	0.245
Cape Mendocino	1992	7.1	Fortuna Blvd	44.0	3.8	000	0.441
						090	0.433

The details of the earthquake ground motions used in the tests are given in Table 5.2. They are the same as those used for the walls. The response spectrum is shown in Chapter 4 along with another ground motion.

As part of the required information to solve the equation of motion of the SDOF system within the pseudo-dynamic algorithm, an equivalent mass of 4500 kg was assumed, corresponding to the expected gravity load (dead load plus about 30% of the live load) for the tributary area to a column within a single storey timber building. An equivalent viscous damping of 5% proportional to the initial stiffness was adopted.

The test of the post-tensioned-only column could not be continued for the whole duration of Landers accelerogram because the maximum drift exceeded the displacement limit of the testing arrangement. The hybrid system, having additional strength and dissipation capacity provided by the dissipaters, was subjected to a 50% higher intensity of the same earthquake record in order to investigate inelastic response and re-centring capability. In spite of the higher intensity of the ground motion, maximum drift was less than the post-tension only case, due to the additional strength and dissipation contribution provided by the external dissipaters. The response of the hybrid solution subject to Landers accelerogram is shown in Figure 5.16. A small residual displacement was observed in the E-W direction due to the smaller out-of-plane recentering capacity of the two prestressing tendons.

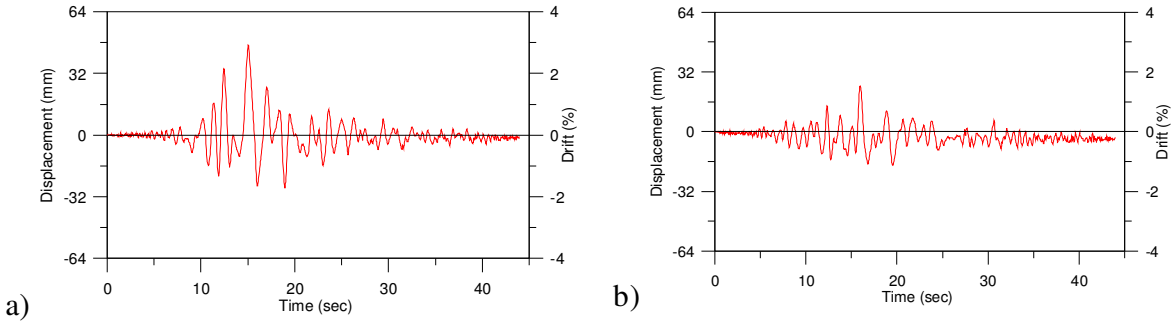

Figure 5.16 Response of Specimen H2 to Landers accelerogram a) N-S direction; b) E-W direction

The column was tested post-tensioned-only under a different accelerogram scaled to have intensity comparable to the Landers earthquake (Table 3). Figure 5.17 shows the response of the post-tensioned-only solution under a recorded Cape Mendocino accelerogram in terms of drift time-history. As expected, the maximum drift in this case was greater than that with the hybrid solution, but full recentering was achieved despite partial asymmetry of the response.

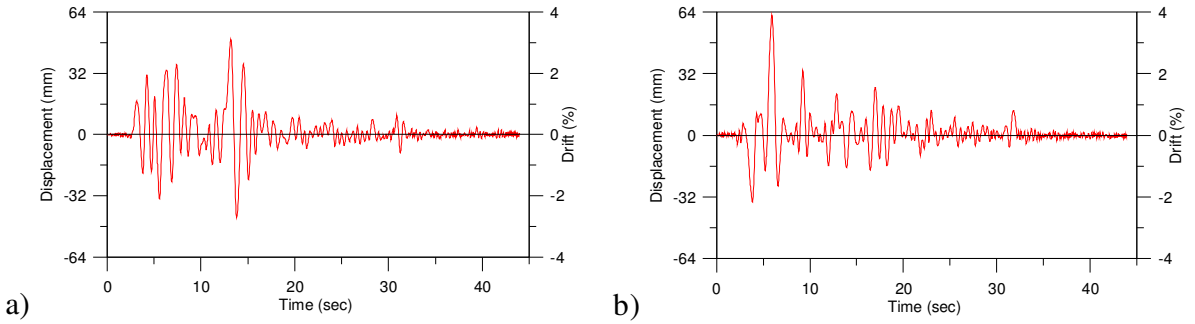

Figure 5.17 Response of Specimen PT to Landers accelerogram a) N-S direction; b) E-W direction

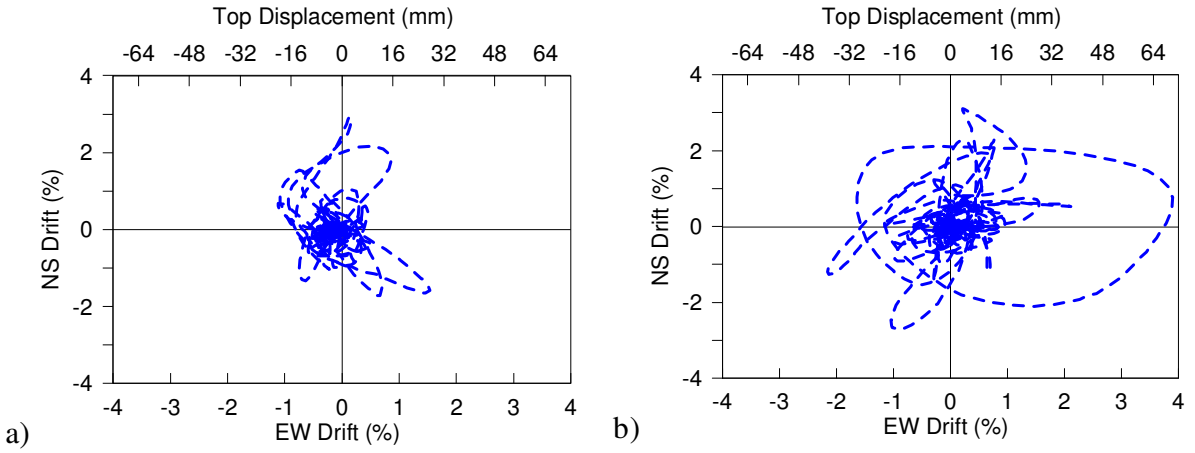

Figure 5.18 Response of column along two directions a) Specimen PT; b) Specimen H1

Combined responses of the column for both the PT-only and Hybrid specimens are shown in Figure 5.18.

5.3.3 Further testing of LVL Column

It was observed after the first series of tests that there was some deterioration of properties of the column. The loading protocol, consisting of three full clover-leaf cycles at each drift level, was deemed to be too demanding since a typical structure would not be expected to go through so many cycles of loading at such drifts. Another series of tests with fewer cycles of loading was thus performed on a new column with identical properties to check for possible degradation of the column properties during the tests. Benchmark tests were undertaken before and after the bi-directional quasi-static tests. The revised loading protocol included one full cloverleaf cycle at

each drift in place of three cycles used in previous tests. The initial prestress level was also raised to increase the recentering capacity of the column and thereby eliminate the possibility of residual displacements observed in some of the earlier tests.

Figure 5.19 and Figure 5.20 show the comparative load-displacement plots before and after the post-tension only and hybrid biaxial test, respectively. No significant degradation of strength was observed during the biaxial testing of the column. This meant that no additional protection was required at the connections in practical applications since the structure was unlikely to experience more than one or two major earthquakes during its lifetime.

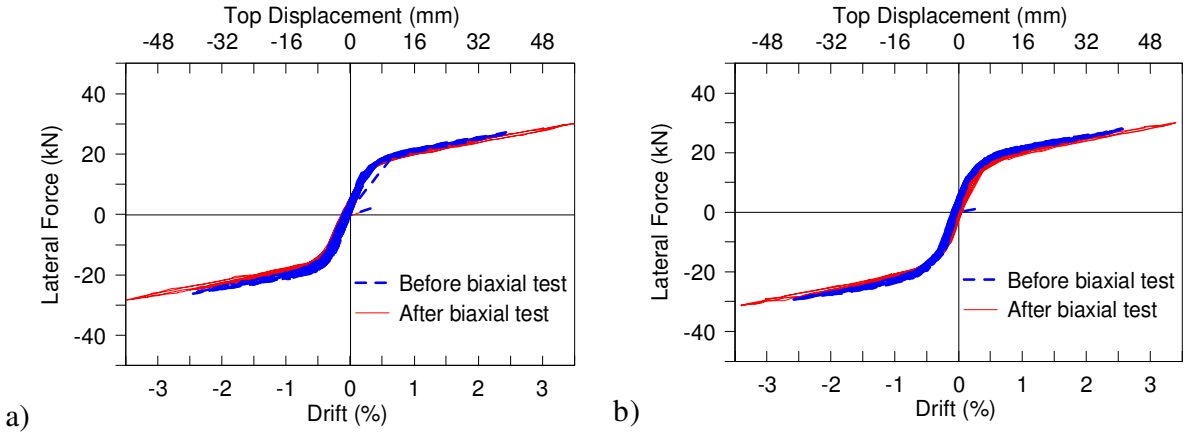

Figure 5.19 Plots of Specimen PT before and after biaxial test a) N-S direction; b) E-W direction

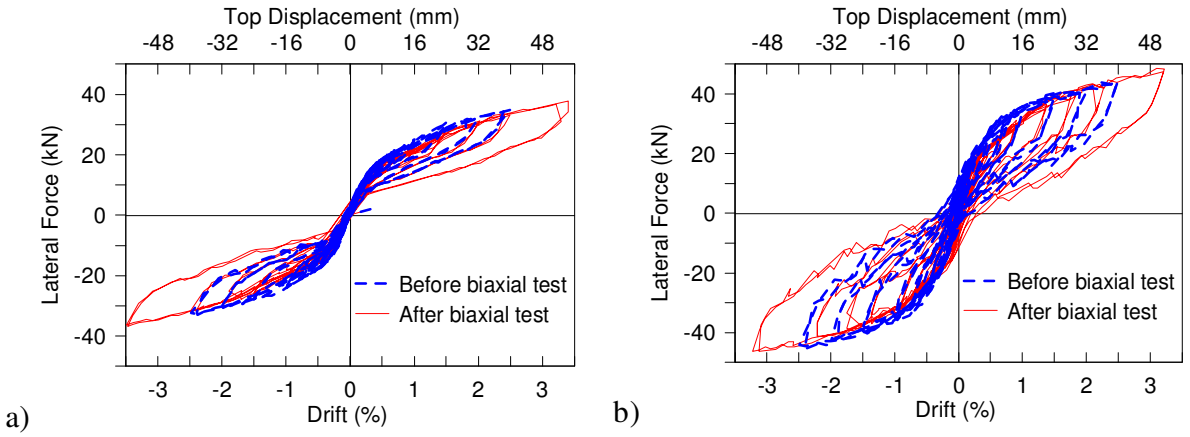

Figure 5.20 Plots of Specimen H1 before and after biaxial test a) N-S direction; b) E-W direction

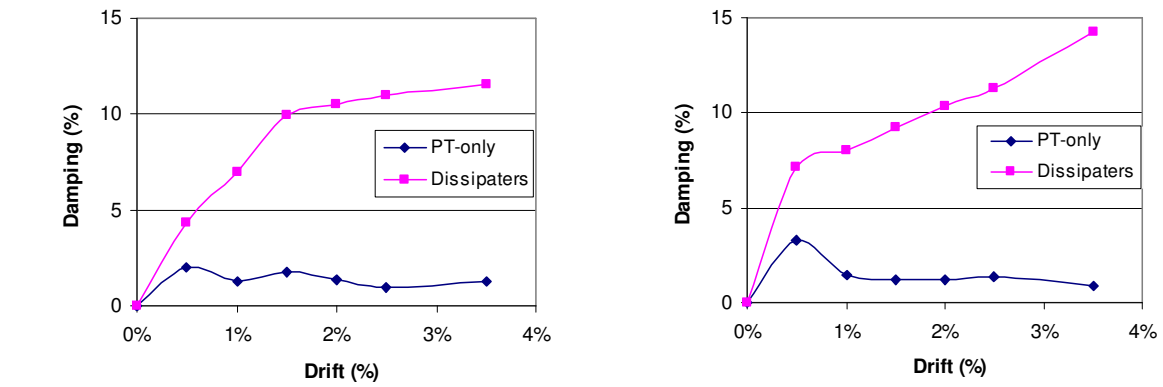

a) b)

Figure 5.21 Damping-drift plots of PT and H1 in uni-directional tests a) N-S direction; b) E-W direction

5.3.4 Bi-directional loading effects

The general failure surface of a symmetric column section under biaxial bending is expressed by an elliptical formulation proposed by (Bresler, 1960). The effects of bi-directional response can be plotted within M_x-M_y diagram:

$$(Mx/Mox)^{\alpha} + (My/Moy)^{\alpha} = 1$$

Where

M_x = x-axis component of the biaxial applied moment

M_y = y-axis component of the biaxial applied moment

M_{ox} = capacity of the section about the principle x-axis

M_{oy} = capacity of the section about the principle y-axis

α is the exponent indicating the degree on interaction. For no interaction between the two directions value of α would be zero, whereas α value of 1.0 means linear interaction.

As explained by Marriott (2009), the 3-dimensional lateral response of a column section is dependant on the displacement path. The biaxial plot matching the displacement path followed by the clover-leaf shaped experimental protocol is indicative of the level of interaction.

The effects of interaction between moment capacities in two orthogonal directions during bi-directional loading at 3.5% drift are plotted in

Figure 5.22. The values of α indicate that the moment capacity in one direction is affected by simultaneous loading in the other direction.

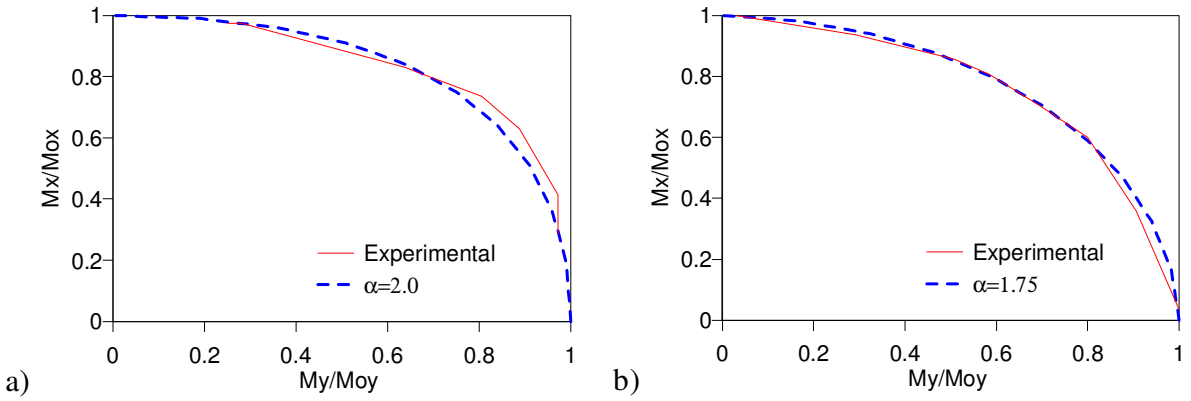

Figure 5.22 Interaction plots of a) Specimen PT; b) Specimen H1

5.4 Summary

The experimental investigations of PT-only and Hybrid column subassembly practically demonstrated the possible behaviour that can be obtained through different combinations of post-tensioning and energy dissipation capacities. It was observed that additional energy dissipation without enough recentering capacity can lead to residual deformations in specimens. Specimens tested under bi-directional loading confirmed the interaction between the two properties along the axes. Significantly, no significant structural damage was observed in any specimen tested under uni or bi-directional loading.

6 EXPERIMENTAL STUDY ON FULL-SCALE BEAM-COLUMN JOINTS

6.1 Introduction

To gain further insight into design of practical hybrid timber structures for seismic design of multi-storied timber buildings, it was necessary to experimentally test a full-scale beam-column subassembly. The plan was to test an exterior beam-column joint initially and then extend that to an interior beam-column joint through addition of another beam to the exterior joint subassembly.

6.2 Test Specimens

The full-scale beam-column joint used in this study was taken from the seismic frame of a six-story timber building located in a high seismic zone, actually constructed in concrete and virtually re-designed in post-tensioned timber (Smith, et al., 2008).

The frame properties represented an optimum structure with beam spans of 9m and floor length of 6m in the other direction. The inter-storey height was 3.2m for all stories. Both exterior and interior joint specimens were tested. To represent the virtual prototype building, the test specimen consisted of 3m long beams and a column 4m in length. The effective height was the inter-storey height of the virtual building this specimen was part of was 3.2m. All three types of test specimens: walls, column and beam-column joint were part of the same six-storey building, with minor variations.

6.2.1 Beam-Column Joint and Connection Details

The experimental study of timber subassemblies upto this research has always been performed on scaled models. It was felt necessary to investigate the additional complexities i.e. possible high deformation of the joint, local damage mechanisms in moving to full scale from a scaled model. It was also necessary to go through the prefabrication process and know about the possible problems and ways to overcome them.

As has been mentioned earlier, the beam-column joint was designed as a part of the seismic frame of a six-storey building located in a high seismic zone. Bay spacing of 6m and the inter-storey height was 3.2m for all stories. The frame was designed following the Direct Displacement-Based Design procedure (Priestley, et al., 2007). The design moment for the exterior joint was 450kN-m at 2.5% drift. The beams were to be prestressed with twelve 12.7mm diameter tendons upto 60% of yield stress ($f_{pti}=0.6f_{pty}$). Each joint interface were designed to have four (two each at close to top and bottom edge) 22mm diameter mild steel energy dissipaters between a beam and the column. It was decided that the specimen would be built in full-scale to study scale effects and also to develop and test practical connection details.

The beams and the column were constructed using available expertise in assembly of timber sections. But additional measures were added to prepare the flat contact surfaces (Figure 6.1). Since the threaded bars were critical for the hybrid connections, they were epoxied with special care (Figure 6.2) so that the connections achieve full strengths. Figure 6.3 shows the beams and the column of the test specimen in a mock-up assembly on the ground. The mild steel dissipaters (Figure 6.4) were essentially the same in nature as the ones used in walls and column, except from the size. Because of the bigger dimensions and spaces between the steel tube cases and the dissipater bars, they had to be epoxied with slightly different arrangements using nuts welded to the steel tubes for sealing.

For the armoured specimens the shear force at the beam-column joint interface was transferred through corbels attached to the armouring plates which in tern relied on friction between to beam and column to transfer the shear. In case of the unarmoured specimens the shear was transferred through friction. The dissipaters in the hybrid specimens were not subject to any significant shear force.

The dissipaters were connected through steel brackets designed to be attach them to the epoxied bars. Figure 6.5 show the completed connection. The instrumentation (Figure 6.6) was put on both faces of the joint to measure deformations in the column and also across the joint interface.

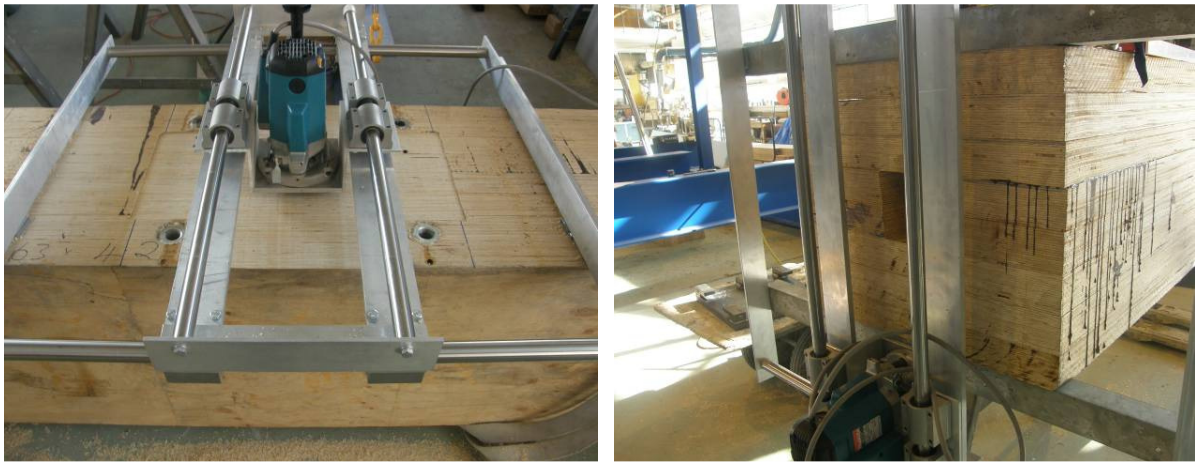

Figure 6.1 Preparation of connection interface and bearing end of column

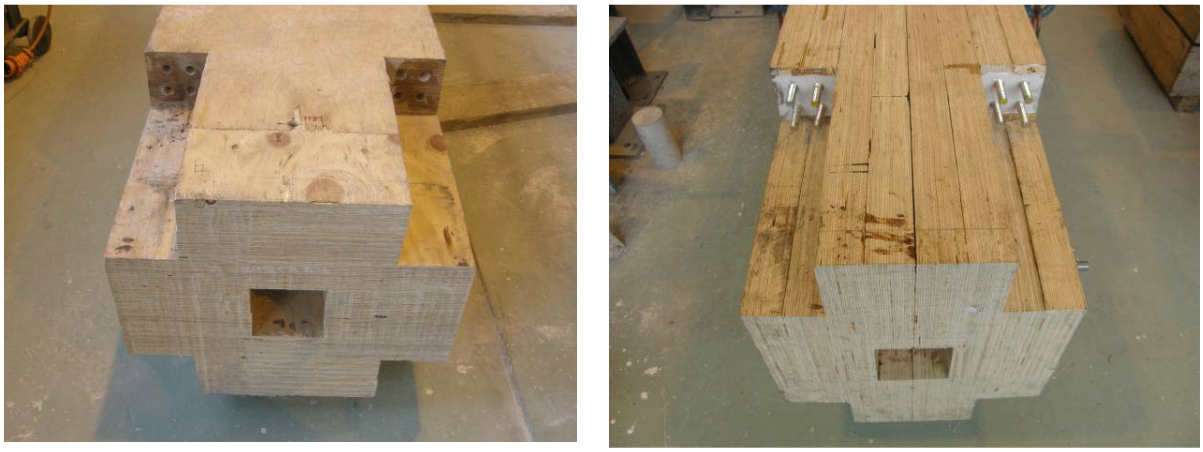

Figure 6.2 Beam end before and after insertion of epoxied threaded bars

a) 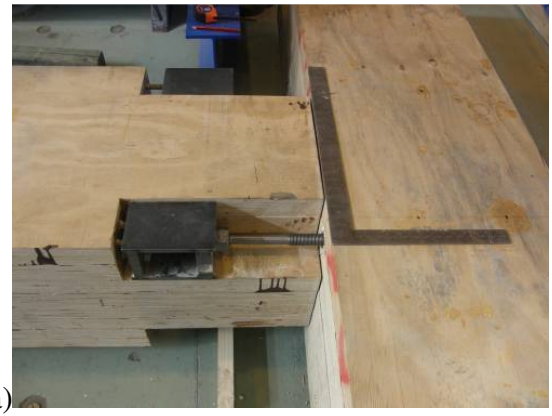 b) 

Figure 6.3 a) components of beam-column joint assembly; b) post-tensioning of test specimen

a)  b) 

Figure 6.4 a) mild steel energy dissipater; b) completed joint assembly with bracket and dissipater

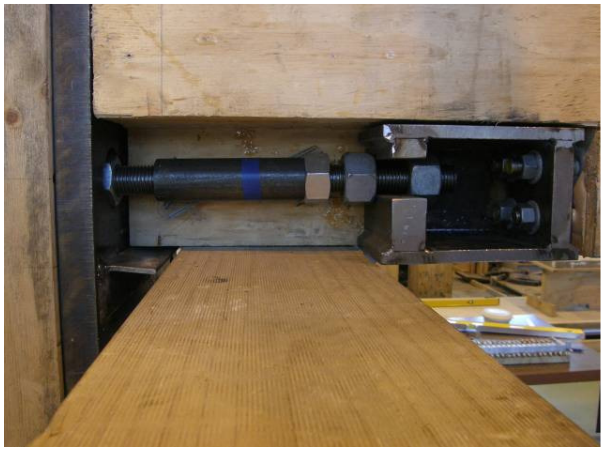 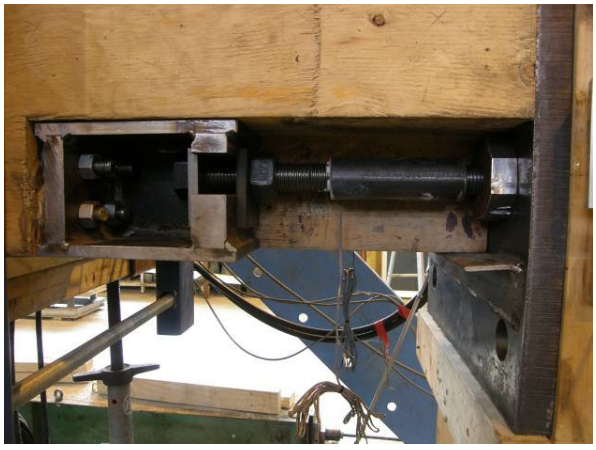

Figure 6.5 Close-up views of dissipater connection through bracket, nuts and washer


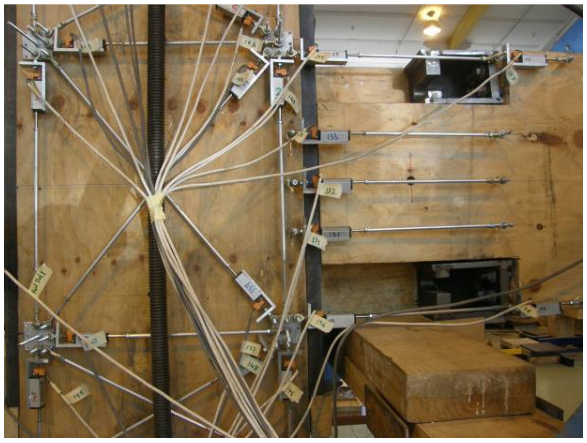

Figure 6.6 Instrumentation on column and across the joint interface

6.2.2 Details of Specimens and Testing Programme

The beam-column joint test specimen was first tested with post-tensioning only under different levels of initial prestressing and then tested with energy dissipaters. The details of the test arrangements are presented in Table 6.1 and Table 6.2.

Table 6.1 Type and Properties of Exterior Joint Specimens Tested

Specimen Type	Initial PT, kN (% yield stress)	Dissipater
PT-only, armored	490 (25%)	None
PT-only, armored	876 (45%)	None
PT-only, armored	997 (55%)	None
Hybrid, armored	966 (54%)	4 - 22mm ϕ

Table 6.2 Type and Properties of Interior Joint Specimens Tested

Specimen Type	Initial PT, kN (% yield stress)	Dissipater
PT-only, armored	560 (30%)	None
PT-only, armored	996 (54%)	None
Hybrid, armored	965 (52%)	8 - 16mm ϕ
Reinforced armored	1089 (59)	None
Reinforced unarmored	1010 (55%)	None
Unreinforced unarmored	1101 (60%)	None

6.2.3 Test Setup and Loading Regime

A series of tests was carried out with the beam-column joint specimen. The test programme started with an exterior joint and later the test specimen was converted into an interior joint with addition of a beam to the other side of the column. All the specimens were subjected to uni-directional loading. The adopted test set-up for quasi-static cyclic tests on beam-column joint subassemblies is shown in Figure 6.3. The beam was 3m long while the column was 4m high. The load was applied at the level of inter-storey height of the column, simulating the point of contra-flexure in a real structure. Additional constant axial force of 900kN was applied through vertical bars anchored to steel plates at the top and bottom of the column simulating gravity load on a column at the ground level of a six-story building with frame properties same as that of the one the beam-column joint was representative of. The quasi-static loading protocol consists of two cycles of increasing inter-storey drift, following the acceptance criteria for moment-frames proposed by the ACI T1.1-01 and ACI T1.1R-01. The load was applied through a hydraulic actuator.

Mild steel energy dissipaters (Figure 6.4) were added to the joint for the hybrid tests. The energy dissipaters consisted of "plug& play" replaceable mild steel rods designed to yield in both tension and in compression. The 22mm diameter rods were encased in steel tubes injected with epoxy to prevent buckling in compression. One end of each dissipater was connected to a steel bracket fixed to the beam, and the other end was attached to a steel threaded bar inside the column through a metal coupler. Each bracket was anchored with four smaller threaded bars embedded inside the beam. All the threaded bars, both in the beams and the column were attached to the timber with epoxy.

Exterior Joint

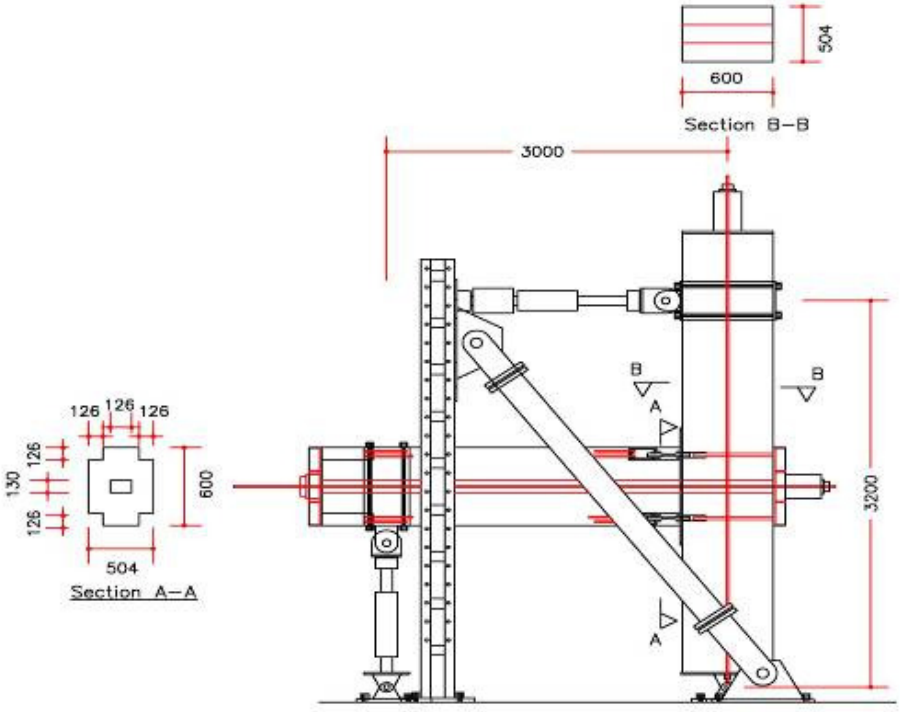

Figure 6.7 Specimen details and test setup

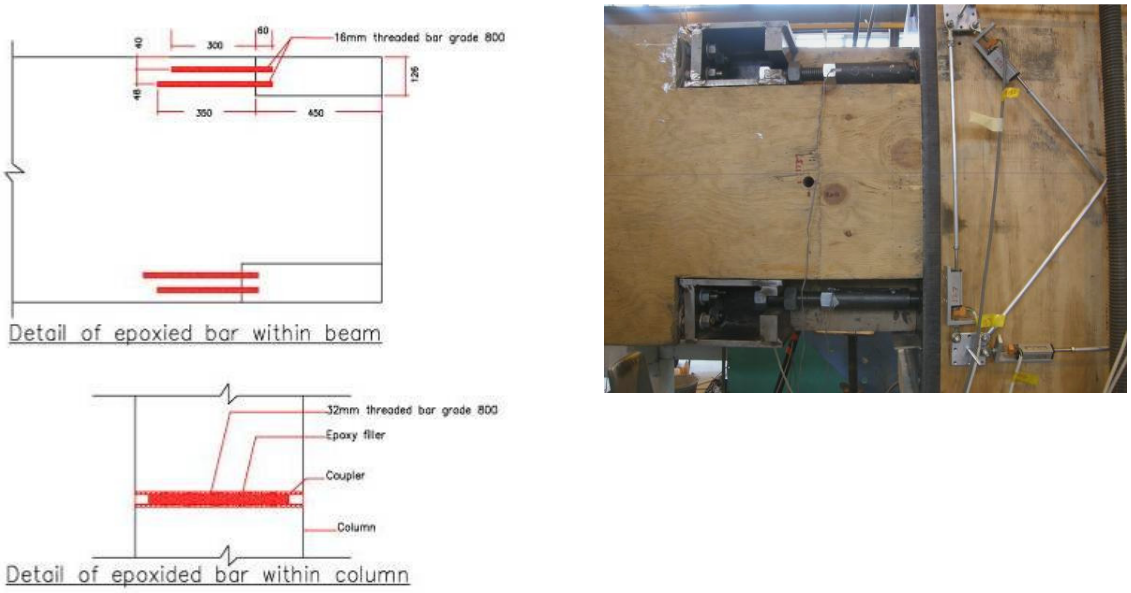

Figure 6.8 Details of dissipater attachment

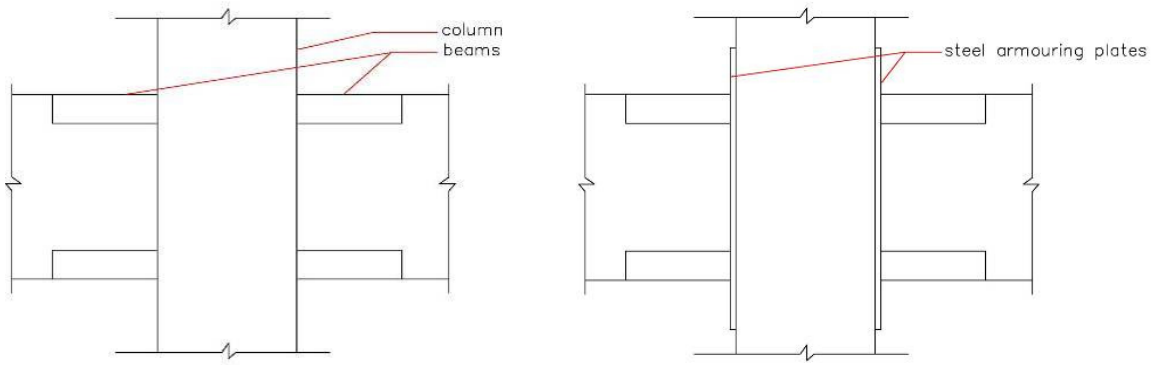

Figure 6.9 Unarmoured and armoured interior joint specimen

Interior Joint

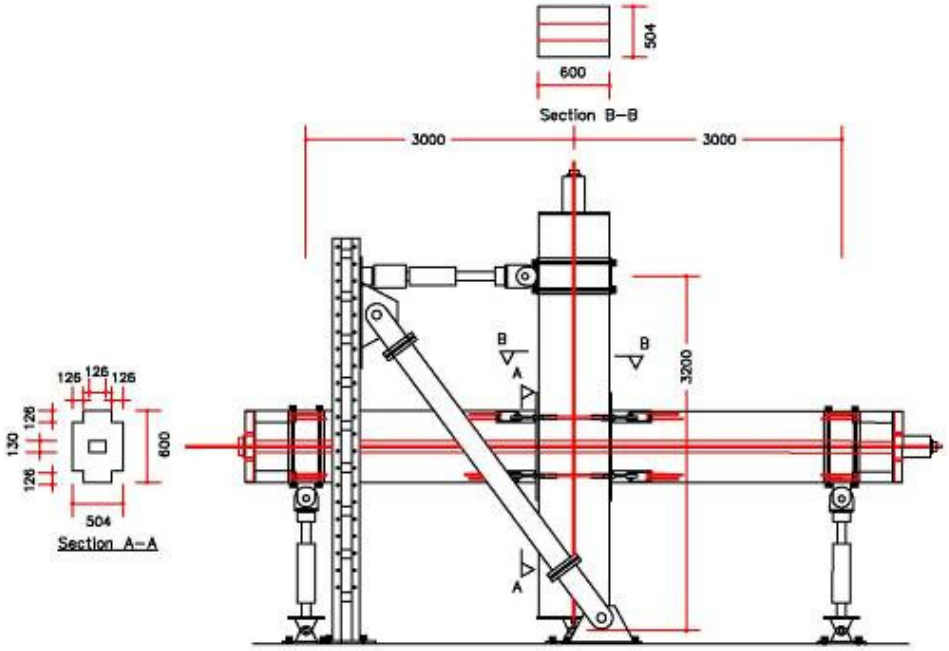

Figure 6.10 Specimen details and test setup

6.3 Test Results

6.3.1 Exterior Joint: Post-tensioned-only solutions

The post-tensioned-only specimens were tested with three levels of initial post-tensioning under the aforementioned loading protocol. Figure 6.11a illustrates the recorded values of lateral force vs. inter-storey drift (ratio of top-displacement and column height), characterised by a non-linear elastic hysteresis with fully re-centring properties.

A minor amount of hysteretic dissipation was provided by the local non-linear behaviour of the LVL material at the column contact section, loaded in compression perpendicular to the grain. The observed loss of linearity or "knee-point", i.e. similar to the yielding point of a dissipative traditional connection, was in this case due to geometrical (instead of material) non-linearity, i.e. a reduction of section stiffness due to a sudden relocation of the neutral axis position. The reduced stiffness after the equivalent "yielding" corresponds to an increase in moment capacity primarily due to the elongation of the tendons as confirmed in Figure 6.11. As anticipated, no visible damage could be detected in the structural elements when lateral deformations were increased up to 2.5% inter-storey drift. The test was terminated at this level to preserve the column specimen from possible damage due to compression crushing perpendicular to the grain before modifying it for the hybrid solution.

From the plots of the tendon forces it is visible that there was a small decrease in tendon forces after each test. This shows that there was because of some inelastic deformation in timber particularly due to higher levels of forces at bigger drifts. But the loss of force was between 1% to 2% of the yield force of the tendons and did not have any significant effect in the overall behaviour of the system.

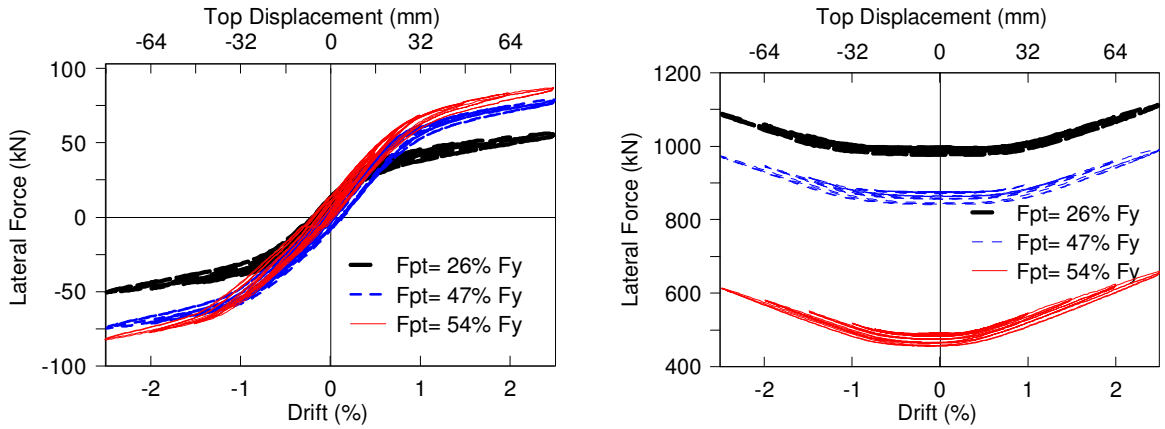

Figure 6.11 Load-drift and tendon force-drift plot of post-tension-only specimen

6.3.2 Exterior Joint Hybrid solution

The same specimen which had been tested up to 2.5% drift in the pure unbonded post-tensioned case was then tested in the hybrid configuration, incorporating the dissipation devices previously described. Addition of the dissipaters meant that there was an energy-dissipating moment contribution to the system of about 2/3 of the moment achieved in post-tensioned-only specimen for a λ value of 1.5. As a result, the "flag-shaped" hysteresis behaviour was obtained. The test results show that there was significant energy dissipation, specially at higher drift levels but there were also some residual displacements because of lower-than-expected stiffness of the connection. The difference in behaviour compared to the post-tensioned-only solution is very clearly visible in Figure 6.12. Also, there was ever more loss of stiffness after the first cycle at 3.5% due to severe yielding and bending of dissipaters. The specimen was tested for two more cycles at the same drift to check for further degradation, but the behaviour was found stable after the first cycle and no further loss of stiffness was observed.

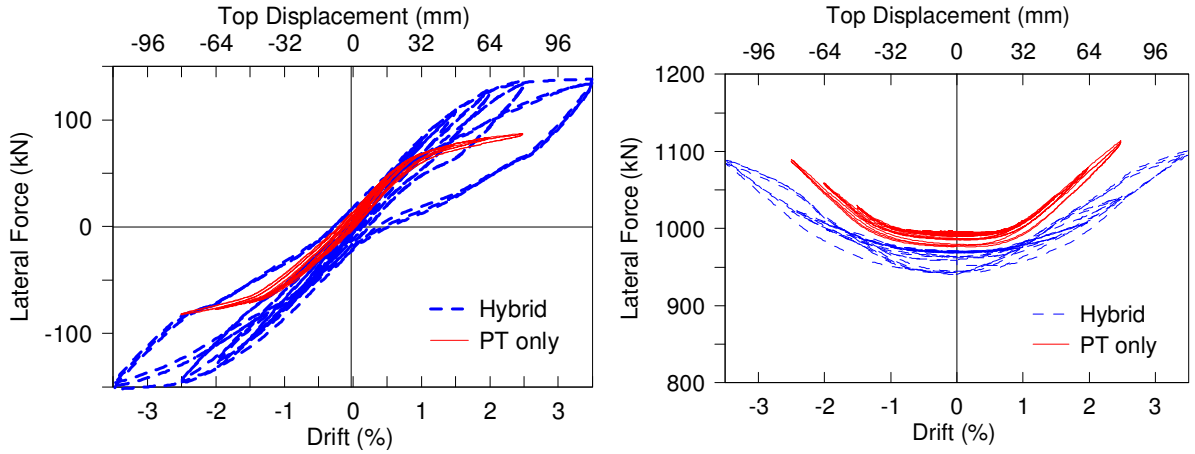

Figure 6.12 Load-drift and tendon force-drift plot of hybrid specimen

Figure 6.13 View of joint at 3.5% drift in each direction

6.3.3 Interior Joint: Post-tensioned-only solutions

For the interior joint, the post-tensioned-only specimens were tested with prestress levels at approximately lower and upper limits of the range used throughout experimental programme. Figure 6.14 illustrates the recorded values of lateral force vs. inter-storey drift (ratio of top-displacement and column height). As in the case of the exterior joint, the plots are characterised by a non-linear elastic hysteresis with fully re-centring properties and a minor amount of hysteretic dissipation.

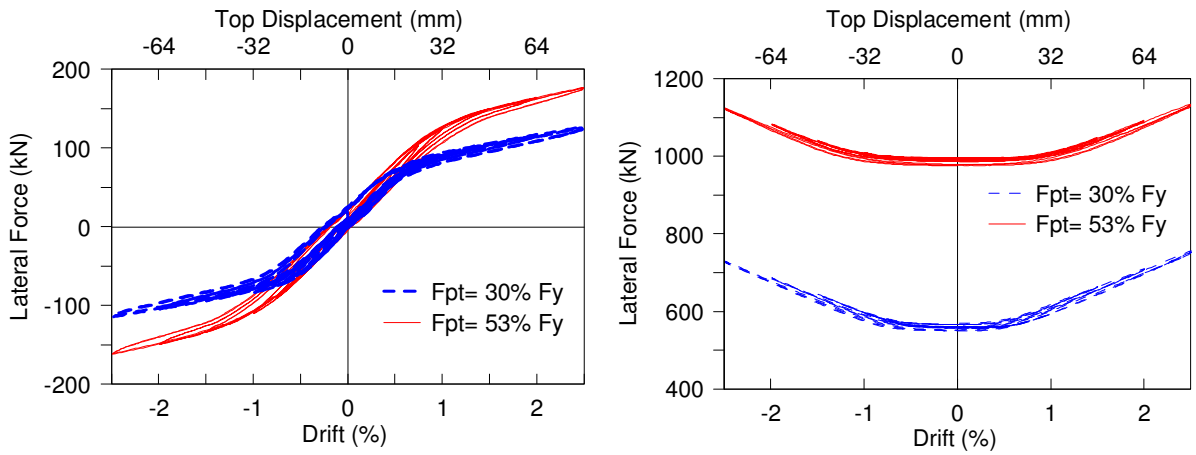

Figure 6.14 Load-drift and tendon force-drift plot of post-tensioned-only specimen

6.3.4 Interior Joint Hybrid solution

The interior joint was also tested with the dissipation devices added to prestress-only specimen. The expected "flag-shaped" hysteresis behaviour was achieved, which indicate significant energy dissipation, specially at higher drift levels. The difference in behaviour compared to the post-tensioned-only solution is very clearly visible in Figure 6.15. But there were also some residual displacements as was the case of the exterior joint.

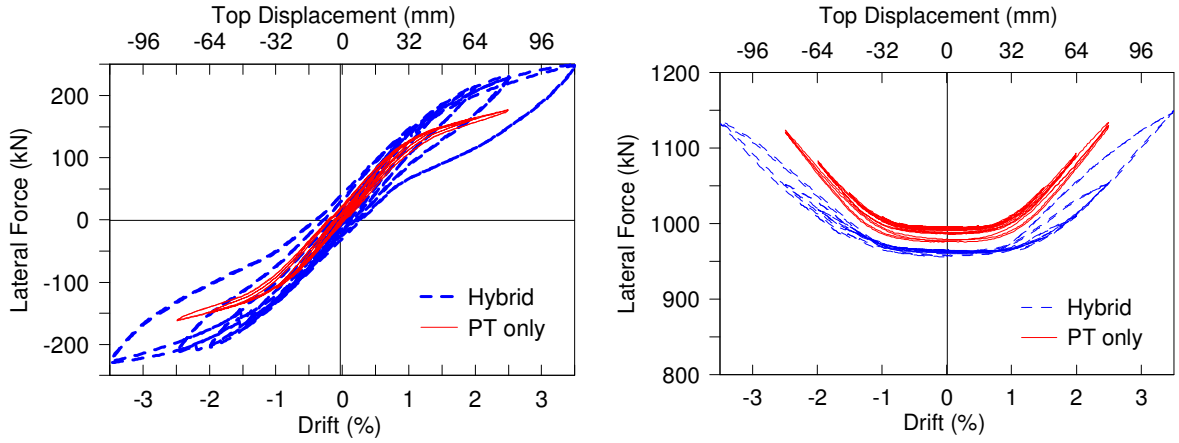

Figure 6.15 Load-drift and tendon force-drift plot of hybrid specimen

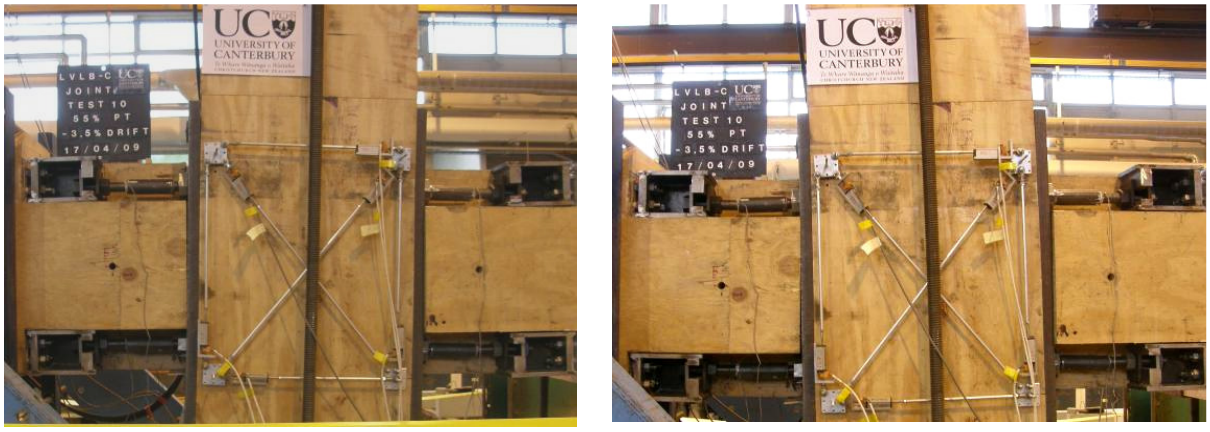

Figure 6.16 View of interior joint at 3.5% drift in each direction

6.3.5 Effect of Steel Armouring on Column

During all the tests discussed so far (with both exterior and interior joints) the joint interface had a 30mm thick steel armouring plate, primarily to protect the column from crushing in direction perpendicular to the grain. To fully investigate the effect of the steel armouring plates, tests were also performed on the interior joint without the plates between the beams and the column. As apparent from the figures, there was a significant reduction of stiffness after removal of the armouring plates. As predicted, the beam crushes the column progressively at each cycle with incremental drift and by the end of the test there was a significant drop from the initial prestressing force due to gradual decrease in the unbonded length.

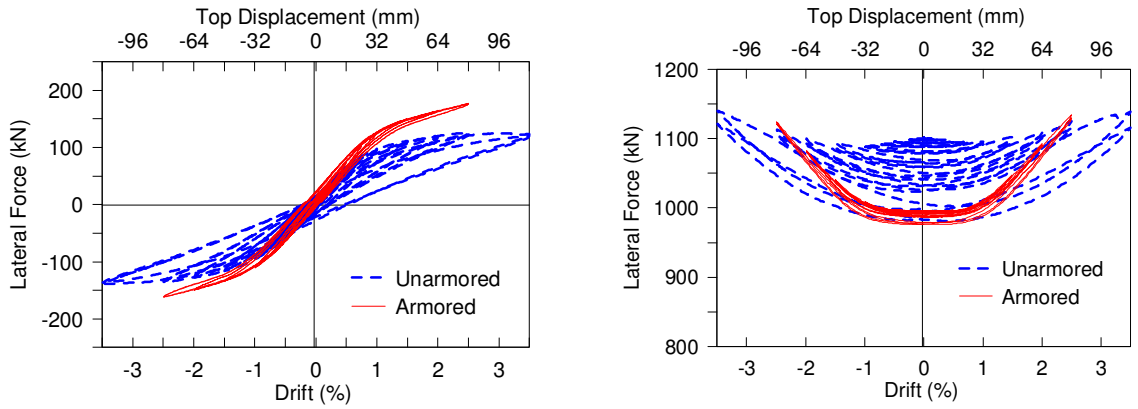

Figure 6.17 Comparative load-drift and tendon force-drift plots of specimens

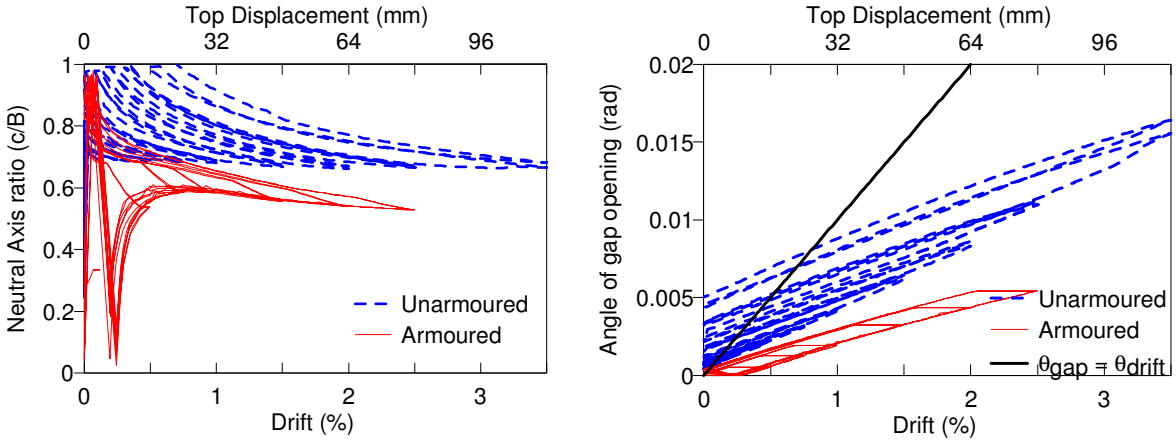

Figure 6.18 Plots of neutral axis locations and gap opening angles with and without armouring

6.3.6 Column Reinforced with Long Screws

To overcome the problems due to very low value of modulus of elasticity of timber in perpendicular-to-grain direction it was decided to use metal screws as reinforcements inside the joint panel region of the column. Special screws upto 600mm of lengths were inserted into the column in both horizontal and diagonal directions (Figure 6.19 and Figure 6.20). Tests were performed on the interior joint specimen first with and then without the steel armouring plates to study the effects of the screws.

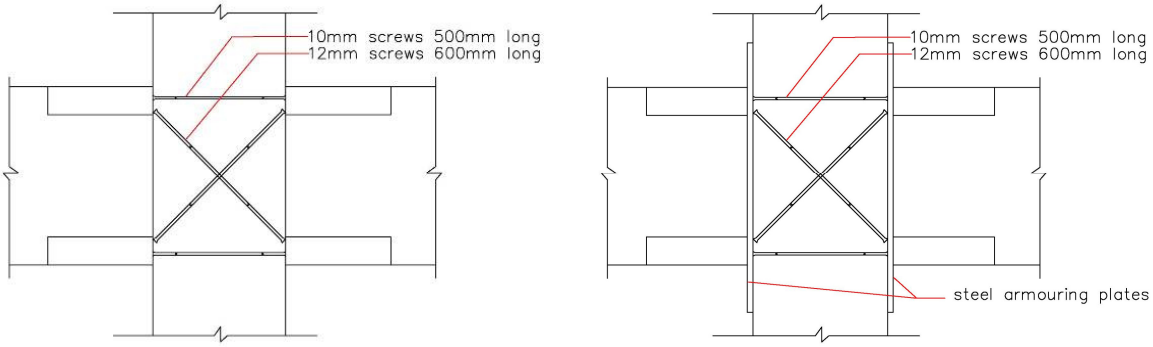

Figure 6.19 Unarmoured and armoured reinforced interior joint specimen

Figure 6.20 Horizontal and Diagonal screws inserted into the column

6.3.7 Effects of screws in unarmored column

Similar to the case with the armored column, the stiffness remains virtually unchanged, but there was a significant reduction in loss of prestress forces due to application of the screws.

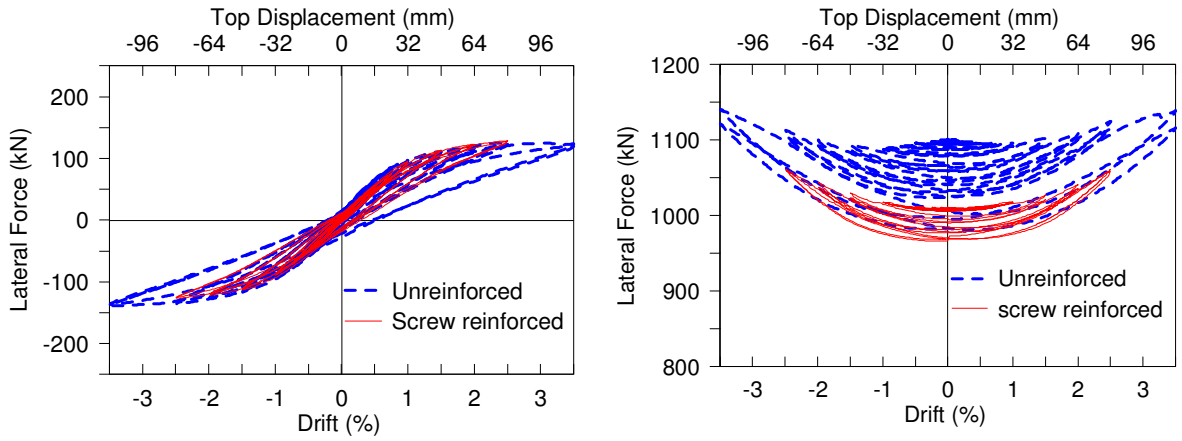

Figure 6.21 Comparative load-drift and tendon force-drift plots of specimens

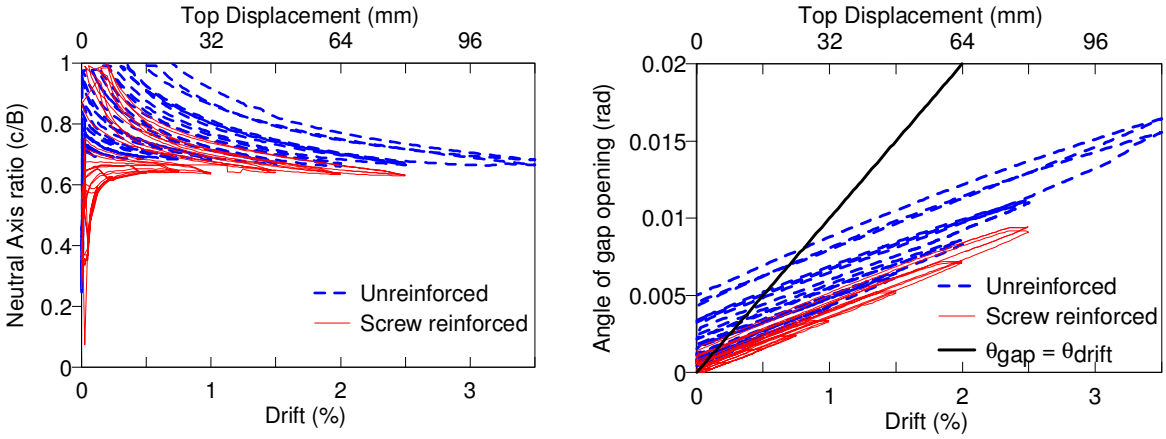

Figure 6.22 Plots of neutral axis locations and gap opening angles with and without reinforcing

6.3.8 Combined effect of armouring and reinforcement

As seen in the case of the specimen without the screws, the stiffness decreases in absence of the steel plates. But noticeably, the crushing of the column and subsequent loss of prestressing force was reduced compared to the case without the screws inside the column.

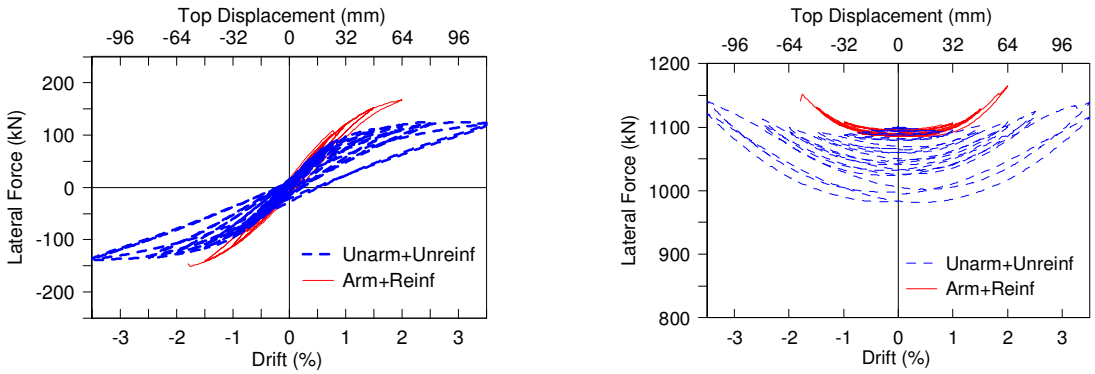

Figure 6.23 Comparative load-drift and tendon force-drift plots of specimens

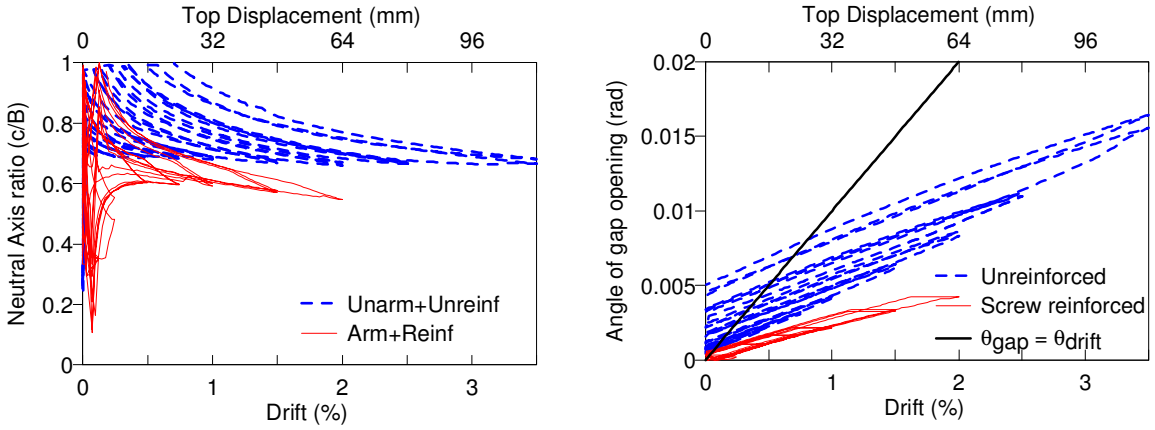

Figure 6.24 Neutral axis locations and gap opening angles with and without armouring and reinforcing together

6.4 Contributions of Joint Deformation Components

6.4.1 Experimental Results

The deformations in the joint region in different specimens are plotted in Figure 6.25 and Figure 6.26. Figure 6.25 shows that armouring increases joint shear deformation in both unreinforced and reinforced joints. It is visible from Figure 6.26 that reinforcing reduces joint shear deformation in both un-armoured and armoured joints.

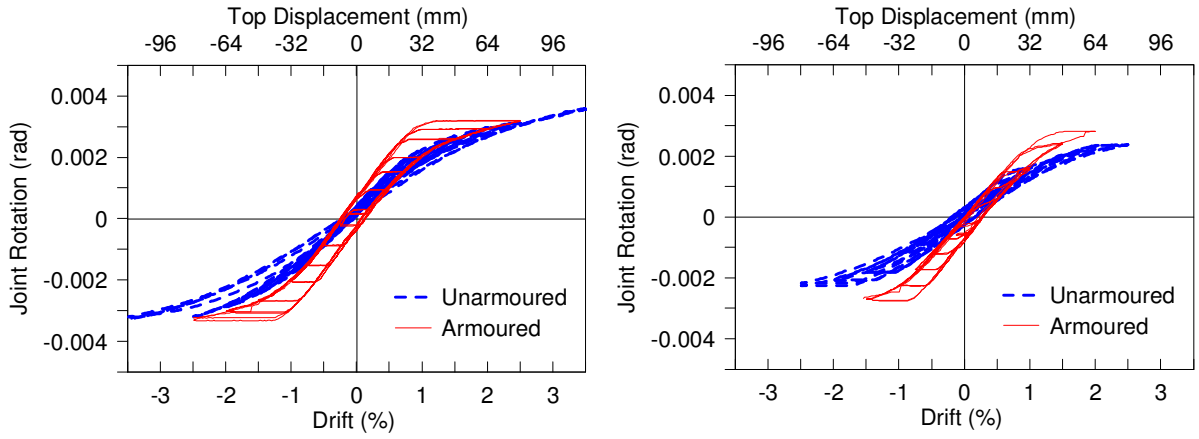

Figure 6.25 Comparative joint rotation plots of a) unreinforced and b) reinforced specimen with and without armouring

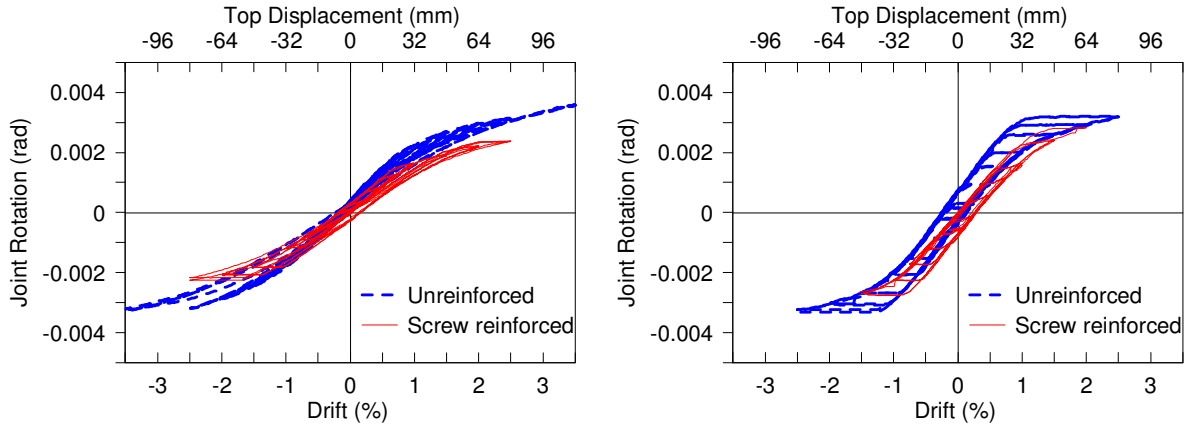

Figure 6.26 Comparative joint rotation plots of a) unarmoured and b) armoured specimen with and without reinforcing

Some interesting deductions can be made summarizing the above statements. Increase in stiffness of 10% to 50% could be achieved through armouring of the joint. But there was increased shear panel zone deformation with armouring. When the armoured joint was reinforced, the joint retained virtually the same stiffness, but reinforcing the joint reduced the shear panel zone deformation and thereby reduced the undesired effect of armouring.

Figure 6.26b shows the comparison between unreinforced unarmoured (plain timber-to-timber) connection and reinforced armoured connection. They are very similar in nature, which indicate that armouring and reinforcements compensate each other's effect on joint shear panel deformation.

6.4.2 Interpretation of Experimental Results

Typically the significant sources of frame yield rotation for a hybrid system are the elastic deformation of the beam and column, joint panel zone deformation and connection rotation, as expressed in Equation $\theta_y = \theta_{b,y} + \theta_{c,y} + \theta_{j,y} + \theta_{conn,y}$ 6.1:

$$\theta_y = \theta_{b,y} + \theta_{c,y} + \theta_{j,y} + \theta_{conn,y} \quad \textbf{6.1}$$

Where $\theta_{b,y} + \theta_{c,y} + \theta_{j,y}$ is the elastic deformation of the beam, column and joint elements respectively and $\theta_{conn,y}$ is the deformation due to rotation within the connection.

The elastic deformations of the frame elements can be calculated from a characteristic interior beam-column joint subassembly. The following expressions can be derived for the beams and the column combining the flexural and shear deformation contributions in both the cases (Buchanan & Fairweather, 1993):

For the beam:

$$\theta_{b,y} = \phi_{b,y}\left(\frac{L_b}{6} + \frac{E_t}{G}\cdot\frac{h_b^{\,2}}{4L_b}\right) \qquad \textbf{6.2}$$

For the column:

$$\theta_{c,y} = \phi_{c,y}\left(\frac{H}{6} + \frac{E_t}{G}\cdot\frac{h_c^{\,2}}{4H}\right) \qquad \textbf{6.3}$$

Where $\theta_{b,y} = \frac{M_{cl}}{E_t I_b}$ and $\theta_{c,y} = \frac{M_{cl}}{E_t I_c}$

For the joint shear deformation:

$$\theta_{j,y} = \gamma_j\left(1 - \frac{h_c}{L_b}\right) - \gamma_j\frac{h_b}{H} \qquad \textbf{6.4}$$

Where $\gamma_j = \gamma_1 + \gamma_2 = \frac{V_{jh}}{GA_{jh,e}} + \frac{V_{jv}}{GA_{jv,e}}$

V_{jh} and V_{jv} is the horizontal and vertical shear force within the joint respectively and $A_{jh,e}$ and $A_{jv,e}$ are the effective shear area of the joint (assumed as 2/3Agross).

The connections contribution to the yield rotation is due to the rocking mechanism. Although this deformation component for timber can not be expressed analytically or estimated simply, it

can be calculated by subtracting the deformations in the beams, column and the joint from the total frame rotation.

Table 6.3 Deformation components and contributions in different types of joints

	Unreinforced Unarmored		Unreinforced Armored		Reinforced Unarmored		Reinforced Armored	
	Value	% total	Value	% total	Value	% total	Value	% total
Beam $\theta_{b,y}$	0.003292	13	0.004745	19	0.003194	13	0.004603	18
Column $\theta_{c,y}$	0.00267	11	0.00385	15	0.002447	10	0.003526	14
Joint $\theta_{j,y}$	0.0089	36	0.010753	43	0.007356	29	0.009169	37
Connection $\theta_{conn,y}$	0.010138	40	0.005652	23	0.012004	48	0.007702	31

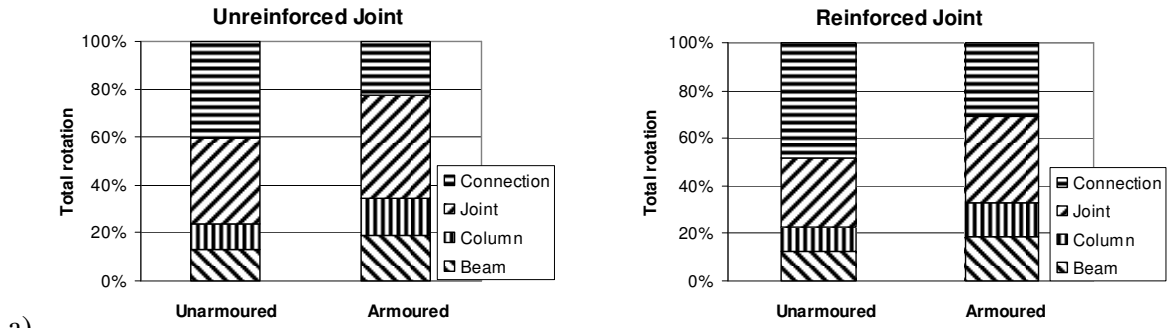

a) b)

Figure 6.27 Contribution of deformation components of a) unreinforced and b) reinforced joint with and without armouring

Comparing the results from unreinforced-unarmoured and reinforced-armoured specimens it is visible from Table 6.3 that the connection rotation is reduced significantly with reinforcement and armouring. This would mean increased gap opening in the reinforced-armoured connection. Overall, armouring and reinforcement together increase stiffness of the connection**.** This implies that for the same inter-storey drift the members sections of a reinforced armoured specimen will be smaller compared to that of an unarmoured unreinforced specimen.

6.5 Summary

The experimental investigation of beam-column joint provided confirmation of the expected behaviour of the subassemblies. In general, they all exhibited almost complete re-centering capacity. The hybrid specimens showed significant energy dissipation. There was no structural damage to any of the specimens tested. There was insignificant amount of residual deformations in some cases. The different configurations of specimens tested also demonstrated the flexibility in design and possibilities for applications in practical structures.

7 ANALYTICAL-EXPERIMENTAL COMPARISON

7.1 Introduction

Analytical and numerical models are developed to predict the behaviour of the subassemblies. This chapter presents the models and the results obtained from them. The models are validated through comparisons with experimental results illustrated in Chapter 4. Inferences are drawn from them for use in further calculations.

7.2 General Modelling Approaches

The numerical models are developed in three steps for the current study. In the first step, the basic characteristic behaviour i.e. the moment-rotation curve is obtained. As explained in Chapter 3, this is done using the revised version of the Monolithic Beam Analogy or MBA (Pampanin, et al., 2001) for jointed ductile connections. In the following, this analytical procedure to calculate the monotonic moment-rotation curve is termed the "analytical model".

Once the moment-rotation curve is established, the next step is to develop computationally intensive "numerical models" for more rigorous analysis of the cyclic behaviour. This is done by implementing the model in a finite element software using macro elements. For this research inelastic finite element software Ruaumoko (Carr, 2005) has been used. Two numerical models used in this research, namely Lumped Plasticity Model and Multi-Axial Spring Model have been described in chapter 3. In general, the relatively simpler Lumped Plasticity Model was developed first, based on the parameters calibrated with the moment-rotation curve derived with MBA. The next step was to formulate the more complex Multi-spring model to compare and validate all the relevant parameters involved in the calculations.

7.3 Representation of Materials

The three basic components of hybrid timber systems i.e. timber members, post-tensioning and energy dissipation elements had to be represented in the models with appropriate elements. The general behaviour is discussed in chapter 3 and shown here in Figure 7.1. In this investigation, the timber members in the test specimens remained within the elastic range and hence they are modelled with elastic elements. The post-tensioning tendons are represented by bilinear elastic (or non-linear elastic) hysteresis rules. Inelastic hysteresis rules (elastoplastic with strain hardening in nature) are chosen to represent the mild steel energy dissipation systems. A number of hysteresis rules: Dodd-Restrepo hysteresis rule designed to allow for the Bauschinger effects in steel (Dodd & Restrepo, 1995), Al-Bermani rule that allows for the Bauschinger effects in steel members using a bounding surface (Zhu, et al., 1995) and Takeda stiffness-degrading hysteresis model for reinforced concrete (Otani, 1981) have been used here for the dissipaters Figure 7.2.

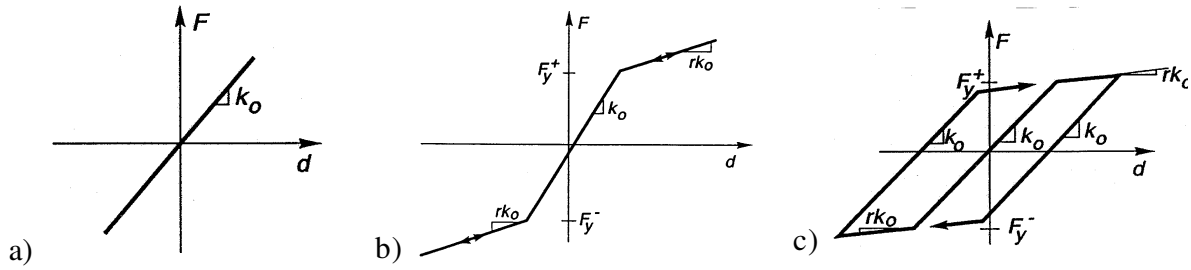

Figure 7.1 Idealized behaviour of a) Timber b) Post-tensioning and c) Mild steel dissipaters

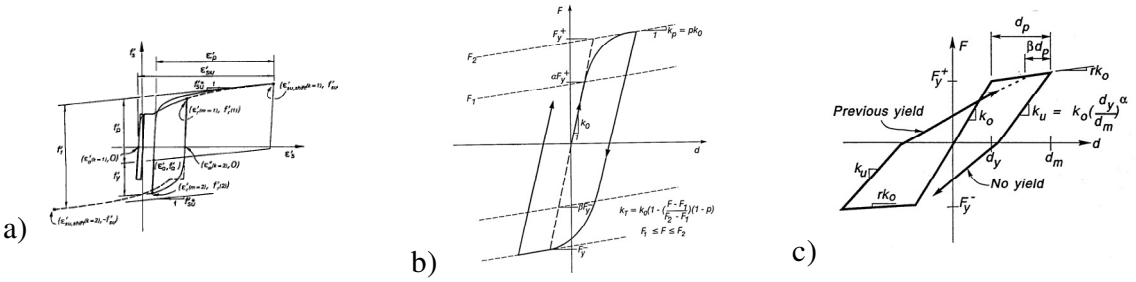

Figure 7.2 a) Dodd-Restrepo b) Al-Bermani and c) Takeda hysteresis rules

7.4 Modelling Energy Dissipation Systems

7.4.1 Axial Dissipaters

To validate the numerical model of the walls through comparison with the experimental results it was first necessary to establish that the behaviour of the axial dissipaters was properly captured by the hysteresis loop adopted within the numerical model. For that axial dissipaters were tested and the numerical model was checked against the test results. Figure 7.3a shows the results of the axial dissipaters used with the walls and column. Result of the axial dissipater used with the beam-column joint specimen is shown in Figure 7.3b. It is visible that the numerical model predicts the behaviour of the dissipaters reasonably well. The basic nature of the response is captured by the model and the differences are probably due to variation in material properties.

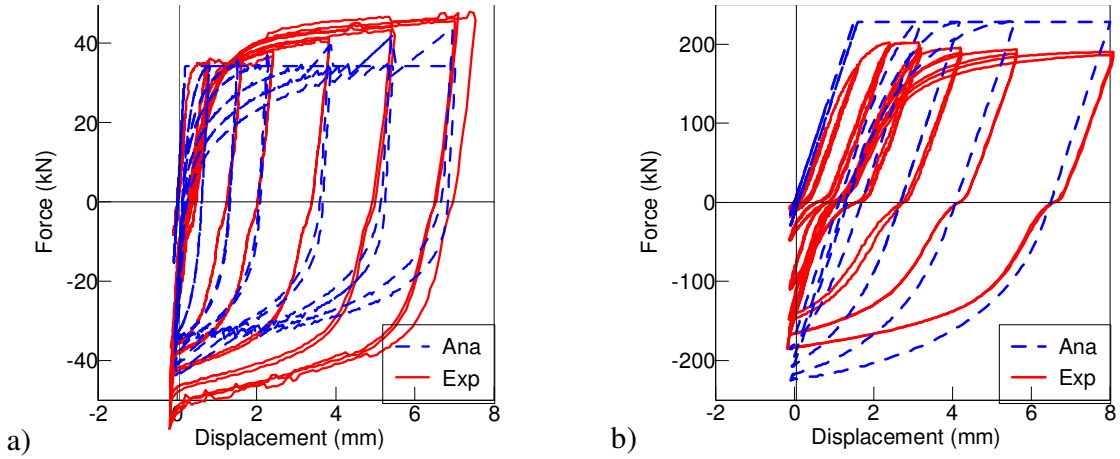

Figure 7.3 Comparison between results of a) 8mm b) 22mm diameter dissipater

7.4.2 U-Shaped Flexural Plates

Similar to the axial dissipaters, component tests were performed on UFPs and the results were checked against that calculated by the numerical model. Figure 7.4 shows that the numerical model predicts the behaviour of the UFPs fairly well and therefore can be incorporated into the larger model of the complete wall system with UFPs. It will be shown in Chapter 8 that the

forces in the UFPs can be known for the design drift levels and strengths of the UFPs can be targeted based on the chosen geometry, as already explained in Chapter 4.

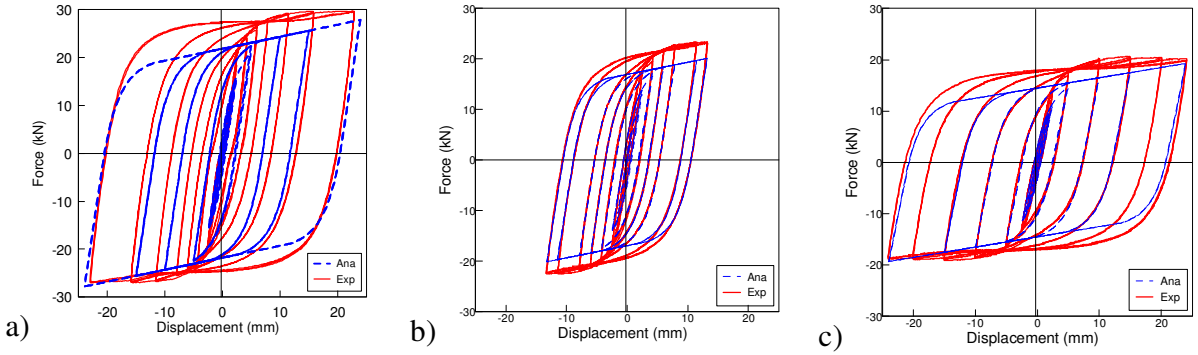

Figure 7.4 Comparison between experimental and analytical results of a) two -5mmx100mm UFPs b) two -5mmx65mm UFPs and c) two -5mmx50mm UFPs

7.5 Walls Modelling

7.5.1 Moment-Rotation Curve from Monolithic Beam Analogy

The monotonic moment-rotation behaviour of the walls was calculated by implementing the analytical "Monolithic Beam Analogy (MBA)" procedure for jointed ductile connections originally proposed by Pampanin et al., (Pampanin, et al., 2001) and subsequently refined by (Palermo, 2004), which relies on a member compatibility condition in terms of displacements between a monolithic and a hybrid solution. Figure 7.5 shows the moment-rotation curves for PT-only and Hybrid Wall specimens compared with the experimental results. It can be seen that the MBA can predict the behaviour fairly accurately.

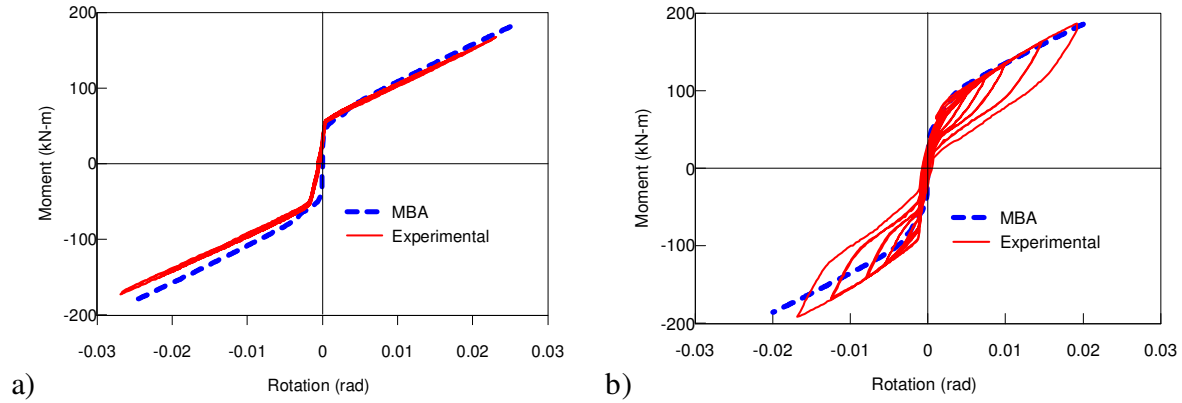

Figure 7.5 Comparisons between Analytical MBA moment-rotation procedure and experiment for a) PT-only and b) Hybrid wall specimens

7.5.2 Lumped Plasticity Model

The approach based on section analysis and lumped plasticity concepts has been used here to develop simple numerical model for cyclic analysis of the three types of walls. AS proposed by Pampanin et al., (2001), fib, (2003), NZS3101:2006, the combined contributions from the prestressing tendons and the energy dissipaters in a hybrid connection can be modelled by two springs in parallel with appropriate hysteresis characteristics to produce the flag-shaped hysteresis loops. The concept is valid for any type of hybrid wall systems, i.e. PT walls with axial dissipaters and with UFPs. The simple rocking wall without dissipaters is clearly a special case of the hybrid wall where the energy dissipaters are not present. Figure 7.6 and Figure 7.7 show the schematic lumped plasticity models of the Hybrid and Coupled Walls. Comparisons of with the experimental results (Figure 7.8) show that the model is in good agreement with the experiment, specially for the PT-only specimen.

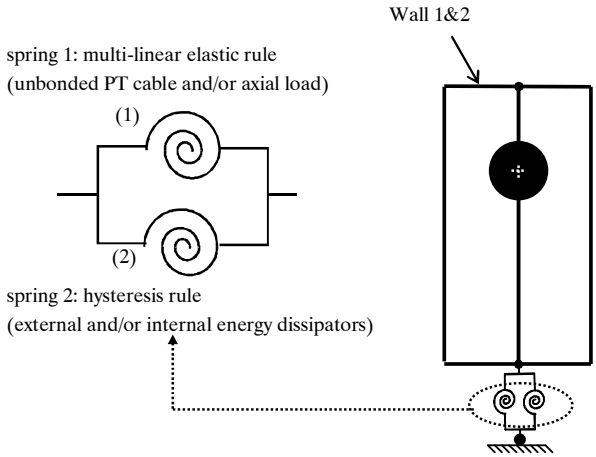

Figure 7.6 Lumped plasticity model of hybrid walls with dissipaters

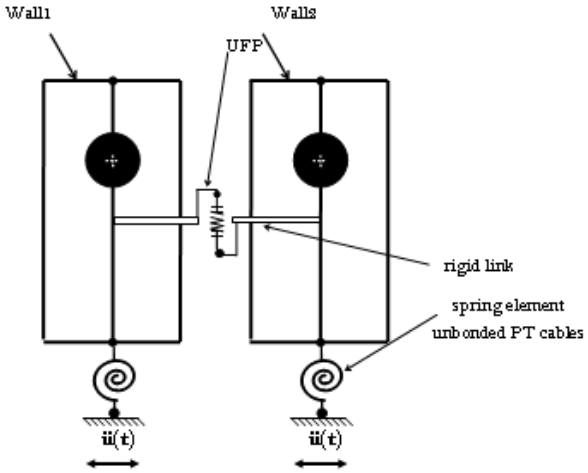

Figure 7.7 Lumped plasticity model of coupled walls

a)

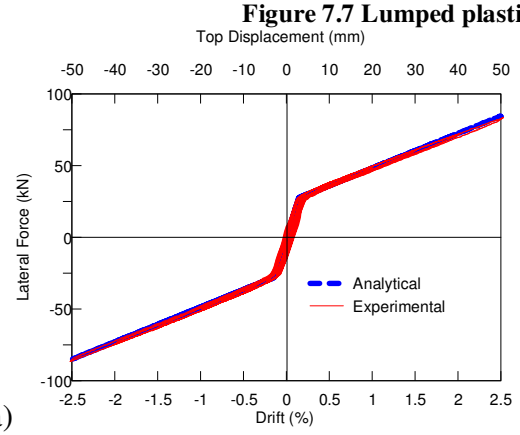

b)

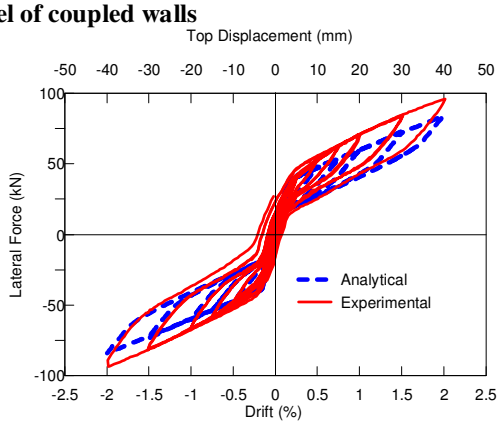

c)

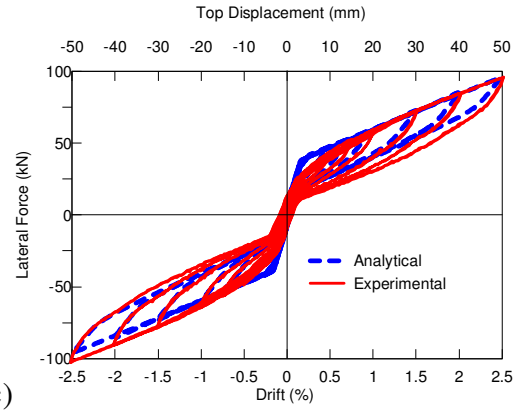

Figure 7.8 Lumped plasticity model and experimental results a) Specimen PT1 b) Specimen HU1 c) Specimen HY

7.5.3 Multi-Axial Spring Model

The multi-spring model also uses the concept of springs in parallel applied in the lumped plasticity model, but in this case axial springs are used in place of rotational springs. In addition, a number of axial springs are added to simulate the contact section interface, as typically done in geotechnical engineering to model the behaviour of continuous foundation on soil. The characteristics of the springs can be chosen, considering the contact behaviour of the section.

The springs of the multi-springs model are calibrated through comparison with the section analysis results. As an initial estimate, a simple empirical relationship developed through trails can be used. For an element with width/depth the same as the interface and unit length, the total stiffness in kN/m can be taken as 1/10th of the elastic modulus of the rocking interface in GPa.

The model achieves a good simulation of the local stresses, strains and variation of the neutral axis position at the joint opening. The unbonded post-tensioned cables are modelled with pre-tensioned longitudinal springs. The hysteretic rule for the unbonded post-tensioned cables can be assumed to be non-linear elastic, while for the axial dissipaters or UFPs a proper hysteretic loop has to be chosen. The wall is represented by elastic finite beam elements. Figure 7.9 shows the

hybrid walls model while Figure 7.10 shows the model of a coupled wall specimen. The single wall in the hybrid wall is representative of two walls since they are independent. The coupled walls, on the other hand, have to be modelled separately with the coupling element in-between.

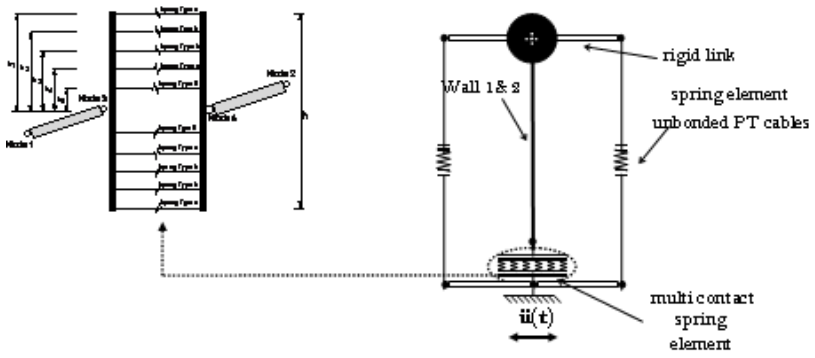

Figure 7.9 Multi spring model of hybrid walls with dissipaters

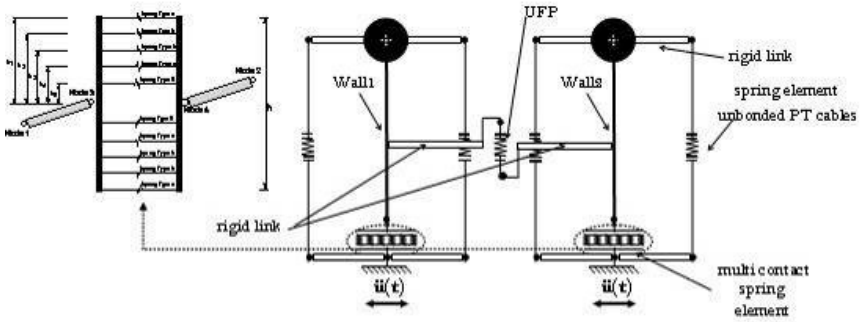

Figure 7.10 Multi spring model of coupled walls

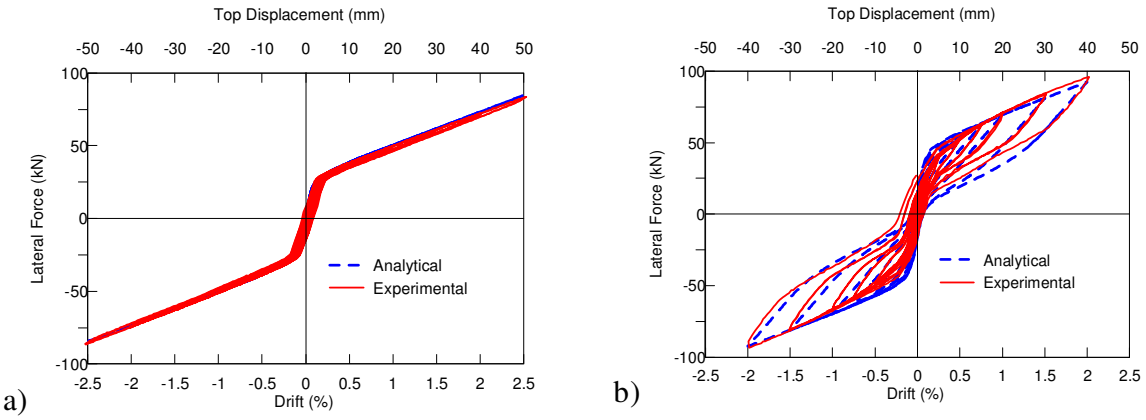

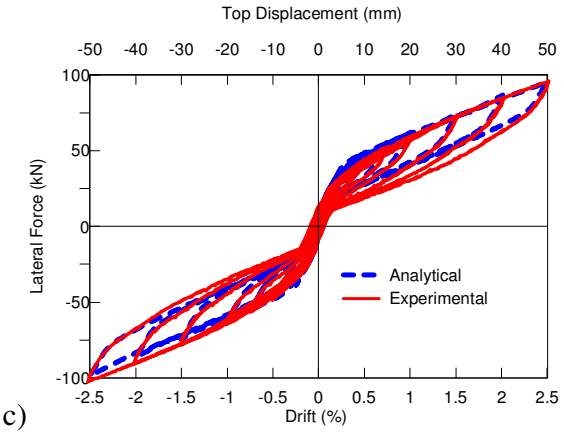

c)

Figure 7.11 Multi-spring model and experimental results: a) Specimen PT1 b) Specimen HU1 c) Specimen HY

To compare the accuracy of the two numerical models, the results of the post-tensioned-only and hybrid specimens with axial dissipaters and UFPs are plotted in Figure 7.12. It can be seen that although there is virtually no difference in case of the PT-only specimen, the multi-spring model follows the experimental results slightly more accurately for the hybrid specimens, particularly at the initiation of gap opening.

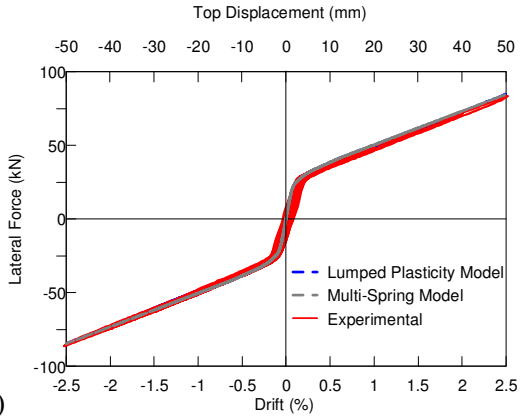

a)

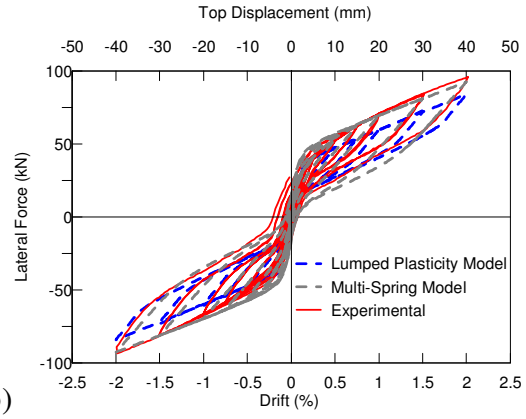

b)

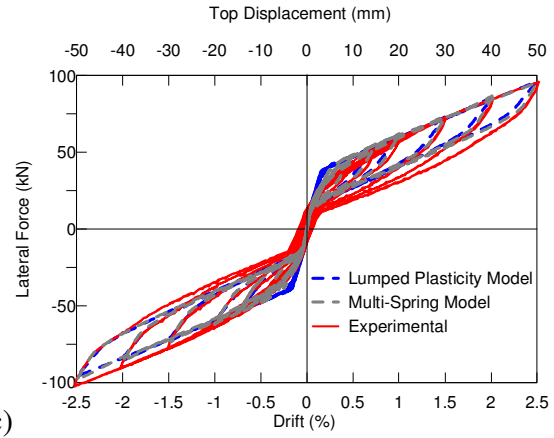

c)

Figure 7.12 Comparison between model and experiment a) Specimen PT1 b) Specimen HU1 c) Specimen HY

Figure 7.13 shows the location of the neutral axis at different drifts. Forces in the tendons in the two walls vs. displacements are plotted in Figure 7.14. The force-displacement and the tendon forces from the numerical model are in good agreement with the experimental results. The neutral axis depth is underestimated compared to the experimental data. The sliding at the base of the walls could have effected the measurements for the neutral axes depths calculations. Furthermore, the neutral axes depth relationships are more sensitive to inaccuracies in experimental recordings than the force displacement relationships because of the geometry and arrangements for measurements. Considering these the differences between the experimental and calculated locations are considered reasonable.

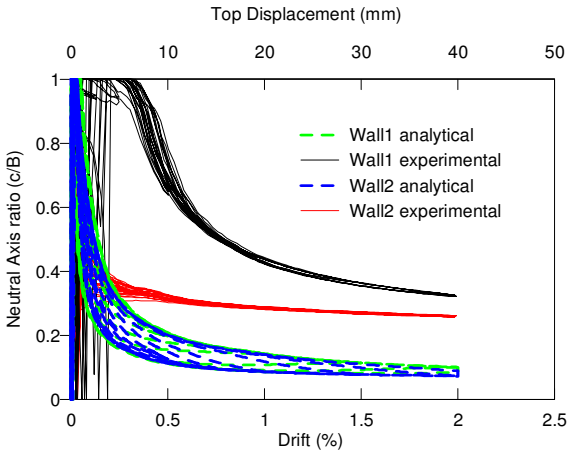

Figure 7.13 Neutral axis location with drift in Specimen HU1 compared with Multi-Spring Analytical Model

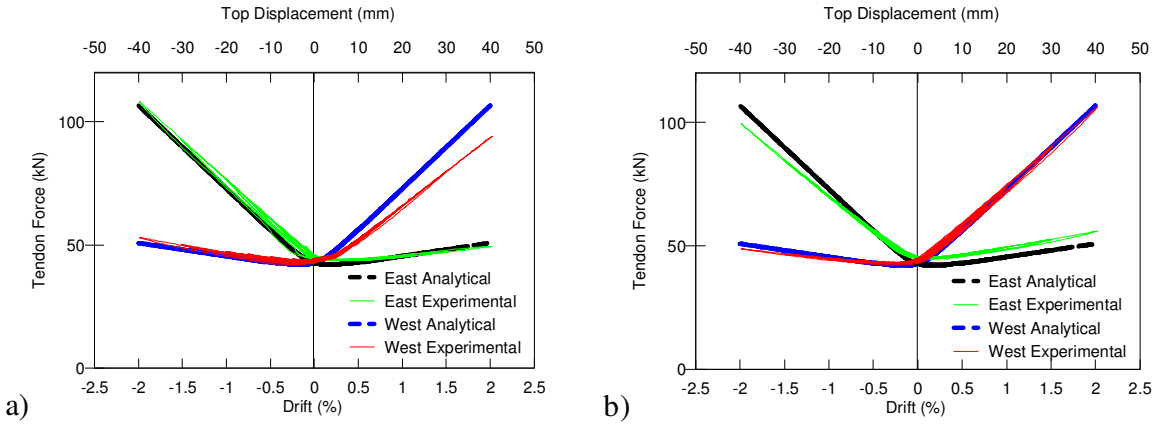

Figure 7.14 Tendon forces with drift in Specimen HU1 for a) Wall 1, b) Wall 2

The multi-spring model developed and verified for Specimen HU1 was also used to verify against quasi-static experimental results of the other specimens. The results are shown in Figure 7.15 and Figure 7.16. In general, the comparisons show good agreement between the numerical model and the experiment, with minor differences primarily due to sliding of the test specimens.

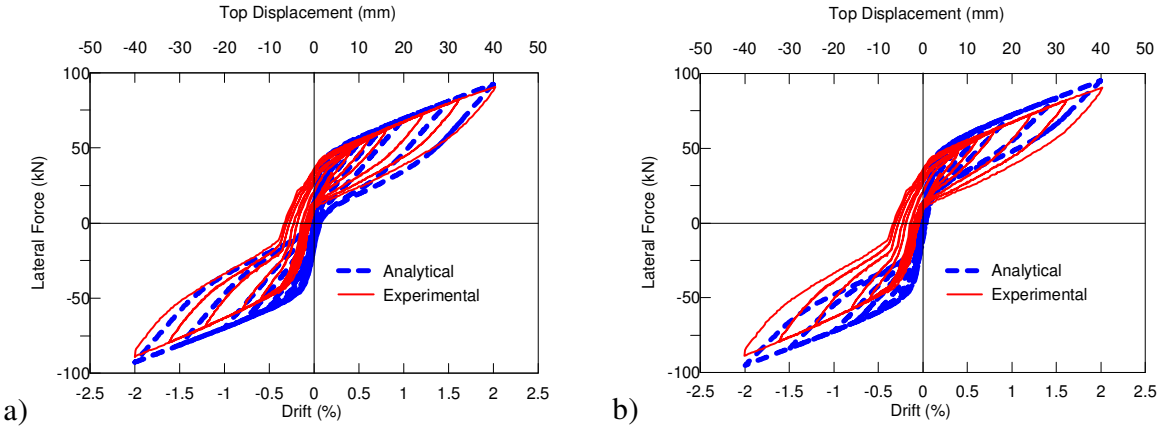

Figure 7.15 Comparison between model and experiment a) Specimen HU2 b) Specimen HU3

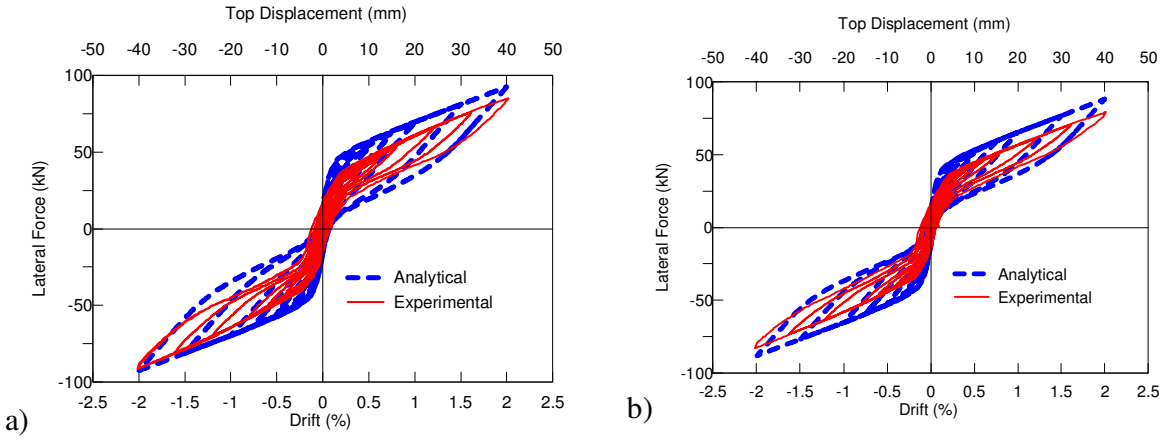

Figure 7.16 Comparison between model and experiment a) Specimen HU4 b) Specimen HU5

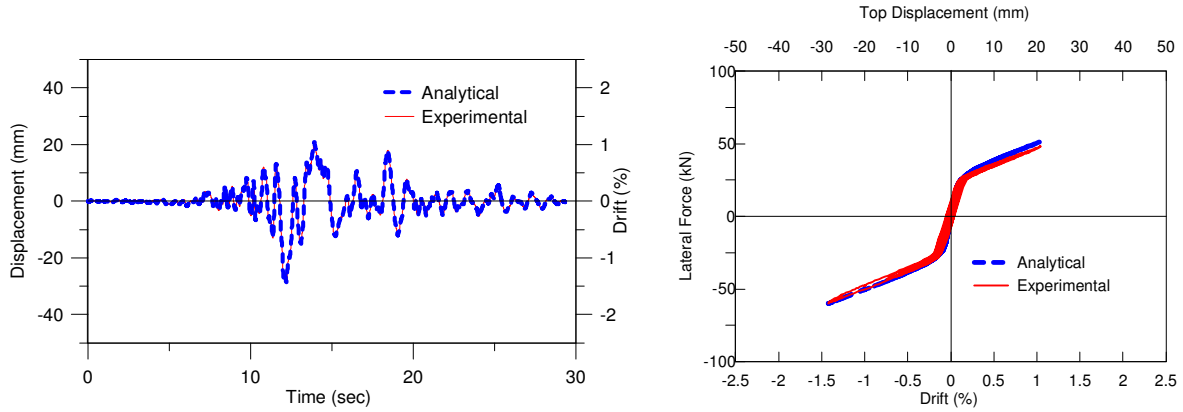

Figure 7.17 Comparison of Pseudo-dynamic responses for Specimen PT1 under EQ1

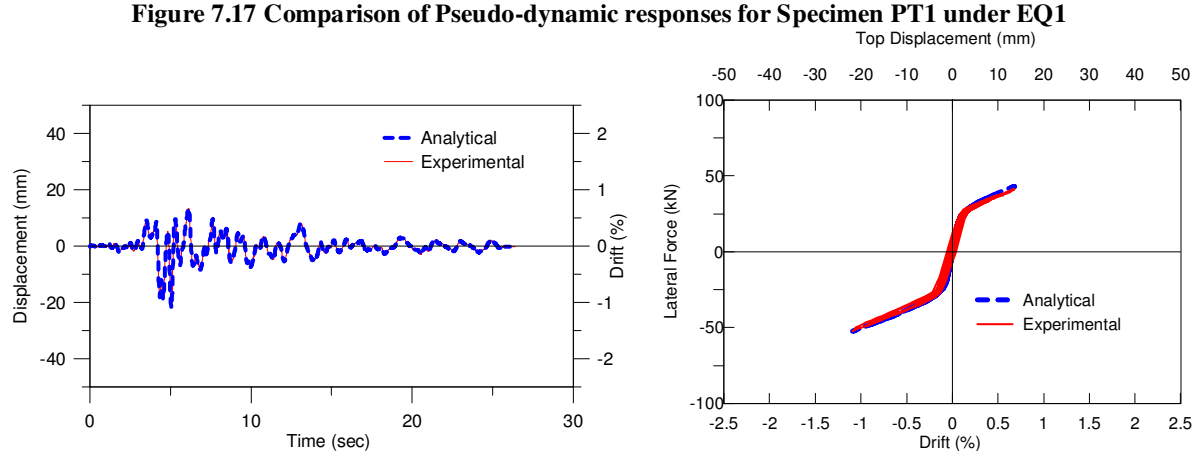

Figure 7.18 Comparison of Pseudo-dynamic responses for Specimen PT1 under EQ2

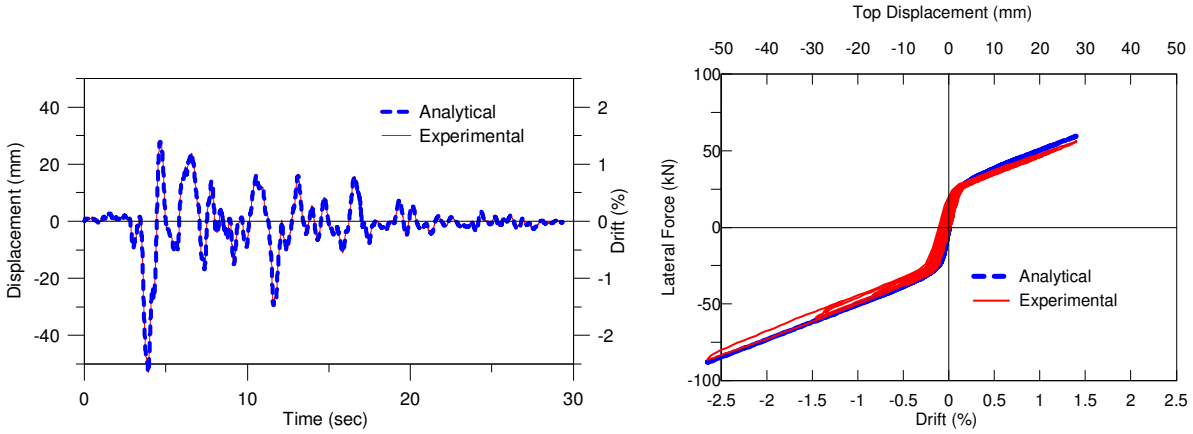

Figure 7.19 Comparison of Pseudo-dynamic responses for Specimen PT1 under EQ3

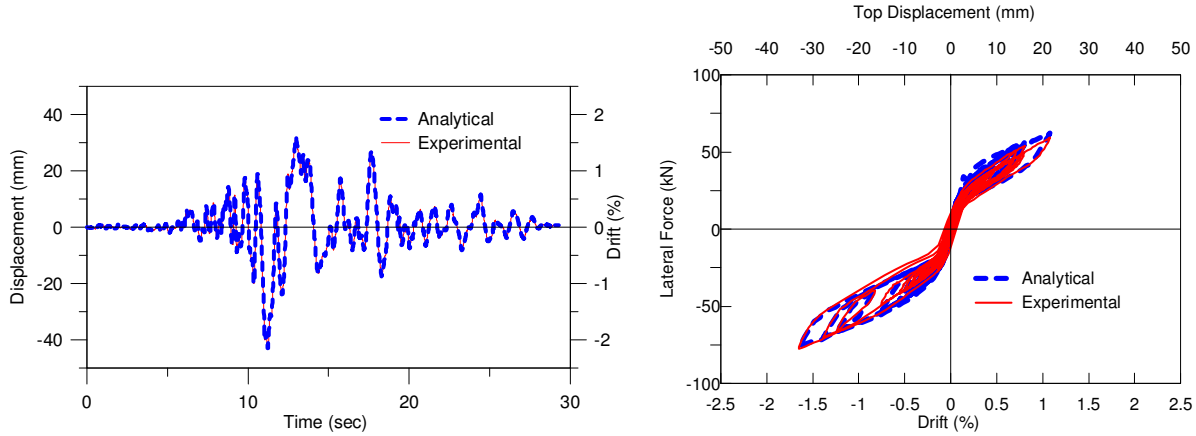

Figure 7.20 Comparison of Pseudo-dynamic responses for Specimen HY under 150% EQ1

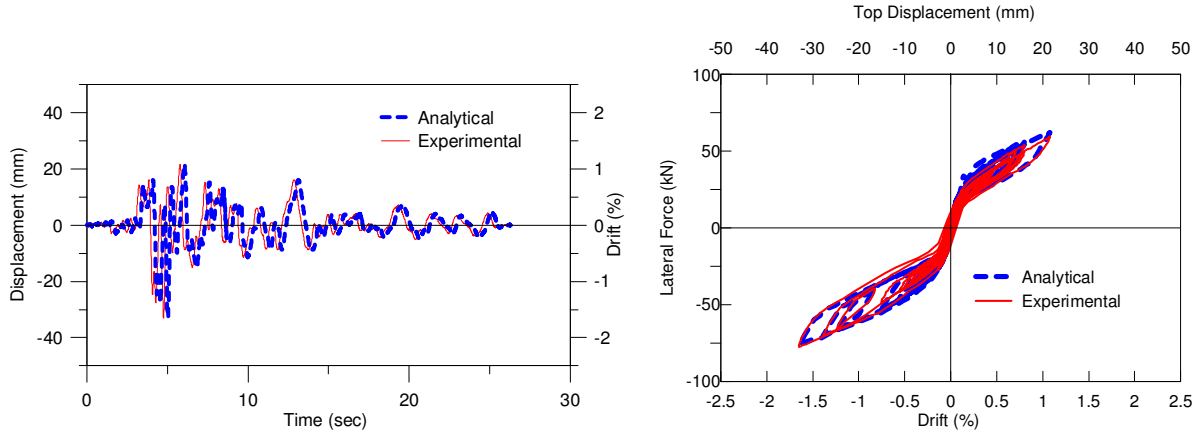

Figure 7.21 Comparison of Pseudo-dynamic responses for Specimen HY under 150% EQ2

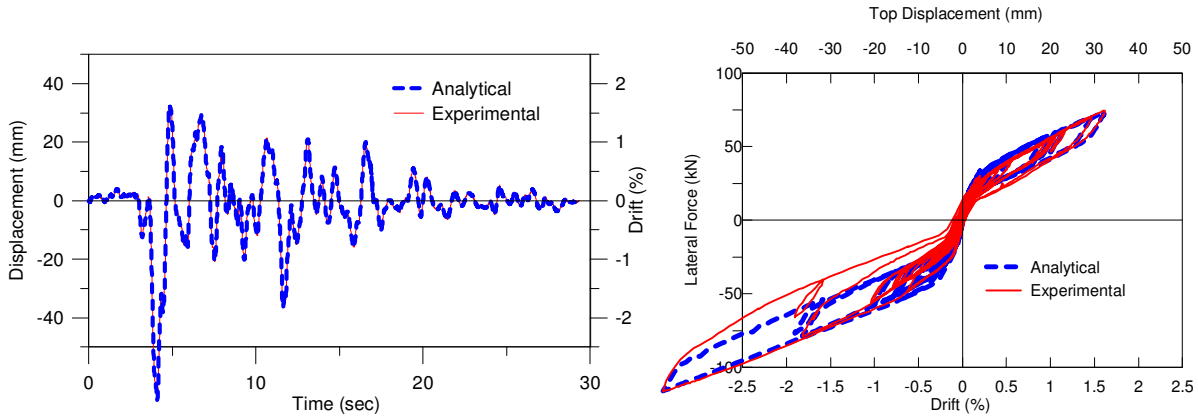

Figure 7.22 Comparison of Pseudo-dynamic responses for Specimen HY under 150% EQ3

The multi-spring model was also used to compare with the results of the pseudo-dynamic tests of hybrid specimens with UFPs. The experimental and the numerical results are compared in Figure 7.23 to Figure 7.27. The small difference in the force-displacement plots may be attributed mostly to slippage and sliding at the bases of the walls during the tests. Effects of the sliding of the walls are also visible in the time-history plots. There are also small offsets of the response from the original positions indicating residual displacements. Overall, the model is judged to have produced accurate results.

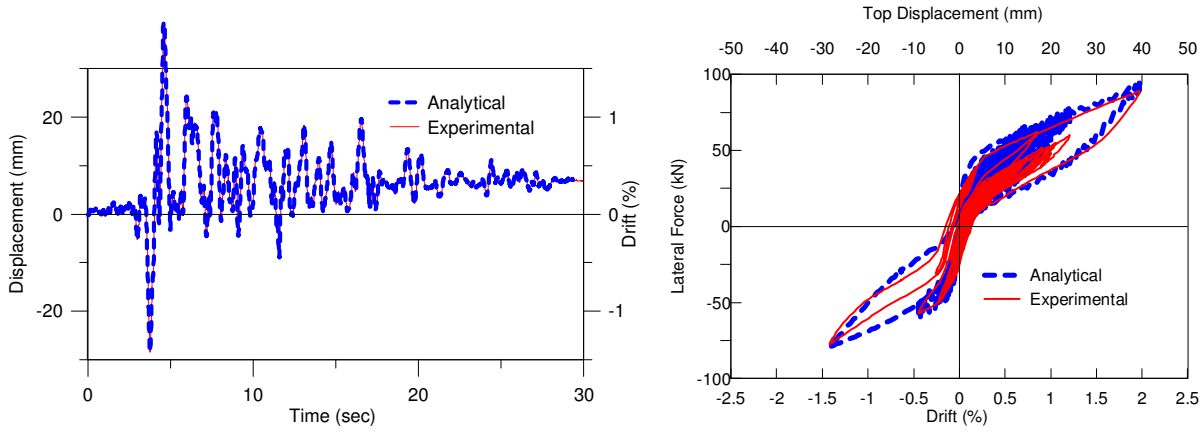

Figure 7.23 Comparison of Pseudo-dynamic responses for Specimen HU1 under 150% EQ3

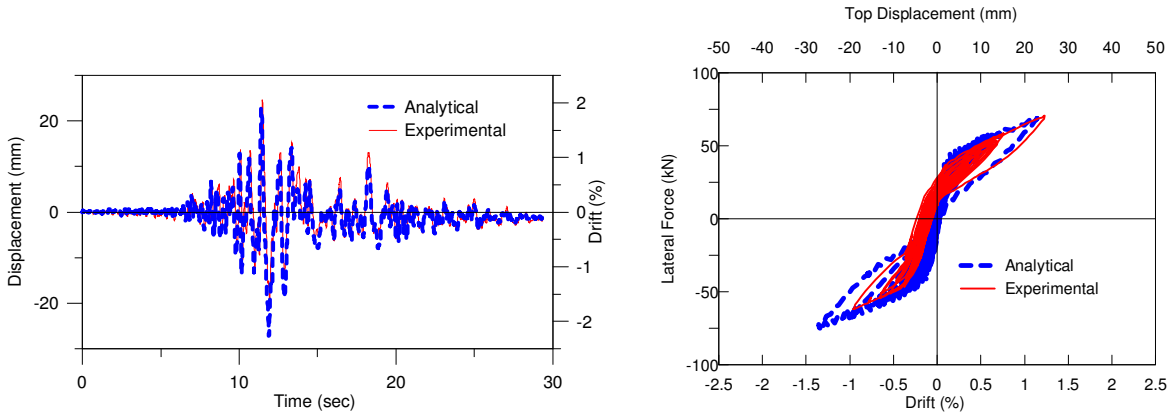

Figure 7.24 Comparison of Pseudo-dynamic responses for Specimen HU2 under 150% EQ1

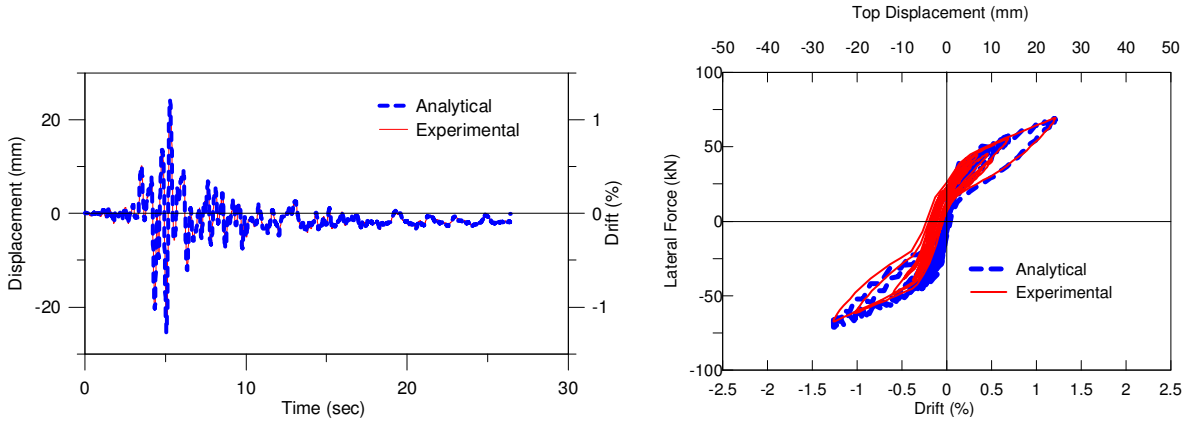

Figure 7.25 Comparison of Pseudo-dynamic responses for Specimen HU3 under 150% EQ2

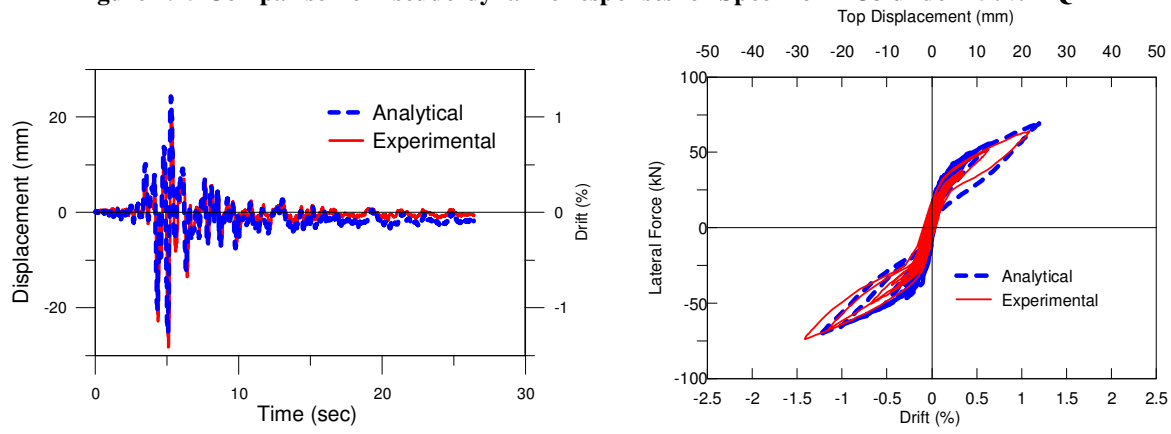

Figure 7.26 Comparison of Pseudo-dynamic responses for Specimen HU4 under 150% EQ2

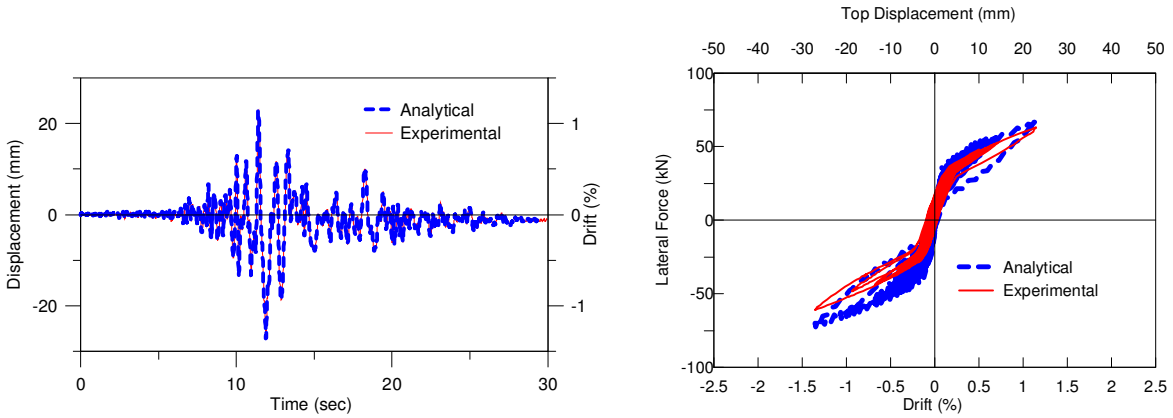

Figure 7.27 Comparison of Pseudo-dynamic responses for Specimen HU5 under 150% EQ1

As in the experimental study, three specimens with varying levels of prestressing and energy dissipation capacities were designed to produce the same level of response. The same approach was followed with the numerical models. Figure 7.28 shows that results obtained for the three specimens.

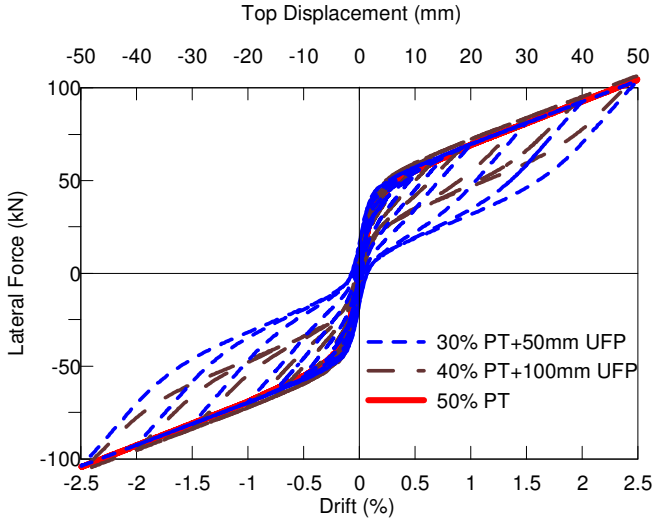

Figure 7.28 Force vs. drift results for different specimens to produce same level of response

It can be noticed that the force levels are almost the same for the three specimens. That means they have the same moment capacity. But the sizes of the hysteresis loops indicating the amount

of energy dissipation are different. The whole exercise demonstrates the flexibility in designing this type of systems and it is shown here that it can be achieved.

7.6 Column Modelling

7.6.1 Analytical Model

The moment-rotation behaviour of the column is calculated by Monolithic Beam Analogy (Palermo, 2004; Pampanin, et al., 2001) for both PT-only and Hybrid specimens. Comparisons for PT-only and Hybrid specimens without interaction are shown in Figure 7.29 and Figure 7.30 respectively. The moment-rotation procedure has then been modified to take account of the bi-directional effects, thus reducing the moment, according to the combination of M_x and M_y shown in Chapter 5. Comparisons between test results and analytical model without and with the bi-directional interaction effects considered are shown in Figure 7.29 to Figure 7.32.

It is visible that the analytical results without considering the interaction are over predicting the moment in the column. This is particularly true for PT-only specimen. The results considering interaction can be generally considered to be in better agreements with the experimental results, particularly for PT-only specimen.

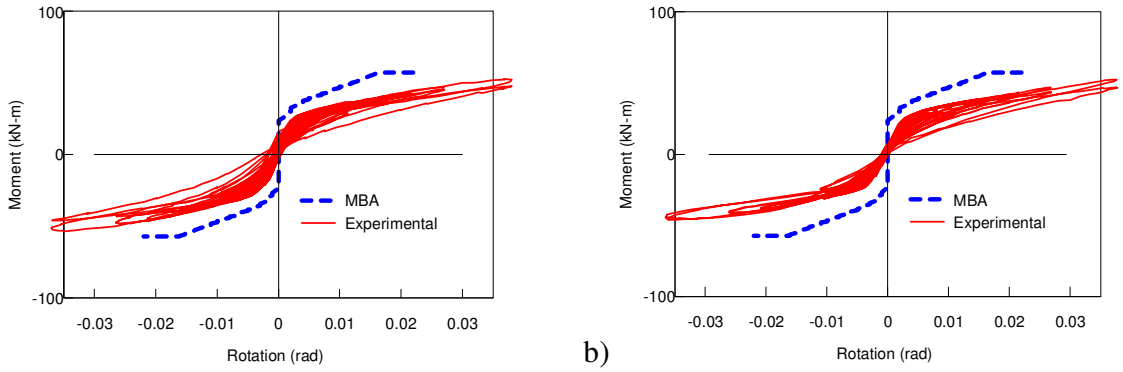

Figure 7.29 Comparisons for PT-only specimen without interaction a) E-W and b) N-S direction

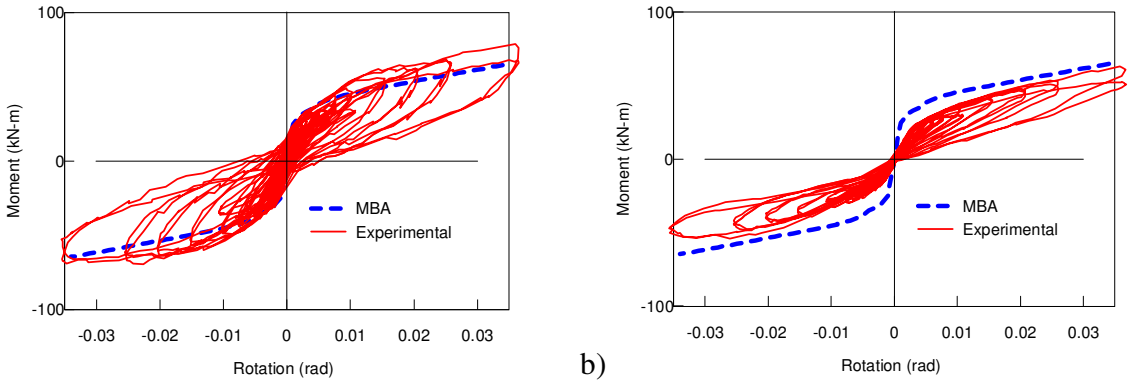

Figure 7.30 Comparisons for Hybrid specimen without interaction a) E-W and b) N-S direction

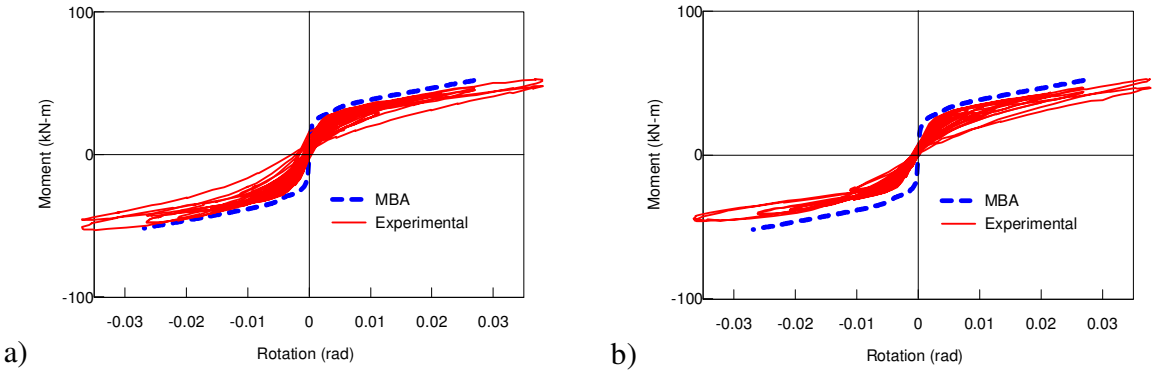

Figure 7.31 Comparisons for PT-only specimen with interaction a) E-W and b) N-S direction

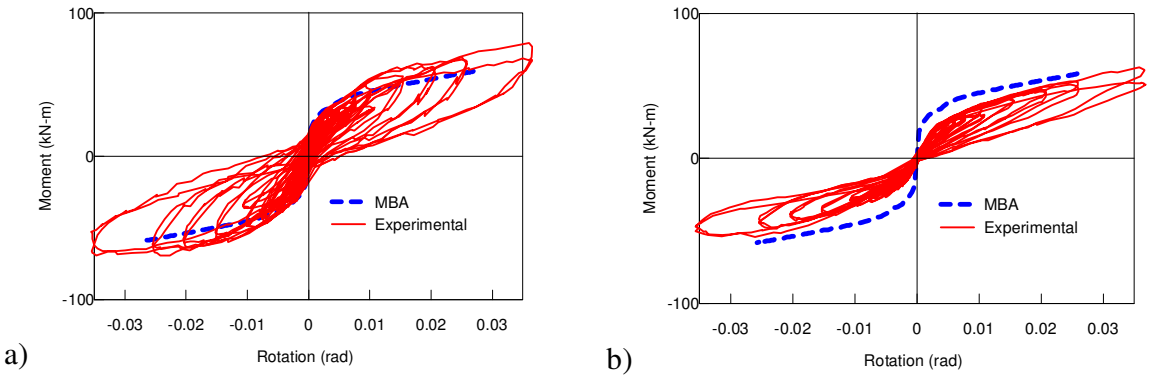

Figure 7.32 Comparisons for Hybrid specimen with interaction a) E-W and b) N-S direction

7.6.2 Lumped plasticity model

The inelastic deformation located at the column-foundation interface can be efficiently represented by lumped plasticity model where rotational inelastic springs are assigned to represent the inelastic action at the column-foundation interface. Two springs in parallel, with

appropriate hysteretic behaviour, represent the post-tensioning and the energy dissipating elements while elastic elements are used to represent the structural members. One rotational spring is assigned a nonlinear elastic rule to represent the self-centring contribution from the post-tensioning, while a hysteresis rule representing the energy dissipation contribution is adopted for the second spring.

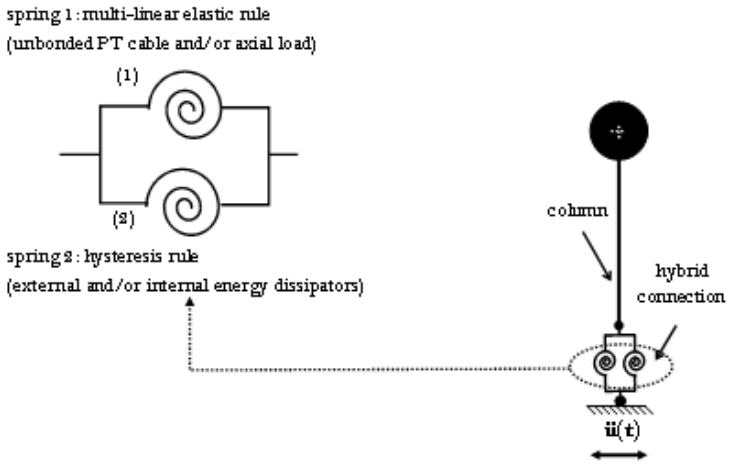

Figure 7.33 Lumped plasticity model of column

Figure 7.33 shows the lumped plasticity model of the column. The computational scheme was implemented with the Ruaumoko (Carr, 2005) finite-element code. A three-dimensional model of the column and its base connection was created to apply the bi-directional loading. Bi-linear elastic elements have been used to model the post-tensioning tendons while modified Takeda hysteresis was used for the energy dissipaters. Figure 7.34 and Figure 7.35 show the comparison between the analytical and experimental results for post-tensioned-only and hybrid solutions respectively. The comparison of displacement time-histories between the analytical and pseudo-dynamic experimental results for post-tensioned-only and hybrid solutions are shown in Figure 7.36 and Figure 7.37 respectively. In general, satisfactory confirmation of the numerical procedure is established from the plots.

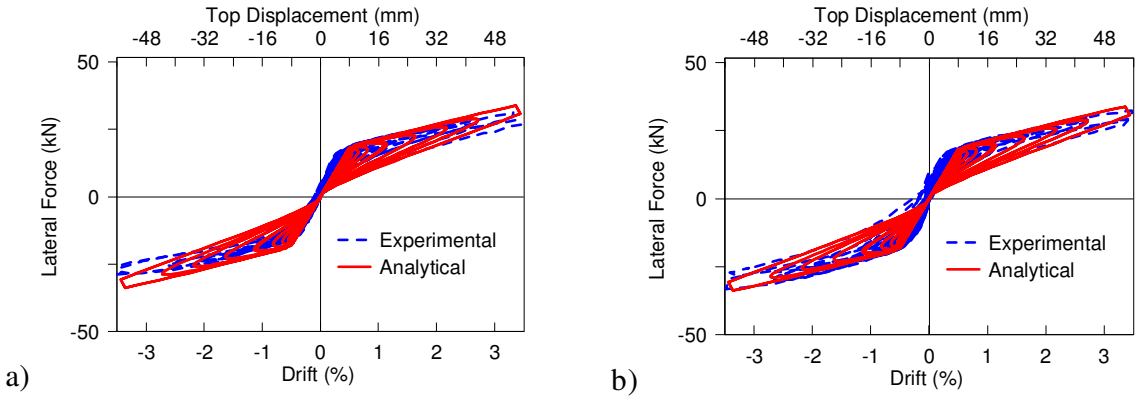

Figure 7.34 Comparative plots of PT-only specimen: a) N-S direction; b) E-W direction

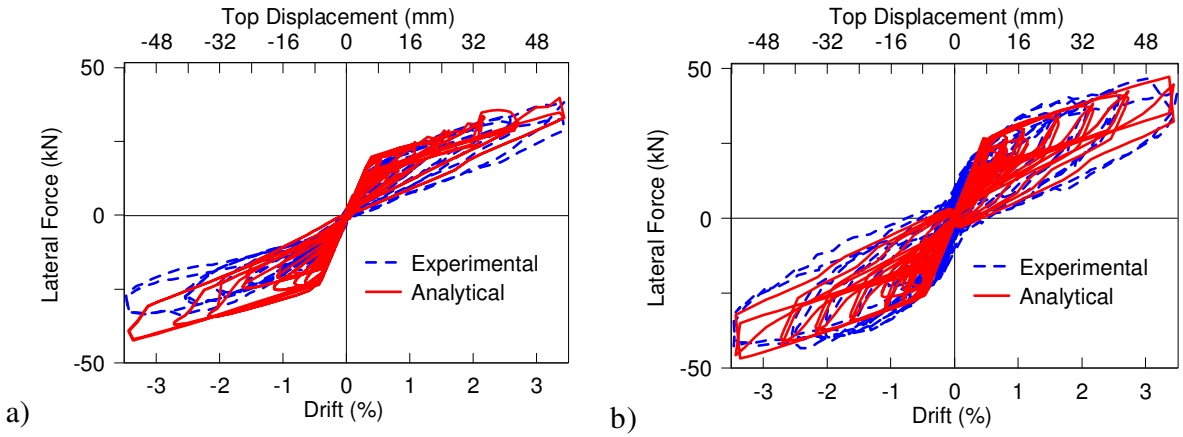

Figure 7.35 Comparative plots of Hybrid specimen: a) N-S direction; b) E-W direction

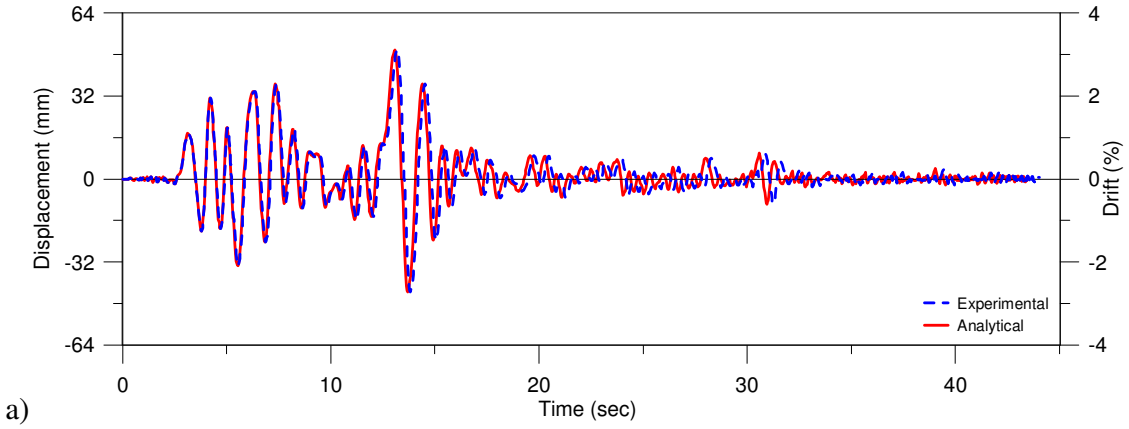

a)

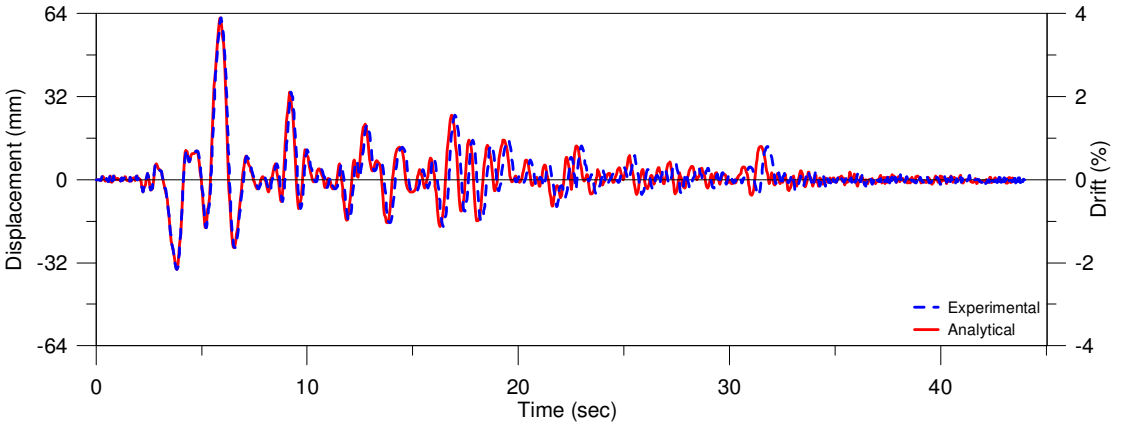

b)

Figure 7.36 Time-history plots of Hybrid specimen: a) N-S direction; b) E-W direction

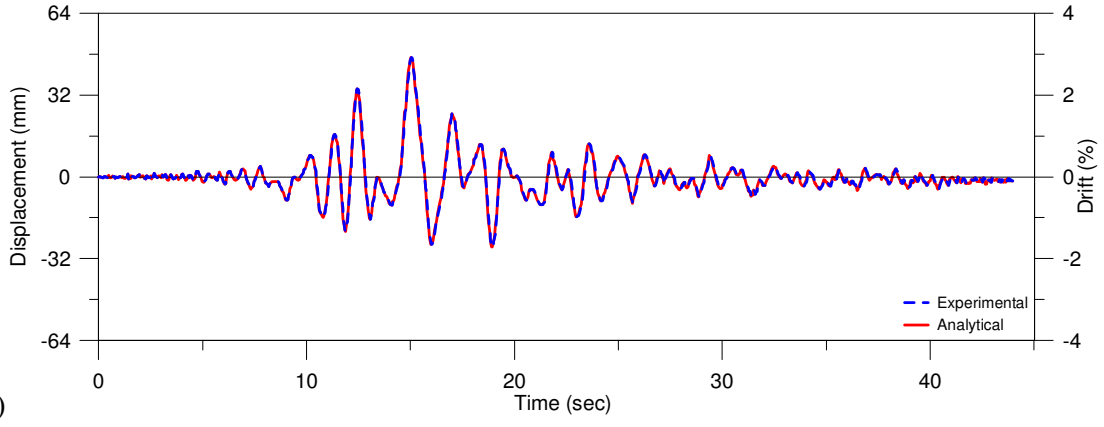

a)

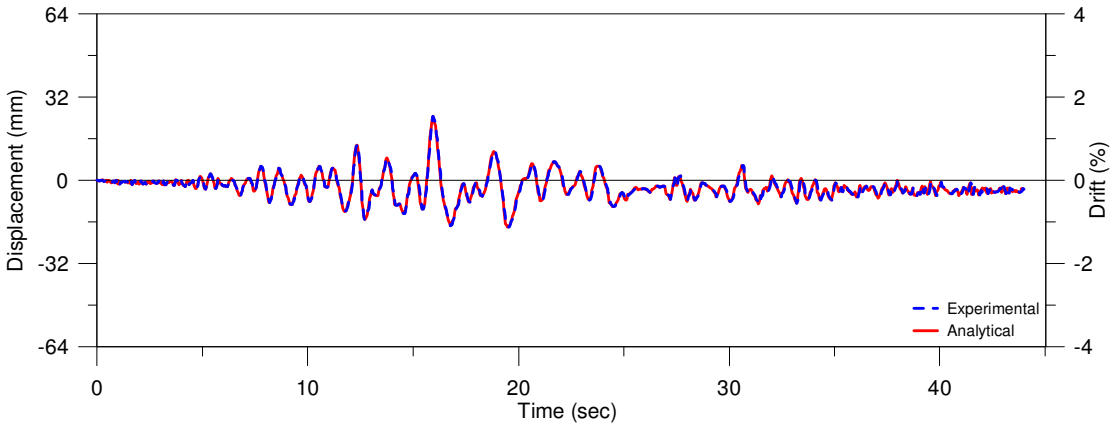

b)

Figure 7.37 Time-history plots of PT-only specimen: a) N-S direction; b) E-W direction

7.6.3 Multi-spring model

As has been shown already, the multi-spring model with parallel axial springs at the contact section interface can represent the behaviour of hybrid connections accurately. The column-to-foundation connection was also modelled using the same concept, shown in Figure 7.38. The three-dimensional model was implemented with Ruaumoko (Carr, 2005) with Dodd-Restrepo hysteretic elements to represent the energy dissipaters.

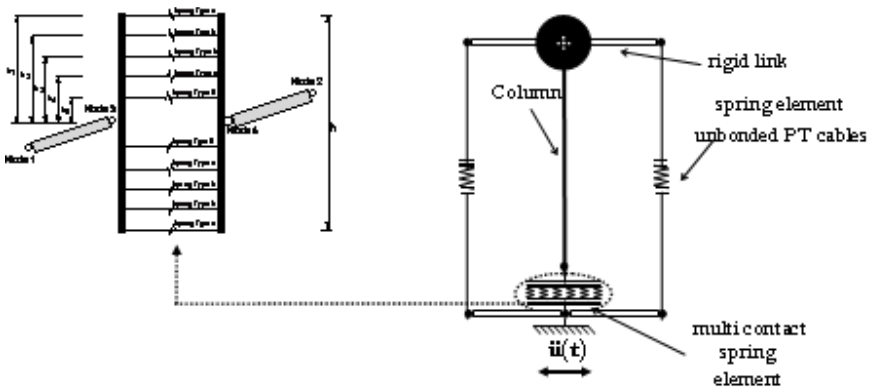

Figure 7.38 Multi-spring model of column

The load-deflection plot of the column is compared with the results of the model in Figure 7.39. Although the loops in the negative drift region are not the typical-shaped due to characteristics of

the hysteresis model used, the model is in good agreement with the experimental results in general.

The comparison of the neutral axis plots are shown in Figure 7.40. Results from the model are within a relatively narrow band compared to the gradual convergence in the test results, but the base lines match reasonably well in the two results. The tendon forces vs. drift comparisons in Figure 7.41 show reasonable agreement in terms of the limits, although the shapes of the loops are somewhat different.

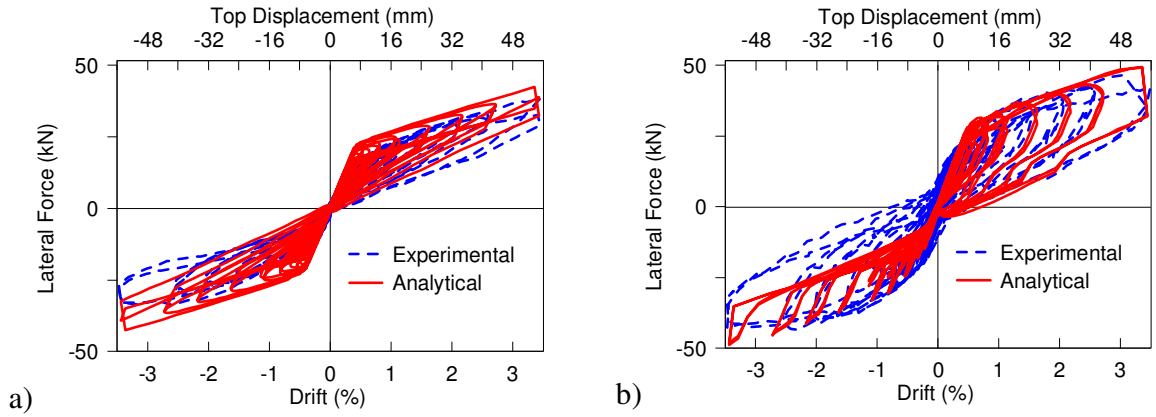

Figure 7.39 Multi-spring model plots of Hybrid specimen: a) N-S direction; b) E-W direction

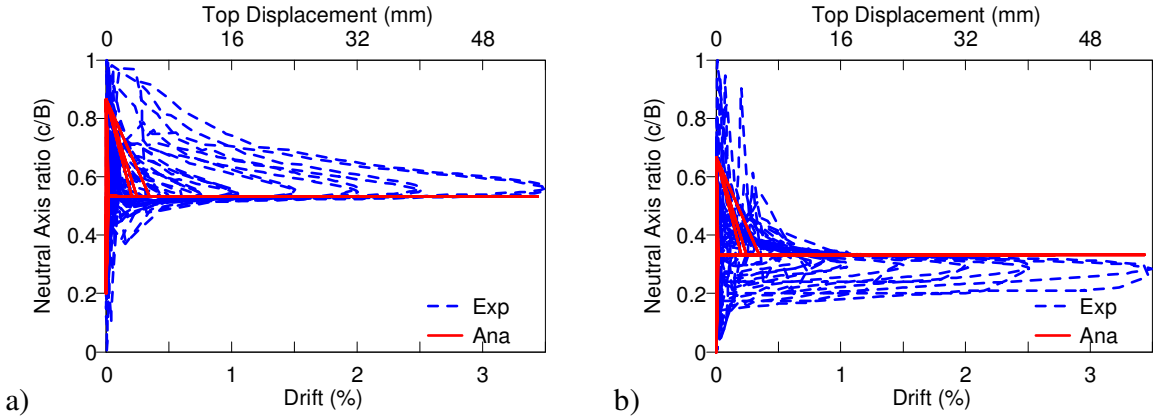

Figure 7.40 Neutral axis locations of PT-only specimen: a) N-S direction; b) E-W direction

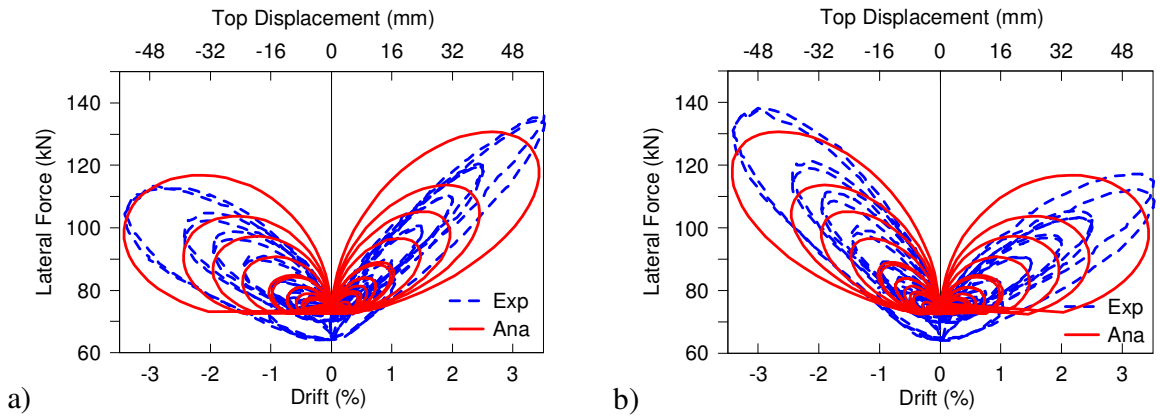

Figure 7.41 Tendon forces of PT-only specimen: a) North tendon; b) South tendon

7.7 Model of Beam-Column Joint

7.7.1 Analytical Model

Moment-rotation behaviour of the beam-column joints are calculated by the Monolithic Beam Analogy procedure. Figure 7.42 to Figure 7.45 show the comparisons between the experimental results and the moment-rotation curve calculated by the analytical model. For the different types of joints they are generally in good agreements.

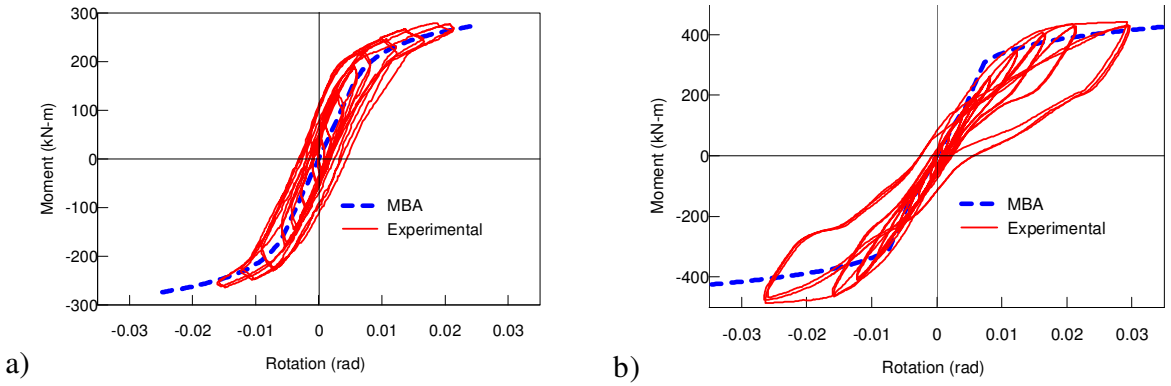

Figure 7.42Comparisons for a) PT-only and b) Hybrid armoured unreinforced exterior specimen

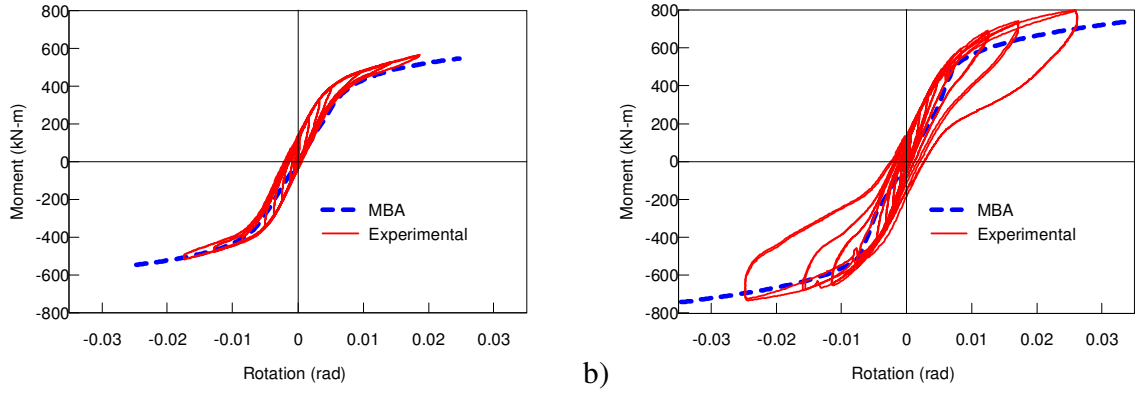

Figure 7.43 Comparisons for a) PT-only and b) Hybrid armoured unreinforced interior specimen

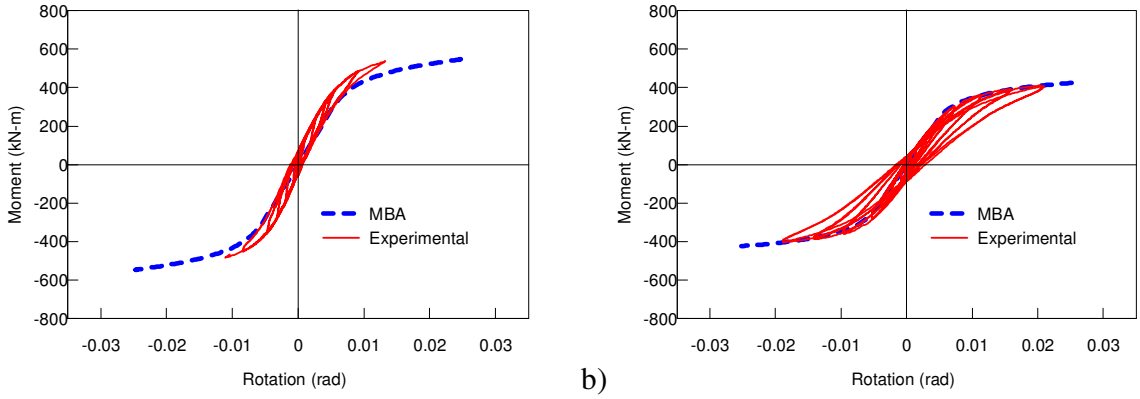

Figure 7.44 Comparisons for a) armoured and b) unarmoured reinforced interior specimens

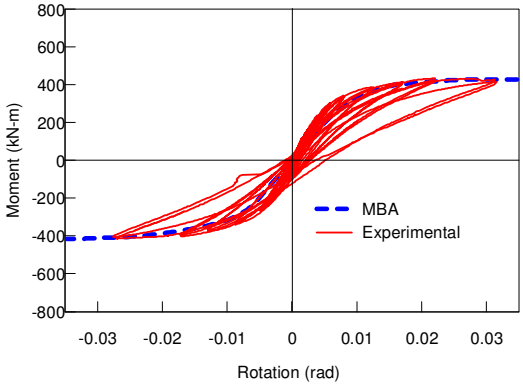

Figure 7.45 Comparison for unarmoured unreinforced PT-only interior joint specimen

7.7.2 Lumped plasticity model

The lumped plasticity model of the beam-column joint is shown in Figure 7.46. The rotational springs are connected to the column through rigid links representing the panel zone.

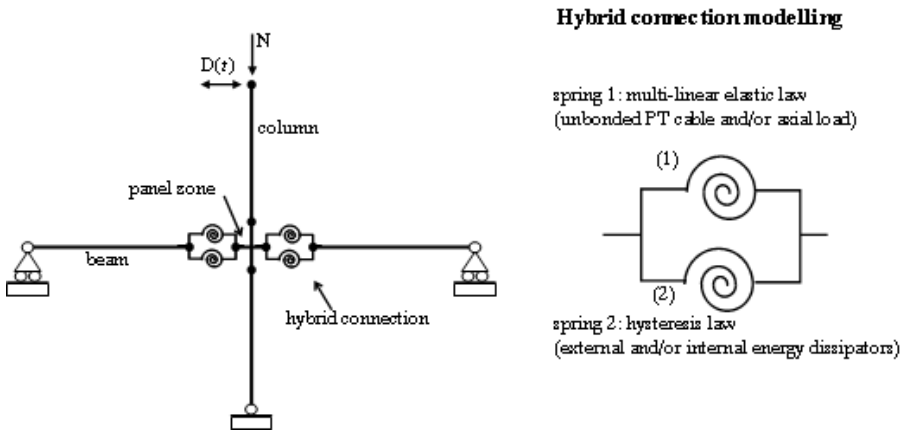

Figure 7.46 Lumped plasticity model of interior beam-column joint

Four typical joint types, two each for both exterior and interior joints, have been modelled for comparison. The plots are shown in Figure 7.47 and Figure 7.48. The forces calculated by the numerical models match well with the experimental results, particularly at high drifts. But the point of gap opening is more distinct in the numerical results, unlike the experiment.

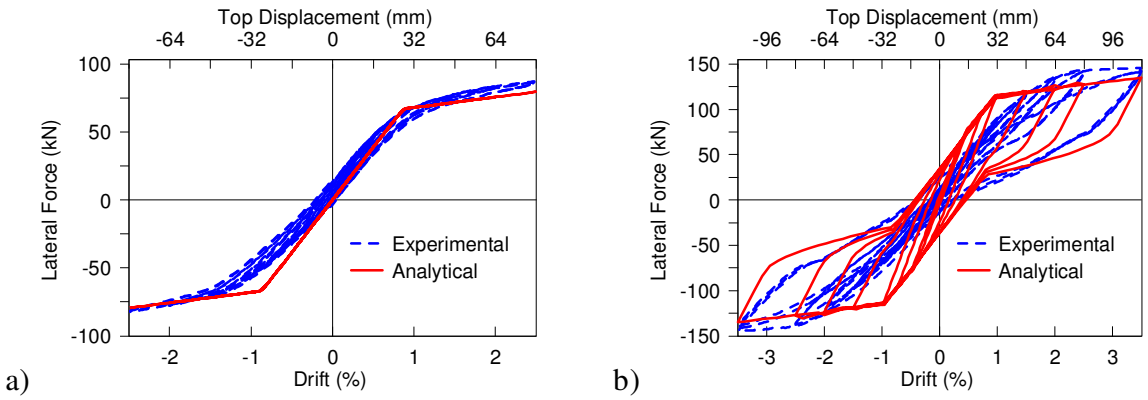

Figure 7.47 Comparisons for a) PT-only and b) Hybrid armoured unreinforced exterior joint

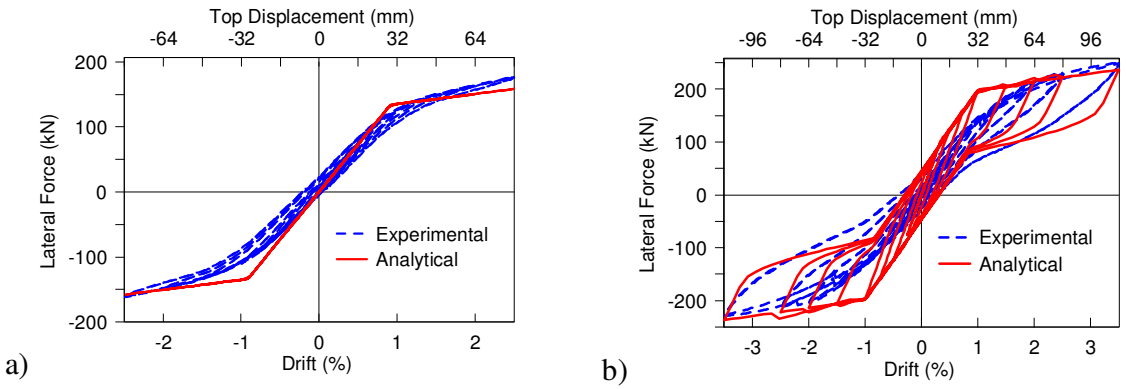

Figure 7.48 Comparisons for a) PT-only and b) Hybrid armoured unreinforced interior joint

7.7.3 Multi-spring model

Figure 7.49 shows the multi-spring model of a beam-column joint specimen. The elements at the beam-column interface also transfer the shear forces between the members.

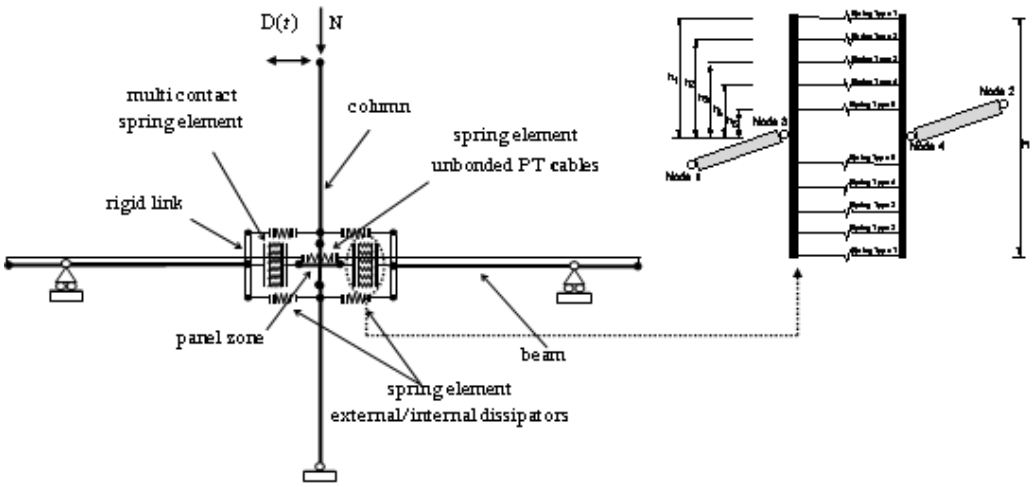

Figure 7.49 Multi spring model of beam-column joint

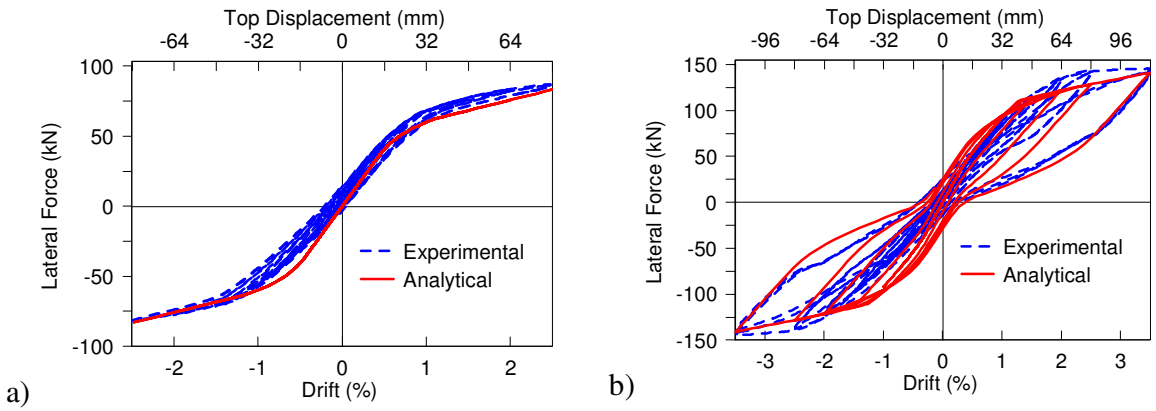

Figure 7.50 Comparisons for a) PT-only and b) Hybrid armoured unreinforced exterior joint

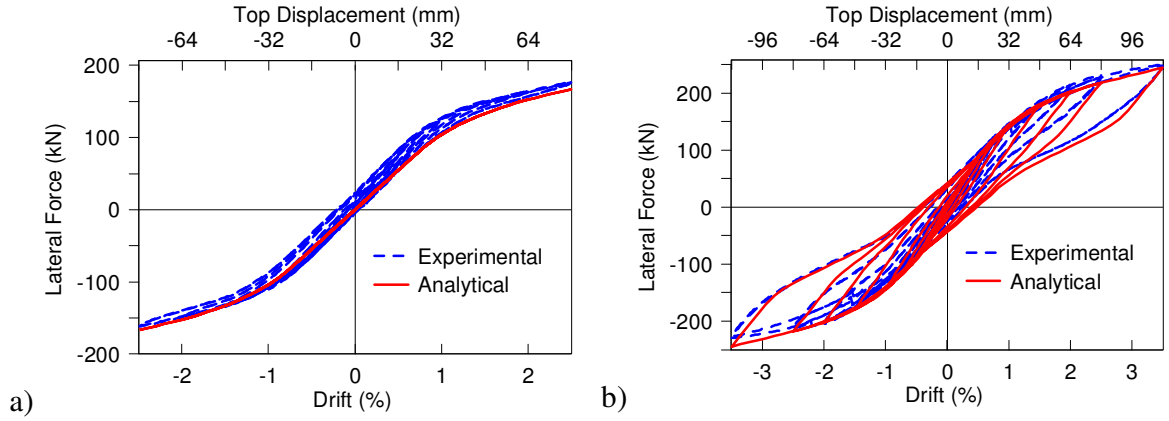

Figure 7.51 Comparisons for a) PT-only and b) Hybrid armoured unreinforced interior joint

The results of the post-tensioned-only and Hybrid specimens of the four typical cases modelled with the lumped plasticity concept are plotted in Figure 7.50 and Figure 7.51. Compared to the lumped plasticity models, the multi-spring model follows the experimental results slightly more accurately, particularly at the initiation of gap opening. The tendon forces and neutral axes locations at different drifts, shown in Figure 7.52 and Figure 7.53 respectively, also demonstrate good agreements between the experiment and the model.

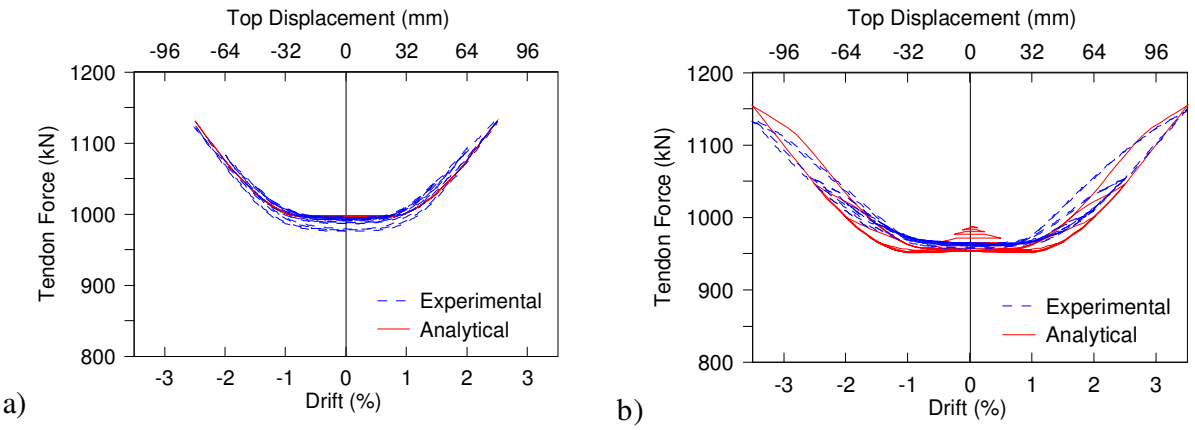

Figure 7.52 Models and experiments: a) PT-only and b) Hybrid armored interior joint

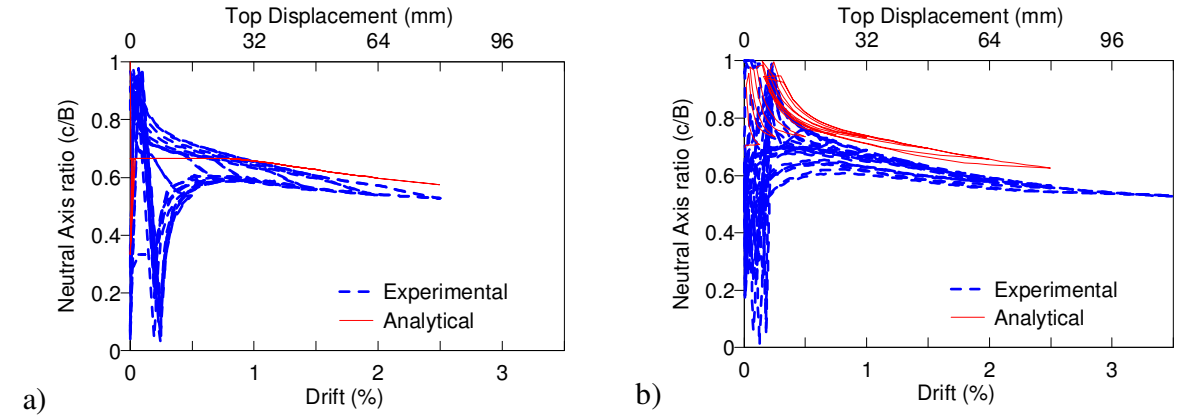

Figure 7.53 Models and experiments: a) PT-only and b) Hybrid armored interior joint

Multi-spring models of other types of joints, without armouring and with reinforcements have also been developed as shown in Figure 7.54 and Figure 7.55. It is noticeable that despite the differences in behaviour with the typical cases, the models match the experimental results for these types of joints as well.

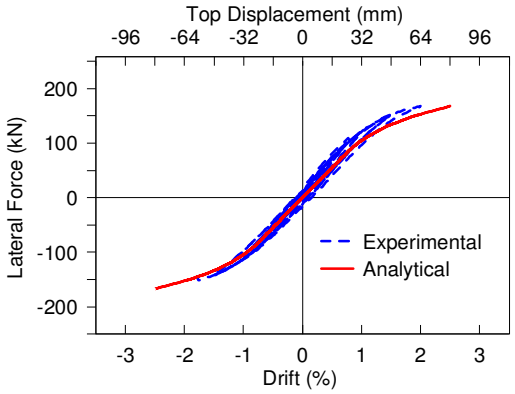

Figure 7.54 Models and experiments: reinforced armored interior joint

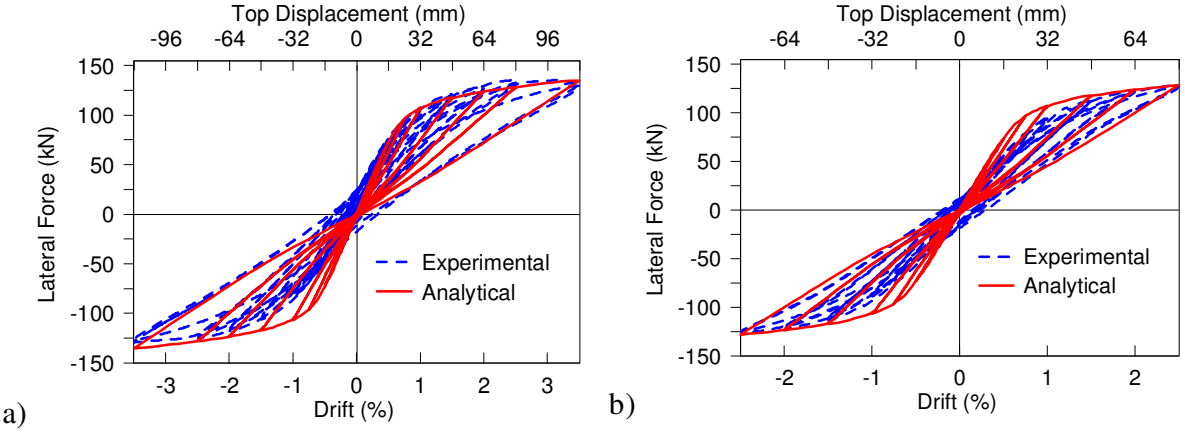

Figure 7.55 Models and experiments: a) unreinforced and b) reinforced unarmored interior joint

7.8 Summary and Parameters Identified from Numerical Models

As discussed in Chapter 2, the modulus of elasticity of timber at the connection interface was different from the typical values for the rest of the member. It is a critical factor in defining the behaviour of the subassemblies. After comparing results from numerical models with the experimental results the value of the Modulus of Elasticity of timber at different connection interfaces can be suggested with more confidence.

Based on a number of experiments on wall, column and beam-column joint, (Newcombe, 2007) suggested following elastic modulus for the connection interface for different connection types:

Table 7.1 Calibrated Elastic Modulus for different connection types

Connection Type	Wall-to-Foundation	Column-to-Foundation	Beam-Column
Interface Modulus	8000MPa	6500MPa	1400MPa

From the experimental and analytical work done for this research, the values are recommended for the coupled walls, column and beam-column joint under uni-directional loading. That means the connection modulus in terms of manufacturer specified (Futurebuild 2006) elastic modulus tentatively suggested by Newcombe et al., 2008 (Newcombe, 2007) are also recommended by this study:

For Wall and Column-to-foundation connections:

$$E_{con} = 0.55E_t \quad \textbf{7.1}$$

For Beam-Column connections:

$$E_{con} = 0.096E_t \quad \textbf{7.2}$$

Where E_t is the mean parallel-to-grain elastic modulus of the timber

It has to be emphasised here that these are very approximate values and further studies currently underway may produce more precise estimates. It is also to be noticed that the Elastic modulus for beam-column joint mentioned in Table 7.1 is for unarmoured connection type.

For a well armoured joint (with thick steel plates at the beam-column connection interface), the connection essentially behaves as a member bearing parallel-to-grain on a rigid interface, essentially the same way as the wall or column on steel foundation. The elastic modulus of the connection, therefore, may be in these cases taken as the same as that of the wall-to-foundation or column-to-foundation (parallel to the grain), depending on the material.

For example, for the beams made of the same grade of LVL as the walls, an elastic modulus of 8000 MPa should be used, which is the same value for wall-to-foundation connection.

It has been seen from the experimental results that screw reinforcements inside the joint region in a beam-column joint reduces the compressibility of the joint region and helps to reduce the joint shear panel deformations. But they have no significant effect on the stiffness of the connections. This implies that the same connection modulus used for unreinforced joints, both armoured and unarmoured, may be used for reinforced joints of the same type as shown in the following Table 7.2.

Table 7.2 Elastic Modulus for different connection types of beam-column connections

Connection Type	Unreinforced Unarmoured	Unreinforced Armoured	Reinforced Unarmoured	Reinforced Armoured
Interface Modulus	1400MPa	8000MPa	1400MPa	8000MPa

8 MOMENT-ROTATION SECTION ANALYSIS OF SUBASSEMBLY CONNECTIONS

8.1 Introduction

The experimental investigations described earlier in this research confirm that hybrid systems with post-tensioning and energy dissipation elements are feasible for timber structures. The last chapter showed how numerical models were developed, compared and/or calibrated with the experimental results. The calibrated models also suggested specific values of some parameters for future predictions.

A more detailed section analysis of the connections tested during the experimental study is performed in this chapter. The procedures to calculate the moment capacities of the subassemblies used in the experimental investigations have been implemented here. The values of the connection modulus suggested by the numerical models are used in the section analysis.

8.2 Section Analysis Procedure

The iterative procedure based on Monolithic Beam Analogy and presented in chapter 3 has been followed for section analysis. Calculations are performed only for ultimate limit state. So serviceability limit state is not considered.

The subassemblies are assumed to go through rigid body motion during rocking at the interface. That means elastic deformations are not considered. It is accepted that the elastic deformations may be of such magnitude that they should be ignored. But it has been found that generally it will be conservative in terms of moment capacities to ignore the elastic deformations in the

subassemblies. The additional tension in the prestressing tendons due to elastic deformations will contribute to the moment capacity of the overall system. So the moment capacity will be slightly underestimated if that is not accounted for in the final calculations.

Caution has to be exercised though for checking the prestressing tendon against yielding because it will be non-conservative to ignore the elastic deformations due to additional stresses in the tendons in reality. One way of taking care that is to keep a safe margin of safety to prevent any possible yielding of tendons. Provisions for this margin may be included in the calculations with a reasonable estimate of the elastic deformations.

Detailed calculation procedures for different types of subassemblies are presented in the following sections. It is to be noted that provisions for additional axial loads at the centre were not utilized in walls and the column during the experiments. It is still shown for completeness of the arrangements and provisions for calculations in all the cases.

8.3 Section Analysis of Walls

As already shown, three types of walls have been tested during the experimental program. Section analysis is performed on each of these walls separately.

8.3.1 Walls with PT only

Details of the PT-only walls are discussed in chapter 4. Double walls with the same arrangements are used here as shown in Figure 8.1.

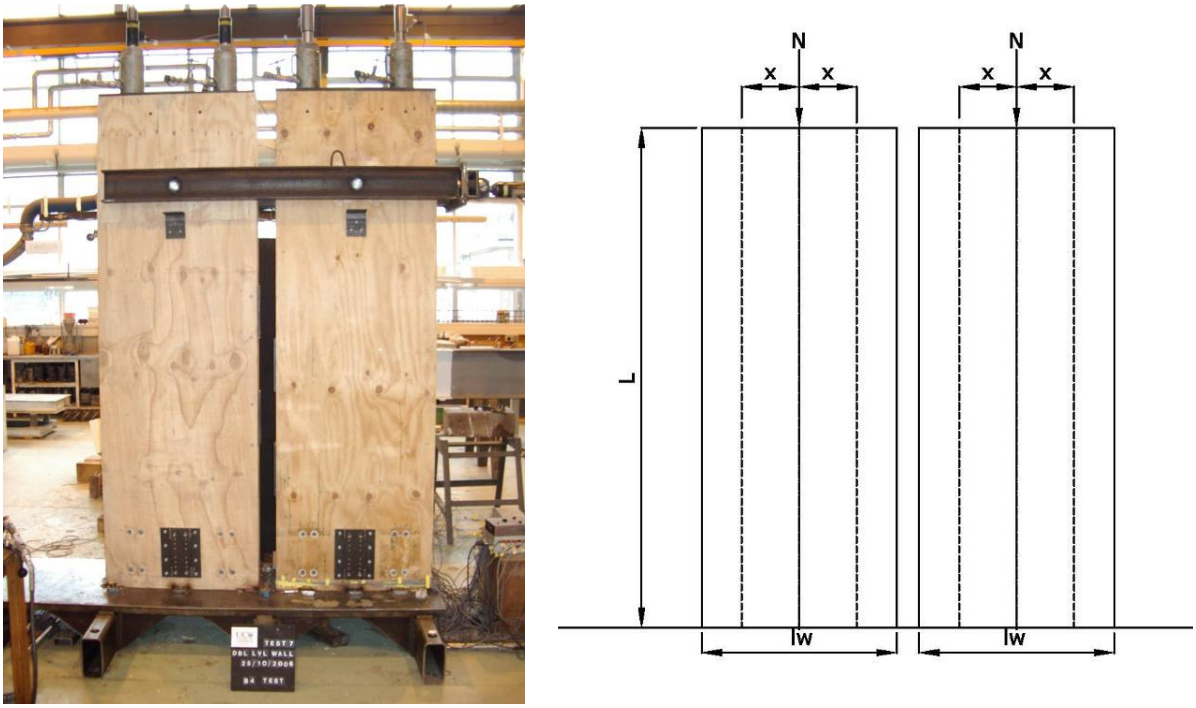

Figure 8.1 View of PT-only walls a) test specimen b) with dimensions

General steps to determine connection flexural capacity:

1: A connection rotation, θ_{imp} is imposed

2: Neutral axis depth c guessed initially

3: Member compatibility is applied:

Elongation of the tendon,

$$\Delta_{pt} = \theta_{imp}\left(\frac{l_w}{2} \pm x_{pt} - c\right) \quad \textbf{8.1}$$

Strain in the tendon,

$$\varepsilon_{pt,t} = \frac{\Delta_{pt,t}}{l_{ub}} \quad \textbf{8.2}$$

$$\varepsilon_{pt,c} = \frac{\Delta_{pt,c}}{l_{ub}} \quad \textbf{8.3}$$

To check the tendon is not yielding,

$$\varepsilon_{pt,i} + \varepsilon_{pt} \leq 0.9\varepsilon_y \quad \textbf{8.4}$$

Where,

$$\varepsilon_{pt,i} = \frac{T_{pt,i}}{A_{pt}E_{pt}} \quad \textbf{8.5}$$

And

$$T_{pt,i} = \rho_{pt} f_y A_{pt} \quad \textbf{8.6}$$

Strain in the timber from Monolithic Beam Analogy:

$$\varepsilon_t = \left(3\frac{\theta_{imp}}{L_{cant}} + \phi_{dec} \right) c \quad \textbf{8.7}$$

Where, L_{cant} is the shear span

And the decompression curvature,

$$\phi_{dec} = \frac{2\left(T_{pt,i} + N\right)}{E_{con} b h^2} \quad \textbf{8.8}$$

To check the timber is not yielding,

$$\varepsilon_{y,t} = \frac{f_c}{E_{con}} > \varepsilon_t \quad \textbf{8.9}$$

4: The compressive force in the timber is calculated:

$$C_t = 0.5 \varepsilon_t E_{con} c b \quad \textbf{8.10}$$

5: Connection equilibrium is checked:

$$C_t = T_{pt} + N \quad \textbf{8.11}$$

Where,

$$T_{pt} = T_{pt,i} + \Delta T_{pt} = \rho_{pt} f_y A_{pt} + \varepsilon_{pt} E_{pt} A_{pt} \quad \textbf{8.12}$$

And,
In tension:

$$T_s = f_y A_s \quad \textbf{8.13}$$

In compression:

$$C_s = f_y A_s \quad \textbf{8.14}$$

If satisfied, step 7 is followed; otherwise steps 1 to 5 are repeated

6: Neutral axis updated and iterated

7: The moment capacity is evaluated

$$\phi M_n = \phi M_{pt} = \phi \left[T_{pt} \left(\frac{l_w}{2} \pm x_{pt} - \frac{c}{3} \right) + N \left(\frac{l_w}{2} - \frac{c}{3} \right) \right] \quad \textbf{8.15}$$

The moment capacity is checked:

$$M^* \leq \phi M_n \quad \textbf{8.16}$$

Section Analysis of Walls with PT- only Test Specimen: Worked Example

Details of the PT-only walls are discussed in chapter 4. Double walls with the same arrangements are used here as shown in Figure 8.1.

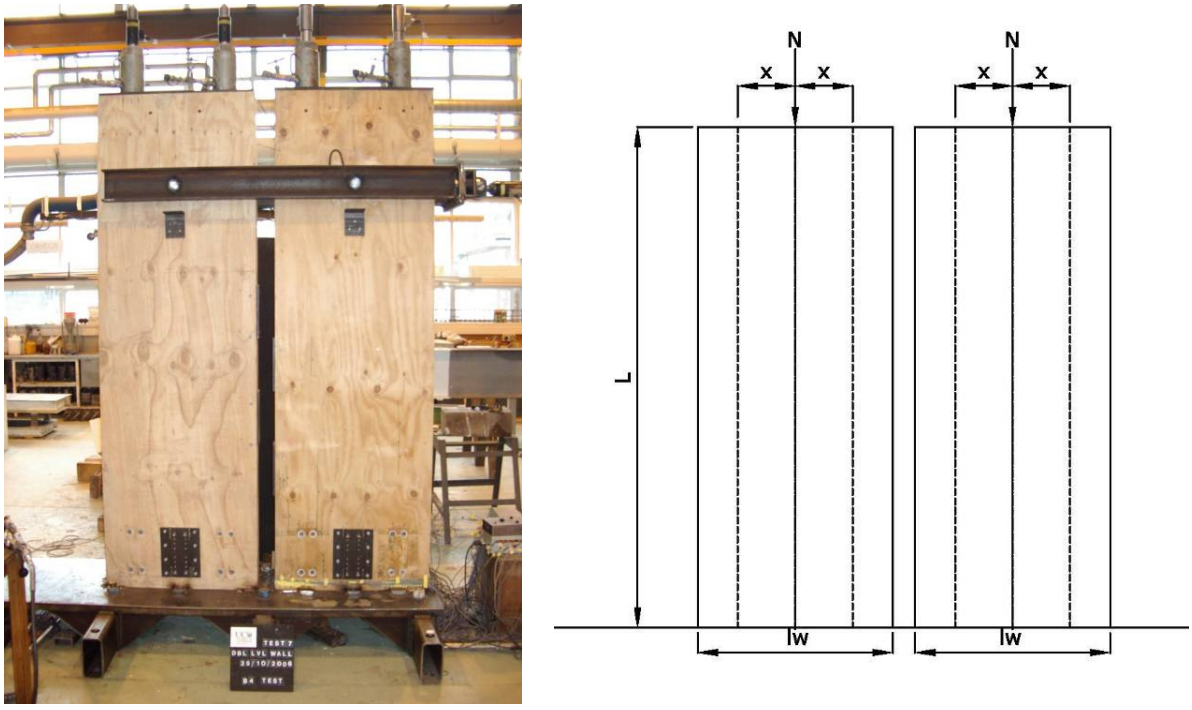

Figure 8.2 View of PT-only walls a) test specimen b) with dimensions

x = 230mm

For lub = 2500mm

Fy= .85*1830= 1560MPa, Ept = 200 GPa and Apt = 99mm2

Initial prestress= 50% of yield, PTi=77.2 kN

Design drift= 2%

Elastic deformation: approximately 0.5%

Steps to determine connection flexural capacity:

Connection rotation, θ_{imp} is imposed
drift, θ=1.5%

Neutral axis depth c (through trial)

c= 0.135lw=105mm

Member compatibility is applied:

Elongation of the tendon,

$$\Delta_{pt} = \theta_{imp}\left(\frac{l_w}{2} \pm x_{pt} - c\right) \quad \textbf{8.17}$$

Δpt1 =0.83mm and Δpt2 = 7.73mm.
Strain in the tendon,

$$\varepsilon_{pt,t} = \frac{\Delta_{pt,t}}{l_{ub}} \quad \textbf{8.18}$$

$$\varepsilon_{pt,c} = \frac{\Delta_{pt,c}}{l_{ub}} \quad \textbf{8.19}$$

εpt1 =0.00033 and εpt2 = 0.00309

To check the tendon is not yielding,

$$\varepsilon_{pt,i} + \varepsilon_{pt} \le 0.9\varepsilon_y \quad \textbf{8.20}$$

Where,

$$\varepsilon_{pt,i} = \frac{T_{pt,i}}{A_{pt}E_{pt}} \quad \textbf{8.21}$$

εpti =0.00309 +εs =0.0039 < 0.9εs =0.007

Strain in the timber from Monolithic Beam Analogy:

$$\varepsilon_t = \left(3\frac{\theta_{imp}}{L_{cant}} + \phi_{dec}\right)c \quad \textbf{8.22}$$

Where, L_{cant} is the shear span = .8*2000=1600mm

And the decompression curvature,

$$\phi_{dec} = \frac{2\left(T_{pt,i} + N\right)}{E_{con}bh^2} \quad \textbf{8.23}$$

φdec = 3.6E-7, εt= 0.006198
To check the timber is not yielding,

$$\varepsilon_{y,t} = \frac{f_c}{E_{con}} > \varepsilon_t \quad \textbf{8.24}$$

εy,t=45/(.55*13200)=006198>.00299
The compressive force in the timber is calculated:

$$C_t = 0.5\varepsilon_t E_{con} cb \quad \textbf{8.25}$$

Ct=222.2
Connection equilibrium is checked:

$$C_t = T_{pt} + N \quad \textbf{8.26}$$

$$T_{pt} = T_{pt,i} + \Delta T_{pt} = \rho_{pt} f_y A_{pt} + \varepsilon_{pt} E_{pt} A_{pt} \quad \textbf{8.27}$$

ΔT1= 6.5 kN and ΔT2= 61.2 kN

$$T_i = T_{initial} + \Delta T_i$$

T initial = 77.2 kN, Tpt1= 83.76 kN and Tpt2= 138.4 kN.

Tpt=222.14

Satisfied

The moment capacity:

$$\phi M_n = \phi M_{pt} = \phi\left[T_{pt}\left(\frac{l_w}{2} \pm x_{pt} - \frac{c}{3}\right) + N\left(\frac{l_w}{2} - \frac{c}{3}\right)\right] \quad \textbf{8.28}$$

Mpt1 = 91.44 kN-m and total moment, M pt = 182.88 kN-m, φMpt = 164.6 kN-m

8.3.2 Hybrid Wall(s) with axial energy dissipaters

Axial dissipaters were added to the PT-only double walls discussed in the last section. Two (one in either side) 8mm diameter dissipaters were attached at the centre of each wall. The other details remained the same.

The arrangements are as shown in Figure 8.3.

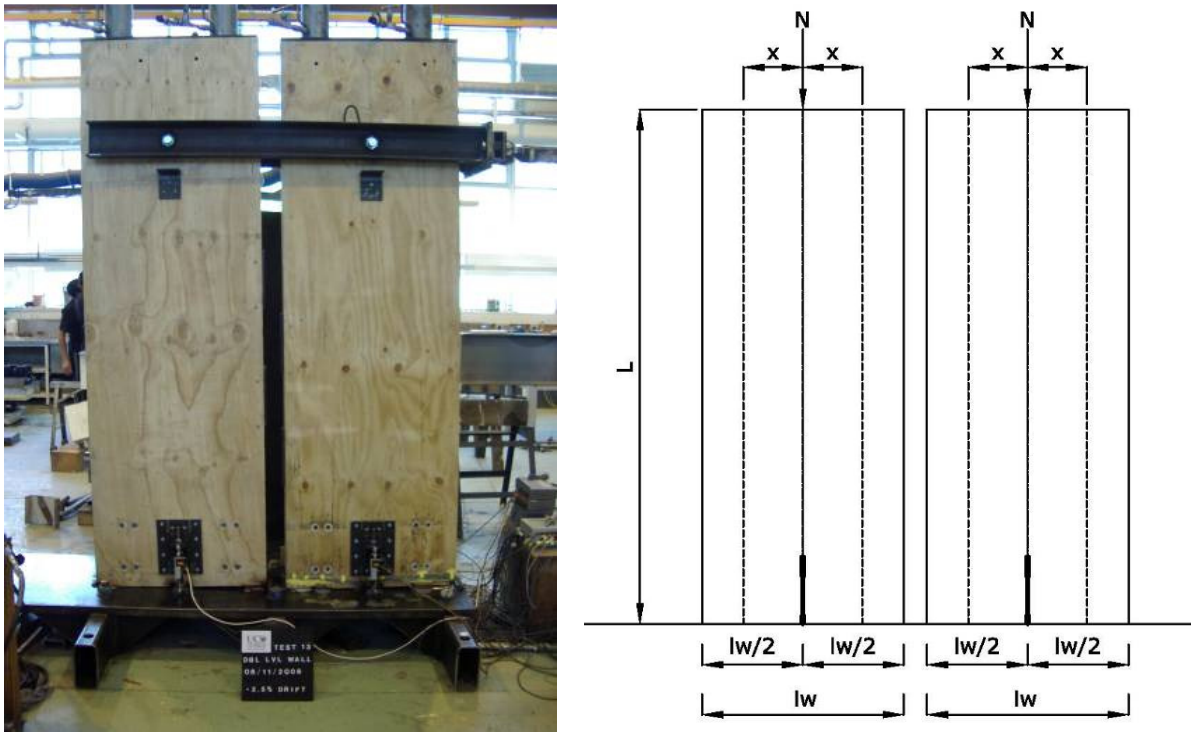

Figure 8.3 View of walls with axial dissipaters a) test specimen b) with dimensions

For Hybrid walls with axial energy dissipaters:

Elongation in energy dissipater,

$$\Delta_s = \theta_{imp}\left(\frac{l_w}{2} - c\right) \quad \textbf{8.29}$$

Strain in the dissipater,

$$\varepsilon_s = \frac{\Delta_s}{l_{ub,d}} \quad \textbf{8.30}$$

To make sure the dissipater has yielded,

$$\varepsilon_s > \varepsilon_{y,s} = \frac{f_s}{E_s} \quad \textbf{8.31}$$

For connection equilibrium:

$$C_t = T_{pt} + N + T_s \quad \textbf{8.32}$$

Where,

$$T_{pt} = T_{pt,i} + \Delta T_{pt} = \rho_{pt} f_y A_{pt} + \varepsilon_{pt} E_{pt} A_{pt} \quad \textbf{8.33}$$

And,

$$T_s = f_y A_s \quad \textbf{8.34}$$

The moment capacity

$$\phi M_n = \phi\left(M_{pt} + M_s\right) = \phi\left[T_{pt}\left(\frac{l_w}{2} \pm x_{pt} - \frac{c}{3}\right) + N\left(\frac{l_w}{2} - \frac{c}{3}\right) + T_s\left(\frac{l_w}{2} - \frac{c}{3}\right)\right] \qquad \textbf{8.35}$$

The re-centering ratio,

$$\lambda = \frac{M_{pt} + M_N}{M_s} \qquad \textbf{8.36}$$

Section Analysis of Hybrid Walls Test Specimen: Worked Example

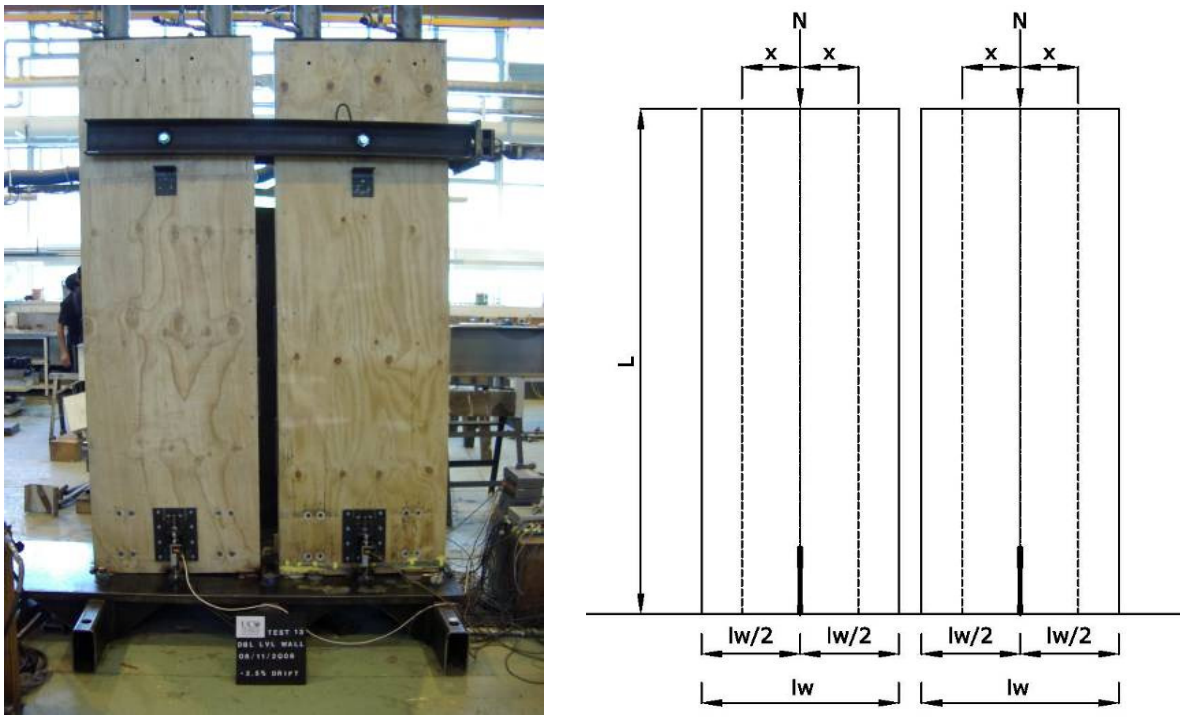

Figure 8.4 View of walls with axial dissipaters a) test specimen b) with dimensions

x = 230mm

For lub = 2500mm

Fy= .85*1830= 1560MPa, Ept = 200 GPa and Apt = 99mm2

Initial prestress= 30% of yield, PTi=46.33 kN

Two 8mm diameter axial dissipaters per wall

Design drift= 2%

Elastic deformation: approximately 0.5%

Steps to determine connection flexural capacity:

Connection rotation, θ_{imp} is imposed
drift, θ=1.5%

Neutral axis depth c (through trial)
c= 0.127w=99mm

Member compatibility is applied:

Elongation of the tendon,

$$\Delta_{pt} = \theta_{imp}\left(\frac{l_w}{2} \pm x_{pt} - c\right) \quad \textbf{8.37}$$

Δpt1 =0.92mm and Δpt2 = 7.82mm.
Strain in the tendon,

$$\varepsilon_{pt,t} = \frac{\Delta_{pt,t}}{l_{ub}} \quad \textbf{8.38}$$

$$\varepsilon_{pt,c} = \frac{\Delta_{pt,c}}{l_{ub}} \quad \textbf{8.39}$$

εpt1 =0.00037 and εpt2 = 0.00313

εpti =0.0023
To check the tendon is not yielding,

$$\varepsilon_{pt,i} + \varepsilon_{pt} \le 0.9\varepsilon_y \quad \textbf{8.40}$$

Where,

$$\varepsilon_{pt,i} = \frac{T_{pt,i}}{A_{pt}E_{pt}} \quad \textbf{8.41}$$

εpti +εpt < 0.9εs =0.007

Elongation in energy dissipater,

$$\Delta_s = \theta_{imp}\left(\frac{l_w}{2} - c\right) \quad \textbf{8.42}$$

Δs = 4.36mm
Strain in the dissipater,

$$\varepsilon_s = \frac{\Delta_s}{l_{ub,d}} \quad \textbf{8.43}$$

εs =0.0436

To make sure the dissipater has yielded,

$$\varepsilon_s > \varepsilon_{y,s} = \frac{f_s}{E_s}$$

εy,s=0.001725
Strain in the timber from Monolithic Beam Analogy:

$$\varepsilon_t = \left(3\frac{\theta_{imp}}{L_{cant}} + \phi_{dec} \right) c \qquad \textbf{8.44}$$

Where, L_{cant} is the shear span = .8*2000=1600mm

And the decompression curvature,

$$\phi_{dec} = \frac{2\left(T_{pt,i} + N\right)}{E_{con} b h^2} \qquad \textbf{8.45}$$

φdec = 2.2E-7, εt= 0.002805
To check the timber is not yielding,

$$\varepsilon_{y,t} = \frac{f_c}{E_{con}} > \varepsilon_t \qquad \textbf{8.46}$$

εy,t=45/(.55*13200)=.006198>.002805
The compressive force in the timber is calculated:

$$C_t = 0.5\varepsilon_t E_{con} c b \qquad \textbf{8.47}$$

Ct=196.6

$$T_{pt} = T_{pt,i} + \Delta T_{pt} = \rho_{pt} f_y A_{pt} + \varepsilon_{pt} E_{pt} A_{pt} \qquad \textbf{8.48}$$

ΔT1= 7.25 kN and ΔT2= 61.9 kN

$$T_i = T_{initial} + \Delta T_i$$

T initial = 46.33 kN, Tpt1= 53.58 kN and Tpt2= 108.23 kN.

$$T_s = f_y A_s \qquad \textbf{8.49}$$

Ts= 34.7 kN

Tpt1+Tpt2+Ts = 196.5 kN
For connection equilibrium:

$$C_t = T_{pt} + N + T_s \qquad \textbf{8.50}$$

Satisfied
Moment capacity:

$$\phi M_n = \phi\left(M_{pt} + M_s\right) = \phi\left[T_{pt}\left(\frac{l_w}{2} \pm x_{pt} - \frac{c}{3} \right) + N\left(\frac{l_w}{2} - \frac{c}{3} \right) + T_s\left(\frac{l_w}{2} - \frac{c}{3} \right) \right] \qquad \textbf{8.51}$$

Mpt1 = 70.34 kN-m and Ms = 12.38 kN-m

Total moment for two walls = 165.44 kN-m, φMpt = 148.89 kN-m

The re-centering ratio, $\lambda = 5.68$

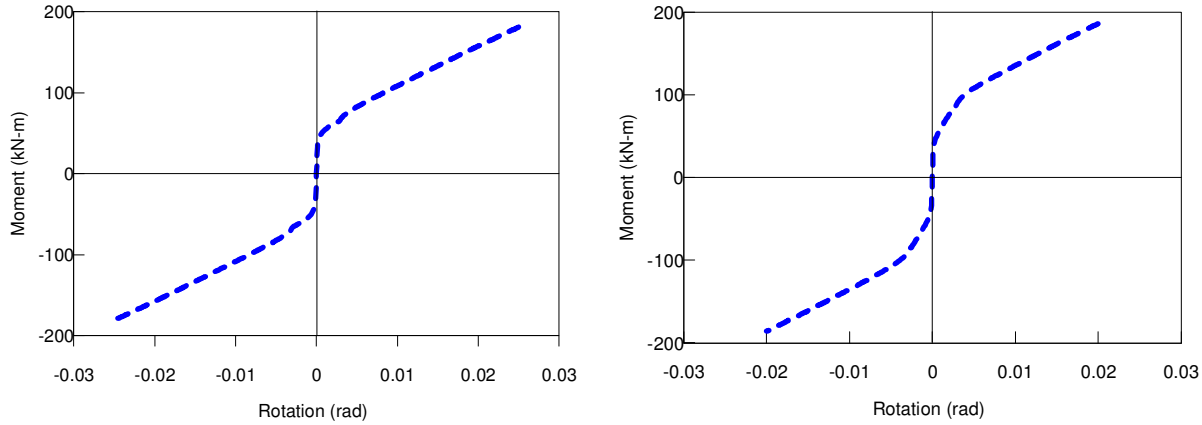

Figure 8.5 Moment-rotation of PT-only and Hybrid wall specimens

8.3.3 Hybrid coupled walls with UFP dissipaters

UFPs were placed in the gap between the two PT-only walls and attached to them. The walls thus become coupled with them. As mentioned before, the UFPs can be in single or double pair. That does not make any difference in the concept or the calculations. Only one pair is shown in the arrangements in Figure 8.6.

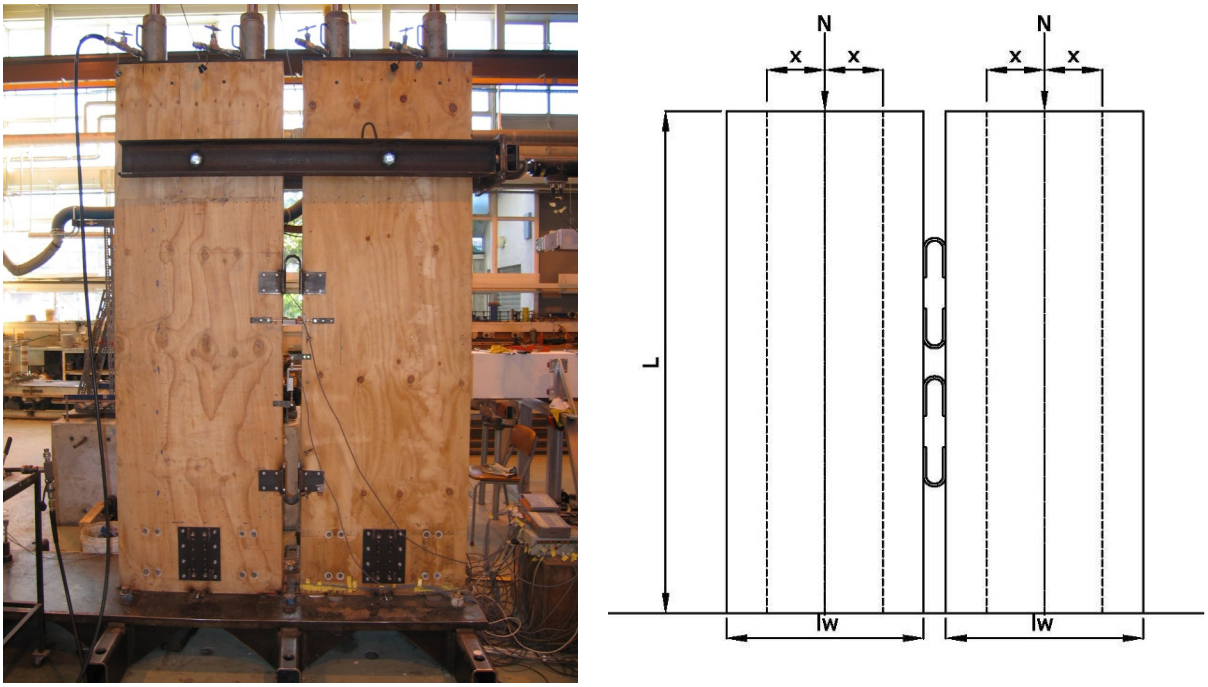

Figure 8.6 View of walls with UFP dissipaters a) test specimen b) with dimensions

For Hybrid walls with UFP dissipaters:

UFP force contributions:

$$V_s = n * 0.5 \frac{bt^2}{D} F_y \quad \textbf{8.52}$$

Wall axial forces:

$$N_1 = N - V_s \quad \textbf{8.53}$$

$$N_2 = N + V_s \quad \textbf{8.54}$$

Connection equilibrium conditions:

$$C_{t1} = T_{pt11} + T_{pt12} + N_1 \quad \textbf{8.55}$$

$$C_{t2} = T_{pt21} + T_{pt22} + N_2 \quad \textbf{8.56}$$

Where,

$$T_{pt} = T_{pt,i} + \Delta T_{pt} = \rho_{pt} f_y A_{pt} + \varepsilon_{pt} E_{pt} A_{pt} \quad \textbf{8.57}$$

The moment capacity

$$M_{pt1} = T_{pt11}\left(\frac{l_w}{2} - x_{pt} - \frac{c_1}{3}\right) + T_{pt12}\left(\frac{l_w}{2} + x_{pt} - \frac{c_1}{3}\right) + N_1\left(\frac{l_w}{2} - \frac{c_1}{3}\right) \quad \textbf{8.58}$$

$$M_{pt2} = T_{pt21}\left(\frac{l_w}{2} - x_{pt} - \frac{c_2}{3}\right) + T_{pt22}\left(\frac{l_w}{2} + x_{pt} - \frac{c_2}{3}\right) + N_2\left(\frac{l_w}{2} - \frac{c_2}{3}\right) \quad \textbf{8.59}$$

$$M_{pt} = M_{pt1} + M_{pt2} \quad \textbf{8.60}$$

$$M_{pt} = \frac{l_w}{2}\left(T_{pt11} + T_{pt12} + T_{pt21} + T_{pt22} + N_1 + N_2\right) - x_{pt}\left(T_{pt11} - T_{pt12} + T_{pt21} - T_{pt22}\right) - \frac{c_1}{3}\left(T_{pt11} + T_{pt12} + N_1\right) - \frac{c_2}{3}\left(T_{pt21} + T_{pt22} + N_2\right) \quad \textbf{8.61}$$

$$M_s = M_{s1} + M_{s2} = V_s\left(\frac{c_1}{3}\right) + V_s\left(l_w - \frac{c_2}{3}\right) = V_s\left(l_w + \frac{c_1 - c_2}{3}\right) \quad \textbf{8.62}$$

Section Analysis Hybrid Walls Sepcimen with UFP dissipaters: Worked Example

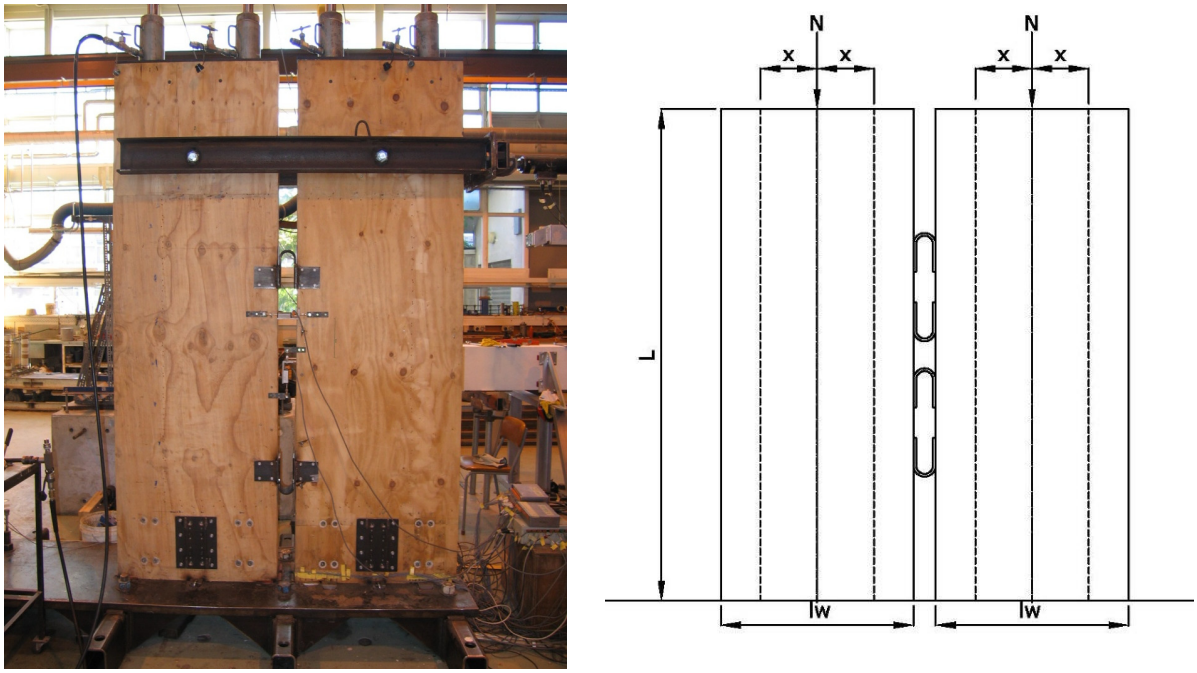

Figure 8.7 View of walls with UFP dissipaters a) test specimen b) with dimensions

x = 230mm

For lub = 2500mm

Fy= .85*1830= 1560MPa, Ept = 200 GPa and Apt = 99mm2

From initial prestress of 30% of yield, PTi=46.33 kN

Design drift= 2%

Four 50 mm wide, 5 mm thickness UFP dissipaters

Elastic deformation: approximately 0.5%

Steps to determine connection flexural capacity:

Connection rotation, θ_{imp} is imposed
drift, θ=1.5%

Neutral axis depth c (through trial)
c1= 0.103w=81mm, c2=0.127w=99mm

Member compatibility is applied:

Elongation of the tendon,

$$\Delta_{pt} = \theta_{imp}\left(\frac{l_w}{2} \pm x_{pt} - c\right) \quad \textbf{8.63}$$

Wall1: Δpt1 =1.19mm and Δpt2 = 8.09mm.
Wall2: Δpt1 =0.91mm and Δpt2 = 7.81mm
Strain in the tendon,

$$\varepsilon_{pt,t} = \frac{\Delta_{pt,t}}{l_{ub}} \quad \textbf{8.64}$$

$$\varepsilon_{pt,c} = \frac{\Delta_{pt,c}}{l_{ub}} \quad \textbf{8.65}$$

Wall1: εpt1 =0.00048 and εpt2 = 0.00324

Wall2: εpt1 =0.00036 and εpt2 = 0.00312

εpti =0.0023
To check the tendon is not yielding,

$$\varepsilon_{pt,i} + \varepsilon_{pt} \le 0.9\varepsilon_y \quad \textbf{8.66}$$

Where,

$$\varepsilon_{pt,i} = \frac{T_{pt,i}}{A_{pt}E_{pt}} \quad \textbf{8.67}$$

εpti +εpt < 0.9εs =0.007

Strain in the timber from Monolithic Beam Analogy:

$$\varepsilon_t = \left(3\frac{\theta_{imp}}{L_{cant}} + \phi_{dec}\right)c \quad \textbf{8.68}$$

Where, L_{cant} is the shear span = .8*2000=1600mm

And the decompression curvature,

$$\phi_{dec} = \frac{2\left(T_{pt,i} + N\right)}{E_{con}bh^2} \quad \textbf{8.69}$$

φdec = 2.2E-7, Wall1, εt= 0.002284, Wall2, εt= 0.006198

To check the timber is not yielding,

$$\varepsilon_{y,t} = \frac{f_c}{E_{con}} > \varepsilon_t \quad \textbf{8.70}$$

εy,t=45/(.55*13200)=.006198>.006198
The compressive force in the timber is calculated:

$$C_t = 0.5\varepsilon_t E_{con} cb \quad \textbf{8.71}$$

Wall1, Ct1=130.3, Wall2, Ct2=197.6

$$T_{pt} = T_{pt,i} + \Delta T_{pt} = \rho_{pt} f_y A_{pt} + \varepsilon_{pt} E_{pt} A_{pt} \quad \textbf{8.72}$$

Wall1: ΔT1= 9.4 kN and ΔT2= 64.1 kN

Wall2: ΔT1= 7.2 kN and ΔT2= 61.9 kN

$$T_i = T_{initial} + \Delta T_i$$

Wall1: T initial = 46.33 kN, Tpt1= 55.77 kN and Tpt2= 110.42 kN.
Wall2: T initial = 46.33 kN, Tpt1= 53.55 kN and Tpt2= 108.2 kN.

UFP force contributions:

$$V_s = n * 0.5 \frac{bt^2}{D} F_y \quad \textbf{8.73}$$

Vs in both Wall1 and Wall2= 35.8 kN (from 4 UFPs)
Wall axial forces:

$$N_1 = N - V_s \quad \textbf{8.74}$$
$$N_2 = N + V_s$$

For connection equilibrium:

$$C_{t1} = T_{pt11} + T_{pt12} + N_1 \quad \textbf{8.75}$$
$$C_{t2} = T_{pt21} + T_{pt22} + N_2 \quad \textbf{8.76}$$

Wall1= 130.3 kN
Wall2= 197.6 kN

Satisfied
Moment capacity:

$$M_{pt1} = T_{pt11}\left(\frac{l_w}{2} - x_{pt} - \frac{c_1}{3}\right) + T_{pt12}\left(\frac{l_w}{2} + x_{pt} - \frac{c_1}{3}\right) + N_1\left(\frac{l_w}{2} - \frac{c_1}{3}\right) \quad \textbf{8.77}$$

$$M_{pt2} = T_{pt21}\left(\frac{l_w}{2} - x_{pt} - \frac{c_2}{3}\right) + T_{pt22}\left(\frac{l_w}{2} + x_{pt} - \frac{c_2}{3}\right) + N_2\left(\frac{l_w}{2} - \frac{c_2}{3}\right) \quad \textbf{8.78}$$

$$M_{pt} = M_{pt1} + M_{pt2} \quad \textbf{8.79}$$

$$M_{pt} = \frac{l_w}{2}\left(T_{pt11} + T_{pt12} + T_{pt21} + T_{pt22} + N_1 + N_2\right) - x_{pt}\left(T_{pt11} - T_{pt12} + T_{pt21} - T_{pt22}\right)$$
$$- \frac{c_1}{3}\left(T_{pt11} + T_{pt12} + N_1\right) - \frac{c_2}{3}\left(T_{pt21} + T_{pt22} + N_2\right) \quad \textbf{8.80}$$

$$M_s = M_{s1} + M_{s2} = V_s\left(\frac{c_1}{3}\right) + V_s\left(l_w - \frac{c_2}{3}\right) = V_s\left(l_w + \frac{c_1 - c_2}{3}\right) \quad \textbf{8.81}$$

Mpt1 = 59.9 kN-m and Ms = 0.96 kN-m

Mpt1 = 83.09 kN-m and Ms = 26.76 kN-m

Total moment for two walls, Mpt = 142.99 kN-m, Ms= 29.73 φMn = 153.65 kN-m

The re-centering ratio, λ = 5.157

8.4 Section Analysis of Column

Two types of column specimens were tested: PT-only and Hybrid. That means the only difference between them was the presence of axial energy dissipation elements.

8.4.1 Column with PT only

The details of the test specimens are discussed in chapter 4. The main features are again shown here in Figure 8.8.

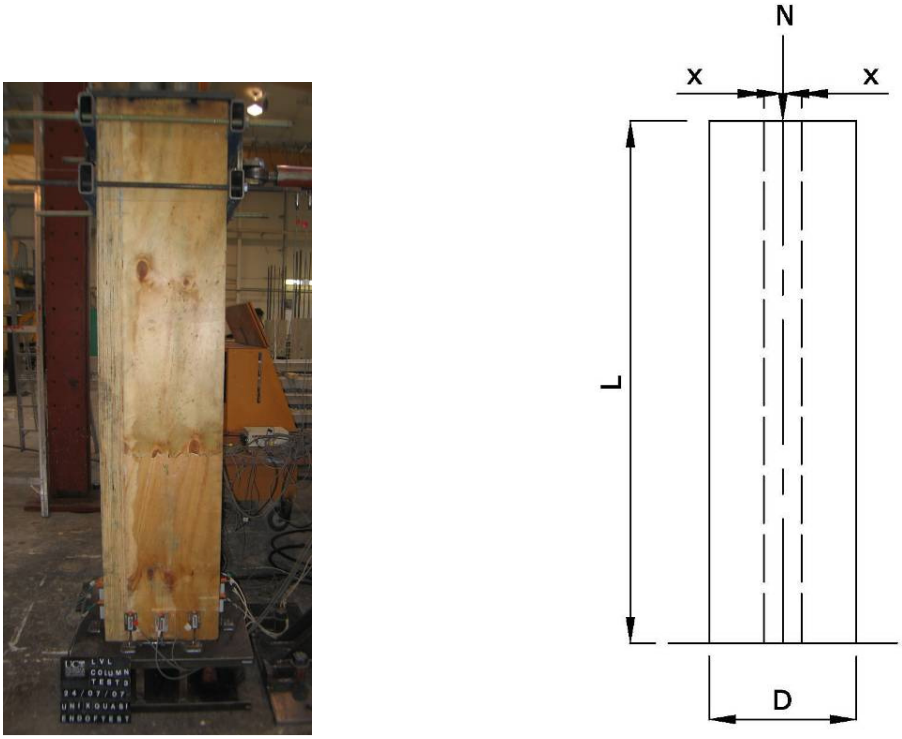

Figure 8.8 View of PT-only column a) test specimen b) with dimensions

Steps to determine connection flexural capacity:

1: A connection rotation, θ_{imp} is imposed

2: Neutral axis depth c guessed initially

3: Member compatibility is applied:

Elongation of the tendon,

$$\Delta_{pti} = \theta_{imp}\left(\frac{D}{2} \pm x_{pti} - c\right) \quad \textbf{8.82}$$

Strain in the tendon,

$$\varepsilon_{pt} = \frac{\Delta_{pt}}{l_{ub}} \quad \textbf{8.83}$$

To check the tendon is not yielding,

$$\varepsilon_{pt,i} + \varepsilon_{pt} \leq 0.9\varepsilon_{y,pt} \quad \textbf{8.84}$$

Where,

$$\varepsilon_{y,pt} = \frac{f_{s,pt}}{E_{s,pt}} \quad \textbf{8.85}$$

$$\varepsilon_{pt,i} = \frac{T_{pt,i}}{A_{pt}E_{s,pt}} \quad \textbf{8.86}$$

And

$$T_{pt,i} = \rho_{pt} f_{y,pt} A_{pt} \quad \textbf{8.87}$$

Strain in the timber from Monolithic Beam Analogy:

$$\varepsilon_t = \left(3\frac{\theta_{imp}}{L_{cant}} + \phi_{dec}\right)c \quad \textbf{8.88}$$

Where, L_{cant} is the shear span,

And the decompression curvature,

$$\phi_{dec} = \frac{2\left(T_{pt,i} + N\right)}{E_{con}BD^2} \quad \textbf{8.89}$$

To check the timber is not yielding,

$$\varepsilon_{y,t} = \frac{f_c}{E_{con}} > \varepsilon_t \quad \textbf{8.90}$$

4: The compressive force in the timber is calculated:

$$C_t = 0.5\varepsilon_t E_{con} cD \quad \textbf{8.91}$$

5: Connection equilibrium is checked:

$$C_t = T_{pt} + N \quad \textbf{8.92}$$

Where,

$$T_{pt} = T_{pt,i} + \Delta T_{pt} = \rho_{pt} f_y A_{pt} + \varepsilon_{pt} E_{pt} A_{pt} \quad \textbf{8.93}$$

6: Neutral axis updated and iteration done

If satisfied, step 7 followed, otherwise steps 2 to 5 followed

7: The moment capacity is calculated:

$$\phi M_n = \phi M_{pt} = \phi\left[T_{pt}\left(\frac{D}{2} \pm x_{pt} - \frac{c}{3}\right) + N\left(\frac{D}{2} - \frac{c}{3}\right)\right] \qquad \textbf{8.94}$$

Moment capacity is checked:

$$M^* \leq \phi M_n \qquad \textbf{8.95}$$

Section Analysis of Column with PT- onlyTest Specimen:Worked Example

The details of the test specimens are discussed in chapter 4. The main features are again shown here in Figure 8.8.

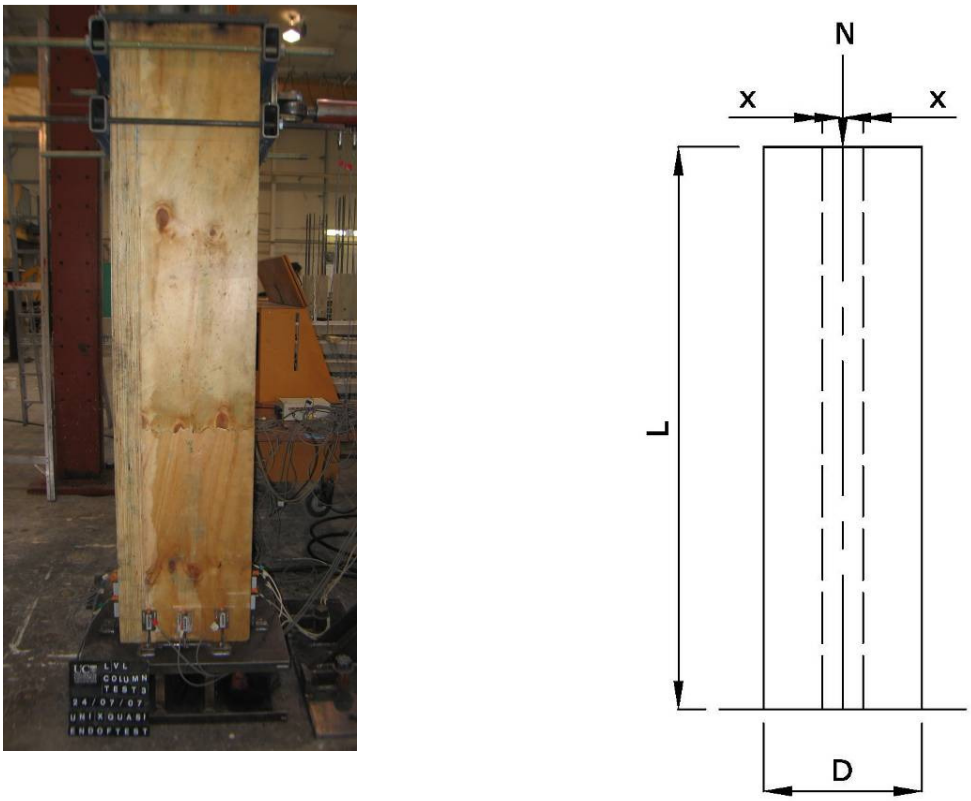

Figure 8.9 View of PT-only column a) test specimen b) with dimensions

Steps to determine connection flexural capacity:

Connection rotation, θ_{imp} is imposed drift, θ=2%

Neutral axis depth c (through trial)
c= 0.16D=72mm

Member compatibility is applied:

Elongation of the tendon,

$$\Delta_{pti} = \theta_{imp}\left(\frac{D}{2} \pm x_{pti} - c\right) \quad \textbf{8.96}$$

Strain in the tendon,

$$\varepsilon_{pt} = \frac{\Delta_{pt}}{l_{ub}} \quad \textbf{8.97}$$

Δpt1 =4.21mm and Δpt2 = 1.91mm.

To check the tendon is not yielding,

$$\varepsilon_{pt,i} + \varepsilon_{pt} \le 0.9\varepsilon_{y,pt} \quad \textbf{8.98}$$

Where,

$$\varepsilon_{y,pt} = \frac{f_{s,pt}}{E_{s,pt}} \quad \textbf{8.99}$$

$$\varepsilon_{pt,i} = \frac{T_{pt,i}}{A_{pt}E_{s,pt}} \quad \textbf{8.100}$$

And

$$T_{pt,i} = \rho_{pt} f_{y,pt} A_{pt} \quad \textbf{8.101}$$

εpt1 =0.00222 and εpt2 = 0.00101

εpti =0.0039 +εs =0.00222 < 0.9εs =0.007

Strain in the timber from Monolithic Beam Analogy:

$$\varepsilon_t = \left(3\frac{\theta_{imp}}{L_{cant}} + \phi_{dec}\right)c \quad \textbf{8.102}$$

Where, L_{cant} the shear span = .5*3200=1600mm

And the decompression curvature,

$$\phi_{dec} = \frac{2\left(T_{pt,i} + N\right)}{E_{con}BD^2} \quad \textbf{8.103}$$

φdec = 3.4E-7, εt= 0.00272

To check the timber is not yielding,

$$\varepsilon_{y,t} = \frac{f_c}{E_{con}} > \varepsilon_t \quad \textbf{8.104}$$

εy,t=28/(.55*9000)=005657> εt=.00272

The compressive force in the timber is calculated:

$$C_t = 0.5\varepsilon_t E_{con} cD \quad \textbf{8.105}$$

Ct=218.5

Connection equilibrium check:

$$C_t = T_{pt} + N \quad \textbf{8.106}$$

Where,

$$T_{pt} = T_{pt,i} + \Delta T_{pt} = \rho_{pt} f_y A_{pt} + \varepsilon_{pt} E_{pt} A_{pt} \quad \textbf{8.107}$$

ΔT1= 43.9 kN and ΔT2= 19.9 kN

$$T_i = T_{initial} + \Delta T_i$$

T initial = 77.2 kN, Tpt1= 121.1 kN and Tpt2= 97.1 kN.

Tpt=218.2

Satisfied

Moment capacity:

$$\phi M_n = \phi M_{pt} = \phi\left[T_{pt}\left(\frac{D}{2} \pm x_{pt} - \frac{c}{3}\right) + N\left(\frac{D}{2} - \frac{c}{3}\right)\right] \quad \textbf{8.108}$$

M pt = 45.24 kN-m, φMpt = 40.72 kN-m

8.4.2 Hybrid Column

As with the walls, the main difference with the PT-only specimen is the presence of the axial dissipaters. In case of columns, two axial dissipaters were placed on each side parallel to the plane of loading, as shown in Figure 8.10.

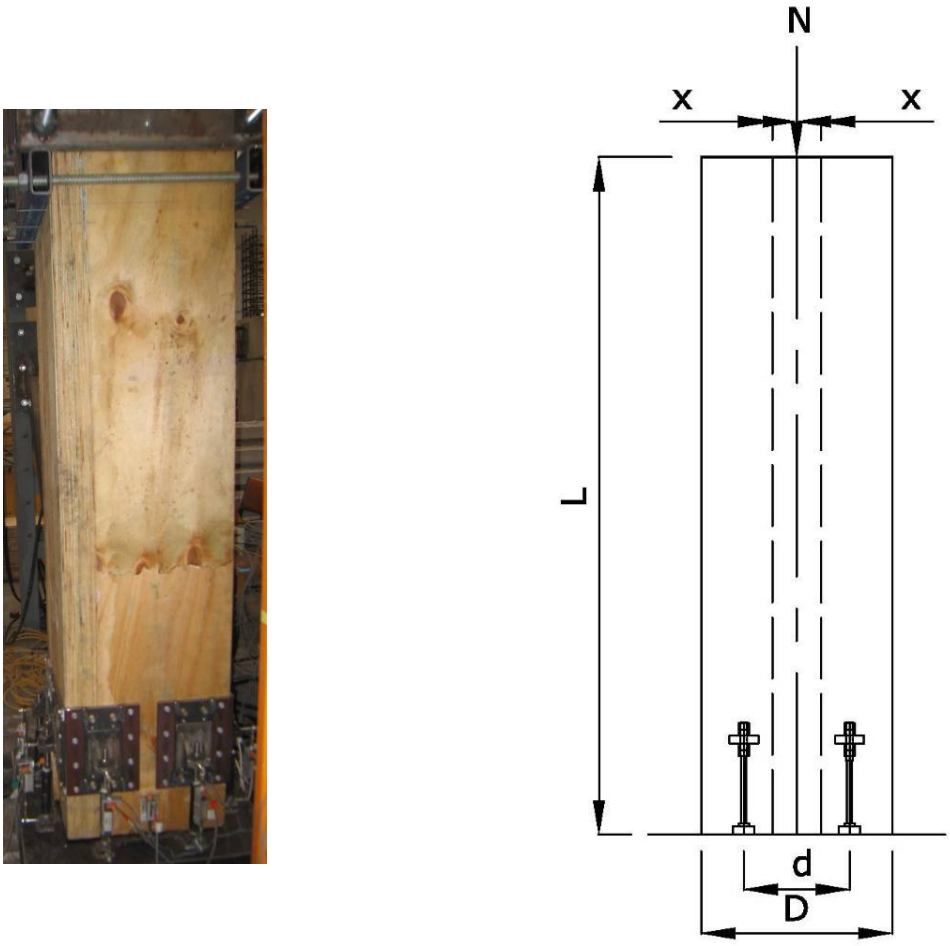

Figure 8.10 View of Hybrid column a) test specimen b) with dimensions

For connection flexural capacity of Hybrid column:

Elongation in energy dissipaters,

Tension steel:

$$\Delta_{st} = \theta_{imp}(d - c) \quad \textbf{8.109}$$

Compression steel:

$$\Delta_{sc} = \theta_{imp}(c - d') \quad \textbf{8.110}$$

Strain in the dissipater,

$$\varepsilon_{st} = \frac{\Delta_{st}}{l_{ub,d}} \quad \textbf{8.111}$$

$$\varepsilon_{sc} = \frac{\Delta_{sc}}{l_{ub,d}} \quad \textbf{8.112}$$

Yield strain of steel,

$$\varepsilon_{y,s} = \frac{f_s}{E_s} \quad \textbf{8.113}$$

To make sure the dissipater has yielded,

Tension steel:

$$\varepsilon_{st} > \varepsilon_{y,s} \quad \textbf{8.114}$$

Compression steel:

$$\varepsilon_{sc} < -\varepsilon_{y,s} \quad \textbf{8.115}$$

Connection equilibrium condition:

$$C_t = T_{pt} + N + T_s - C_s \quad \textbf{8.116}$$

Where,

$$T_{pt} = T_{pt,i} + \Delta T_{pt} = \rho_{pt} f_y A_{pt} + \varepsilon_{pt} E_{pt} A_{pt} \quad \textbf{8.117}$$

And, In tension:

$$T_s = f_y A_s \quad \textbf{8.118}$$

In compression:

$$C_s = f_y A_s \quad \textbf{8.119}$$

The moment capacity

$$\phi M_n = \phi\left(M_{pt} + M_s\right) = \phi\left[T_{pt}\left(\frac{D}{2} \pm x_{pt} - \frac{c}{3}\right) + N\left(\frac{D}{2} - \frac{c}{3}\right) + T_s\left(d - \frac{c}{3}\right) + C_s\left(\frac{c}{3} - d'\right)\right] \quad \textbf{8.120}$$

Section Analysis of Hybrid column Test Specimen:Worked Example

Elongation in energy dissipaters,

Tension steel: $\Delta_{st} = \theta_{imp}\left(d - c\right)$ **8.121**

Δstt = 5.56mm

Compression steel: $\Delta_{sc} = \theta_{imp}\left(c - d'\right)$ **8.122**

Δstc = -0.56mm

Strain in the dissipater, $\varepsilon_{st} = \frac{\Delta_{st}}{l_{ub,d}}$ **8.123**

$$\varepsilon_{sc} = \frac{\Delta_{sc}}{l_{ub,d}} \quad \textbf{8.124}$$

εst = 0.0556

εsc = -0.0056

Yield strain of steel, $$\varepsilon_{y,s} = \frac{f_s}{E_s} \quad \textbf{8.125}$$

εyst = 0.0015

εsysc = -0.0015

To make sure the dissipater has yielded,

Tension steel: $$\varepsilon_{st} > \varepsilon_{y,s} \quad \textbf{8.126}$$

Compression steel: $$\varepsilon_{sc} < -\varepsilon_{y,s} \quad \textbf{8.127}$$

Connection equilibrium condition: $C_t = T_{pt} + N + T_s - C_s$ **8.128**

Where, $$T_{pt} = T_{pt,i} + \Delta T_{pt} = \rho_{pt} f_y A_{pt} + \varepsilon_{pt} E_{pt} A_{pt} \quad \textbf{8.129}$$

Dissipater in tension: $$T_s = f_y A_s \quad \textbf{8.130}$$

Ts = 30.2 kN

Dissipater in compression: $$C_s = f_y A_s \quad \textbf{8.131}$$

Cs = -30.2 kN

The moment capacity

$$\phi M_n = \phi\left(M_{pt} + M_s\right) = \phi\left[T_{pt}\left(\frac{D}{2} \pm x_{pt} - \frac{c}{3}\right) + N\left(\frac{D}{2} - \frac{c}{3}\right) + T_s\left(d - \frac{c}{3}\right) + C_s\left(\frac{c}{3} - d'\right)\right] \quad \textbf{8.132}$$

M pt = 45.24 kN-m, Ms = 7.54 kN-m, φMpt = 40.72 kN-m, λ= 6.0

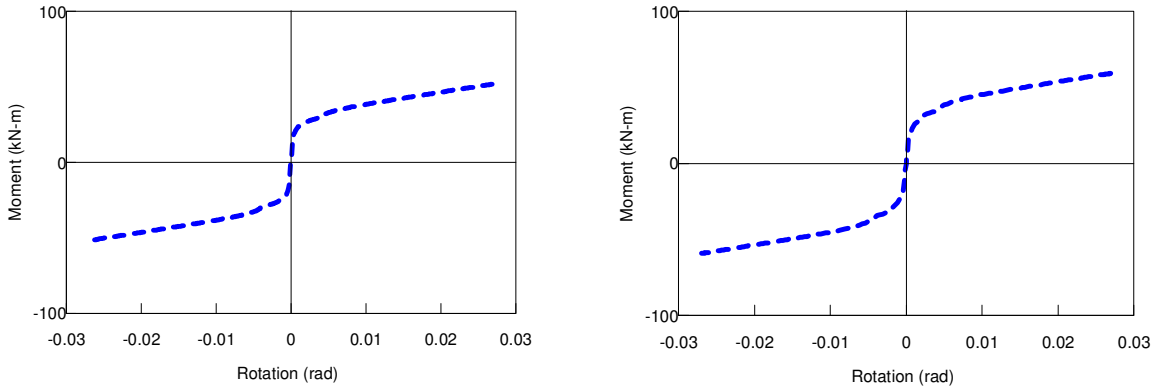

Figure 8.11 Moment-rotatio curve of PT-only and Hybrid column

8.4.3 Column with PT only under bi-directional loading

The same specimen used for uni-directional loading has been used for bi-directional loading. So the dimensions and other details remain the same.

Steps to determine connection flexural capacity:

1: A connection rotation θ_{imp} at an angle θ to the x axes imposed

Imposed connection rotations along two orthogonal directions,

$$\theta_{impx} = \theta_{imp} \sin 2\theta \cos\theta$$
$$\theta_{impy} = \theta_{imp} \sin 2\theta \sin\theta$$

2: Initial guessed neutral axes, c_x and c_y

3: From member compatibility

Elongation of the tendons,

$$\Delta_{ptx} = \theta_{impx}\left(\frac{D_x}{2} \pm x_{ptx} - c_x\right) \quad \textbf{8.133}$$

$$\Delta_{pty} = \theta_{impy}\left(\frac{D_y}{2} \pm x_{pty} - c_y\right) \quad \textbf{8.134}$$

Strain in the tendons,

$$\varepsilon_{ptx} = \frac{\Delta_{ptx}}{l_{ub}} \quad \textbf{8.135}$$

$$\varepsilon_{pty} = \frac{\Delta_{pty}}{l_{ub}} \quad \textbf{8.136}$$

Combined elongation of the tendons,

$$\Delta_{pt} = \sqrt{\Delta_{ptx}{}^2 + \Delta_{pty}{}^2} \quad \textbf{8.137}$$

To check the tendon is not yielding,

$$\varepsilon_{pt,i} + \varepsilon_{pt} \leq 0.9\varepsilon_{y,pt} \quad \textbf{8.138}$$

Where,

$$\varepsilon_{pt,i} = \frac{T_{pt,i}}{A_{pt} E_{s,pt}} \quad \textbf{8.139}$$

and $T_{pt,i} = \rho_{pt} f_{y,pt} A_{pt}$ **8.140**

$$\varepsilon_{pt} = \frac{\Delta_{pt}}{l_{ub}} \quad \textbf{8.141}$$

$$\varepsilon_{y,pt} = \frac{f_{s,pt}}{E_{s,pt}} \quad \textbf{8.142}$$

Strains in the timber from Monolithic Beam Analogy:

$$\varepsilon_{tx} = \left(3\frac{\theta_{impx}}{L_{cant}} + \phi_{dec} \right) c_x \quad \textbf{8.143}$$

$$\varepsilon_{ty} = \left(3\frac{\theta_{impy}}{L_{cant}} + \phi_{dec} \right) c_y \quad \textbf{8.144}$$

And the decompression curvature,

$$\phi_{dec} = \frac{2\left(T_{pt,i} + N\right)}{E_{con} B D^2} \quad \textbf{8.145}$$

Combined strains in timber,

$$\varepsilon_t = \sqrt{\varepsilon_{tx}{}^2 + \varepsilon_{ty}{}^2} \quad \textbf{8.146}$$

To check the timber is not yielding,

$$\varepsilon_t < \varepsilon_{y,t} \quad \textbf{8.147}$$

Where,

$$\varepsilon_{y,t} = \frac{f_c}{E_{con}} \quad \textbf{8.148}$$

4: Calculated compressive forces in the timber:

$$C_{tx} = 0.5\varepsilon_{tx} E_{con} c_x D_x \quad \textbf{8.149}$$

$$C_{ty} = 0.5\varepsilon_{yx} E_{con} c_y D_y \quad \textbf{8.150}$$

5: Connection equilibrium conditions:

$$C_{tx} = T_{ptx} + N \quad \textbf{8.151}$$

$$C_{ty} = T_{pty} + N \quad \textbf{8.152}$$

Where,

$$T_{ptx} = T_{pt,i} + \Delta T_{ptx} = \rho_{pt} f_y A_{pt} + \varepsilon_{ptx} E_{pt} A_{pt} \quad \textbf{8.153}$$

$$T_{pty} = T_{pt,i} + \Delta T_{pty} = \rho_{pt} f_y A_{pt} + \varepsilon_{pty} E_{pt} A_{pt} \quad \textbf{8.154}$$

6: Neutral axis updated and iterated

If satisfied, go to step 7, otherwise steps 2 to 5 repeated

7: The moment capacities evaluated:

$$M_{nx} = T_{ptx}\left(\frac{D_x}{2} \pm x_{ptx} - \frac{c_x}{3}\right) + N\left(\frac{D_x}{2} - \frac{c_x}{3}\right) \quad \textbf{8.155}$$

$$M_{ny} = T_{pty}\left(\frac{D_y}{2} \pm x_{pty} - \frac{c_y}{3}\right) + N\left(\frac{D_y}{2} - \frac{c_y}{3}\right) \quad \textbf{8.156}$$

Moment capacities checked:

$$M_x^* \le \phi M_{nx} \quad \textbf{8.157}$$

$$M_y^* \le \phi M_{ny} \quad \textbf{8.158}$$

8.4.4 Hybrid Column under bidirectional loading

Like the PT-only case, the same specimen has been analyzed for both uni-directional and bi-directional case. It is to be noted here that although the specimen is analyzed for bi-directional loading, there are axial dissipaters only on two sides of the column. So the properties along one direction are different from those in the other direction.

For Hybrid column:

Elongation in energy dissipaters,

Tension steel:

$$\Delta_{stx} = \theta_{impx}\left(d_x - c_x\right) \quad \textbf{8.159}$$

$$\Delta_{sty} = \theta_{impy}\left(d_y - c_y\right) \quad \textbf{8.160}$$

Compression steel:

$$\Delta_{scx} = \theta_{impx}\left(c_x - d'_x\right) \quad \textbf{8.161}$$

$$\Delta_{scy} = \theta_{impy}\left(c_y - d'_y\right) \quad \textbf{8.162}$$

Combined strains in energy dissipaters,

$$\Delta_{st} = \sqrt{\Delta_{stx}^{\ 2} + \Delta_{sty}^{\ 2}} \quad \textbf{8.163}$$

$$\Delta_{sc} = \sqrt{\Delta_{scx}{}^2 + \Delta_{scy}{}^2} \quad \textbf{8.164}$$

Strains in the dissipaters,

$$\varepsilon_{st} = \frac{\Delta_{st}}{l_{ub,d}} \quad \textbf{8.165}$$

$$\varepsilon_{sc} = \frac{\Delta_{sc}}{l_{ub,d}} \quad \textbf{8.166}$$

Yield strain of steel,

$$\varepsilon_{y,s} = \frac{f_s}{E_s} \quad \textbf{8.167}$$

To make sure the dissipater has yielded,

Tension steel:

$$\varepsilon_{st} > \varepsilon_{y,s} \quad \textbf{8.168}$$

Compression steel:

$$\varepsilon_{sc} < -\varepsilon_{y,s} \quad \textbf{8.169}$$

Combined strains in timber,

$$\varepsilon_t = \sqrt{\varepsilon_{tx}{}^2 + \varepsilon_{ty}{}^2} \quad \textbf{8.170}$$

To check the timber is not yielding,

$$\varepsilon_t < \varepsilon_{y,t} \quad \textbf{8.171}$$

Where,

$$\varepsilon_{y,t} = \frac{f_c}{E_{con,b}} \quad \textbf{8.172}$$

Compressive forces in the timber:

$$C_{tx} = 0.5\varepsilon_{tx} E_{con,b} c_x D_x \quad \textbf{8.173}$$

$$C_{ty} = 0.5\varepsilon_{yx} E_{con,b} c_y D_y \quad \textbf{8.174}$$

Connection equilibrium conditions:

$$C_{tx} = T_{ptx} + T_s - C_s + N \quad \textbf{8.175}$$

$$C_{ty} = T_{pt} + T_s - C_s + N \quad \textbf{8.176}$$

Where,

$$T_{ptx} = T_{pt,i} + \Delta T_{ptx} = \rho_{pt} f_y A_{pt} + \varepsilon_{ptx} E_{pt} A_{pt} \quad \textbf{8.177}$$

$$T_{pty} = T_{pt,i} + \Delta T_{pty} = \rho_{pt} f_y A_{pt} + \varepsilon_{pty} E_{pt} A_{pt} \quad \textbf{8.178}$$

And,

Forces in dissipaters in tension:

$$T_s = f_y A_s \quad \textbf{8.179}$$

Forces in dissipaters in compression:

$$C_s = f_y A_s \quad \textbf{8.180}$$

The moment capacities,

$$M_{ptx} = T_{ptx}\left(\frac{D_x}{2} \pm x_{ptx} - \frac{c_x}{3}\right) + N\left(\frac{D_x}{2} - \frac{c_x}{3}\right) \quad \textbf{8.181}$$

$$M_{pty} = T_{pty}\left(\frac{D_y}{2} \pm x_{pty} - \frac{c_y}{3}\right) + N\left(\frac{D_y}{2} - \frac{c_y}{3}\right) \quad \textbf{8.182}$$

$$M_{sx} = T_s\left(d_x - \frac{c_x}{3}\right) + C_s\left(\frac{c_x}{3} - d'_x\right) = T_s\left(d_x - d'_x\right) = C_s\left(d_x - d'_x\right) \quad \textbf{8.183}$$

$$M_{sy} = T_s\left(d_y - \frac{c_y}{3}\right) + C_s\left(\frac{c_y}{3} - d'_y\right) = T_s\left(d_y - d'_y\right) = C_s\left(d_y - d'_y\right) \quad \textbf{8.184}$$

$$\phi M_{nx} = \phi\left(M_{ptx} + M_{sx}\right) \quad \textbf{8.185}$$

$$\phi M_{ny} = \phi\left(M_{pty} + M_{sy}\right) \quad \textbf{8.186}$$

The re-centering ratios,

$$\lambda_x = \frac{M_{ptx}}{M_{sx}} \quad \textbf{8.187}$$

$$\lambda_y = \frac{M_{pty}}{M_{sy}} \quad \textbf{8.188}$$

8.5 Section Analysis of Beam-Column Joint

A number of beam-column joint specimens were tested during the experimental investigation, as mentioned in chapter 4. The two basic types were the PT-only and Hybrid specimens with axial dissipaters. Other specimens are different only in terms of the connection interface and/or joint region.

8.5.1 B-C Joint with PT only

The details of the typical exterior beam-column joint are shown in Figure 8.12. It includes steel armouring plates at the interface between the beam and the column.

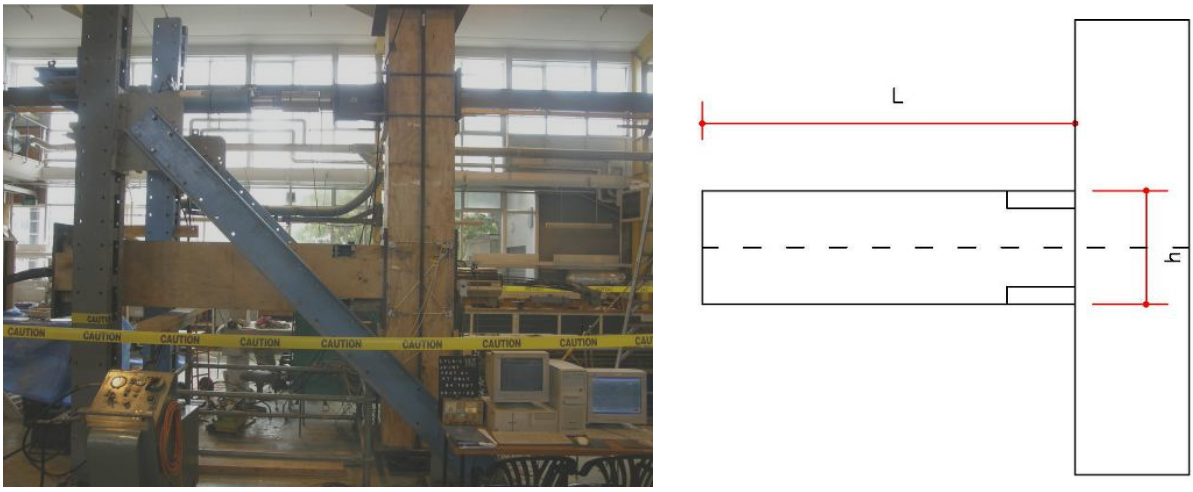

Figure 8.12 View of PT-only beam-column joint a) test specimen b) with dimensions

Steps to determine connection flexural capacity:

1: Connection rotation, θ_{imp} imposed

2: Neutral axis depth c guessed

3: Member compatibility applied:

Elongation of the tendon,

$$\Delta_{pt} = \theta_{imp}\left(\frac{h}{2} - c\right) \quad \textbf{8.189}$$

Strain in the tendon,

$$\varepsilon_{pt} = \frac{n\Delta_{pt}}{l_{ub}} \quad \textbf{8.190}$$

To check the tendon is not yielding,

$$\varepsilon_{pt,i} + \varepsilon_{pt} \leq 0.9\varepsilon_{y} \quad \textbf{8.191}$$

Where,

$$\varepsilon_{pt,i} = \frac{T_{pt,i}}{A_{pt}E_{s}} \quad \textbf{8.192}$$

And

$$T_{pt,i} = \rho_{pt} f_{y} A_{pt} \quad \textbf{8.193}$$

Strain in the timber from Monolithic Beam Analogy:

$$\varepsilon_{t} = \left(3\frac{\theta_{imp}}{L_{cant}} + \phi_{dec}\right)c \quad \textbf{8.194}$$

Where, the shear span,

$$L_{cant} = (L_{bay} - h_c)/2 \quad \textbf{8.195}$$

And the decompression curvature,

$$\phi_{dec} = \frac{2T_{pt,i}}{E_{con} b h^2} \quad \textbf{8.196}$$

To check the timber is not yielding,

$$\varepsilon_{y,t} = \frac{f_c}{E_{con}} > \varepsilon_t \quad \textbf{8.197}$$

4: The compressive force in the timber

$$C_t = 0.5 \varepsilon_t E_{con} c b \quad \textbf{8.198}$$

5: Connection equilibrium checked:

$$C_t = T_{pt} \quad \textbf{8.199}$$

Where,

$$T_{pt} = T_{pt,is} + \Delta T_{pt} = \rho_{pt} f_y A_{pt} + \varepsilon_{pt} E_{pt} A_{pt} \quad \textbf{8.200}$$

If satisfied, step 7 is follwed, otherwise steps 1 to 5 repeated

6: Neutral axis updated and iterated

7: Moment capacity evaluated:

$$\phi M_n = \phi(M_{pt}) = \phi\left[T_{pt}\left(\frac{h}{2} - \frac{c}{3}\right)\right] \quad \textbf{8.201}$$

Moment capacity check:

$$M^* \leq \phi M_n \quad \textbf{8.202}$$

Section Analysis of B-C Joint with PT onlyTest Specimen: Worked Example

The details of the typical exterior beam-column joint are shown in Figure 8.12. It includes steel armouring plates at the interface between the beam and the column.

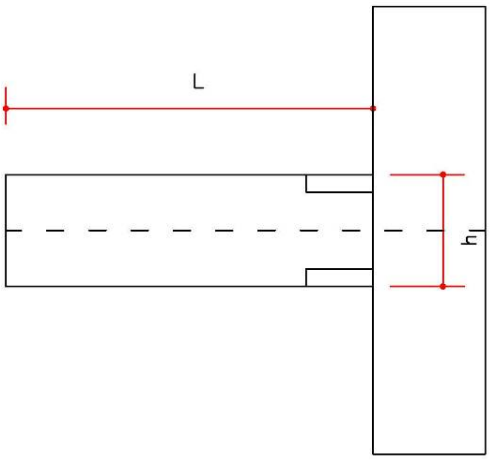

Figure 8.13 View of PT-only beam-column joint a) test specimen b) with dimensions

Steps to determine connection flexural capacity:

Connection rotation, θ_{imp} imposed drift, θ=2%

Neutral axis depth c (through trial)
c= 0.287h=173mm

Member compatibility applied:

Elongation of the tendon,

$$\Delta_{pt} = \theta_{imp}\left(\frac{h}{2} - c\right) \quad \textbf{8.203}$$

Strain in the tendon,

$$\varepsilon_{pt} = \frac{n\Delta_{pt}}{l_{ub}} \quad \textbf{8.204}$$

Δpt =2.55mm

To check the tendon is not yielding,

$$\varepsilon_{pt,i} + \varepsilon_{pt} \le 0.9\varepsilon_{y} \quad \textbf{8.205}$$

Where,

$$\varepsilon_{pt,i} = \frac{T_{pt,i}}{A_{pt}E_{s}} \quad \textbf{8.206}$$

And

$$T_{pt,i} = \rho_{pt} f_{y} A_{pt} \quad \textbf{8.207}$$

εpt = 0.00081

εs =0.0047

εpt + εs < 0.9εs =0.007

Strain in the timber from Monolithic Beam Analogy:

$$\varepsilon_t = \left(3\frac{\theta_{imp}}{L_{cant}} + \phi_{dec} \right) c \qquad \textbf{8.208}$$

Where, the shear span,

$$L_{cant} = (L_{bay} - h_c)/2 \qquad \textbf{8.209}$$

Lcant = 2700mm

And the decompression curvature,

$$\phi_{dec} = \frac{2T_{pt,i}}{E_{con} b h^2} \qquad \textbf{8.210}$$

φdec = 1.7E-6, εt= 0.004128

To check the timber is not yielding,

$$\varepsilon_{y,t} = \frac{f_c}{E_{con}} > \varepsilon_t \qquad \textbf{8.211}$$

εy,t=45/(.55*13200)=006198>.004128

The compressive force in the timber

$$C_t = 0.5\varepsilon_t E_{con} c b \qquad \textbf{8.212}$$

Ct=1304.1

Connection equilibrium check:

$$C_t = T_{pt} \qquad \textbf{8.213}$$

Where,

$$T_{pt} = T_{pt,is} + \Delta T_{pt} = \rho_{pt} f_y A_{pt} + \varepsilon_{pt} E_{pt} A_{pt} \qquad \textbf{8.214}$$

ΔT= 192.1 kN

$$T_i = T_{initial} + \Delta T_i$$

T initial = 1112 kN, Tpt= 1304.1 kN

Satisfied

Moment capacity:

$$\phi M_n = \phi(M_{pt}) = \phi\left[T_{pt}\left(\frac{h}{2} - \frac{c}{3}\right)\right] \quad \textbf{8.215}$$

M pt = 316.17 kN-m, φMpt = 284.55 kN-m

8.5.2 Hybrid Beam-Column Joint

As was the case with walls and column, the Hybrid specimen is different from the PT-only specimen because it includes axial energy dissipaters. The exterior hybrid beam-column joint had two 22mm diameter axial dissipaters at each face of the joint, in vertical planes parallel to the plane of loading as shown in Figure 8.14.

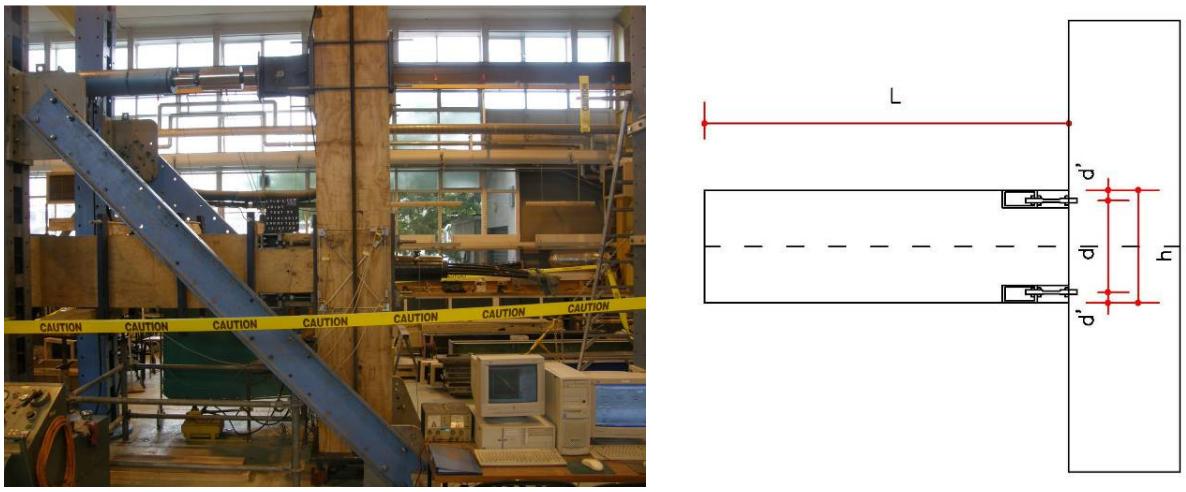

Figure 8.14 View of Hybrid beam-column joint a) test specimen b) with dimensions

For Hybrid beam-column joint:

Elongations in energy dissipater,

Tension steel:

$$\Delta_{st} = \theta_{imp}(d - c) \quad \textbf{8.216}$$

Compression steel:

$$\Delta_{sc} = \theta_{imp}(c - d') \quad \textbf{8.217}$$

Strain in the dissipaters,

$$\varepsilon_{st} = \frac{\Delta_{st}}{l_{ub,d}} \quad \textbf{8.218}$$

$$\varepsilon_{sc} = \frac{\Delta_{sc}}{l_{ub,d}}$$

Yield strain of steel,

$$\varepsilon_{y,s} = \frac{f_s}{E_s} \quad \textbf{8.219}$$

To make sure the dissipater has yielded,

Tension steel:

$$\varepsilon_{st} > \varepsilon_{y,s} \quad \textbf{8.220}$$

Compression steel:

$$\varepsilon_{sc} < -\varepsilon_{y,s} \quad \textbf{8.221}$$

Connection equilibrium conditions:

$$C_t = T_{pt} + T_s - C_s \quad \textbf{8.222}$$

Where,

$$T_{pt} = T_{pt,is} + \Delta T_{pt} = 0.5 f_y A_{pt} + \varepsilon_{pt} E_{pt} A_{pt} \quad \textbf{8.223}$$

And,

In tension:

$$T_s = f_y A_s \quad \textbf{8.224}$$

In compression:

$$C_s = f_y A_s \quad \textbf{8.225}$$

Moment capacity,

$$\phi M_n = \phi\left(M_{pt} + M_s\right) = \phi\left[T_{pt}\left(\frac{h}{2} - \frac{c}{3}\right) + T_s\left(d - \frac{c}{3}\right) + C_s\left(\frac{c}{3} - d'\right)\right] \quad \textbf{8.226}$$

Moment capacity check:

$$M^* \le \phi M_n \quad \textbf{8.227}$$

The re-centering ratio,

$$\lambda = \frac{M_{pt}}{M_s} \quad \textbf{8.228}$$

Section Analysis of Hybrid B-C Joint Test Specimen: Worked Example

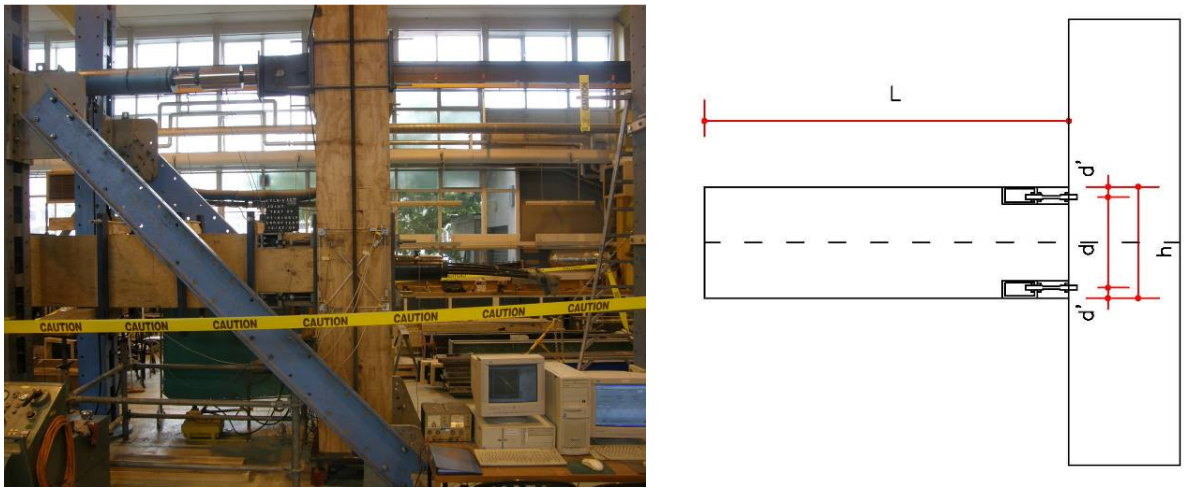

Figure 8.15 View of Hybrid beam-column joint a) test specimen b) with dimensions

Steps to determine connection flexural capacity:

Connection rotation, θ_{imp} imposed

drift, θ=2%

Neutral axis depth c (through trial)

c= 0.287h=172mm

Member compatibility applied:

Elongation of the tendon,

$$\Delta_{pt} = \theta_{imp}\left(\frac{h}{2} - c\right) \qquad \textbf{8.229}$$

Strain in the tendon,

$$\varepsilon_{pt} = \frac{n\Delta_{pt}}{l_{ub}} \quad \textbf{8.230}$$

Δpt =2.56mm

To check the tendon is not yielding,

$$\varepsilon_{pt,i} + \varepsilon_{pt} \leq 0.9\varepsilon_{y} \quad \textbf{8.231}$$

Where,

$$\varepsilon_{pt,i} = \frac{T_{pt,i}}{A_{pt}E_{s}} \quad \textbf{8.232}$$

$$T_{pt,i} = \rho_{pt} f_{y} A_{pt} \quad \textbf{8.233}$$

εpt = 0.00077

εs =0.0047

εpt + εs < 0.9εs =0.007

Elongations in energy dissipater,

Tension steel:

$$\Delta_{st} = \theta_{imp}(d - c) \quad \textbf{8.234}$$

Δst= 7.06mm

Compression steel:

$$\Delta_{sc} = \theta_{imp}(c - d') \quad \textbf{8.235}$$

Δsc= 1.94mm

Strain in the dissipaters,

$$\varepsilon_{st} = \frac{\Delta_{st}}{l_{ub,d}} \quad \textbf{8.236}$$

$$\varepsilon_{sc} = \frac{\Delta_{sc}}{l_{ub,d}}$$

εst=0.064

εsc=-0.017

Yield strain of steel,

$$\varepsilon_{y,s} = \frac{f_s}{E_s} \quad \textbf{8.237}$$

εs=-0.0015

To make sure the dissipater has yielded,

Tension steel:

$$\varepsilon_{st} > \varepsilon_{y,s} \quad \textbf{8.238}$$

Compression steel:

$$\varepsilon_{sc} < -\varepsilon_{y,s} \quad \textbf{8.239}$$

Strain in the timber from Monolithic Beam Analogy:

$$\varepsilon_t = \left(3\frac{\theta_{imp}}{L_{cant}} + \phi_{dec} \right) c \quad \textbf{8.240}$$

Where, the shear span,

$$L_{cant} = (L_{bay} - h_c)/2 \quad \textbf{8.241}$$

Lcant = 2700mm

And the decompression curvature,

$$\phi_{dec} = \frac{2T_{pt,i}}{E_{con} b h^2} \quad \textbf{8.242}$$

φdec = 1.7E-6, εt= 0.004117

To check the timber is not yielding,

$$\varepsilon_{y,t} = \frac{f_c}{E_{con}} > \varepsilon_t \quad \textbf{8.243}$$

εy,t=45/(.55*13200)=006198>.004117

The compressive force in the timber

$$C_t = 0.5 \varepsilon_t E_{con} c b \quad \textbf{8.244}$$

Ct=1296.7

$$T_{pt} = T_{pt,is} + \Delta T_{pt} = 0.5 f_y A_{pt} + \varepsilon_{pt} E_{pt} A_{pt} \quad \textbf{8.245}$$

Tpti= 1112 kN, ΔTpt= 184.1 kN, Tpt= 1296.1 kN

In tension:

$$T_s = f_y A_s \quad \textbf{8.246}$$

Ts= 456.2 kN

In compression:

$$C_s = f_y A_s \quad \textbf{8.247}$$

Cs= 456.2 kN

Connection equilibrium conditions:

$$C_t = T_{pt} + T_s - C_s \quad \textbf{8.248}$$

Satisfied

Moment capacity,

$$\phi M_n = \phi\left(M_{pt} + M_s\right) = \phi\left[T_{pt}\left(\frac{h}{2} - \frac{c}{3}\right) + T_s\left(d - \frac{c}{3}\right) + C_s\left(\frac{c}{3} - d'\right)\right] \qquad \textbf{8.249}$$

Mpt= 314.44 kN-m, Ms= 205.27 kN-m, φMn= 467.74 kN-m

The re-centering ratio, λ= 1.53

8.5.3 Hybrid Beam-Column Joint with steel plate armouring and screw reinforcements

The procedure to calculate ultimate moment capacities of beam-column joints (both PT-only and Hybrid) with steel armouring and/or reinforcements in the joint region would be basically the same as that for the unarmoured and unreinforced joints. The only difference would be in the elastic modulus of timber at the connection interface. As explained in chapter 5, the elastic modulus for armoured joints should be the same as that for walls or column, depending on the type of LVL the beam is made of. Reinforced joints, on the other hand, should have the same modulus as the unreinforced joints, for both armoured and unarmoured cases, since the reinforcements inside the joint region has no significant effect on the stiffness of the interface.

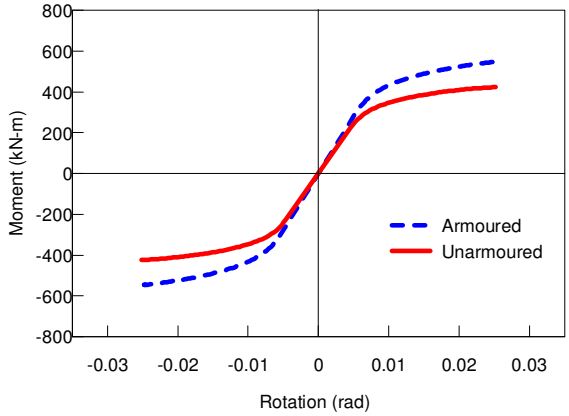

Figure 8.16 Moment-rotation comparison of armoured and unarmoured reinforced joint

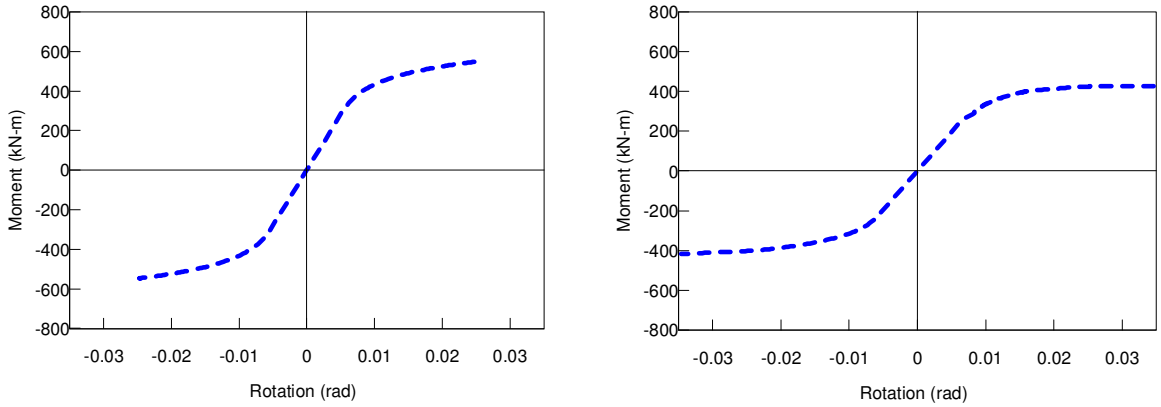

Figure 8.17 Moment rotation of armoured reinforcedand unarmoured unreinforced joint

8.6 Moment Capacities of Generalized Subassemblies

The procedure for calculation of moment capacities of the subassemblies used in the experimental investigations has been shown in the last chapter. In this chapter the procedure is applied to subassemblies with configurations different from the tested specimens. The calculation scheme is essentially the same but the geometry and arrangements of the subassemblies are slightly different. With these modified arrangements, the three types of subassemblies are shown to have the same basic characteristics. They are classified in a single group and a general procedure applicable to all subassemblies of that group is developed.

8.7 Moment Capacity of Generalized Pt-only Subassembly

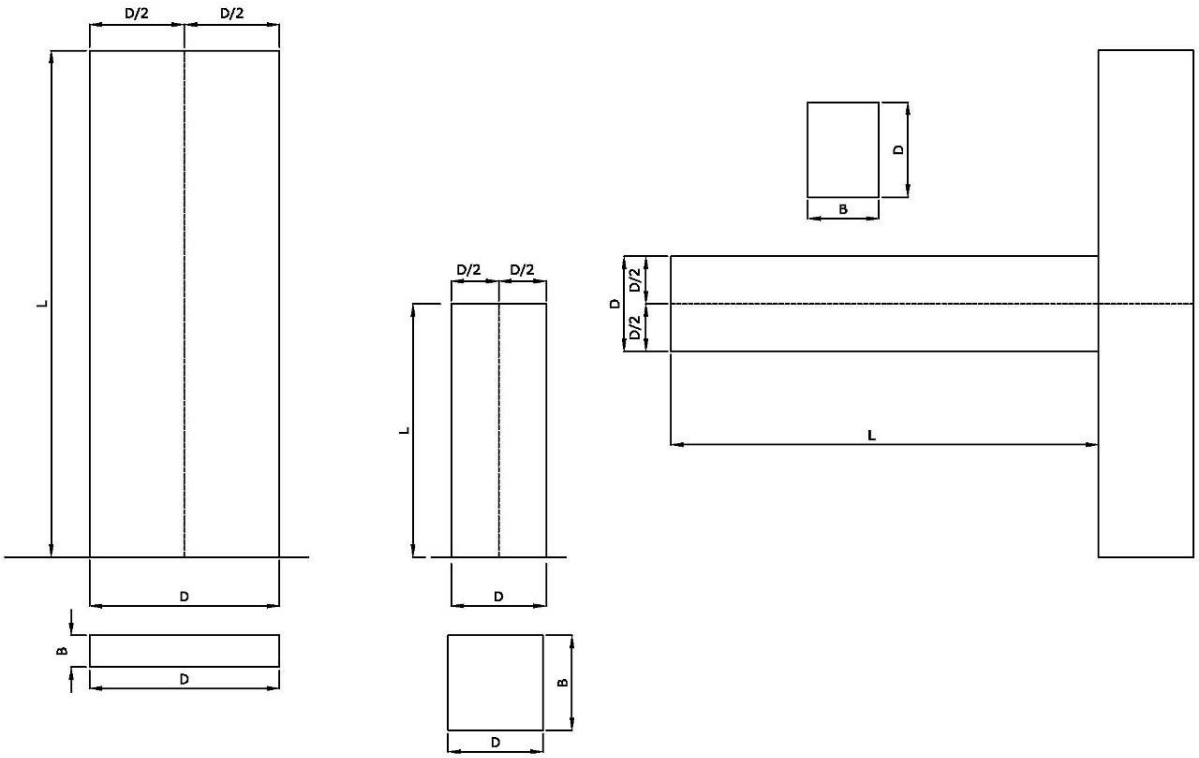

Figure 8.18 Configurations of the group of PT-only subassemblies

Steps to determine connection flexural capacity:

1: A connection rotation, θ_{imp} imposed

2: Neutral axis, c guessed

3: Member compatibility applied

Elongation of the tendon,

$$\Delta_{pti} = \theta_{imp}\left(\frac{D}{2} - c\right) \qquad \textbf{8.250}$$

Strain in the tendon,

$$\varepsilon_{pt} = \frac{n\Delta_{pt}}{l_{ub}} \qquad \textbf{8.251}$$

To check the tendon is not yielding,

$$\varepsilon_{pt,i} + \varepsilon_{pt} \le 0.9\varepsilon_{y,pt} \qquad \textbf{8.252}$$

Where,

$$\varepsilon_{y,pt} = \frac{f_{s,pt}}{E_{s,pt}} \quad \textbf{8.253}$$

$$\varepsilon_{pt,i} = \frac{T_{pt,i}}{A_{pt} E_{s,pt}} \quad \textbf{8.254}$$

And

$$T_{pt,i} = \rho_{pt} f_{y,pt} A_{pt} \quad \textbf{8.255}$$

Strain in the timber from Monolithic Beam Analogy:

$$\varepsilon_t = \left(3\frac{\theta_{imp}}{L_{cant}} + \phi_{dec} \right) c \quad \textbf{8.256}$$

And the decompression curvature,

$$\phi_{dec} = \frac{2\left(T_{pt,i} + N\right)}{E_{con} B D^2} \quad \textbf{8.257}$$

To check the timber is not yielding,

$$\varepsilon_{y,t} = \frac{f_c}{E_{con}} > \varepsilon_t \quad \textbf{8.258}$$

4: The compressive force in the timber

$$C_t = 0.5 \varepsilon_t E_{con} c D \quad \textbf{8.259}$$

5: Connection equilibrium condition is checked:

$$C_t = T_{pt} + N \quad \textbf{8.260}$$

Where,

$$T_{pt} = T_{pt,i} + \Delta T_{pt} = \rho_{pt} f_y A_{pt} + \varepsilon_{pt} E_{pt} A_{pt} \quad \textbf{8.261}$$

6: Neutral axis updated and iterated

If satisfied, step 7 followed, otherwise steps 2 to 5 repeated

7: The moment capacity evaluated:

$$\phi M_n = \phi M_{pt} = \phi \left[T_{pt} \left(\frac{D}{2} - \frac{c}{3} \right) + N \left(\frac{D}{2} - \frac{c}{3} \right) \right] \quad \textbf{8.262}$$

The moment capacity is checked,

$$M^* \leq \phi M_n \quad \textbf{8.263}$$

8.8 Moment Capacity of Generalized Hybrid Subassembly

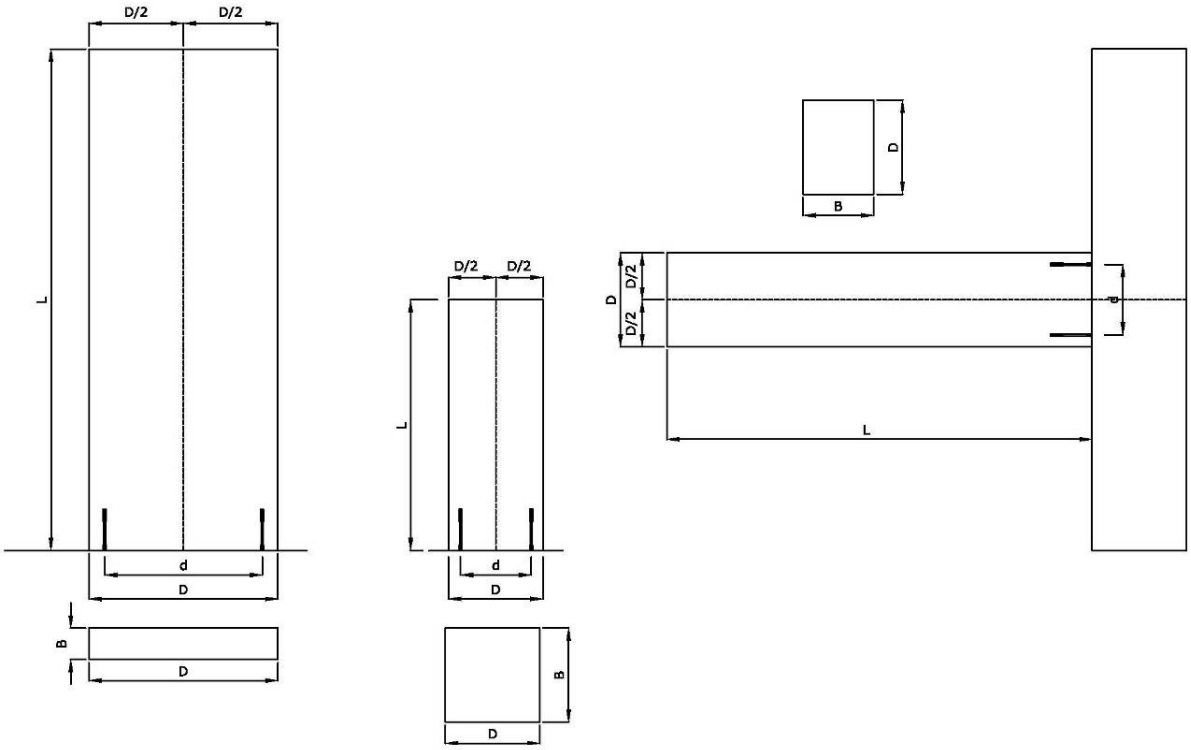

Figure 8.19 Configurations of the group of Hybrid subassemblies

For flexural capacity of Hybrid specimen:

Elongation in energy dissipater,

Tension steel:

$$\Delta_{st} = \theta_{imp}(d - c) \qquad \textbf{8.264}$$

Compression steel:

$$\Delta_{sc} = \theta_{imp}(c - d') \qquad \textbf{8.265}$$

Strain in the dissipater,

$$\varepsilon_{st} = \frac{\Delta_{st}}{l_{ub,d}} \qquad \textbf{8.266}$$

$$\varepsilon_{sc} = \frac{\Delta_{sc}}{l_{ub,d}} \qquad \textbf{8.267}$$

Yield strain of steel,

$$\varepsilon_{y,s} = \frac{f_s}{E_s} \qquad \textbf{8.268}$$

To make sure the dissipater has yielded,

Tension steel:

$$\varepsilon_{st} > \varepsilon_{y,s} \quad \textbf{8.269}$$

Compression steel:

$$\varepsilon_{sc} < -\varepsilon_{y,s} \quad \textbf{8.270}$$

Connection equilibrium condition:

$$C_t = T_{pt} + T_s - C_s + N \quad \textbf{8.271}$$

Where,

$$T_{pt} = T_{pt,i} + \Delta T_{pt} = \rho_{pt} f_y A_{pt} + \varepsilon_{pt} E_{pt} A_{pt} \quad \textbf{8.272}$$

And,

In tension:

$$T_s = f_y A_s \quad \textbf{8.273}$$

In compression:

$$C_s = f_y A_s \quad \textbf{8.274}$$

The moment capacity

$$\phi M_n = \phi\left(M_{pt} + M_s\right) = \phi\left[T_{pt}\left(\frac{D}{2} - \frac{c}{3}\right) + N\left(\frac{D}{2} - \frac{c}{3}\right) + T_s\left(d - \frac{c}{3}\right) + C_s\left(\frac{c}{3} - d'\right)\right] \quad \textbf{8.275}$$

8.9 Moment Capacities of Hybrid coupled walls with UFP dissipaters

The single tendon arrangement of the PY-only walls is also used for walls with UFP. The rest of the arrangement remains the same as the test specimens, as shown in Figure 8.20.

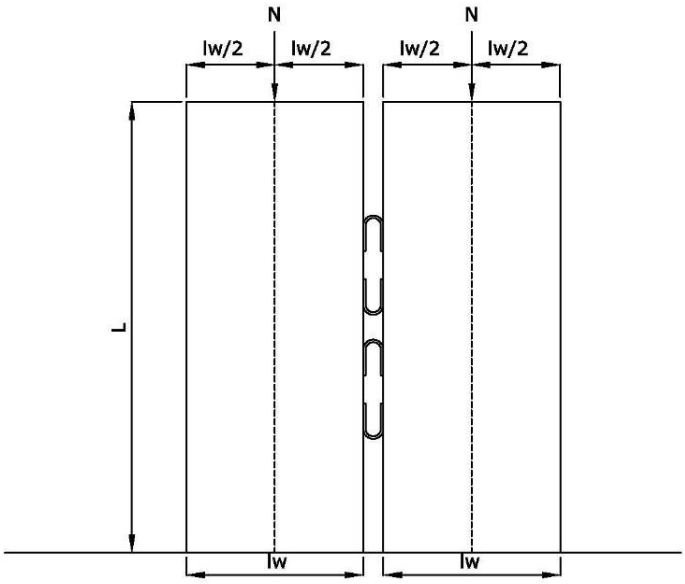

Figure 8.20 Configuration of coupled walls with single tendon

Steps to determine connection flexural capacity:

UFP force contributions:

$$V_s = n * 0.5 \frac{bt^2}{D} F_y \quad \textbf{8.276}$$

Recalculated wall axial forces:

$$N_1 = N - V_s \quad \textbf{8.277}$$

$$N_2 = N + V_s \quad \textbf{8.278}$$

Neutral axis updated with N1 and N2 for wall1 and wall2 separately, then iteration done

Connection equilibrium conditions:

$$C_{t1} = T_{pt1} + N_1 \quad \textbf{8.279}$$

$$C_{t2} = T_{pt2} + N_2 \quad \textbf{8.280}$$

Where,

$$T_{pt} = T_{pt,i} + \Delta T_{pt} = \rho_{pt} f_y A_{pt} + \varepsilon_{pt} E_{pt} A_{pt} \quad \textbf{8.281}$$

Moment capacities:

$$M_{pt1} = T_{pt1}\left(\frac{l_w}{2} - \frac{c_1}{3}\right) + N_1\left(\frac{l_w}{2} - \frac{c_1}{3}\right) = \left(T_{pt1} + N_1\right)\left(\frac{l_w}{2} - \frac{c_1}{3}\right) \quad \textbf{8.282}$$

$$M_{pt2} = T_{pt2}\left(\frac{l_w}{2} - \frac{c_2}{3}\right) + N_2\left(\frac{l_w}{2} - \frac{c_2}{3}\right) = \left(T_{pt2} + N_2\right)\left(\frac{l_w}{2} - \frac{c_2}{3}\right) \quad \textbf{8.283}$$

$$M_{pt} = M_{pt1} + M_{pt2} \quad \textbf{8.284}$$

$$M_{pt} = \left(T_{pt1} + N_1\right)\left(\frac{l_w}{2} - \frac{c_1}{3}\right) + \left(T_{pt2} + N_2\right)\left(\frac{l_w}{2} - \frac{c_2}{3}\right) \quad \textbf{8.285}$$

$$M_s = M_{s1} + M_{s2} = V_s\left(\frac{c_1}{3}\right) + V_s\left(l_w - \frac{c_2}{3}\right) = V_s\left(l_w + \frac{c_1 - c_2}{3}\right) \quad \textbf{8.286}$$

$$\phi M_n = \phi\left(M_{pt} + M_s\right) \quad \textbf{8.287}$$

8.10 Moment Capacity of Generalized PT-only Subassembly under Bidirectional Loading

Steps to determine connection flexural capacity:

1: Impose a connection rotation θ imp at an angleθ to the x axes

Impose connection rotations along two orthogonal directions, θ_{impx} and θ_{impy}

$$\theta_{impx} = \theta_{imp} \sin 2\theta \cos\theta \quad \textbf{8.288}$$

$$\theta_{impy} = \theta_{imp} \sin 2\theta \sin\theta \quad \textbf{8.289}$$

2: Guess neutral axes, c_x and c_y

3: Apply member compatibility

Elongation of the tendons,

$$\Delta_{ptx} = \theta_{impx}\left(\frac{D_x}{2} - c_x\right) \quad \textbf{8.290}$$

$$\Delta_{pty} = \theta_{impy}\left(\frac{D_y}{2} - c_y\right) \quad \textbf{8.291}$$

Strain in the tendons,

$$\varepsilon_{ptx} = \frac{\Delta_{ptx}}{l_{ub}} \quad \textbf{8.292}$$

$$\varepsilon_{pty} = \frac{\Delta_{pty}}{l_{ub}} \quad \textbf{8.293}$$

The combined elongation of the tendon along two orthogonal directions along the tendon length,

$$\Delta_{pt} = \sqrt{\Delta_{ptx}{}^2 + \Delta_{pty}{}^2} \quad \textbf{8.294}$$

To check the tendon is not yielding,

$$\varepsilon_{pt,i} + \varepsilon_{pt} \le 0.9\varepsilon_{y,pt} \quad \textbf{8.295}$$

Where,

$$\varepsilon_{pt,i} = \frac{T_{pt,i}}{A_{pt}E_{s,pt}} \quad \textbf{8.296}$$

$$\text{and } T_{pt,i} = \rho_{pt} f_{y,pt} A_{pt} \quad \textbf{8.297}$$

$$\varepsilon_{pt} = \frac{\Delta_{pt}}{l_{ub}} \quad \textbf{8.298}$$

$$\varepsilon_{y,pt} = \frac{f_{s,pt}}{E_{s,pt}} \quad \textbf{8.299}$$

Strains in the timber from Monolithic Beam Analogy:

$$\varepsilon_{tx} = \left(3\frac{\theta_{impx}}{L_{cant}} + \phi_{dec}\right)c_x \quad \textbf{8.300}$$

$$\varepsilon_{ty} = \left(3\frac{\theta_{impy}}{L_{cant}} + \phi_{dec}\right)c_y \quad \textbf{8.301}$$

And the decompression curvature,

$$\phi_{dec} = \frac{2\left(T_{pt,i} + N\right)}{E_{con}BD^2} \quad \textbf{8.302}$$

Combined strains in energy dissipaters,

$$\varepsilon_t = \sqrt{\varepsilon_{tx}{}^2 + \varepsilon_{ty}{}^2} \quad \textbf{8.303}$$

To check the timber is not yielding,

$$\varepsilon_t < \varepsilon_{y,t} \quad \textbf{8.304}$$

Where,

$$\varepsilon_{y,t} = \frac{f_c}{E_{con}} \quad \textbf{8.305}$$

4: Calculate the compressive forces in the timber

$$C_{tx} = 0.5\varepsilon_{tx}E_{con}c_xD_x \quad \textbf{8.306}$$

$$C_{ty} = 0.5\varepsilon_{yx}E_{con}c_yD_y \quad \textbf{8.307}$$

5: Check connection equilibrium:

$$C_{tx} = T_{ptx} + N \quad \textbf{8.308}$$

$$C_{ty} = T_{pty} + N \quad \textbf{8.309}$$

Where,

$$T_{ptx} = T_{pt,i} + \Delta T_{ptx} = \rho_{pt} f_y A_{pt} + \varepsilon_{ptx} E_{pt} A_{pt} \quad \textbf{8.310}$$

$$T_{pty} = T_{pt,i} + \Delta T_{pty} = \rho_{pt} f_y A_{pt} + \varepsilon_{pty} E_{pt} A_{pt} \quad \textbf{8.311}$$

6: Update neutral axis and iterate

If ok, go to step 7, otherwise repeat steps 2 to 5

7: Evaluate the moment capacities,

$$M_{nx} = T_{ptx}\left(\frac{D_x}{2} - \frac{c_x}{3}\right) + N\left(\frac{D_x}{2} - \frac{c_x}{3}\right) \quad \textbf{8.312}$$

$$M_{ny} = T_{pty}\left(\frac{D_y}{2} - \frac{c_y}{3}\right) + N\left(\frac{D_y}{2} - \frac{c_y}{3}\right) \quad \textbf{8.313}$$

Check the moment capacities,

$$M_x{}^* \le \phi M_{xn} \quad \textbf{8.314}$$

$$M_y{}^* \le \phi M_{yn} \quad \textbf{8.315}$$

The re-centering ratios,

$$\lambda_x = \frac{M_{ptx}}{M_{sx}} \quad \textbf{8.316}$$

$$\lambda_y = \frac{M_{pty}}{M_{sy}} \quad \textbf{8.317}$$

8.11 Moment Capacity of Generalized Hybrid Subassembly under Bidirectional Loading

In case of Hybrid connection:

Elongation in energy dissipaters,

Tension steel:

$$\Delta_{stx} = \theta_{impx}\left(d_x - c_x\right) \quad \textbf{8.318}$$

$$\Delta_{sty} = \theta_{impy}\left(d_y - c_y\right) \quad \textbf{8.319}$$

Compression steel:

$$\Delta_{scx} = \theta_{impx}\left(c_x - d'_x\right) \quad \textbf{8.320}$$

$$\Delta_{scy} = \theta_{impy}\left(c_y - d'_y\right) \quad \textbf{8.321}$$

Combined strains in energy dissipaters,

$$\Delta_{st} = \sqrt{\Delta_{stx}{}^2 + \Delta_{sty}{}^2} \quad \textbf{8.322}$$

$$\Delta_{sc} = \sqrt{\Delta_{scx}{}^2 + \Delta_{scy}{}^2} \quad \textbf{8.323}$$

Strains in the dissipaters,

$$\varepsilon_{st} = \frac{\Delta_{st}}{l_{ub,d}} \quad \textbf{8.324}$$

$$\varepsilon_{sc} = \frac{\Delta_{sc}}{l_{ub,d}} \quad \textbf{8.325}$$

Yield strain of steel,

$$\varepsilon_{y,s} = \frac{f_s}{E_s} \quad \textbf{8.326}$$

To make sure the dissipater has yielded,

Tension steel:

$$\varepsilon_{st} > \varepsilon_{y,s} \quad \textbf{8.327}$$

Compression steel:

$$\varepsilon_{sc} < -\varepsilon_{y,s} \quad \textbf{8.328}$$

Connection equilibrium condition:

$$C_{tx} = T_{ptx} + T_s - C_s + N \quad \textbf{8.329}$$

$$C_{ty} = T_{pt} + T_s - C_s + N \quad \textbf{8.330}$$

Where,

$$T_{ptx} = T_{pt,i} + \Delta T_{ptx} = \rho_{pt} f_y A_{pt} + \varepsilon_{ptx} E_{pt} A_{pt} \quad \textbf{8.331}$$

$$T_{pty} = T_{pt,i} + \Delta T_{pty} = \rho_{pt} f_y A_{pt} + \varepsilon_{pty} E_{pt} A_{pt} \quad \textbf{8.332}$$

And,

Forces in dissipaters in tension:

$$T_s = f_y A_s \quad \textbf{8.333}$$

Forces in dissipaters in compression:

$$C_s = f_y A_s \quad \textbf{8.334}$$

Moment capacities,

$$M_{ptx} = T_{ptx}\left(\frac{D_x}{2} - \frac{c_x}{3}\right) + N\left(\frac{D_x}{2} - \frac{c_x}{3}\right) \quad \textbf{8.335}$$

$$M_{pty} = T_{pty}\left(\frac{D_y}{2} - \frac{c_y}{3}\right) + N\left(\frac{D_y}{2} - \frac{c_y}{3}\right) \quad \textbf{8.336}$$

$$M_{sx} = T_s\left(d_x - \frac{c_x}{3}\right) + C_s\left(\frac{c_x}{3} - d'_x\right) = T_s\left(d_x - d'_x\right) = C_s\left(d_x - d'_x\right) \quad \textbf{8.337}$$

$$M_{sy} = T_s\left(d_y - \frac{c_y}{3}\right) + C_s\left(\frac{c_y}{3} - d'_y\right) = T_s\left(d_y - d'_y\right) = C_s\left(d_y - d'_y\right) \quad \textbf{8.338}$$

$$\phi M_{nx} = \phi\left(M_{ptx} + M_{sx}\right) \quad \textbf{8.339}$$

$$\phi M_{ny} = \phi\left(M_{pty} + M_{sy}\right) \quad \textbf{8.340}$$

8.12 Design Procedure for General Hybrid Subassembly

Moment capacity re-centering elements (PT and N):

$$M_{pt} = \left(T_{pt} + N\right)\left(\frac{D}{2} - \frac{c}{3}\right) \quad \textbf{8.341}$$

Neutral axis location c can be known through trials

Forces in energy dissipaters,

In tension:

$$T_s = f_y A_s \quad \textbf{8.342}$$

In compression:

$$C_s = f_y A_s \quad \textbf{8.343}$$

Both T_s and C_s are independent of neutral axis location, but they have to be included in the section equilibrium check.

Moment capacity of the energy dissipaters:

$$M_s = T_s\left(d - \frac{c}{3}\right) + C_s\left(\frac{c}{3} - d'\right) = T_s\left(d - d'\right) = C_s\left(d - d'\right) \quad \textbf{8.344}$$

Therefore, M_s is also independent of neutral axis location and independent of drift level as well.

T_s, C_s are also independent of M_{pt} which means dissipaters can be designed separately, independent of PT and drift levels, as long as they yield.

Design flowchart for Sub-assemblies with Axial Dissipaters:

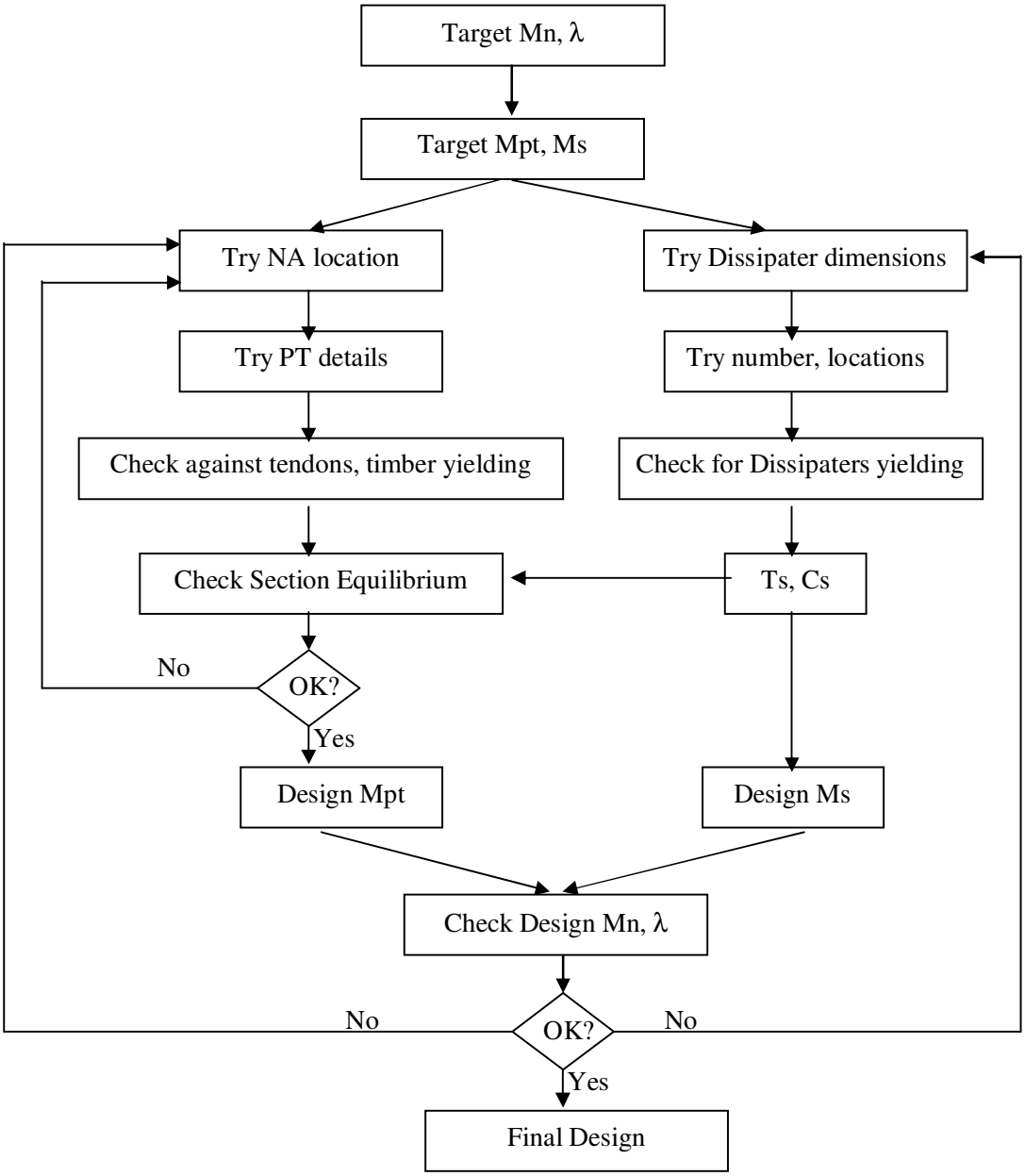

Figure 8.21 Flowchart for design of general Hybrid subassembly

8.13 Design of Walls Coupled with UFP Dissipaters

Moment capacity of Walls with UFP dissipaters:

Wall1:

$$M_{pt1} = \left(T_{pt1} + N_1\right)\left(\frac{l_w}{2} - \frac{c_1}{3}\right) \qquad \textbf{8.345}$$

Wall2:

$$M_{pt2} = \left(T_{pt2} + N_2\right)\left(\frac{l_w}{2} - \frac{c_2}{3}\right) \quad \textbf{8.346}$$

Total Re-centering Moment from PT:

$$M_{pt} = M_{pt1} + M_{pt2} \quad \textbf{8.347}$$

$$M_{pt} = \left(T_{pt1} + N_1\right)\left(\frac{l_w}{2} - \frac{c_1}{3}\right) + \left(T_{pt2} + N_2\right)\left(\frac{l_w}{2} - \frac{c_2}{3}\right) \quad \textbf{8.348}$$

$$M_{pt} = \frac{l_w}{2}\left(T_{pt1} + N_1\right) - \frac{c_1}{3}\left(T_{pt1} + N_1\right) + \frac{l_w}{2}\left(T_{pt2} + N_2\right) - \frac{c_2}{3}\left(T_{pt2} + N_2\right) \quad \textbf{8.349}$$

$$M_{pt} = \frac{l_w}{2}\left(T_{pt1} + N_1 + T_{pt2} + N_2\right) - \frac{c_1}{3}\left(T_{pt1} + N_1\right) - \frac{c_2}{3}\left(T_{pt2} + N_2\right) \quad \textbf{8.350}$$

Total Moment from UFP:

$$M_s = M_{s1} + M_{s2} = V_s\left(\frac{c_1}{3}\right) + V_s\left(l_w - \frac{c_2}{3}\right) = V_s\left(l_w + \frac{c_1 - c_2}{3}\right) \quad \textbf{8.351}$$

Total force in UFP, V_s, is independent of M_{pt} but it has to be included in check for section equilibrium. M_s is a function of the difference in neutral axes locations of the two walls (c1-c2).

The difference in the neutral axes of the two walls is a particular value for a particular combination of UFPs and initial post-tensioning. Therefore, the energy dissipation is not totally independent of PT. This is because for the same set of UFPs and at the same drift level the value of (c1-c2) is different for different initial PT levels.

For a particular set of UFPs deliver a certain vertical force that act on each wall in opposite directions. The effect of these two opposite forces is the difference in the neutral axes locations of the two walls. The significance of these forces relative to the post-tensioning forces determines the magnitude of the difference in the neutral axes.

Design flowchart for Hybrid coupled walls with UFPs:

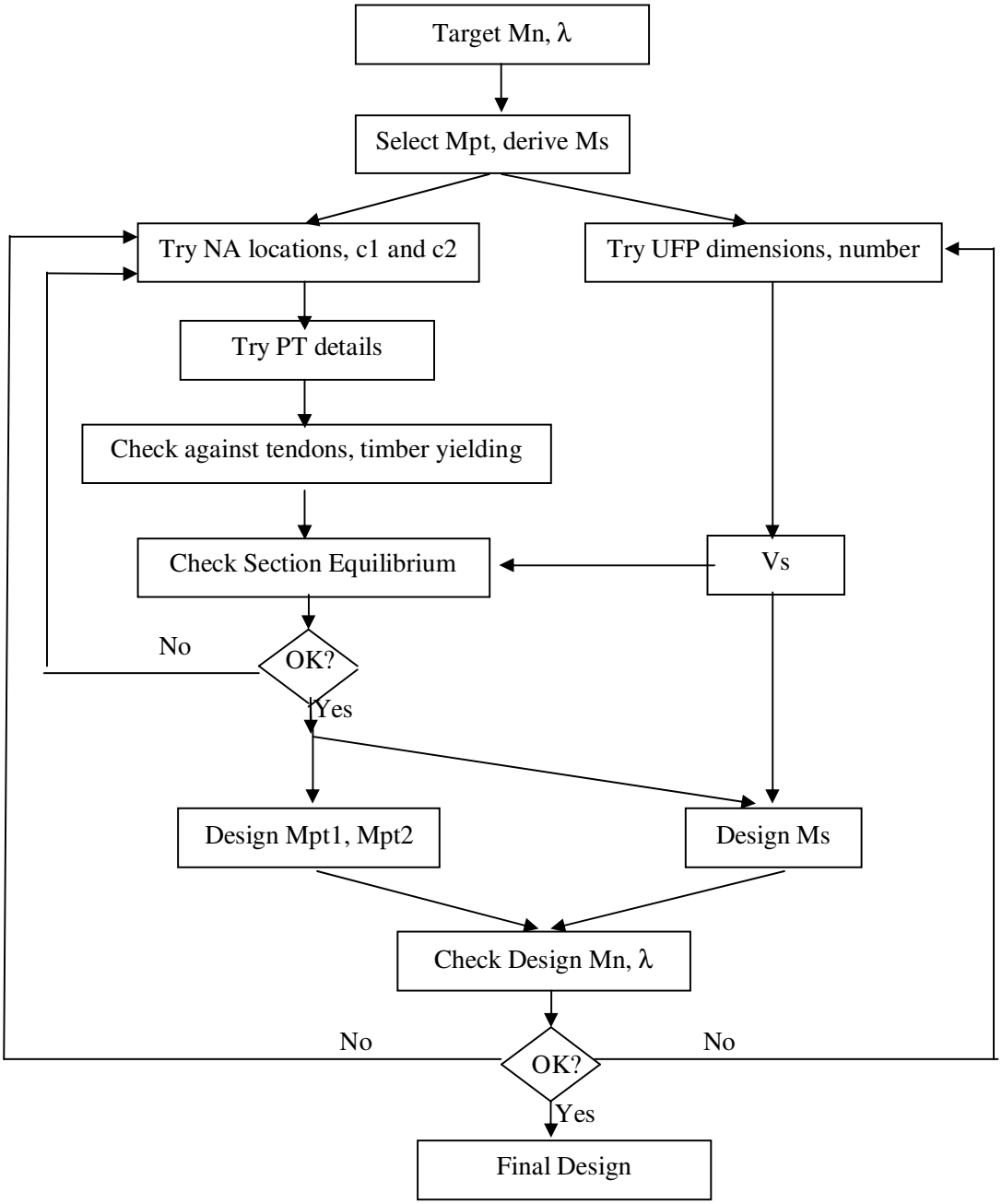

Figure 8.22 Flowchart for design of Hybrid coupled walls with UFP

8.14 Design of General Hybrid Subassembly under Bi-Directional Loading

Moment capacity re-centering elements (PT and N):

$$M_{nx} = T_{ptx}\left(\frac{D_x}{2} - \frac{c_x}{3}\right) + N\left(\frac{D_x}{2} - \frac{c_x}{3}\right) \quad \textbf{8.352}$$

$$M_{ny} = T_{pty}\left(\frac{D_y}{2} - \frac{c_y}{3}\right) + N\left(\frac{D_y}{2} - \frac{c_y}{3}\right) \quad \textbf{8.353}$$

Neutral axis location c can be known through trials

Forces in dissipaters in tension:

$$T_s = f_y A_s \quad \textbf{8.354}$$

Forces in dissipaters in compression:

$$C_s = f_y A_s \quad \textbf{8.355}$$

Moment capacity of the energy dissipaters in x and y directions:

$$M_{sx} = T_s\left(d_x - \frac{c_x}{3}\right) + C_s\left(\frac{c_x}{3} - d'_x\right) = T_s\left(d_x - d'_x\right) = C_s\left(d_x - d'_x\right) \quad \textbf{8.356}$$

$$M_{sy} = T_s\left(d_y - \frac{c_y}{3}\right) + C_s\left(\frac{c_y}{3} - d'_y\right) = T_s\left(d_y - d'_y\right) = C_s\left(d_y - d'_y\right) \quad \textbf{8.357}$$

Like uni-directional case, Ms is also independent of neutral axis location and independent of drift level as well. Dissipaters can be designed separately, independent of PT and drift levels, as long as they yield.

Steps in the design flowchart have to be followed for both x and y directions separately. But this may need a few more trials since change in one direction will also have effects on the other.

Simplified design procedure with bi-directional loading would be similar to that for the unidirectional case, just has to be followed for the two directions separately.

8.15 Design Example

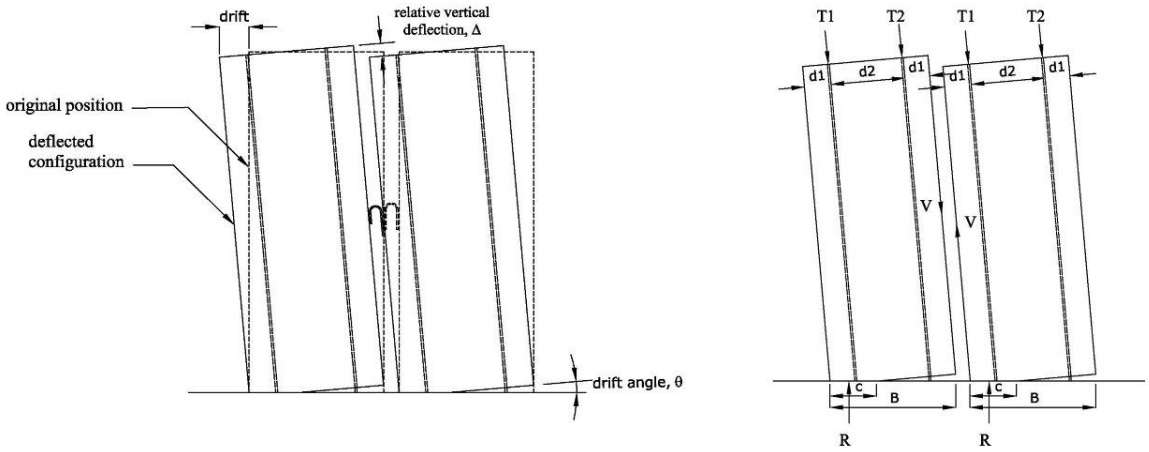

Figure 8.23 a) Deflected shape of coupled walls; b) forces in walls coupled with UFPs

To demonstrate the tools for designing a wall system with specified behaviour, a set specimen with of different combinations of initial prestressing and dissipation capacities was designed and tested. The goal was to design a pair of coupled walls for a particular moment capacity with of different types of energy dissipation systems targeting the same value of the ratioλ.

Two alternative hybrid solutions and one post-tensioned-only solution all with the targeted moment capacity of 300 kN at 2% drift were designed.

In order to achieve different combinations of initial prestressing levels were used. The first trial was for post-tensioning-only with 10% initial prestressing; the second combination had 20% initial prestressing with two 8mm diameter axial dissipaters per wall. The third combination was with 20% initial prestressing and four 100mm wide 5mm thick UFPs.

Walls with PT only

Details of the PT-only walls are discussed in chapter 4. Double walls with the same arrangements are used here as shown in Figure 8.1.

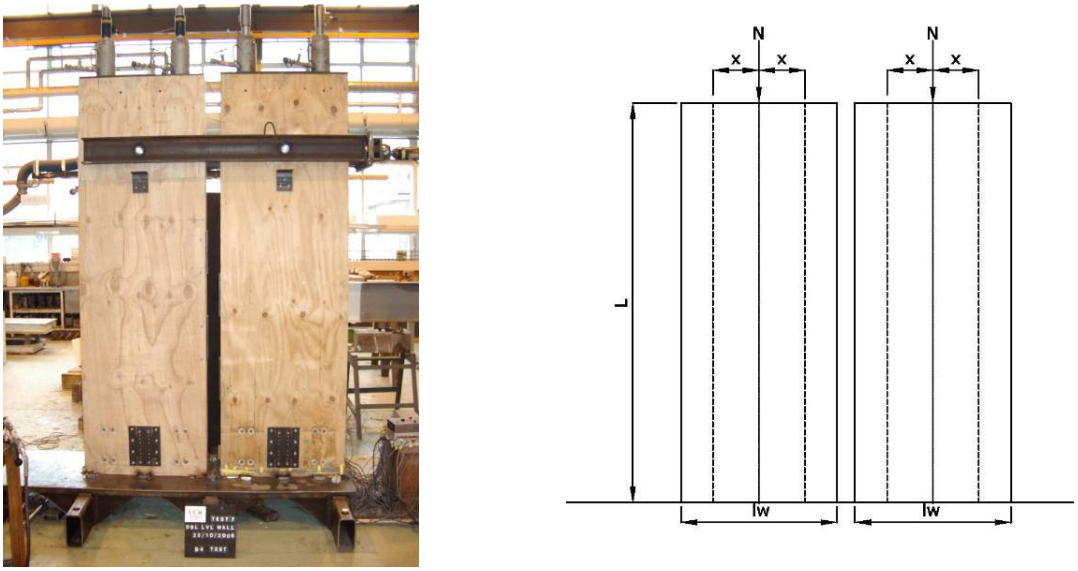

Figure 8.24 View of PT-only walls a) test specimen b) with dimensions

x = 230mm

For lub = 2500mm

Fy= .85*1830= 1560MPa, Ept = 200 GPa and Apt = 99mm2

Number of strands per tendon=2

Initial prestress= 10% of yield, PTi=20.89 kN

Design drift= 2%

Elastic deformation: approximately 0.5%

Steps to determine connection flexural capacity:

Connection rotation, θ_{imp} is imposed
drift, θ=1.5%

Neutral axis depth c (through trial)
c= 0.09lw=107.14mm

Member compatibility is applied:

Elongation of the tendon,

$$\Delta_{pt} = \theta_{imp}\left(\frac{l_w}{2} \pm x_{pt} - c\right) \qquad \textbf{8.358}$$

Δpt1 =2.89mm and Δpt2 = 12.34mm.

Strain in the tendon,

$$\varepsilon_{pt,t} = \frac{\Delta_{pt,t}}{l_{ub}} \quad \textbf{8.359}$$

$$\varepsilon_{pt,c} = \frac{\Delta_{pt,c}}{l_{ub}} \quad \textbf{8.360}$$

εpt1 =0.00083 and εpt2 = 0.00353

To check the tendon is not yielding,

$$\varepsilon_{pt,i} + \varepsilon_{pt} \leq 0.9\varepsilon_y \quad \textbf{8.361}$$

Where,

$$\varepsilon_{pt,i} = \frac{T_{pt,i}}{A_{pt}E_{pt}} \quad \textbf{8.362}$$

εs =0.0008
εpti +εs < 0.9εs =0.007

Strain in the timber from Monolithic Beam Analogy:

$$\varepsilon_t = \left(3\frac{\theta_{imp}}{L_{cant}} + \phi_{dec}\right)c \quad \textbf{8.363}$$

Where, L_{cant} is the shear span = .8*2000=1600mm

And the decompression curvature,

$$\phi_{dec} = \frac{2\left(T_{pt,i} + N\right)}{E_{con}bh^2} \quad \textbf{8.364}$$

φdec = 3.9E-7, εt= 0.002013
To check the timber is not yielding,

$$\varepsilon_{y,t} = \frac{f_c}{E_{con}} > \varepsilon_t \quad \textbf{8.365}$$

εy,t=45/(.55*13200)=006198>.002013
The compressive force in the timber is calculated:

$$C_t = 0.5\varepsilon_t E_{con} cb \quad \textbf{8.366}$$

Ct=234.9
Connection equilibrium is checked:

$$C_t = T_{pt} + N \quad \textbf{8.367}$$

$$T_{pt} = T_{pt,i} + \Delta T_{pt} = \rho_{pt} f_y A_{pt} + \varepsilon_{pt} E_{pt} A_{pt} \quad \textbf{8.368}$$

ΔT1= 32.7 kN and ΔT2= 139.37kN

$$T_i = T_{initial} + \Delta T_i$$

T initial = 20.89 kN, Tpt1= 63.62 kN and Tpt2= 170.54 kN.

Tpt=234.2

Satisfied

The moment capacity:

$$\phi M_n = \phi M_{pt} = \phi\left[T_{pt}\left(\frac{l_w}{2} \pm x_{pt} - \frac{c}{3}\right) + N\left(\frac{l_w}{2} - \frac{c}{3}\right)\right] \quad \textbf{8.369}$$

Mpt1 = 169.32 kN-m and total moment (for two walls), M pt = 338.65 kN-m, φMpt = 304.78

kN-m

Hybrid Walls

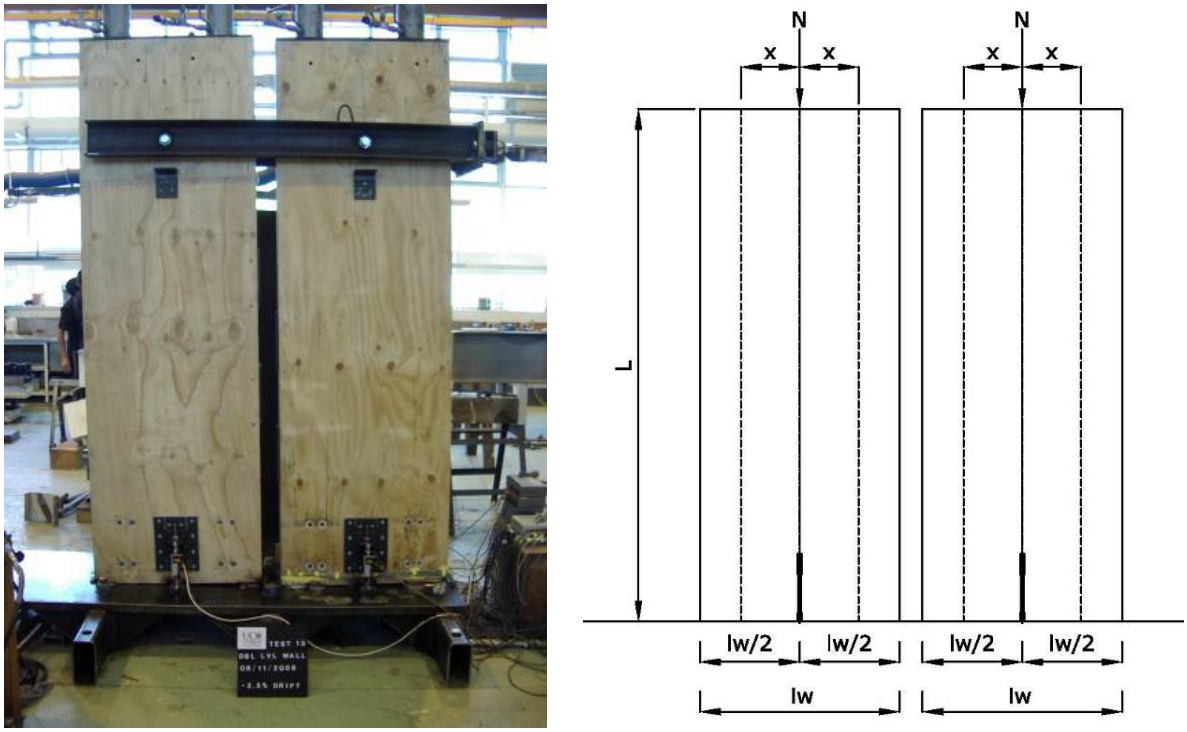

Figure 8.25 View of walls with axial dissipaters a) test specimen b) with dimensions

Target Mn = 300 kN-m

Target φMn = 333 kN-m

Target Lambda = 1.5

Target Mpt= 200 kN-m

Target Ms= 133 kN-m

x = 230mm

For lub = 2500mm

Fy= .85*1830= 1560MPa, Ept = 200 GPa and Apt = 99mm2

Number of strands per tendon=1

Initial prestress= 20% of yield, PTi=30.89 kN

Two 15mm diameter axial dissipaters per wall

Design drift= 2%

Elastic deformation: approximately 0.5%

Steps to determine connection flexural capacity:

Connection rotation, θ_{imp} is imposed
drift, θ=1.5%

Neutral axis depth c (through trial)
c= 0.095lw=114.5mm

Member compatibility is applied:

Elongation of the tendon,

$$\Delta_{pt} = \theta_{imp}\left(\frac{l_w}{2} \pm x_{pt} - c\right) \quad \textbf{8.370}$$

Δpt1 =2.78mm and Δpt2 = 12.23mm.
Strain in the tendon,

$$\varepsilon_{pt,t} = \frac{\Delta_{pt,t}}{l_{ub}} \quad \textbf{8.371}$$

$$\varepsilon_{pt,c} = \frac{\Delta_{pt,c}}{l_{ub}} \quad \textbf{8.372}$$

εpt1 =0.00079 and εpt2 = 0.00349

εpti =0.0023
To check the tendon is not yielding,

$$\varepsilon_{pt,i} + \varepsilon_{pt} \leq 0.9\varepsilon_y \quad \textbf{8.373}$$

Where,

$$\varepsilon_{pt,i} = \frac{T_{pt,i}}{A_{pt}E_{pt}} \quad \textbf{8.374}$$

εpti +εpt < 0.9εs =0.007

Elongation in energy dissipater,

$$\Delta_s = \theta_{imp}\left(\frac{l_w}{2} - c\right) \quad \textbf{8.375}$$

Δs = 7.28mm
Strain in the dissipater,

$$\varepsilon_s = \frac{\Delta_s}{l_{ub,d}} \quad \textbf{8.376}$$

εs =0.0728
To make sure the dissipater has yielded,

$$\varepsilon_s > \varepsilon_{y,s} = \frac{f_s}{E_s}$$

εy,s=0.001725
Strain in the timber from Monolithic Beam Analogy:

$$\varepsilon_t = \left(3\frac{\theta_{imp}}{L_{cant}} + \phi_{dec}\right)c \quad \textbf{8.377}$$

Where, L_{cant} is the shear span = .8*2000=1600mm

And the decompression curvature,

$$\phi_{dec} = \frac{2\left(T_{pt,i} + N\right)}{E_{con}bh^2} \quad \textbf{8.378}$$

φdec = 3.9E-8, εt= 0.00215
To check the timber is not yielding,

$$\varepsilon_{y,t} = \frac{f_c}{E_{con}} > \varepsilon_t \quad \textbf{8.379}$$

εy,t=45/(.55*13200)=.006198>.00215
The compressive force in the timber is calculated:

$$C_t = 0.5\varepsilon_t E_{con} cb \quad \textbf{8.380}$$

Ct=268.3

$$T_{pt} = T_{pt,i} + \Delta T_{pt} = \rho_{pt} f_y A_{pt} + \varepsilon_{pt} E_{pt} A_{pt} \quad \textbf{8.381}$$

ΔT1= 15.7 kN and ΔT2= 69.2 kN

$$T_i = T_{initial} + \Delta T_i$$

T initial = 30.89 kN, Tpt1= 46.63 kN and Tpt2= 100.09 kN.

$$T_s = f_y A_s \qquad 8.382$$

Ts= 121.9 kN

Tpt1+Tpt2+Ts = 268.7 kN
For connection equilibrium:

$$C_t = T_{pt} + N + T_s \qquad \textbf{8.383}$$

Satisfied
Moment capacity:

$$\phi M_n = \phi\left(M_{pt} + M_s\right) = \phi\left[T_{pt}\left(\frac{l_w}{2} \pm x_{pt} - \frac{c}{3}\right) + N\left(\frac{l_w}{2} - \frac{c}{3}\right) + T_s\left(\frac{l_w}{2} - \frac{c}{3}\right)\right] \qquad \textbf{8.384}$$

Mpt = 202.94 kN-m and Ms = 137.01 kN-m

Total moment for two walls = 339.95 kN-m, φMpt = 305.96 kN-m

The re-centering ratio, λ = 1.48

Hybrid Walls with UFP dissipaters

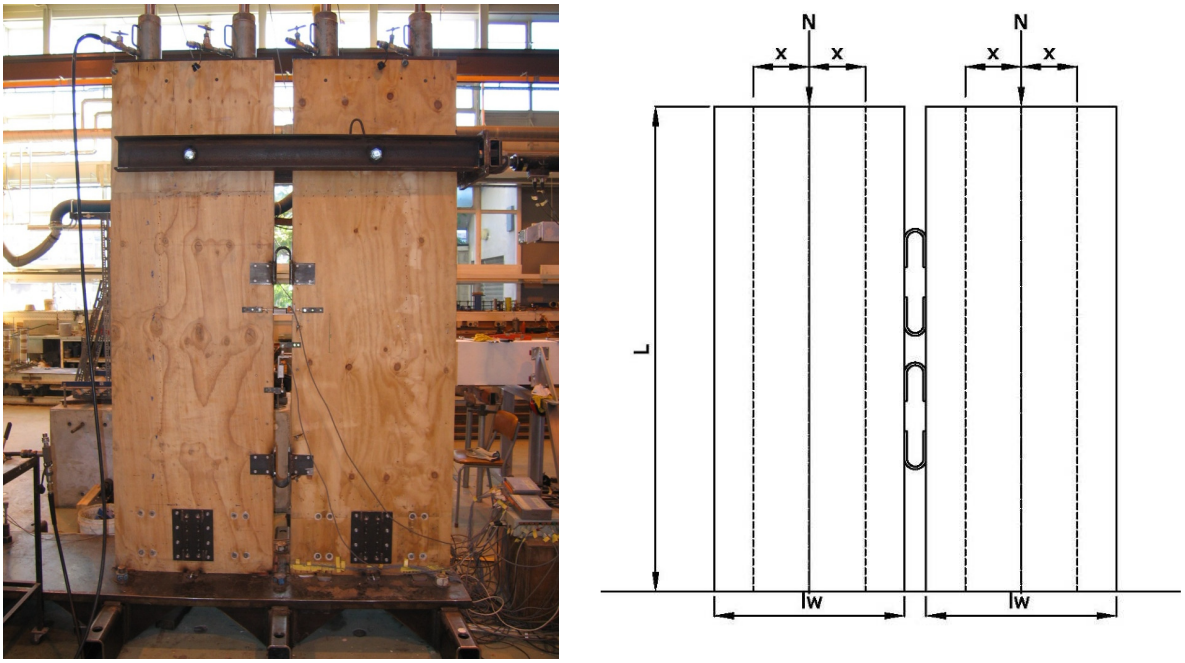

Figure 8.26 View of walls with UFP dissipaters a) test specimen b) with dimensions

Target Mn = 300 kN-m

Target φMn = 333 kN-m

Target Lambda = 1.5

Target Mpt= 200 kN-m

Target Ms= 133 kN-m

x = 230mm

For lub = 2500mm

Fy= .85*1830= 1560MPa, Ept = 200 GPa and Apt = 99mm2

Number of strands per tendon=1

From initial prestress of 20% of yield, PTi=30.89 kN

Design drift= 2%

Four 50 mm wide, 5 mm thickness UFP dissipaters

Elastic deformation: approximately 0.5%

Steps to determine connection flexural capacity:

Connection rotation, θ_{imp} is imposed
drift, θ=1.5%

Neutral axis depth c (through trial)
c1= 0.037lw=44.28mm, c2=0.094lw=112.89mm

Member compatibility is applied:

Elongation of the tendon,

$$\Delta_{pt} = \theta_{imp}\left(\frac{l_w}{2} \pm x_{pt} - c\right) \quad \textbf{8.385}$$

Wall1: Δpt1 =3.84mm and Δpt2 = 12.84mm.
Wall2: Δpt1 =2.81mm and Δpt2 = 11.81mm
Strain in the tendon,

$$\varepsilon_{pt,t} = \frac{\Delta_{pt,t}}{l_{ub}} \quad \textbf{8.386}$$

$$\varepsilon_{pt,c} = \frac{\Delta_{pt,c}}{l_{ub}} \quad \textbf{8.387}$$

Wall1: εpt1 =0.0011 and εpt2 = 0.00367

Wall2: εpt1 =0.0008 and εpt2 = 0.00337

εpti =0.0016
To check the tendon is not yielding,

$$\varepsilon_{pt,i} + \varepsilon_{pt} \leq 0.9\varepsilon_y \quad \textbf{8.388}$$

Where,

$$\varepsilon_{pt,i} = \frac{T_{pt,i}}{A_{pt}E_{pt}} \quad \textbf{8.389}$$

εpti +εpt < 0.9εs =0.007

Strain in the timber from Monolithic Beam Analogy:

$$\varepsilon_t = \left(3\frac{\theta_{imp}}{L_{cant}} + \phi_{dec}\right)c \quad \textbf{8.390}$$

Where, L_{cant} is the shear span = .8*2000=1600mm

And the decompression curvature,

$$\phi_{dec} = \frac{2\left(T_{pt,i} + N\right)}{E_{con}bh^2} \quad \textbf{8.391}$$

φdec = 3.9E-8, Wall1, εt= 0.000832, Wall2, εt= 0.00212

To check the timber is not yielding,

$$\varepsilon_{y,t} = \frac{f_c}{E_{con}} > \varepsilon_t \quad \textbf{8.392}$$

εy,t=45/(.55*13200)=.006198>.00212>0.00832
The compressive force in the timber is calculated:

$$C_t = 0.5\varepsilon_t E_{con} cb \quad \textbf{8.393}$$

Wall1, Ct1=40.1, Wall2, Ct2=260.8

$$T_{pt} = T_{pt,i} + \Delta T_{pt} = \rho_{pt} f_y A_{pt} + \varepsilon_{pt} E_{pt} A_{pt} \quad \textbf{8.394}$$

Wall1: ΔT1= 21.7 kN and ΔT2= 72.6 kN

Wall2: ΔT1= 15.9 kN and ΔT2= 66.8 kN

$$T_i = T_{initial} + \Delta T_i$$

Wall1: T initial = 30.89 kN, Tpt1= 52.59 kN and Tpt2= 103.5 kN
Wall2: T initial = 30.89 kN, Tpt1= 46.77 kN and Tpt2= 97.68 kN

UFP force contributions:

$$V_s = n * 0.5\frac{bt^2}{D}F_y \quad \textbf{8.395}$$

Vs in both Wall1 and Wall2= 116.1 kN (from 6 UFPs)

Wall axial forces:

$$N_1 = N - V_s \quad \textbf{8.396}$$

$$N_2 = N + V_s$$

For connection equilibrium:

$$C_{t1} = T_{pt11} + T_{pt12} + N_1 \quad \textbf{8.397}$$

$$C_{t2} = T_{pt21} + T_{pt22} + N_2 \quad \textbf{8.398}$$

Wall1= 40.0 kN
Wall2= 260.5 kN

Satisfied
Moment capacity:

$$M_{pt1} = T_{pt11}\left(\frac{l_w}{2} - x_{pt} - \frac{c_1}{3}\right) + T_{pt12}\left(\frac{l_w}{2} + x_{pt} - \frac{c_1}{3}\right) + N_1\left(\frac{l_w}{2} - \frac{c_1}{3}\right) \quad \textbf{8.399}$$

$$M_{pt2} = T_{pt21}\left(\frac{l_w}{2} - x_{pt} - \frac{c_2}{3}\right) + T_{pt22}\left(\frac{l_w}{2} + x_{pt} - \frac{c_2}{3}\right) + N_2\left(\frac{l_w}{2} - \frac{c_2}{3}\right) \quad \textbf{8.400}$$

$$M_{pt} = M_{pt1} + M_{pt2} \quad \textbf{8.401}$$

$$M_{pt} = \frac{l_w}{2}\left(T_{pt11} + T_{pt12} + T_{pt21} + T_{pt22} + N_1 + N_2\right) - x_{pt}\left(T_{pt11} - T_{pt12} + T_{pt21} - T_{pt22}\right) - \frac{c_1}{3}\left(T_{pt11} + T_{pt12} + N_1\right) - \frac{c_2}{3}\left(T_{pt21} + T_{pt22} + N_2\right) \quad \textbf{8.402}$$

$$M_s = M_{s1} + M_{s2} = V_s\left(\frac{c_1}{3}\right) + V_s\left(l_w - \frac{c_2}{3}\right) = V_s\left(l_w + \frac{c_1 - c_2}{3}\right) \quad \textbf{8.403}$$

Mpt1 = 38.68 kN-m and Ms = 1.71 kN-m

Mpt1 = 161.8 kN-m and Ms = 134.95 kN-m

Total moment for two walls, Mpt = 200.48 kN-m, Ms= 136.66 φMn = 303.43 kN-m

The re-centering ratio, λ = 1.467

Summary of design of three types of walls:

Type	**M_{PT} (kN-m)**	**M_S (kN-m)**	**φM_{TOT} (kN-m)**	**λ**
PT-only	338.65	-	304.78	-
Hybrid	202.94	137.01	305.96	1.48
UFP	200.48	136.66	303.43	1.467

8.16 Summary

The Section Analysis scheme to calculate ultimate moment-capacities of the subassemblies has been applied to all the different configurations of the three types of subassemblies. Despite the variations in type and geometry, the procedure has been found suitable for all the subassembly specimens.

The general design approach put forward some interesting observations. For any typical subassembly the energy dissipation system is found to be independent of the neutral axis or drift level as long as they yield during the deformation. This means that the energy dissipation components can be designed irrespective of the post-tensioning arrangement. The post-tensioing system has to be designed taking the effect of energy dissipation system into account. The resultant internal reactions within a member due to the combined effects of the two different actions (i.e. re-centering and energy dissipation) can be obtained by superimposing the separately calculated reactions of the two actions. Noticeably, this is reflected in the formation of flag-shaped characteristics through superposition of post-tensioning and energy dissipation:

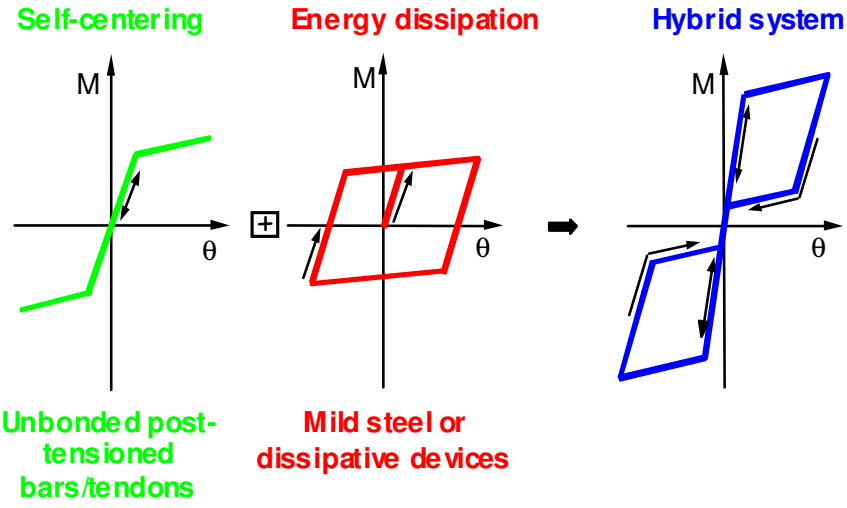

Figure 8.27 Idealized "flag-shaped" hysteresis behaviour in a hybrid connection (fib, 2003, NZS3101:2006)

Since the contribution of the energy dissipation system can be calculated independent of the post-tensioing arrangements, it can be designed separately. Once the properties of the energy dissipation system are known, it is simple and convenient to design the post-tensioning system to act in combination with the energy dissipation system and produce the desired behaviour in a subassembly.

9 CONCLUSIONS

9.1 Conclusions from the Current Research

Three basic structural subassemblies of post-tensioned multi-storey timber structural systems have been investigated in this research: walls, columns and beam-column joints. The following specific conclusions have been reached on particular types of subassemblies:

Walls:

The post-tensioned shear walls achieved full re-centering after quasi-static and pseudo-dynamic loading cycles. The hybrid walls with axial dissipaters show significant hysteretic energy dissipation in addition to re-centering. The coupled walls with UFP dissipaters utilize the rocking motion to dissipate energy through the UFPs. The hysteretic behaviour of both the axial dissipaters and the UFPs are very stable and predictable. Virtually no damage was observed in the structural members after many cycles of seismic loading, which ensures low cost for post-earthquake repairs. The separate and independent recentering and energy dissipation characteristics of both the axial dissipaters and the UFPs present a significant design flexibility of the hybrid systems.

Column:

The hybrid column tested under bi-directional loading showed energy dissipation and complete recentering, in the same way as in uni-directional loading. No degradation of strength was observed after repeated cycles of bi-directional loading at high drifts. As expected, there was interaction between the two axes (bi-directional loading regime) resulting in a reduction of

moment, when compared to the resistance observed under uni-directional loading, but that could be detected and taken into consideration during analysis.

Beam-Column Joint:

The full-scale beam-column joint revealed useful information about behaviour of a number of different types of connection interfaces. In addition to confirming the typical recentering and energy dissipation characteristics of post-tensioned-only and hybrid connections, it provided important insight into characteristics of different types of connections.

It was, in particular, found that the overall moment capacity of the specimen is less compared to other two types of connections (i.e. in walls and columns) due to lower stiffness of timber perpendicular to grain. The connection stiffness can be increased through addition of steel armouring plates at the interface. Reinforcing the joint region via long screws was found to decrease the perpendicular-to-grain crushing of the column without significantly improving the overall stiffness of the joint. A combination of armouring and reinforcements can, therefore, achieve higher stiffness and reduced perpendicular-to-grain deformations in the connection.

The armouring and reinforcement of beam-column joints has a significant effect on controlling the overall frame behaviour. It has been observed that the reinforced-armoured specimen has stiffer connection compared to the unreiforced-unarmoured specimen. This is helpful for designers because, by providing reinforcing and armouring, more economical member sizes can be used to achieve the same inter-storey drift.

The following general conclusions are drawn from the investigation:

- The seismic behaviour of the subassemblies has been defined through extensive experimental investigation. They have shown excellent seismic resistance with full recentering and significant energy dissipation in the hybrid systems. No significant

structural damage was observed in any of the test specimen throughout the testing program.

- Characteristic properties of the material were determined from the experimental results and those were used in numerical models of the subassemblies. Results from the numerical models accurately matched the experimental results.
- Detailed design procedures based on section analysis were developed for each of the tested subassemblies. The procedure was then extended to generalized subassemblies, making it applicable to a wider range of members varying in geometry and details.

9.2 Recommendations for Future Study

The following areas should be investigated in future studies:

- The current studies included only quasi-static and pseudo-dynamic tests. Real time dynamic tests, including shake table tests of specimen should be performed to learn more about the damping, strain rate and degradation characteristics of the subassemblies.
- The testing of full-scale specimens provided very useful information on the subassemblies beyond the limited testing of small-scale tests and numerical analysis. More full-scale tests of all types of subassemblies will provide further useful information.
- Further investigations are needed on beam-column joints with different types of connection interfaces. Parametric testing analysis should be performed with varying armouring plate thicknesses, reinforcement ratio and reinforcement arrangements.
- Local effects like stress concentrations at the connection interfaces, energy dissipater connections and post-tensioning anchorages, should be studied further in-depth with both

experimental and numerical investigations.

References

ACI (2001). Acceptance Criteria for Moment Frames Based on Structural Testing (T1.1-01) and commentary (T1.1R-01), *ACI T1.1-01 & ACI T1.1R-01 2001*.

Allen, M., & Kurama, Y. (2002). Design of rectangular openings in precast walls under combined vertical and lateral loads. *PCI Journal, 47*(2), 58-83.

Amaris, A., Pampanin, S., & Palermo, A. (2006). *Uni and Bi-directional Quasi Static Tests on Alternative Hybrid Precast Beam Column Joint Subassemblies*. Paper presented at the Annual Conference of New Zealand Society for Earthquake Engineering.

Bresler, B. (1960). Design criteria for reinforced concrete columns under axial load and biaxial bending. *ACI Journal, 57*(11), 481-490.

Buchanan, A. H. (2007). *Timber Design Guide*. Christchurch: New Zealand Timber Industry Federation

Buchanan, A. H., & Fairweather, R. H. (1993). Seismic design of glulam structures. *Bulletin of the New Zealand National Society for Earthquake Engineering, 26*(4), 415-436.

Carr, A. J. (2005). *RUAUMOKO Program for Inelastic Dynamic Analysis - Users Manual*. Christchurch: Dept. of Civil Engineering, University of Canterbury.

Cattanach, A., & Pampanin, S. (2008). *21st Century Precast: the Detailing and Manufacture of NZ's First Multi-Storey PRESSS-Building*. Paper presented at the NZ Concrete Industry Conference.

Ceccotti, A. (1989). *Structural behaviour of timber constructions in seismic zones.* Paper presented at the CEG DG III, Florence, Italy.

Christopoulos, C., & Folz, B. (2002). Posttensioned energy dissipating connections for moment-resisting steel frames. *ASCE Journal of Structural Engineering, 128*(9), 1111-1120.

Christopoulos, C., Pampanin, S., & Priestley, M. J. N. (2003). Performance-based seismic response of frame structures including residual deformations. Part I: Single-degree of freedom systems. *Journal of Earthquake Engineering, 7*(1), 97-118.

Conley, J. R. (2000). *Seismic Response of Unbonded Post-Tensioned Precast Concrete Walls with Ductile Vertical Connections: Analytical Modeling and Pretest Prediction of the PRESSS Five-Story Building*. University of California, San Diego.

Davies, M. (2006). Internal Research Report: Compressive Tests on 90x90x270mm Laminated Veneer Lumber Specimens. Christchurch: University of Canterbury.

Deam, B. L. (1997). *Seismic Design and Behaviour of Multi-storey Plywood sheathed timber framed Shearwalls*. Christchurch: Dept. of Civil Engineering, University of Canterbury, NZ.

Dodd, L. L., & Restrepo, J. I. (1995). Model for Predicting Cyclic Behaviour of Reinforcing Steel. *ASCE Journal of Structural Engineering, 121*(3), 433-445.

El-Sheikh, M., Sause, R., Pessiki, S., & Lu, L. W. (1999). Seismic Behavior and Design of Unbonded Post-Tensioned Precast Concrete Frames. *PCI Journal, 44*(3), 54-71.

FEMA (l997). *NEHERP provisions for the rehabilitation of buildings. FEMA No. 273 (Guidelines) and 274 (Commentary)*.

fib (2003). Seismic Design of Precast Concrete Building Structures, *fib Bulletin 27*. Lausanne.

Filiatrault, A., Fischer, D., Folz, B., & Uang, C. M. (2002). Seismic testing of two-story woodframe house: Influence of wall finish materials. *Journal of Structural Engineering, 128*(10), 1337-1345.

Filiatrault, A., & Folz, B. (2002). Performance-Based Seismic Design of Wood Framed Buildings. *Journal of Structural Engineering, 128*(1), 39-47.

futurebuild (2006a). *Limit States Design Information for Specific Engineering Design for New Zealand Construction* futurebuild.

Futurebuild (2006b). Limit States Design Information for Specific Engineering Design for New Zealand Construction. In C. H. H. Limited (Ed.). Auckland.

Halliday, M. A., & Buchanan, A. H. (1993). Feasibility of Medium Rise Office Structures in Timber. *IPENZ Transactions, 19*(1/CE), 13-20.

Holden, T. J. (2001). *A Comparison of the Seismic Performance of Precast Wall Construction: Emulation and Hybrid Approaches*: University of Canterbury.

ICBO (Ed.) (2000). International Conference of Building Officials.

Iqbal, A., Pampanin, S., & Buchanan, A. H. (2008a). *Experimental Study of Prestressed Timber Columns under Bi-directional Seismic Loading*. Paper presented at the NZSEE Annual Conference, Wairakei.

Iqbal, A., Pampanin, S., & Buchanan, A. H. (2008b). *Seismic Behaviour of Prestressed Timber Columns under Bi-directional Loading*. Paper presented at the 10th World Conference on Timber Engineering, Miyazaki, Japan.

Iqbal, A., Pampanin, S., & Buchanan, A. H. (2009). *Seismic Response of Full-Scale Prestressed Timber Beam-Column Joint.* Paper presented at the NZSEE Annual Conference, Christchurch, New Zealand.

Iqbal, A., Pampanin, S., & Buchanan, A. H. (2010a). *Seismic Performance of Prestressed Timber Beam-Column Sub-Assemblies*. Paper presented at the NZSEE Annual Conference, Wellington, New Zealand.

Iqbal, A., Pampanin, S., Buchanan, A. H., & Palermo, A. (2010b). *Seismic Performance of Full-Scale Post-Tensioned Timber Beam-Column Joints.* Paper presented at the 11th World Conference on Timber Engineering, Trentino, Italy.

Iqbal, A., Pampanin, S., Buchanan, A. H., & Palermo, A. (2010c). *Seismic Response of Post-Tensioned Timber Walls.* Paper presented at the 14th European Conference on Earthquake Engineering, Ohrid, Macedonia.

Jacobsen, L. S. (1960). *Damping in composite structures.* Paper presented at the 2nd World Conference on Earthquake Engineering, Tokyo and Kyoto.

Kelly, J. M., Skinner, R. I., & Heine, A. J. (1972). Mechanism of Energy Absorbtion in Special Devices for Use in Earthquake Resistant Structures. *Bulletin of N. Z. Society for Earthquake Engineering, 5*(3), 63-88.

Kim, J. K. (2002). *Behaviour of Hybrid Frames under Seismic Loading*: University of Washington.

Kurama, Y. (2000). Seismic Design of Unbonded Post-Tensioned Precast Walls with Supplemental Viscous Damping. *ACI Structural Journal, 97*(4), 648-658.

Kurama, Y. (2001). Simplified Seismic Design Approach for Friction-Damped Unbonded Post-Tensioned Precast Walls. *ACI Structural Journal,, 98*(5), 705-716.

Kurama, Y., Pessiki, S., Sause, R., & Lu, L. W. (1999). Seismic Behavior and Design of Unbonded Post-Tensioned Precast Concrete Walls. *PCI Journal, 44*(3), 72-89.

MacRae, G. A., & Kawashima, K. (1997). Post-earthquake residual displacements of bilinear oscillators. *Earthquake engineering & structural dynamics, 26*(7), 701-716.

Marriott, D. J. (2009). *The Development of High-Performance Post-Tensioned Rocking Systems forthe Seismic Design of Structures.* University of Canterbury.

Marriott, D. J., Pampanin, S., Bull, D., & Palermo, A. (2008). Dynamic Testing of Precast, Post-tensioned Rocking Wall Systems with alternative dissipating solutions. *Bulletin of the New Zealand Society for Earthquake Engineering, 41*(2), 90-102.

Morcarz, P., & Krawinkler, H. (1981). *Theory and Application of Experimental Model Analysis in Earthquake Engineering*: John Blume Earthquake Engineering Center, Department of Civil and Environmental Engineering, stanford University, Report No. 50.

Newcombe, M. P. (2005). *Seismic Resisting Structural Systems using Laminated Veneer Lumber*. Christchurch: University of Canterbury.

Newcombe, M. P. (2007). *Seismic Design of Multi-storey Post-Tensioned Timber Buildings.* Rose School, Pavia, Italy.

Newcombe, M. P. (2008). *Seismic Design of Multi-storey Post-Tensioned Timber Buildings.* Rose School, Pavia, Italy.

Newcombe, M. P., Carradine, D., Pampanin, S., Buchanan, A. H., Deam, B. L., van Beerschoten, W. A., et al. (2009a). *In-Plane Experimental Testing of Timber-Concrete Composite Floor Diaphragms.* Paper presented at the NZSEE Annual Conference, Christchurch, New Zealand.

Newcombe, M. P., Cusiel, M. R., Palermo, A., & Buchanan, A. H. (2010). *Simplified Design of Post-tensioned Timber Frames.* Paper presented at the CIB Conference, Christchurch, New Zealand.

Newcombe, M. P., Pampanin, S., & Buchanan, A. H. (2010a). *Design and Construction of a Two Storey Pres-Lam Timber Building.* Paper presented at the 11th World Conference on Timber Engineering, Trentino, Italy.

Newcombe, M. P., Pampanin, S., & Buchanan, A. H. (2010b). *Global Response of a Two Storey Pres-Lam Timber Building*. Paper presented at the NZSEE Annual Conference, Wellington, New Zealand.

Newcombe, M. P., Pampanin, S., Buchanan, A. H., & Palermo, A. (2008a). Section Analysis and Cyclic Behavior of Post-Tensioned Jointed Ductile Connections for Multi-Story Timber Buildings. *Journal of Earthquake Engineering, 11 (Special Edition)*, 83-110.

Newcombe, M. P., Pampanin, S., Buchanan, A. H., & Palermo, A. (2008b). *Seismic Design and Numerical Validation of Post-tensioned Timber Frames.* Paper presented at the 14th World Conference on Earthquake Engineering, Beijing, China.

Newcombe, M. P., Pampanin, S., Buchanan, A. H., & Palermo, A. (2009b). *Seismic Design and Numerical Response of Post-tensioned Timber Frames.* Paper presented at the NZSEE Annual Conference, Christchurch, New Zealand.

Newcombe, M. P., & van Beerschoten, W. A. (2010). *In-Plane Experimental Testing of Timber-Concrete Composite Floor Diaphragms*: University of Canterbury.

NZCS (2010). *PRESSS Design Handbook*: New Zealand Concrete Society, Wellington, New Zealand.

NZS3101:2006 *Appendix B: Special Provisions for Seismic Design of Ductile Jointed Precast Concrete Structural Systems*: New Zealand Standards.

Otani, S. (1981). Hysteresis models of reinforced concrete for earthquake response analysis. *Journal of Faculty of Engineering, University of Tokyo, 36*(2), 407-441.

PacificSteel (2007). Reinforcing Bar and Coil.

Palermo, A. (2004). *The Use of Controlled Rocking in the Seismic Design of Bridges.* Technical University of Milan, Italy.

Palermo, A., Pampanin, S., & Buchanan, A. H. (2006a). *Experimental Investigations on LVL Seismic Resistant Wall and Frame Subassemblies.* Paper presented at the First European Conference on Earthquake Engineering and Seismology, Geneva, Switzerland.

Palermo, A., Pampanin, S., Buchanan, A. H., & Newcombe, M. P. (2005a, March 11th-13th). *Seismic Design of Multi-storey Buildings Using Laminated Veneer Lumber (LVL).* Paper presented at the NZSEE Conference, Wairakei, New Zealand.

Palermo, A., Pampanin, S., & Carr, A. J. (2005b). *Efficiency of simplified alternative modelling approaches to predict the seismic response of precast concrete hybrid systems.* Paper presented at the Proc. fib Symposium "Keep Concrete Attractive", Budapest, Hungary.

Palermo, A., Pampanin, S., Fragiacomo, M., Buchanan, A. H., & Deam, B. L. (2006b). *Innovative Seismic Solutions for mMulti-Storey LVL Timber Buildings.* Paper presented at the 9th World Conference on Timber Engineering, Portland, Oregon.

Palermo, A., Pampanin, S., Fragiacomo, M., Buchanan, A. H., Deam, B. L., & Pasticier, L. (2006c). *Quasi-Static Cyclic Tests on Seismic-Resistant Beam-to-Column and Column-to-Foundation Subassemblies using Laminated Veneer Lumber (LVL).* Paper presented at the Australasian Conference on Mechanics and Materials, Christchurch, New Zealand.

Pampanin, S. (2005). Emerging Solutions for High Seismic Performance of Precast/prestressed Concrete Buildings. *Journal of Advanced Concrete Technology, 3*(2), 207-223.

Pampanin, S. (2010). *Retrofit Solutions for pre-1970 R.C. Buildings: an Overview of Latest Research Developments in New Zealand.* Paper presented at the 14th European Conference on Earthquake Engineering, Ohrid, Macedonia.

Pampanin, S., Christopoulos, C., & Priestley, M. J. N. (2002). *Residual deformations in the performance-based seismic assessment of frame structures*: Rose School, Pavia.

Pampanin, S., & Nishiyama, M. (2002). *Critical Aspects in Modelling the Seismic Behaviour of Precast/Prestressed Concrete Building Connections and Systems.* Paper presented at the *1st fib Congress*, Osaka.

Pampanin, S., Priestley, M. J. N., & Sritharan, S. (2001). Analytical Modelling of the Seismic Behaviour of Precast Concrete Frames Designed with Ductile Connections. *Journal of Earthquake Engineering, 5*(3), 329-367.

Pino, D. P. M., Pampanin, S., Buchanan, A. H., & Deam, B. L. (2010a). *Shake Table Response of Multi-Storey Post-Tensioned Timber Buildings.* Paper presented at the NZSEE Annual Conference, Wellington, New Zealand.

Pino, D. P. M., Pampanin, S., Buchanan, A. H., & Deam, B. L. (2010b). *Shake Table Response of Multi-Storey Post-Tensioned Timber Buildings.* Paper presented at the 11th World Conference on Timber Engineering, Trentino, Italy.

Popovics, S. (1973). A Numerical Approach to the Complete Stress-strain Curve of Concrete. *Cement and Concrete Research, 3*(5), 583-599.

Prakash, V., Powell, G., & Campbell, S. (1993). *DRAIN-2DX Base Program Description and User Guide; Version 1.10*: University of California, Berkeley.

Priestley, M. J. N. (1991). Overview of the PRESSS Research Program. *PCI Journal, 36*(4), 50-57.

Priestley, M. J. N. (1996). The PRESSS program: Current Status and Proposed Plans for Phase III. *PCI Journal, 41*(2), 22-40.

Priestley, M. J. N., Calvi, G. M., & Kowalsky, M. J. (2007). Displacement-Based Seismic Design of Structures. *IUSS Press, Pavia*.

Priestley, M. J. N., Sritharan, S., Conley, J. R., & Pampanin, S. (1999). Preliminary Results and Conclusions from the PRESSS Five-Story Precast Concrete Test Building. *PCI Journal, 44*(6), 42-67.

Rahman, A. M., & Restrepo, J. I. (2000). *Earthquake Resistant Precast Concrete Buildings: Seismic Performance of Cantilever Walls Prestressed Using Unbonded Tendons*: University of Canterbury.

Schultz, A. E., & Magana, R. (1996). *Seismic Behavior of Connections in Precast Concrete Walls.* Paper presented at the Mete A. Sozen Symposium.

Sepeith, H. A., Carr, A. J., Pampanin, S., Murahidy, A. G. and Mander, J. B. (2004). *Modelling of Precast Prestressed Concrete Frame Structures with Rocking Beam-Column Connections*: University of Canterbury.

Smith, T. (2006). *LVL Rocking Shear Walls: With external dissipater attachment*: University of Canterbury.

Smith, T., Ludwig, F., Pampanin, S., Fragiacomo, M., Buchanan, A. H., Deam, B. L., et al. (2007). *Seismic Response of Hybrid-LVL Coupled Walls under Quasi-static and Pseudo-dynamic Testing.* Paper presented at the NZSEE Conference, Palmerston North, New Zealand.

Smith, T., Pampanin, S., Fragiacomo, M., & Buchanan, A. H. (2008). *Design and Construction of Prestressed Timber Buildings for Seismic Areas.* Paper presented at the World Conference on Timber Engineering, Miyazaki, Japan.

SNZ (2004). NZS 1170.5 Structural design acions Part 5: Earthquake actions - New Zealand.

Stanton, J., Stone, W. C., & Cheok, G. S. (1997). A Hybrid Reinforced Precast Frame for Seismic Regions. *PCI Journal, 42*(2), 20-32.

Stewart, W. G. (1987). *The Seismic Design of Plywood Sheathed Shear Walls.* University of Canterbury, Christchurch.

Thomas, G. C., Buchanan, A. H., & Dean, J. A. (1993). The Structural Design of a Multi-storey Light Timber Frame Residential Building. *IPENZ Transactions, 19*(1/CE), 35-41.

Zhu, K., Al-Bermani, F. G. A., Kitipornchi, S., & Li, B. (1995). Dynamic Response of Flexibly Jointed Frames. *Engineering Structures, 17*(8), 575-580.